Thèse

pour l'obtention du grade de

Docteur de l'Université Lille 1
Mention Mécanique

présentée par

Yassine Waddad

Équipe d'accueil : Laboratoire de Mécanique de Lille (FRE 3723)
École Doctorale : Ecole doctorale Sciences Pour l'Ingénieur (SPI) n° 72
Composante universitaire : Université Lille 1

Titre de la thèse :

Multiscale thermomechanical strategies for rough contact modeling - Application to braking systems

Soutenue le 19 Juin 2017
Composition du jury :

Jury

D. Nélias	Prof., INSA LYON (France)	*Rapporteur*
M. Ciavarella	Prof., Politecnico di Bari (Italy)	*Rapporteur*
M. Bigerelle	Prof., Université de Valenciennes (France)	*Examinateur*
E. Rouhaud	Prof, Université Technologique de Troyes (France)	*Examinateur*
B. Desmet	Prof., Université de Valenciennes (France)	*Examinateur*

Encadrement

P. Dufrénoy	Prof., Université Lille 1 (France)	*Directeur de thèse*
G. De Saxcé	Prof., Université Lille 1 (France)	*Co-Directeur de thèse*
V. Magnier	M.d.C., Université Lille 1 (France)	*Encadrant*

Remerciements

Mon engouement pour la recherche a fait que j'ai décidé de faire une thèse à la suite de mon cursus d'ingénieur. La réalisation de ma thèse n'aurait pas été possible sans l'aide de plusieurs personnes, auxquelles je tiens à témoigner ma profonde gratitude et mon entière reconnaissance.

Mes pensées vont tout d'abord à mon directeur de thèse Philippe Dufrénoy que je remercie pour la confiance qu'il m'a accordée ainsi que sa disponibilité tout au long de ma thèse. Ses qualités humaines et sa rigueur professionnelle ont rendues bonnes mes conditions de travail et m'ont marqué sur le plan professionnel et personnel.

Je voudrais ensuite remercier chaleureusement Vincent Magnier pour avoir encadré ma thèse, en me guidant avec enthousiasme vers les différentes pistes de travail tout en me laissant une grande autonomie qui m'a permis de m'épanouir durant ma thèse. Je le remercie pour le temps qu'il m'as accordé, sa présence permanente a permis l'avancement de mon travail sans interruption.

J'adresse mes remerciements également à Géry de Saxcé qui a co-dirigé cette thèse; ses conseils précieux et ses idées ont participé indéniablemet à l'aboutissement de ce travail. Je le remercie pour ses encouragements et sa disponibilité malgré ses responsabilités multiples.

J'aimerais remercier Daniel Nélias et Michele Ciavarella d'avoir accepté de rapporter mon mémoire et pour l'intérêt qu'ils ont pu porter à mes travaux. Je tiens aussi à remercier vivement Emmanuelle Rouhaud, Maxence Bigerelle et Bernard Desmet qui ont examiné avec attention ce travail.

Je tiens à remercier tous les membres de l'équipe μFrein et du Laboratoire de Mécanique de Lille en général. Je souhaiterais remercier en particulier Quentin, Loic, Itziar, Sofiane, Florent, Ruddy et Jean-François pour la bonne ambiance et les moments de détente et de partage passés au sein de la "D252".

J'adresse mes remerciements également à tous mes ami(e)s pour leur aide et leur soutien moral. La liste est tellement longue que je ne peux pas citer vos noms, mais je voudrais remercier particulièrement Hassan, Zouhair, Yassine et Ayoub pour l'aide qu'ils m'ont apporté avant d'entamer ma thèse.

C'est enfin à ma famille que j'adresse mes derniers remerciements : mes parents Fatima et Mohamed et mon frère Anas pour leur affection infaillible et le soutien moral et financier qu'ils m'ont toujours offert, et, en dernier lieu, mon épouse Maryam pour sa tendre présence, son soutien indéféctible et son amour inconditionnel.

Yassine

Abstract

Keywords :

Contact analysis, Surface Roughness, Finite element method, Multi-scale analysis, Thermo-mechanical modeling

Abstract

Friction brakes are subjected to important developments aiming to increase their energetic efficiency and durability on the one hand and, on the other hand, decrease their maintenance costs and their impacts on the environment (noise, particle emissions,etc.). In these applications, the contact interface between the rotating part of the brake and the static one, is central to its functioning as it presents the location of heat dissipation, thermal exchanges and mechanical interactions. Indeed, these phenomena are a source of wear, leading thus to the constant modification of the contact surface and material properties which may affect the braking performances. To address these issues, the current approach used by manufacturers, which is based on feedback tests, is expensive and inefficient against the new technical and environmental requirements. Besides, experiments can not give precise measures of contact surface data. Hence, theoretical modeling and numerical simulations can help to fill this gap.

The main objective of this work is to propose a numerical strategy consisting of modeling contact applications like brakes with realistic assumptions made at the contact interface by considering micro-contact phenomena, unlike the classical approaches which assume perfect contact conditions. This challenge has been overcome by building a methodology which associates a large scale Finite Element model of the system and several refined micro-contact models considering only the interface and covering the thermal, mechanical and wear features.

At micro-scale modeling, contact analysis has been performed with semi-analytic approaches considering the real contact area for a given topography. The thermal and the mechanical features are both considered and the contact problem is solved by means of quadratic programming. The case of a normal gradient of properties has also been investigated, which is often encountered in case of severe thermal loadings. Moreover, the evolution of surface roughness has been considered by modeling wear with Archard's law. From the micro-scale analysis, several contact parameters have been calculated such as contact stiffness, thermal conductance, wear volume, heat distribution, etc. The dependency of all these parameters on many physical properties has been investigated.

Thereafter, these parameters have been integrated into a Finite Element large scale model using an embedding strategy which conserves the surface flatness at the system scale and considers the effects of roughness and its evolution. With this technique, the contact phenomena complexity is transformed into homogenized contact laws and parameters that are integrated into the macro-scale model. The advantage is the considerable reduction of computation time while maintaining the precision of calculations in comparison to classical Finite Element ones. This multi-scale methodology has been used for dynamic and thermo-mechanical analysis of braking systems with the aim of evaluating their performances considering micro-scale issues. With this strategy, the interaction between non uniform surface and system behavior is clearly shown. The results of numerical simulations highlight the impact of the contact interface and its evolution on the braking performances, and vice versa.

Résumé

Mots-clés :

contact, rugosité, éléments finis, Multi-échelle, modélisation thermo-mécanique

Résumé

Les freins à friction font l'objet d'importants développements visant à améliorer d'une part leur efficacité énergétique et leur durabilité, et d'autre part, réduire leurs coûts de maintenance ainsi que leurs impacts environnementaux. Dans ces applications, l'interface de contact entre la partie statique du frein et sa partie mobile, est importante dans leur fonctionnement, puisqu'elle présente l'endroit où est dissipée l'énergie et où se produisent des échanges thermiques et des interactions mécaniques. De plus, ces phénomènes sont à l'origine de l'usure, conduisant ainsi à une évolution continue de la surface de contact et des propriétés des matériaux, ce qui peut influencer les performances du système. Afin de traiter ces problèmes, les industriels se basent actuellement sur des retours d'expériences de type essai/erreur qui sont coûteuses et peu efficaces face aux nouvelles exigences et réglementations. De plus, les mesures expérimentales sont difficilement accessibles dans les aires de contact. Ainsi, la modélisation numérique présente une des solutions alternatives permettant de diminuer le nombre d'essais et de mieux cerner les phénomènes de contact.

L'objectif principal de cette thèse est de proposer une stratégie numérique consistant à modéliser des systèmes, présentant un contact mécanique tel qu'un frein à friction, avec des hypothèses réalistes au niveau du contact consistant à considérer les phénomènes se produisant à l'échelle microscopique. Ce challenge a été surmonté en développant une méthodologie qui associe un modèle Éléments Finis macroscopique du système et plusieurs modèles micro qui considèrent l'interface de contact réelle et ses aspects thermique et mécanique ainsi que son usure.

A l'échelle microscopique, la modélisation du contact a été faite en se basant sur des approches semi-analytiques qui considèrent l'aire de contact réelle pour une topographie donnée. Les aspects thermique et mécanique sont tous les deux considérés et le problème est résolu avec des techniques d'optimisation sous contraintes. Le cas d'un matériau à gradient de propriétés normal à la surface a été aussi considéré, qui est souvent rencontré dans le cas de sollicitations thermiques sévères L'usure est modélisée par la loi d'Archard. Á partir de ces calculs, l'évolution de plusieurs paramètres physiques a été étudiée, tels que la raideur de contact, l'aire de contact réelle, la conductance thermique, la distribution de chaleur, la température de surface, etc.

Ensuite, ces paramètres ont été intégrés dans un modèle macroscopique en utilisant une stratégie d'enrichissement qui conserve la planéité des surfaces de contact tout en considérant l'effet de la rugosité et de son évolution. Avec cette technique, la complexité des phénomènes de contact est traduite par des paramètres/lois de contact homogénéisés qui sont intégrés dans le modèle macroscopique. L'avantage de cette méthode est la réduction considérable du temps de calcul en comparaison à des calculs Éléments Finis complets, tout en accédant à des informations locales précieuses. Cette stratégie de modélisation multi-échelle a été adoptée pour l'analyse dynamique et thermo-mécanique des systèmes de freinage afin d'évaluer leurs performances prenant en compte l'effet de l'interface de contact. Avec cette stratégie, les interactions entre l'interface et le système sont bien éclaircies. Les résultats des simulations numériques montrent l'impact de l'interface et de son évolution sur les performances du frein et vice-versa.

Contents

General introduction

0.1 Context of the thesis

The transport domain has been subjected to important developments in the recent years. For instance, the progress achieved in railway and automotive sectors helped to increase the maximal speed. However, the operating speed is limited to much lower values. For example, a vehicle could reach easily a speed of $200km/h$ while the speed limit on highways is $130km/h$. These limitations are related to transport operating costs and maintenance which increase with the operating speed.
To overcome this obstacle, for instance, the manufacturers seek to improve braking systems by reducing their weights and numbers, and increasing their efficiency and life cycle. Nevertheless, the improvement of braking systems is subjected to environmental requirements related to noise pollution and particle emissions. A compromise has therefore to be found between the different needs and requirements.
Most brakes commonly use friction to absorb the mechanical energy and inhibit the motion of the system. In friction brakes, the braking action is generally performed by pressing together the surface of a static friction material into a rotating solid (e.g. an axle or a wheel). This contact surface is central to the braking action, as it represents the location where several complex and prominent phenomena occur.
On one hand, friction transforms mainly the kinetic energy into heat. The consequence is a rise of temperature reaching high levels that cause wear at the interface and possible degradation of the contacting materials (damage, fracture, etc.). Furthermore, air quality is also affected by particle emissions originating from wear. Thus, the knowledge of surface temperature is of high interest, as it allows to choose efficiently the friction brake materials, and thus reduce the maintenance costs and increase their performance (durability, etc.).
On the other hand, during braking, a small part of energy may be converted into acoustic energy, contributing to noise pollution. Indeed, it has been shown that the contact interface between the disc and the friction material generates numerous kinds of high-pitched noises, of whom squeal is the most encountered. For instance, in the automotive industry, even if squeal does not significantly affect performances, such noise causes a high customer complaints warranty cost each year. Thus, the understanding of the system dynamics is prominent to study the noise generation propensity.
The contact interface is therefore involved in many issues affecting braking performances. Actually, to face up these issues, manufacturers implemented solutions which are mainly based on the use of feedback based tests and the empirical trial/error methods. Such method leads to complex friction material development. This kind of methods reflects a lack of a real understanding of the mechanisms governing friction brakes needing a high number of trial tests which is very costly and inefficient in front of the new technical and environmental requirements.
Furthermore, the phenomena occurring in the interface are of high complexity since they cover many areas of physics like thermic, mechanics and tribology. To deal with such a problem, small-scale experiments are of great interest, allowing a real understanding of contact interface phenomena. However, despite the recent advances in measuring techniques, it is difficult to set up an experiment within the contact

area to measure surface data (temperature, pressure, contact area, etc). Thus, theoretical modeling and numerical simulations can help to fill this gap.
In the recent years, with the development of computational tools, several numerical strategies covering various aspects such as dynamics and thermo-mechanics, have been proposed for braking systems modeling. However, even if these aspects have been well handled from a structural point of view, there are still some points related to contact phenomena, which are often simplified or not considered at all.
In fact, on one side, the classical modeling approaches consider only the scale of brake components and assume that the contact interface is smooth and perfect, neglecting thus the effects of roughness, thermal and stress localizations, wear and many other features happening in several scales smaller than the brake system's scale.
On the other side, contact phenomena have been widely studied using various analytical and numerical models, by targeting a particular physic (mechanical, electrical, thermal, etc.) and choosing the appropriate scale (meso, micro or nano-scale). Nevertheless, such models do not consider the system's induced interactions.
Thus, this work objective is to propose a numerical strategy going beyond the existing ones by considering the contact complex phenomena at the system's scale and the different couplings presents in the system (mechanics, thermal, tribology, etc.). This is a real challenge as it allows to take an important step toward developing realistic numerical strategies that can be integrated into the industrial design processes. Indeed, the developed approach should not only consider the real contact phenomena but also provide results within a reasonable computational time.
With the purpose of bringing the reader into the contact phenomena issues, the following section presents these points from a physical point of view. Afterwards, existing modeling solutions are briefly presented, as they will be discussed, in detail, in the following chapters of this thesis. Finally, the modeling strategy proposed in this work will be presented.

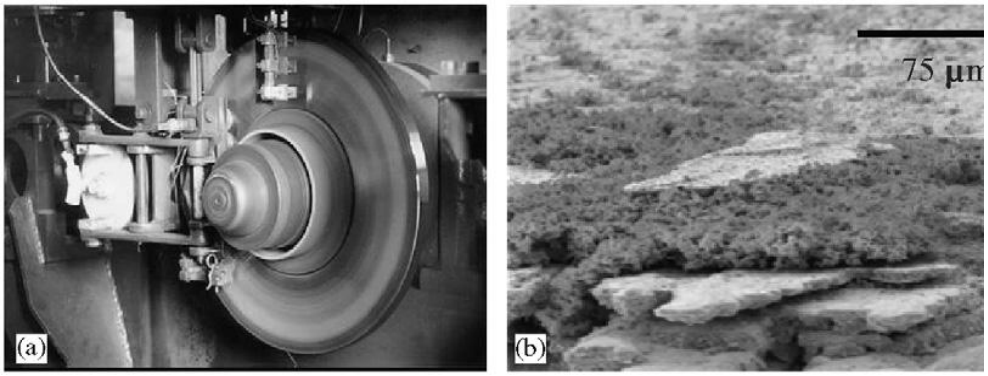

Figure 1: (a) TGV braking system (b) Microscopic image of a friction material surface [Roussette *et al.*(2001)]

0.2 The contact problem : physical point of view

The contact problem is one of the most relevant issues in engineering applications. A proper understanding of the contact mechanisms is crucial in the design process. Contact between two solids allows transferring mechanical loads, heat and electrical power in some applications. These exchanges are performed from one solid to another through the contact surface. The knowledge of the contact area is of great interest,

as it influences these exchanges.
Real surfaces are generally non-smooth, thus the real contact area is much smaller than the nominal one. Indeed, real solids have rough surfaces, and make contact only at separated zones where the asperities of the two mating surfaces are in contact. Thus, the interactions between the contacting solids are mainly performed through these micro zones.
Therefore, contact forces are concentrated in these areas and, in case of the presence of a thermal gradient, heat flows mainly throw these zones and marginally through the air contained in these gaps and radiation. As the contact load increases, the gap between the two surface decreases and the contact area increases. This evolution affects both the stiffness and the thermal conductance of the contact, and certainly depends on the surface topography, and both thermal and mechanical loads, with respect to material properties.
In sliding contact problems, which is the case of braking systems, frictional forces appear in the real contact zones as a resistance to the sliding motion. As it is commonly known, the largest percentage of the frictional energy is transformed into a thermal energy through several mechanisms (plastic deformations, atomic scale interactions, etc.). As a consequence, high elevations of temperature occur near to the contact area. Since the micro-contact zones are very small, the temperatures and stresses near to them would be severe, and could damage the material, accelerate the wear process and change the material properties by overheating[Archard(1959), Furey(1964), Kennedy(1984), Bos and Moes(1995)]. Moreover, the thermal expansion around contact zones can give birth to the phenomenon known as thermoelastic instability which disturbs the pressure and temperature distribution [Barber(1969)]. Therefore, the knowledge of the mechanisms that originate heat generation, their location and the ability to measure or predicate surface temperature, is important to avoid material failure.
Furthermore, high temperatures may lead to melting which cause wear with sliding. In addition, the wear process can be accentuated by micro-cracks due to high stresses and chemical transformations if the environment is corrosive [Meng(1995), Masen(2005)]. Moreover, there is several types of wear : adhesive, abrasive, corrosive and fatigue (see Fig.2). Generally, in real contact systems, wear does not take place through a single mechanism [Kato(2000)]. However, with regard to many factors (material properties, dynamic behavior, environment, etc), it may be possible that one or more of these types are the dominant ones. Thus, to estimate correctly the material loss, it is necessary to know the dominant mode with respect to the system, the contact situation and material properties.
The main consequence of wear is the change of the contact surface topography due to material removal. The removed material debris integrate what is commonly known as the "tribologic circuit" (see Fig.3). Indeed, a part of surface debris circulates within the contact interface while another one is ejected from the contact system. The part remaining inside the contact system can either continue its circulation or be compacted to form a thin layer called "third body". As sliding continues, this third body is in turn fragmented progressively and its debris recirculate within the interface. Thus, this circuit traduces the cycle life of a particle from its creation to its ejection from the system or the end of the sliding motion if the particle is still within it [Eriksson *et al.*(1999)]. Fig.4 illustrates a 3D image of a worn surface. In this image, we can remark the presence of what is namely called "contact plateaus". These zones correspond either to the compacted third body zones or the worn zones of the surface.
The presence of the third body modifies the exchanges between the contacting solids, as it represents an additional obstacle at the interface. Moreover, the complexity of the third body lies in the various states in which it exists. Indeed, the third body presents the wear particles, the agglomerated debris that can be at different stages and the compacted ones. Thus, its physical properties depend surely on its state.
Surface roughness is implicated in several issues. Its evolution during contact affects the dynamic behavior of the system [Bergman(1998), Eriksson *et al.*(2002)]. As is shown in [Eriksson *et al.*(1999)], the change of surface roughness leads to a change of the pressure and temperature distributions, these two factors having the major impact on the generation of brake squeal. Indeed, squeal appears mainly when the system is

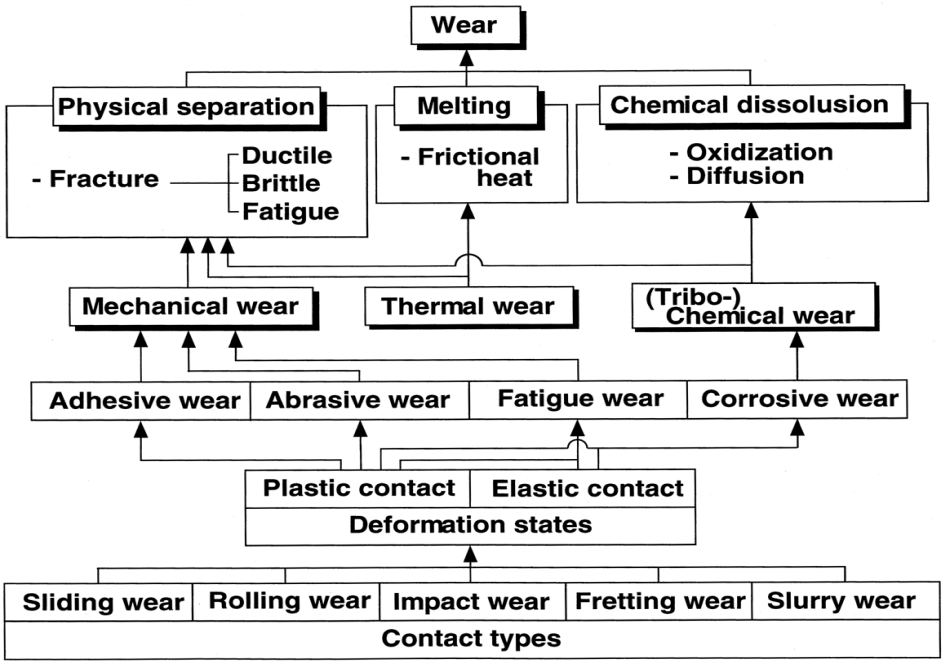

Figure 2: Classification of wear modes and their interrelations [Kato(2000)]

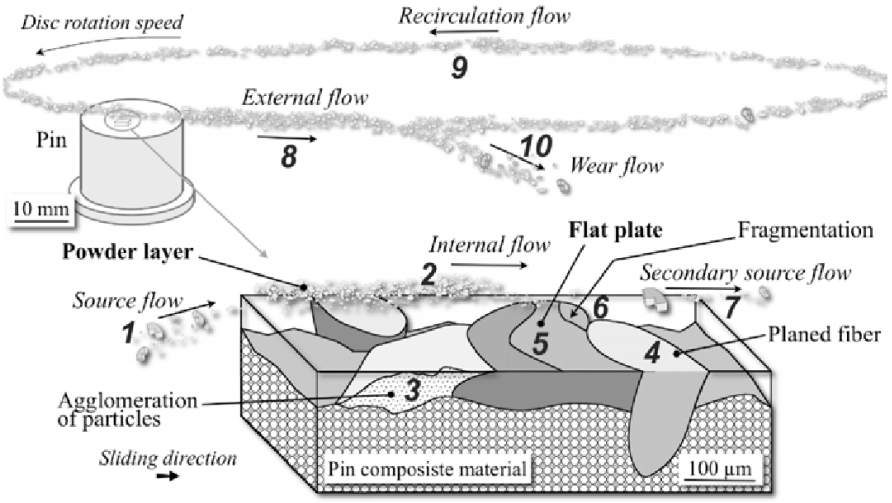

Figure 3: Schematic of the tribologic circuit in a sliding frictional contact [François *et al.*(2006)]

unstable. This is the case when the deformation energy of the system is higher than the dissipated one and the contact interface is involved in the dissipation process [Fieldhouse and Newcomb(1996)]. For instance, Fig. 5 shows a hologram of an unstable mode of a braking system reconstructed using interferometry. Furthermore, the increase of the real contact area with friction, by wear and third body compaction, leads to an increase of the friction coefficient [Bergman *et al.*(1999)]. As a consequence, the squeal generation

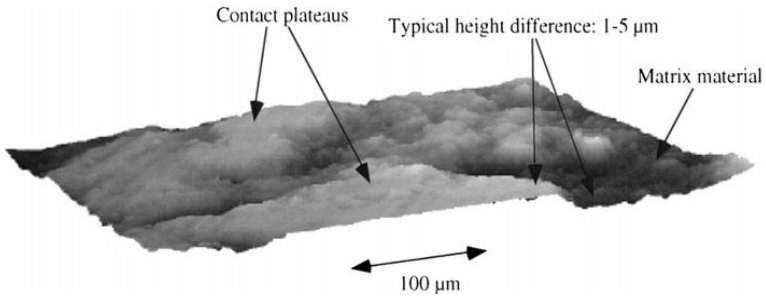

Figure 4: 3D image of a worn rough surface obtained with white light interferometry [Eriksson *et al.*(1999)]

increases dramatically with friction (see Fig.6). Thus, the contact surface evolution plays a key role in squeal generation.

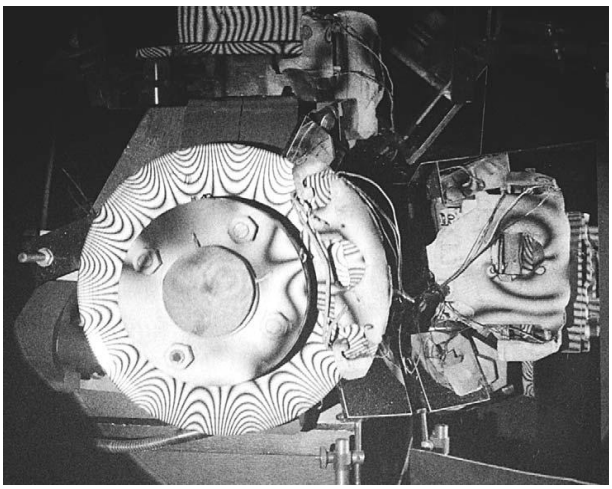

Figure 5: Fieldhouse and Newcomb's reconstructed hologram of a squealing disc brake system [Fieldhouse and Newcomb(1996)]

Furthermore, thermal contact phenomena originate a thermal gradient which may cause thermal damage and early failures. Indeed, surface topography and thermal expansions lead to localized contact areas and hot spots [Dufrénoy and Weichert(1995), Majcherczak *et al.*(2006)]. For detailed informations about the classification of these gradients and their characteristics, the reader may refer to [Dufrénoy and Weichert(1995)]. The shape and the size of these hot spots depend on many factors and control the shape of cracks, surface degradations and transformations and the flow of wear debris. Besides, the rheology of the resultant third body plays a key role in speed accommodation [Majcherczak *et al.*(2006)]. For instance, in Fig.7 are shown surface cracks induced in a rotating system developed by [Majcherczak *et al.*(2007)]. Thus, to prevent the initiation of these cracks and to understand the way as they spread, it is interesting to estimate correctly these gradients and their resulting stresses.
Physics in the contact interface is of high complexity. This brief and non-exhaustive review does not present all the contact phenomena features. Indeed, here, our concern is only focused on some meso and

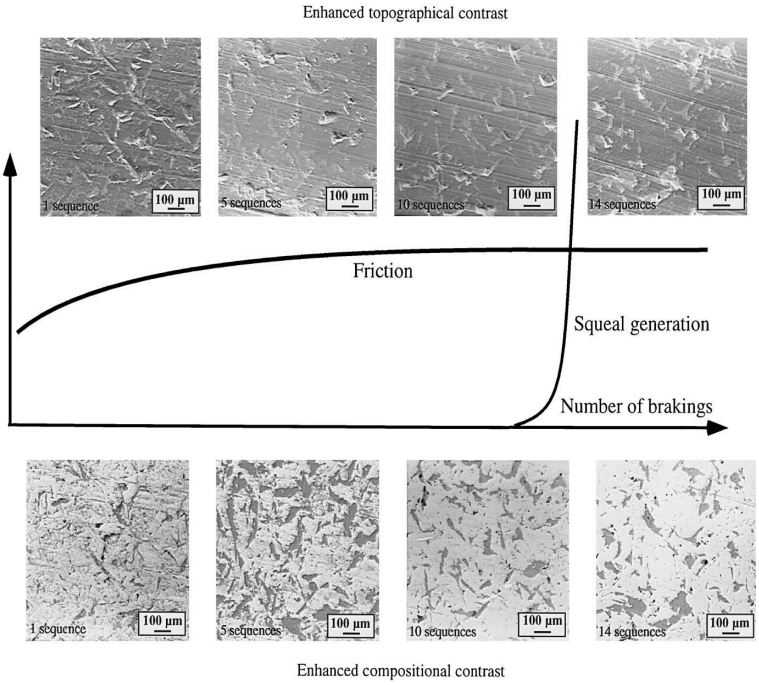

Figure 6: Gradual change of the disc surface and corresponding friction and squeal generation curves [Bergman *et al.*(1999)]

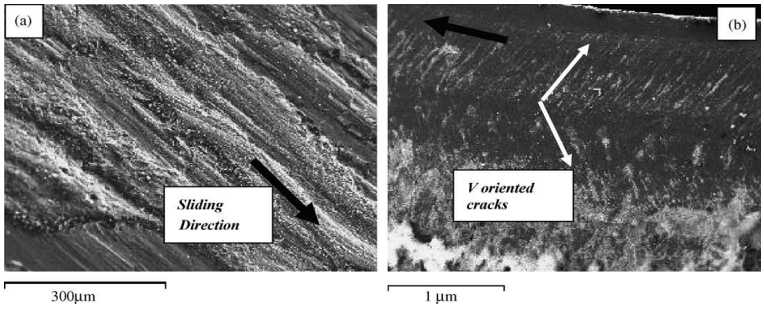

Figure 7: Orientation of surface cracks in the mobile side of a sliding contact for two kind of materials (a: C35 steel and b: sapphire) [Majcherczak *et al.*(2006)]

micro-scale issues. But in fact, the contact complexity goes beyond these scales to cover the atomic scale. For instance, friction and adhesion are related to inter-atomic potentials [Landman *et al.*(1993)].
In the contact surface take place several phenomena which are linked to each other. As we can see, their effects on the functioning of the system are considerable. In the next paragraph, are presented some modeling solutions for these phenomena.

0.3 The contact problem : modeling solutions

0.3.1 Contact modeling of rough surfaces : mechanical and thermal aspects

Many different models have been proposed to solve the contact mechanics problem. The first contact model goes back to the pioneering work of Hertz (1882). As is well known, his theory considers the frictionless smooth contact between two elastic solids with curved surfaces. Only since the middle of the twentieth century, researchers made many advancements in contact phenomena like friction, adhesion and roughness. For instance, surface roughness effects have been highlighted by the experiments of [Bowden and Tabor(1939)], by measuring the electrical conductance for a wide range of loads. Their results allow to estimate the contact area and confirm that the real contact area is very small comparing to the apparent one.
Surface roughness analysis is the first step when dealing with the contact problem. Its characterization can be performed either with statistical approaches or fractal techniques [Abbot and Firestone(1933), Longuet-Higgins(1957), Nayak(1971)]. Besides, numerical surfaces can be generated with surface parameters obtained from measurements. For instance, the spectral density or the auto-correlation function can both be used to generate random rough samples [Persson *et al.*(2005)].

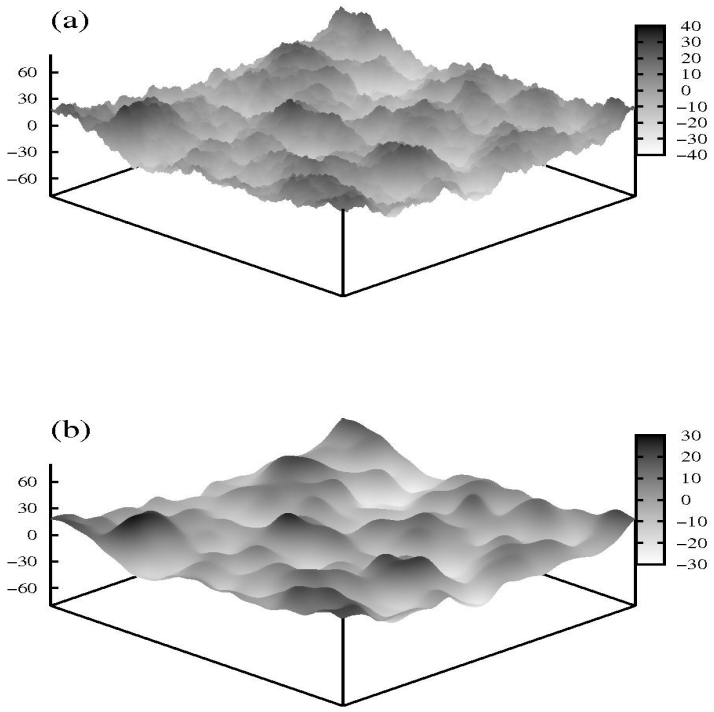

Figure 8: Two rough fractal surfaces generated numerically using the power spectrum density [Yang and Persson(2008)]. The two samples correspond to two different surface scales

With the statistical surface parameters, several contact theories have been proposed [Archard(1953), Greenwood and Williamson(1966), Bush *et al.*(1975)]. These works consider a rough surfaces as a random set of spherical or parabolic asperities. However, these models suffer from many weaknesses such as their dependencies on the surface statistical parameters and several simplifying assumptions, for instance

the non-consideration of interactions between asperities. Nevertheless, these theories have been improved through the last years [Ciavarella *et al.*(2006)] and have been very successful until the end of the twentieth century.

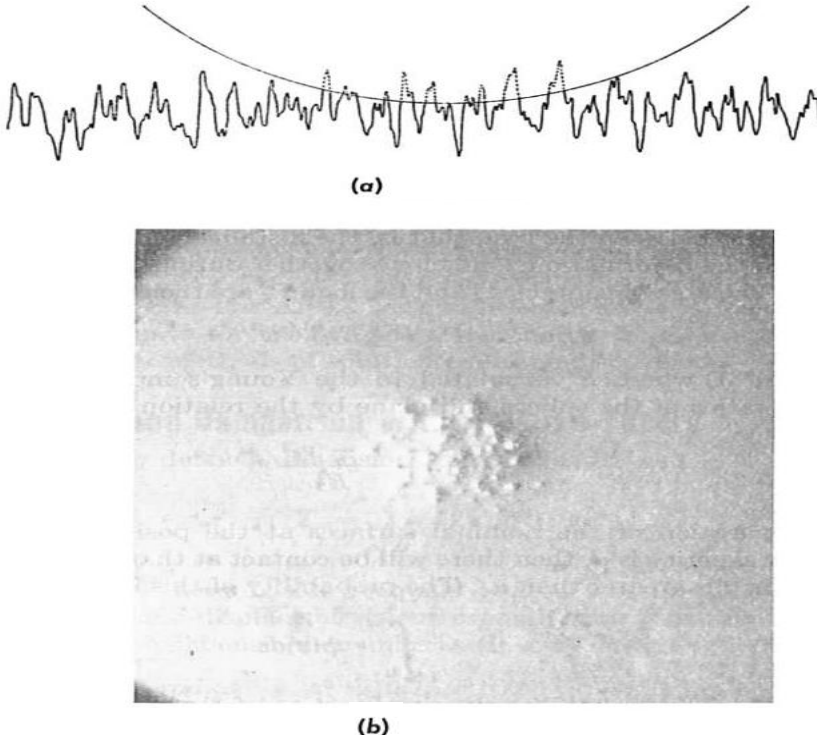

Figure 9: Contact between smooth sphere and rough plane. (a) Schematic of the problem, (b) Actual contact spots for steel ball pushed against glass block [Greenwood and Tripp(1967)]

With the increasingly advancement in computing industry, the use of numerical methods has become very important in the last years. Contact modeling has been one of the most treated topics. Using constrained optimization techniques, this problem has been solved with the Finite Element Method (FEM) [Wriggers(2006)]. Smooth contact has been extensively studied in many applications while the rough contact problem is poorly explored since the needed computational time to address it increases with roughness[Pei(2005)]. Indeed, a highly refined mesh is necessary to perform a precise estimation of a rough contact evolution, which can be extremely costly in terms of time, especially for industrial research. Another numerical technique has been also used to solve the rough contact problem, which consists of meshing only the surface and define the so-called influence coefficients[Johnson(1987), Willner(2008)]. The problem is solved with optimization methods. The most important point of this method is its rapidity comparing to FEM. This method can also be accelerated with the Fast Fourier Transform [Gallego *et al.*(2010)]. Moreover the frictional contact problem can also be treated with this method in a coupled way such as in [Willner(2008)] or by decoupling the normal problem and the tangential one such as in [Gallego *et al.*(2010)]. Nevertheless, from these works, it seems that the tangential behavior have a relatively negligible effect on contact properties like the real area and wear. Indeed, the elastic tangential deformations are much lower comparing to the normal ones, the latter define mainly the contact area and the normal pressure. The tangential deformations can change the shape of the pressure distribution but

the total normal load remains almost the same [Willner(2008)].
Furthermore, other methods have been used to solve the rough contact problem like the continuum approach of [Persson *et al.*(2002)] which is based on the surface spectral density. Indeed, he derives a diffusion-like equation for the stress distribution. This approach is interesting as it exhibits the multi-scale nature of the rough contact problem. Besides, the dynamic molecular approach have been also used for rough contact modeling [Almqvist *et al.*(2011)], which is a particle based approach. However, this method is limited to the contact problem at the atomistic scale since it needs a huge amount of computation time.

Contact mechanics modeling allows defining the real contact area distribution. The knowledge of the contact area is beneficial for several contact features such as heat conduction [Cooper *et al.*(1969), Mikic(1974), Yovanovich(2005)] and generation [Tian and Kennedy(1994), Vick(2001)]. For these thermal issues, the most used theoretical framework is the method of heat sources that allows getting thermal solutions for simple geometries like circles and squares [Blok(1937), Carslaw and Jaeger(1959), Zeng *et al.*(1997)]. From these elementary solutions, rough contact modeling can be solved by superposing all heat sources [Chao and Trigger(1956), Coulibaly *et al.*(2014)]. Other numerical methods have been also used to solve the thermal contact problem [Laraqi(1996), Laraqi *et al.*(2009), Sadowski *et al.*(2010)], but often considering a simplified geometry of the surface.

0.3.2 Third body modeling

While the above cited approaches are dedicated to rough contact modeling from a static point of view, other approaches are used for the third body, which is a dynamic problem. Most of these methods are based on particle interactions. For instance, the Discrete Element Method (DEM)[Renouf *et al.*(2004), Renouf *et al.*(2011)] considers the third body as a flowing granular medium made from rigid or deformable particles. While this approach does not account for the large scale interactions between the contacting bodies, an improved approach called “Non Smooth Contact Dynamics" [Moreau(1986)] has been used in [Nhu(2017)] combining the FEM for contact bodies deformation and the DEM for the third body particles.
Other approaches are also used for the third body flowing issue such as the Cellular Automaton[Muller and Ostermeyer(2007)]. In this method, the medium is seen as a discrete set of cells having different states and linked to each other by many rules controlling the evolution of the third body. The state of each cell is defined by the state of its neighboring cells. An enhancement of this method is the Movable Cellular Automaton approach[Psakhie *et al.*(2001), Dimitriev *et al.*(2010)] which consists of pairing two cells by a state corresponding to their chemical bonds. Thereafter, a general equation is obtained to describe the motion of the automaton considering the links between the cells and the force of inter-cell interaction. To solve the problem, a response function is introduced to consider the material behavior (elastic, plastic, etc.) by linking the cell deformation to stress.

0.3.3 Braking system modeling

Concerning braking simulations, contact modeling is often simplified by considering only flat surfaces. The FEM has been widely used to solve this problem. For instance, braking systems modeling has been performed in [Newcomb(1960), Day and Newcomb(1988), Kao *et al.*(2000), Dufrénoy and Weichert(2003), Naidoo(2014), Mann(2017)] by considering a perfect contact. Furthermore, by reducing the degrees of freedom, other minimal approaches have been also proposed for the purpose of studying the dynamic behavior of the system. For instance, with mode Lock-in theory, the stability of frictional systems has been analyzed using simplified mass-spring systems [Hoffmann *et al.*(2002), Magnier *et al.*(2014)].
Since the scale of roughness is lower than the system's scale, there are several approaches allowing to

consider roughness effects [Zavarise *et al.*(1992), Bandeira *et al.*(2004), De Lorenzis and Wriggers(2013)]. The interesting point is that there is no need to mesh finely the contact surface. Indeed, the surface is flat and contact interface laws or parameters, traducing the micro-contact evolution, are integrated into a large scale model of the studied system. Besides, it considers both of the interface and the system behaviors and allows to reduce the computation time. For instance, [Wriggers and Reinelt(2009)] proposed a multi-scale strategy to compute a homogenized coefficient of friction that reflects the influence of roughness on a frictional contact. This kind of methods are of great interest and will be addressed in this thesis.

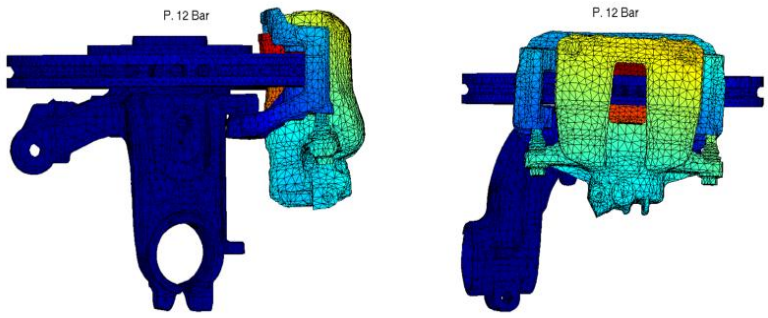

Figure 10: A finite element model of a complete braking system [G. Vermot des Roches(2011)]

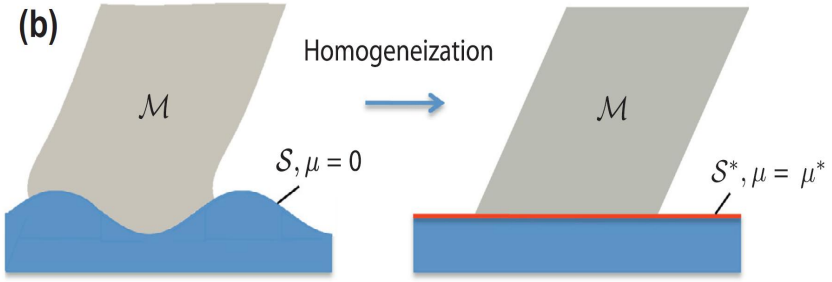

Figure 11: A finite element modeling strategy to compute a homogenized friction coefficient [Wriggers and Reinelt(2009)]

In addition to this brief review of the existing methods for contact modeling, complementary detailed reviews will be presented in the thesis chapters. With regard to the contribution of this work, the built modeling strategy is based on the different approaches described before. The choice of a method instead of another one depends on two main factors : the accuracy and the computation time.
In what follows, we present the objectives and the main lines of the realized work in this thesis.

0.4 Aim of the thesis

The aim of this thesis is to build a strategy which allows modeling large scale contact problems considering interface phenomena occurring at lower scales. The establishment of the strategy needs :

- The definition of the surface scale and the related contact phenomena;
- The development of contact models which consider these phenomena;
- The development of a strategy which integrates the interface behavior into a large scale numerical model.

In this thesis, the surface scale is the one of roughness (meso and micro scale). At this scale, contact modeling allows analyzing the evolution of contact properties under the effect of contact phenomena (thermal and mechanical loadings). Then, the calculated parameters are incorporated in a large scale numerical model of the system. In what follows, the latter two points are presented.

0.4.1 Micro-contact modeling

At the roughness scale, the first step in contact modeling is the definition of the real contact area. This will be done using several contact mechanics models. These models relate the load to area and displacements. With respect to the existing modeling solutions, the different models presented in this thesis are inspired from the semi-analytic asperity based models which consider interactions between asperities and the numerical models which discretize only the surface using the so-called influence coefficients. The Finite Element Method will be used as a verification tool of the developed models.
Furthermore, these models consider that the material is homogeneous. But, as noted earlier, there are material transformations occurring near to the interface (damage, phase change,etc.). In order to consider these transformations, we examine the case when a gradient of material properties emerges with heating and mechanical loadings. In this work, this gradient is considered to be normal to the interface. Moreover, due to the lack of informations about the way the material properties are varying, an in-depth material gradient has been introduced to describe various situations. Furthermore, the solid having a gradient of material properties will be assimilated as a multi-layered solid. Thus, the solid will be discretized in the normal direction to the interface into many layers, as explained later.
Another feature which has to be included is the surface roughness evolution due to wear in sliding contacts. For this, we consider that wear process occurs according to Archard's law. Here, many simplified assumptions have been considered to realize this objective. First, the contact is assumed to be perfectly sliding and the frictional forces are supposed not to cause elastic deformations within the solid, which means that friction is assumed not to change the contact area. Besides, the tribological circuit is not studied, thus wear debris flow, circulation and compaction will not be included in this thesis.
Once the contact area is defined, the thermal phenomena are studied by considering heat conduction and heat generation phenomena. These problems are also solved with the same philosophy adopted for the contact mechanics problem. The heat conduction problem is solved under stationary conditions by considering either homogeneous materials or a material properties gradient. With regard to the problem of heat generation, the problem is solved, under transient conditions, using the heat source method. Both works consider only a discretized surface. From these two works, the thermal conductance, surface temperatures and the distribution of heat are found for a given load, velocity, roughness and material properties. Note that, at this scale, thermal expansion, which can modify the contact area, is not considered.
Thus, with regard to the contact phenomena, this thesis will focus on the surface evolution under mechanical loads and wear. The thermal contact study provides the thermal conductance and heat partition, and allows to compute surface temperatures that can be used in wear modeling (e.g. a wear rate depending on temperature). With respect to the existing modeling solutions, many improvements and new solutions are presented in this thesis. The developed approaches are based on half-space solutions, potential theory, heat source method, integral transforms and optimization techniques. The studied surface samples are

generated with fractal methods using a spectral density. Several examples are presented with the aim to show the efficiency of the proposed models.

0.4.2 Multi-scale embedding strategy

In order to integrate the micro-scale calculations into a large scale model of a system, an embedding strategy is developed in this thesis which consists of defining, for each zone of the studied surface, a homogenized interface parameter/law obtained from the micro-contact analysis. These parameters are : stiffness, thermal conductance and the heat coefficient partition. They depend on both mechanical and thermal loadings and wear. As regards the friction coefficient, it will be fixed at both scales.
Two applications of this work strategy will be presented :

- The first one aims to investigate the interface effect on the dynamic behavior of a complete braking system using the Finite Element Method. The calculations are based on a quasi-static analysis which is followed by a complex modal analysis. The idea is to analyze the stability of the system modes using mode Lock-in theory for a given contact situation. Here, only the mechanical features are analyzed by considering only the contact stiffness. Note that, in this application, surface roughness does not evolve (wear is not considered).

- In the second study, we present a FEM thermo-mechanical analysis of a pin-on-disc system. Here, all the micro-scale studied features are integrated. The aim of this work is to evaluate the temperature field in the system considering surface evolution. Besides, the analysis is transient and the macro-scale thermal expansion is considered, which could affect the contact area. Compared to the first application, here, there is a time evolution of the contact surface with wear and temperature.

Through these two applications, the aim is to show the different features of the multi-scale strategy proposed in this work. The results highlight the role of the interface in defining the system's response.
Finally, this work presents an important step toward numerical modeling of contact applications considering a realistic contact interface behavior.

0.5 Outline of the thesis

The outline of this thesis follows the path of the strategy presented above. The different elements of this work are shown in Fig.12. The thesis can be divided into two parts. The first part deals with the contact mechanics problem while the second aims to investigate the thermal contact issues.
In Part 1, Chapter 1 describes the development of the multi-scale model for the contact mechanics problem considering roughness. This chapter is divided into two parts. The first part deals with the **micro contact problem** and the second one describes how the **interface behavior is embedded into a Finite Element model** using the strategy proposed in this work. At this point, the contact analysis is done for homogeneous solids.
In Chapter 2, the analysis is extended by considering a gradient of material properties by modeling the rough contact of **multi-layered solids**. The asperity based model proposed in Chapter 1 is extended to cover the case of the gradient using integral transforms and the transfer matrix technique.
In Chapter 3, a contact mechanics analysis is performed considering **wear process**. In this chapter, a different approach is used to solve the contact problem and wear is modeled using Archard's law. Here, the surface is fully discretized contrary to the asperity based approaches developed in the previous chapters. The case of a gradient of properties is also investigated.
Finally, Chapter 4 comes at the end of Part 1 to present the first application of the proposed strategy.

Indeed, a Finite Element analysis of a complete brake system is performed, considering the interface behavior. In this chapter, the study is done with the aim to show the **influence of roughness on mode Lock-in of a braking system**.
Part 2 begins by Chapter 5 which deals with the problem of the **stationary heat conduction in presence of roughness**. The case of the **in depth gradient** is also considered. While this chapter considers only the steady problem and a static contact, Chapter 6 extends the study to cover the **transient thermal problem of sliding contact with frictional heat generation**. For both chapters, the real contact area is considered from contact mechanics calculations presented in Part1. In these two chapters, a parametric study is presented with the aim to define the influence of each of the contact parameters.
Finally, at the end of Part 2, in Chapter 7, **a thermo-mechanical analysis of a pin-on-disc system** is described. Here, the multi-scale strategy is used and both thermal and mechanical features of the contact are considered. Moreover, surface evolution due to wear is also considered. An example is presented for a given load and velocity, with the aim to highlight the effects of the time evolution of the interface.
Of course, there are still many features that are not addressed in this thesis. Also, there are many weaknesses arising from many simplified assumptions that should be improved in future works. This is why the main results and assumptions are recalled at the end of this thesis, and the prospects and possible improvements are proposed.

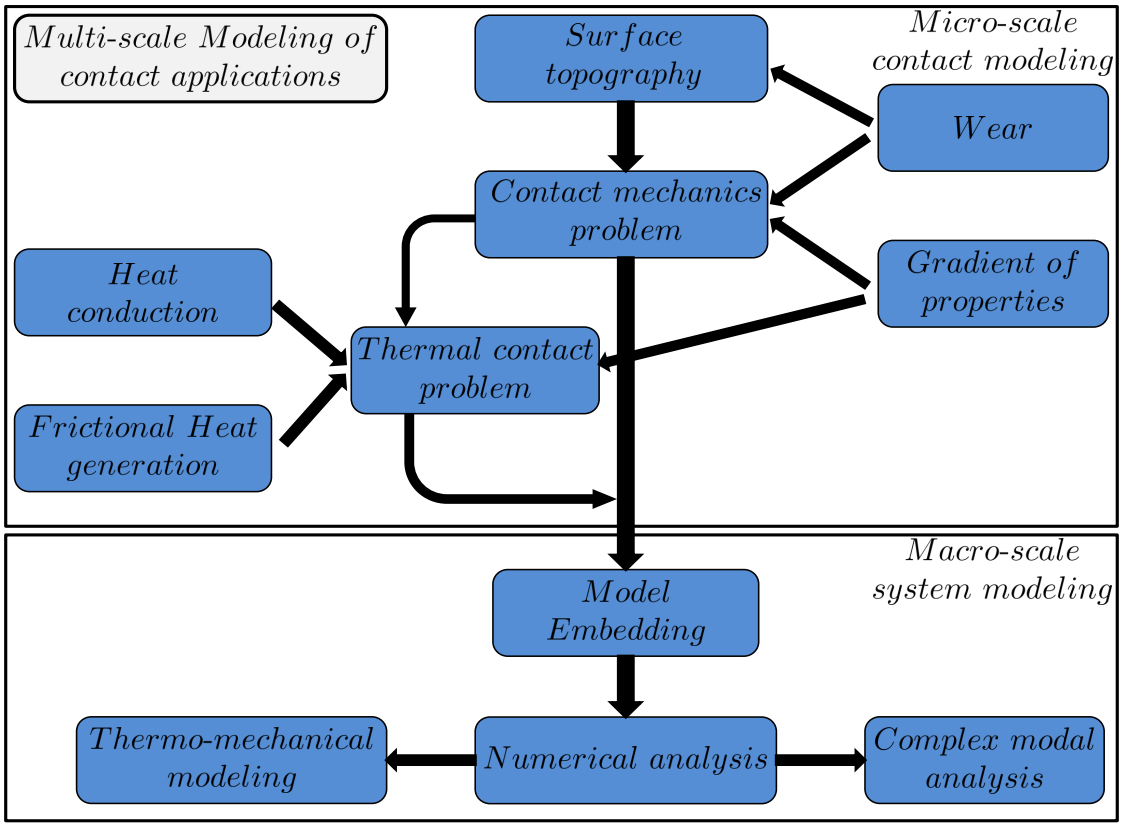

Figure 12: Outline of the thesis

Bibliography

[Abbot and Firestone(1933)] Abbott, E & Firestone, F. *Specifying surface quality: a method based on accurate measurement and comparison*. Journal of Mechanical Engineering, No. 55, 1933, 569-572.

[Almqvist *et al.*(2011)] Almqvist, A., Campana, C., Prodanov, N., & Persson, B. N. J. *Interfacial separation between elastic solids with randomly rough surfaces: comparison between theory and numerical techniques*. Journal of the Mechanics and Physics of Solids, 2011, 59(11), 2355-2369.

[Archard(1953)] Archard, J. F. *Contact and rubbing of flat surfaces*. Journal of Applied Physics, 1953, 24(8), 981-988.

[Archard(1959)] Archard, J. F. *The temperature of rubbing surfaces*. Wear, 1959, 2(6), 438-455.

[Bandeira *et al.*(2004)] Bandeira, A., Wriggers, P. & de Mattos Pimenta, P. *Numerical derivation of contact mechanics interface laws using a finite element approach for large 3D deformation*. International Journal for numerical methods in Engineering, Wiley Online Library, 2004, 59, 173-195

[Barber(1969)] Barber, J. R. *Thermoelastic instabilities in the sliding of comforming solids*. In Proceedings of the Royal Society of London A: Mathematical, Physical and Engineering Sciences, 1969, 312(1510), 381–394.

[Bergman(1998)] F. Bergman *Tribological nature of squealing disc brakes*. Uppsala University, 1998.

[Bergman *et al.*(1999)] Bergman, F., Eriksson, M., & Jacobson, S. *Influence of disc topography on generation of brake squeal*. Wear, 1999, 225, 621–628.

[Blok(1937)] Blok, H. *Theoretical Study of Temperature Rise at Surfaces of Actual Contact under Oiliness Conditions*. Proc. Inst, of Mechanical Engineers General Discussion of Lubrication, 1937, 2, 222-235.

[Blok(1963)] Blok, H. *The flash temperature concept*. Wear, 1963, 6(6), 483-494.

[Bos and Moes(1995)] Bos, J., & Moes, H. *Frictional heating of tribological contacts*. Journal of tribology, 1995, 117(1), 171-177.

[Bowden and Tabor(1939)] Bowden, FP & Tabor, D. *The area of contact between stationary and between moving surfaces*. Proceedings of the Royal Society of London. Series A, Mathematical and Physical Sciences, 1939, 169(938), 391–413.

[Bush *et al.*(1975)] Bush, A., Gibson, R. & Thomas, T. *The elastic contact of a rough surface*. Wear, 1975, 35, 87-111

[Carslaw and Jaeger(1959)] Carslaw, H. S., & Jaeger, J. C.*Conduction of heat in solids*. Oxford: Clarendon Press, 1959

[Chao and Trigger(1956)] Chao, B. T., & Trigger, K. J. C. *Temperature distribution at tool-chip and tool-work interface in metal cutting.* ASME, 1956.

[Ciavarella *et al.*(2006)] Ciavarella, M., Delfine, V. & Demelio, G. *A re-vitalized Greenwood and Williamson model of elastic contact between fractal surfaces.* Journal of the Mechanics and Physics of Solids, 2006, 54, 2569-2591

[Cooper *et al.*(1969)] Cooper, M. G., Mikic, B. B., & Yovanovich, M. M. *Thermal contact conductance.* International Journal of heat and mass transfer, 1969, 12(3), 279-300.

[Coulibaly *et al.*(2014)] Coulibaly, M., Chassaing, G., & Philippon, S. *Thermomechanical coupling of rough contact asperities sliding at very high velocity.* Tribology International, 2014, 77, 86-96.

[Day and Newcomb(1988)] Day, A..J & Newcomb, T.P. *The dissipation of frictional energy from interface of an annular disc brake.* Proc. Inst. Mech. Eng. Part F: J Rail Rapid Transit, 1988, 202, 91-99.

[De Lorenzis *et al.*(2013)] De Lorenzis, L. & Wriggers, P., *Computational homogenization of rubber friction on rough rigid surfaces.* Computational Materials Science, 2013, 77, 264-280.

[Denape and Laraqi(2000)] Denape, J., & Laraqi, N. *Aspect thermique du frottement: mise en évidence expérimentale et éléments de modélisation.* Mécanique & industries, 2000, 1(6), 563-579.

[Dimitriev *et al.*(2010)] Dmitriev, A. I., Schargott, M., & Popov, V. L. *Direct modelling of surface topography development in a micro-contact with the movable cellular automata method.* Wear, 2010, 268(7), 877-885.

[Dufrénoy and Weichert(1995)] Dufrénoy, P., & Weichert, D. *Prediction of railway disc brake temperatures taking the bearing surface variations into account.* Proc IMechE Part F: J Rail Rapid Transit, 1995, 209, 67-76.

[Dufrénoy and Weichert(2003)] Dufrénoy, P., & Weichert, D. *A thermomechanical model for the analysis of disc brake fracture mechanisms.* Journal of Thermal Stresses, 2003, 26(8), 815-828.

[Eriksson *et al.*(1999)] Eriksson, M., Bergman, F., & Jacobson, S. *Surface characterization of brake pads after running under silent and squealing conditions.* Wear, 1999, 232(2), 163-167.

[Eriksson *et al.*(2002)] Eriksson, M., Bergman, F. & Jacobson, S. *On the nature of tribological contact in automotive brakes.* Wear, Elsevier, 2002, 252, 26-36

[Fieldhouse and Newcomb(1996)] J.D. Fieldhouse & T.P. Newcomb *Double pulsed holography used to investigate noisy brakes.* Optics and lasers in Engineering, 1996, 25, 455–494.

[François *et al.*(2006)] François, M., Desplanques, Y., and Degallaix, G. *Méthodologie d'observation in situ des surfaces frottantes en freinage ferroviaire.* Tribologie dans les transports Actes des JIFT 2005, 2006, 27-36.

[Furey(1964)] Furey, M. J. *Surface temperatures in sliding contact.* ASLE TRANSACTIONS, 1964, 7(2), 133-146.

[Gallego *et al.*(2010)] Gallego, L., Nelias, D. & Deyber, S. *A fast and efficient contact algorithm for fretting problems applied to fretting modes I, II and III.* Wear, 2010, 268, 208–222.

[Greenwood and Williamson(1966)] Greenwood, J. & Williamson, J. *Contact of nominally flat surfaces.* Proceedings of the Royal Society of London. Series A. Mathematical and Physical Sciences, The Royal Society, 1966, 295, 300-319

[Greenwood and Tripp(1967)] Greenwood, J. & Tripp, H. *The elastic contact of rough spheres.* Journal of Applied Mechanics. 1967, 295, 153-159

[Hetzler and Willner(2012)] Hetzler, H. & Willner, K. *On the influence of contact tribology on brake squeal.* Wear, Elsevier, 2012, 46, 237-246

[Hoffmann *et al.*(2002)] Hoffmann, N., Fischer, M., Allgaier, R., & Gaul, L. *A minimal model for studying properties of the mode-coupling type instability in friction induced oscillations.* Mechanics Reasearch Communications, 2002, 29, 197–205.

[Johnson(1987)] Johnson, K. L. *Contact mechanics.* Cambridge university press, 1987

[Kao *et al.*(2000)] Kao, T., Richmond, J.W., Douarre, A. *Brake disc hot spotting and thermal judder: an experimental and finite element study.* Int. J. Vehicle Des., 2000, 23, 276-296.

[Kato(2000)] Kato, K. *Wear in relation to friction—a review.* Wear, 2000, 241(2), 151-157.

[Kennedy(1984)] Kennedy, F. E., *Thermal and thermomechanical effects in dry sliding.* Wear, 1984, 100(1), 453-476.

[Landman *et al.*(1993)] Landman, U., Luedtke, W.D., & Ringer, E.M. *Molecular dynamics simulations of adhesive contact formation and friction, in Fundamentals of Friction: Macroscopic and Microscopic Processes, Singer, I.L. and Pollock, H.M. (Eds.), Kluwer Academic Publishers, Dordrecht, 463.*. Kluwer Academic Publishers, 1993, Dordrecht, 463.

[Laraqi(1996)] Laraqi, N. *Phénomène de constriction thermique dans les contacts glissants.* International journal of heat and mass transfer, 1996, 39(17), 3717-3724.

[Laraqi *et al.*(2009)] Laraqi, N., Alilat, N., de Maria, J. G., & Baïri, A. *Temperature and division of heat in a pin-on-disc frictional device—exact analytical solution.* Wear, 2009, 266(7), 765-770.

[Longuet-Higgins(1957)] Longuet-Higgins, M. S. *The statistical analysis of a random, moving surface.* Philosophical Transactions of the Royal Society of London. Series A, Mathematical and Physical Sciences, 1957, 321-387

[Magnier *et al.*(2014)] Magnier, V., Brunel, J.F. & Dufrénoy, P. *Impact of contact stiffness heterogeneities on friction-induced vibration.* International Journal of Solids and Structures, Elsevier, 2014, 51, 1662–1669

[Majcherczak *et al.*(2006)] Majcherczak, D., Dufrenoy, P., Berthier, Y., & Nait-Abdelaziz, M. *Experimental thermal study of contact with third body.* Wear, 2006, 261(5), 467-476.

[Majcherczak *et al.*(2007)] Majcherczak, D., Dufrenoy, P., & Berthier, Y. *Tribological, thermal and mechanical coupling aspects of the dry sliding contact.* Tribology International, 2007, 40(5), 834-843.

[Mann(2017)] Mann, R., *Experiments and thermomechanical modelling of braking application and friction material characterization with loading history effect.* Université de Lille , 2017

[Masen(2005)] Masen, M. A., De Rooij, M. B., & Schipper, D. J. *Micro-contact based modelling of abrasive wear*. Wear, 2005, 258(1), 339-348.

[Meng(1995)] Meng, H. C., & Ludema, K. C. *Wear models and predictive equations: their form and content*. Wear, 1995, 181, 443-457.

[Mikic(1974)] Mikić, B. B. *Thermal contact conductance; theoretical considerations*. International Journal of heat and mass transfer, 1974, 17(2), 205-214.

[Moreau(1986)] Moreau, J.-J. *Une formulation du contact à frottement sec ; application au calcul numérique*. Comptes Rendus Acad. Sci. Paris, Series II, vol. 302, 1986, p. 779-801.

[Muller and Ostermeyer(2007)] Muller, M., & Ostermeyer, G.P. *A cellular automaton model to describe the three dimensional friction and wear mechanism of brake systems*. Wear, 2007, 263, 1175–1188.

[Naidoo(2014)] Naidoo R., D. *Influence of friction material & test sequence on disc brake squeal*. Université Lille-1 , 2014

[Nayak(1971)] Nayak, P. R. *Random process model of rough surfaces*. Journal of Tribology, American Society of Mechanical Engineers, 1971, 93, 398-407

[Newcomb(1960)] Newcomb, T.P. *Temperatures reached in disc brakes*. J. Mech. Eng. Sci., 1960, 2(3), 167–177.

[Pei(2005)] Pei, L., Hyun, S., Molinari, J. F. & Robbins, M. O.*Finite element modeling of elasto-plastic contact between rough surfaces*. Journal of the Mechanics and Physics of Solids, 2005, 53, 2385-2409

[Persson *et al.*(2002)] Persson, B., Bucher, F. & Chiaia, B. *Elastic contact between randomly rough surfaces: comparison of theory with numerical results*. Physical Review-Series B-, American Physical Society, 2002, 65, 184106

[Persson *et al.*(2005)] Persson, B., Albohr, O., Tartaglino, U., Volokitin, A. & Tosatti, E. *On the nature of surface roughness with application to contact mechanics, sealing, rubber friction and adhesion*. Journal of Physics: Condensed Matter, IOP Publishing, 2005, 17, R1-R62

[Psakhie *et al.*(2001)] Psakhie, S. G., Horie, Y., Ostermeyer, G. P., Korostelev, S. Y., Smolin, A. Y., Shilko, E. V., ... & Zavšek, S. *Movable cellular automata method for simulating materials with mesostructure*. Theoretical and applied fracture mechanics, 2001, 37(1), 311-334.

[Renouf *et al.*(2004)] Renouf, M., Dubois, F., & Alart, P. *A parallel version of the non smooth contact dynamics algorithm applied to the simulation of granular media*. Journal of Computational and Applied Mathematics, 2004, 168(1), 375-382.

[Renouf *et al.*(2011)] Renouf, M., Cao, H. P., & Nhu, V. H. *Multiphysical modeling of third-body rheology*. Tribology International, 2011, 44(4), 417-425.

[Roussette *et al.*(2001)] Roussette O, Desplanques Y, Degallaix G & Gallo Y, *Comportement tribologique en freinage á haute énergie de garnitures en matériaux organiques*. JFT 2001 Tribologie des Matériaux Organiques, Obernai, France, 2001.

[Sadowski and Stupkiewicz(2010)] Sadowski, P., & Stupkiewicz, S. *A model of thermal contact conductance at high real contact area fractions*. Wear , 2010, 268(1), 77-85.

[Tian and Kennedy(1994)] Tian, X., & Kennedy, F. E.,*Maximum and average flash temperatures in sliding contacts*. Journal of Tribology, 1994, 116(1), 167-174.

[G. Vermot des Roches(2011)] Vermot des Roches, G., *Frequency and time simulation of squeal instabilities. Application to the design of industrial automotive brakes*. PhD thesis, Centrale Paris, 2011.

[Vick(2001)] Vick, B., & Furey, M. J. *A basic theoretical study of the temperature rise in sliding contact with multiple contacts*. Tribology International, 2001, 34(12), 823-829.

[Nhu(2017)] Nhu, V. H. *Dialogues numériques entre échelles tribologiques*. INSA de Lyon, 2013

[Willner(2008)] Willner, K. *Fully coupled frictional contact using elastic halfspace theory*. Journal of Tribology, American Society of Mechanical Engineers, 2008, 031405, 1–8.

[Wriggers (2006)] Wriggers, P. *Computational contact mechanics*. 2nd ed., Springer, 2006.

[Wriggers and Reinelt(2009)] Wriggers, P. & Reinelt, J., *Multi-scale approach for frictional contact of elastomers on rough rigid surfaces*. Computer Methods in Applied Mechanics and Engineering, Elsevier, 2009, 198, 1996-2008

[Yang and Persson(2008)] Yang, C., & Persson, B. N. J. *Contact mechanics: contact area and interfacial separation from small contact to full contact*. Journal of Physics: Condensed Matter, 2008, 20(21), 215214.

[Yastrebov *et al.* (2015)] Yastrebov, V. A., Anciaux, G. & Molinari, J.-F. *From infinitesimal to full contact between rough surfaces: evolution of the contact area*. International Journal of Solids and Structures, 2015, 52, 83-102.

[Yovanovich(2005)] Yovanovich, M. M. *Four decades of research on thermal contact, gap, and joint resistance in microelectronics*. IEEE transactions on components and packaging technologies, 2005, 28(2), 182-206.

[Zeng *et al.*(1997)] Zeng, Z., Brown, J. M. B., & Vardy, A. E. *On moving heat sources*. Heat and mass transfer, 1997, 33(1-2), 41-49.

[Zavarise *et al.*(1992)] Zavarise, G., Wriggers, P., Stein, E. & Schrefler, BA. *Real contact mechanisms and finite element formulation - a coupled thermomechanical approach*. International Journal for Numerical Methods in Engineering, Wiley Online Library, 1992, 35, 767-785

Part I

Contact mechanics of rough surfaces

Transition

The first part of this thesis is related to the contact mechanics issues. Its first chapter is dedicated to the modeling of the normal contact of rough surfaces and homogeneous solids.
In this chapter, the contact mechanics problem is solved considering surface asperities and their interactions. The asperities are considered either spherical or elliptical and the problem solving is done by minimizing an objective function. Thereafter, the micro-contact behavior is integrated into a large scale numerical model using an embedding strategy based on the penalty method.
Finally, several examples are presented and compared with the Finite Element Method results, with the objective of showing the efficiency of the proposed strategy.
This chapter presents the first step towards the implement of the complete multi-scale strategy proposed in this thesis.

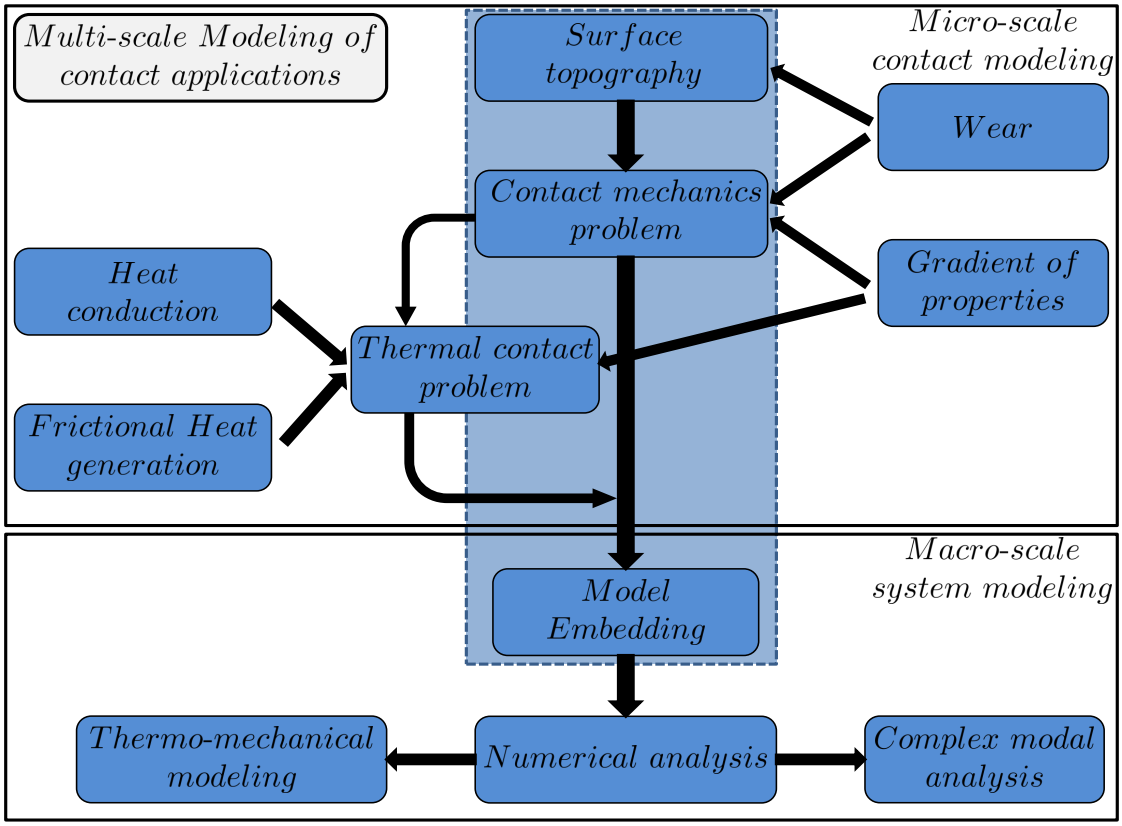

This figure presents the complete plan of this thesis. The first chapter position is highlighted by a blue box in the background.

Chapter 1

A multiscale method for frictionless contact mechanics of rough surfaces

Contents

A multiscale method for frictionless contact mechanics of rough surfaces

Y. Waddad, V. Magnier, P. Dufrénoy, G. De Saxcé

Université de Lille Nord de France, F-59000 Lille, France
Lille1-LML, F-59655 Villeneuve d'Ascq, France
CNRS, FRE 8107, F-59655 Villeneuve d'Ascq, France

Abstract

An efficient methodology is proposed for the analysis of frictionless contact between rough surfaces. The surface is described by parabolic asperities which deform according to Hertz Theory. The problem is solved considering interactions between elliptic contact zones. Such analysis provide interface laws that are incorporated into a macroscopic numerical model where contact surfaces are flat. This operation is done by means of Love solution for elastic half spaces and the penalty method.
A numerical example of this multi-scale method is presented to show its robustness. In comparison with a purely numerical model where roughness is explicitly described, the proposed strategy provides good results and saves a considerable amount of time.

keywords : Surface roughness, Hertz theory, Contact mechanics, Finite element method.

1.1 Introduction

Contact mechanics is a fundamental problem in mechanical engineering. It provides necessary information to design safely many systems involving two or more bodies that are contacting each other, such as braking systems, blade-abradable seals and many others.
The first work in this domain dates back to 1882 with the pioneering Hertz theory. This theory describes the frictionless contact between two elastic curved surfaces. However, real surfaces are rough, thus the real contact area is very small compared to the apparent one. The problem is of permanent concern since the real contact area and the stress distribution affect a large number of physical properties such as friction, heat transfer and wear. For example, the topography of brake lining surfaces has a strong influence on thermal and braking noise issues, and can change the dynamic behavior of this systems[Hetzler and Willner(2012), Heussaff *et al.*(2012), Magnier *et al.*(2014)].
Surface roughness can be seen as a random process, therefore, the random process theory is used for its analysis. Statistical parameters such as the average roughness and the root mean square are commonly used to describe surface height fluctuations against the center-line [Abbot and Firestone(1933)]. Moreover, one of the most interesting surface characteristics is the power spectral density [Nayak(1971)]. It allows to characterize the periodicities and the fractal nature of surface roughness in the frequency domain [Persson *et al.*(2005)]. Furthermore, a surface can be seen as a set of asperities. Thus, the surface analysis goes through the geometrical properties of these asperities [Greenwood and Williamson(1966), Bush *et al.*(1975)]. For instance, the asperities of fractal rough surfaces have been characterized using a special method in [Bigerelle *et al.*(2004)]. The concept of their approach is to reformulate the notion of roughness peaks by linking the surface curvature to the observation scale.
With regard to contact mechanics of rough surfaces, the first consistent model was proposed by [Greenwood and Williamson(1966)]. Their model deals with the contact between a deformable rough surface and a rigid flat surface. They assumed that roughness can be described as a spatial distribution of spherical

asperities with the same radius of curvature and randomly distributed heights (see Fig.1.1). The contact on asperities is described by Hertz theory and interactions between asperities are neglected.
A more general model was proposed by [Bush *et al.*(1975)]. They studied the elastic contact between an isotropically rough surface and a flat surface by assuming that the cap of each asperity is replaced by a paraboloid having the same height and principal curvatures as the asperity's summit. The basic assumption is to consider a random process of asperity summit heights and principal curvatures, and that each asperity deforms according to the Hertzian solution for elastic non-conforming smooth surfaces (see [Johnson(1987)]). The model is based on statistical analyses of isotropic randomly rough surfaces (see [Longuet-Higgins(1957), Nayak(1971)]).
This class of models has the advantage of simplicity and speed, and can be used to evaluate the influence of roughness parameters on the surface behavior and obtain some significant correlations as in [Yastrebov *et al.*(2015), Zahouani *et al.*(2009)]. However there are many limitations which arise from the following approximations: the dependency of statistical roughness parameters on the sampling length, the geometrical approximation of asperities shapes and the non-consideration of interaction effect [Persson *et al.*(2002), Yastrebov *et al.*(2015)]. Nevertheless, these models have been enriched by many authors. For example, the interaction between asperities has been included by means of semi-analytical models [Ciavarella *et al.*(2006), Ciavarella *et al.*(2008), Yastrebov *et al.*(2011)]. Otherwise, a multi-scale approach has been developed by [Persson *et al.*(2002), Persson *et al.*(2005)] which considers only the spectral density of the surface. Using this theory, one can obtain the distribution of contact stresses and the contact real area corresponding to a given scale that is controlled by a magnification factor. Comparing to multi-asperity models, Persson's theory gives the exact result when there is a perfect contact. Within this theory, it is not possible to give a full description of contact zones distribution because the only information that is used is the surface spectral density.
In the last few years, there were many improvements in numerical simulations of contact between rough surfaces. Two main techniques can be distinguished: the finite element method and the half-space solution. In the first class of methods, the problem is solved using optimization methods [Wriggers(1995)] and the computational time is high since surface discretization must be enough fine to capture all roughness details. Using this method, elastic contact and elasto-plastic contact have been analyzed in [Hyun *et al.*(2004), Pei(2005)], the results obtained are quite similar to analytic predictions. Finite element method (FEM) was also used in many works to define some micro mechanical contact laws that are embedded in macroscopic models. In those approaches a RVE (Representative Volume Element) is defined and many calculations are made to get a macroscopic physical quantity depending on roughness. For example, in [Yastrebov *et al.*(2011)], a phenomenological contact model based on finite element calculations has been proposed to rapidly analyze the plastic contact of a rough surface. Similarly, in [Wriggers and Reinelt(2009), De Lorenzis and Wriggers(2013)] a multi-scale approach has been developed to obtain an homogenized coefficient of friction that reflects the roughness's influence on a frictional contact.
Comparing to FEM methods, the second class of numerical methods is more attractive because of its reduced computational time. In those methods, only the surface is discretized and the solid is considered as a half space. The resolution is done using [Boussinesq(1885)] solution for elastic half spaces. This technique has been used in many works (see [Björklund and Andersson(1994), Putignano *et al.*(2012), Willner(2008), Zahouani *et al.*(2009)]) and provide very accurate results. Using the FFT technique, a fast version of this method, has been developed in [Leroux *et al.*(2010)] to model the contact of heterogeneous half spaces, and in [Gallego *et al.*(2010)] to model the fretting problems.
One of the most important issues treated by contact theories is the interface gap evolution against a normal force. For a perfect contact, the gap is always equal to zero, which is not true for real surfaces. The gap evolution can be characterized by analyzing contact stiffness. This parameter influences many mechanical and physical properties such as thermal and electric conductivity [Patewska *et al.*(1992)].

The influence of the gap evolution has been considered in many works. In [Hetzler and Willner(2012)], the gap's influence on the dynamic behavior of a braking system has been tested using Greenwood and Williamson theory. Also, using Persson's theory, the same parameter has been considered in [Dapp *et al.*(2002)] to evaluate the leakage in seal systems. Experimentally, the gap evolution has been analyzed in [Lorenz *et al.*(2010)] and been compared to contact theories. The experiments results show that multi-asperity models fail to give a reasonable estimation of the load-gap relationship even for large separations and that Persson's theory is more accurate. This is due to the fact that interactions are not considered in the multi-asperity models.

In the present work, our interest is focused on some mechanical systems such as friction brakes where contact area evolves continuously, and the size and the distribution of contact zones influence drastically the global behavior of the surrounding components [Eriksson *et al.*(2002), Magnier *et al.*(2014)]. The main purpose is to propose a numerical strategy allowing to consider contact roughness in a large-scale model, in particular the interface gap evolution. As mentioned before, the explicit meshing of contact roughness in this kind of models is computationally expensive, so there is clearly a need to define a multi-scale homogenization strategy allowing to consider roughness effect. Moreover this multi-scale homogenization technique must be done zone by zone, so that each zone has its local contact properties. Hence the implementation of such technique allows to get some sort of macroscopic contact localizations depending only on the size and the geometry of each homogenized zone.

Therefore, the strategy that is proposed in this paper, incorporates two mains steps. The first one is to analyze the micro-mechanical behavior of an interface involving rough surfaces. The second one aims to integrate this behavior in a macroscopic numerical model.

In the first step, the analysis of the evolution of contact stresses against contact kinematics taking into account the surface roughness, is performed using a semi-analytic contact model inspired from the work of [Ciavarella *et al.*(2006)]. More precisely, the surface is considered as a discrete set of asperities and the interaction effect is included using an analytic solution for surface displacements in an elastic half space. This choice is motivated by the fact that this model fulfills two main criteria : speed and accuracy. Furthermore, this model is distinguished from the classical models by its discrete formulation and the consideration of interactions. The use of a discrete formulation is important because it is necessary to know accurately the localization of contact points. Comparing to the paper of [Ciavarella *et al.*(2006)], the problem is solved using a different iterative scheme and also, the model is generalized to cover the case of elliptic contact, which provide a more realistic description of the contact geometry. An example is then presented to analyze the evolution of some relevant quantities such as the real contact area, contact stresses and kinematics.

The second step is to use the results issued from the semi-analytic model and to integrate them into a large-scale (macroscopic) model. Indeed, one of the most practical ways is to consider that the surface is flat, and then, the numerical model is embedded by the interface constitutive law (see [Bandeira *et al.*(2004), Wriggers(1995), Zavarise *et al.*(1992)]). Comparing to these works, this operation is done zone by zone, and each zone has it owns parameters, and also, an intermediate step is added to consider the geometry of each zone. Theoretically, the penalty method [Kikuchi and Song(1981)] is used which gives an approximation of contact pressure by linking it to the interface's normal gap. Moreover, the contact laws are recomputed using Love solution for elastic half spaces [Love(1929)]. This operation is important as it allows to consider the geometry of the homogenized zone and to ensure that the large-scale model has the same response as the original microscopic model, as will be detailed in section 1.4.

Finally, a numerical example is selected to show the ability of the proposed strategy. It concerns an elastic block with a rough surface which is compressed against a rigid solid having a flat surface. Comparisons will be done with another numerical model where roughness is explicitly described.

This strategy allows a macroscopic description of the interface evolution, provides a more accurate analy-

sis of the physical phenomena in the numerical large-scale model and saves a considerable amount of time. One of the most interesting points of this method is that the global response of the system is not very dependent on the contact interface mesh which makes this technique easily integrated into the industrial large scale numerical models.

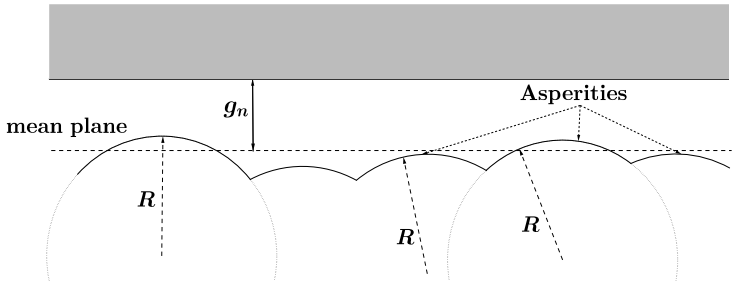

Figure 1.1: The Greenwood-Williamson theory of contact of rough surfaces. The roughness is described by spherical asperities of equal radius R. g_n is the separation distance between the mean plane and the rigid flat surface.

1.2 Contact models

1.2.1 Hertz theory

Let us recall some basic results within the Hertz theory framework. This theory describes the frictionless contact between a paraboloidal body and a flat surface considered as an elastic half spaces with smooth surfaces (see Fig.1.2). Hertz theory gives exact solution as long as strains are small. Let us denote E_1 and

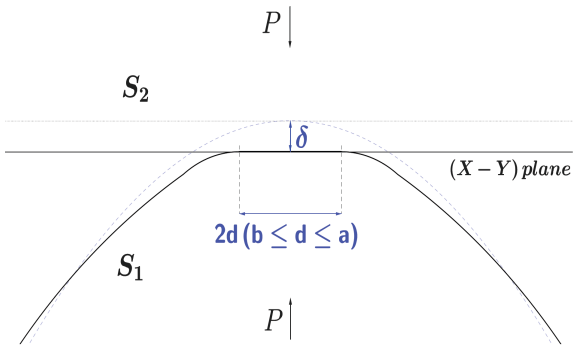

Figure 1.2: Hertzian contact between an elastic paraboloid and a flat plan. Contact area spreads into an elliptic zone while the deflection δ is growing

E_2 the Young modulus of the solids and ν_1 and ν_2 the corresponding Poisson ratios. We also introduce the equivalent radius R given by $R = (R'R")^{\frac{1}{2}}$, where R' and $R"$ are defined as the principal relative radii of curvature and their expressions are given in [Johnson(1987)].
Assuming that a normal compressive load P is applied to the two bodies. The initial point of contact

spreads into an elliptical surface, having semi-axis a and b ($a > b$), thus we introduce the eccentricity $e = \sqrt{1 - \frac{b^2}{a^2}}$.
If δ design the mutual approach on the center of contact area, one can show that

$$P = \frac{4}{3} E^* R^{\frac{1}{2}} F_1(e) \delta^{\frac{3}{2}} \tag{1.1}$$

where $\frac{1}{E^*} = \frac{1-\nu_1^2}{E_1} + \frac{1-\nu_2^2}{E_2}$,
$F_1(e) = \frac{\pi}{e\sqrt{2}} \left[\left(\frac{1}{1-e^2} E(e) - K(e) \right) (K(e) - E(e)) \right]^{\frac{1}{4}} K(e)^{-\frac{3}{2}}$
where $K(e)$ and $E(e)$ are respectively the complete elliptic integrals of the first and the second kind.
The eccentricity depends only on R' and $R"$ and is approximately given by [Johnson(1987)]

$$e = \sqrt{1 - \left(\frac{R"}{R'} \right)^{\frac{4}{3}}} \tag{1.2}$$

Contact area may be written

$$A = \pi ab = \pi A_1(e) R\delta \tag{1.3}$$

where $A_1(e) = \sqrt{1-e^2} \left(\frac{2K(e) F_1(e)}{\pi} \right)^2$.
and the pressure distribution is

$$p_n(x,y) = \frac{3}{2} \frac{P}{A} \sqrt{1 - \left(\frac{x}{a} \right)^2 - \left(\frac{y}{b} \right)^2} \tag{1.4}$$

In the simpler case of solids of revolution ($a = b$, $R' = R"$ and $e = 0$), contact area is circular and $F_1(e) = A_1(e) = 1$. The pressure distribution read

$$p_n(x,y) = p_n(r) = \frac{3}{2} \frac{P}{A} \sqrt{1 - \left(\frac{r}{a} \right)^2} \tag{1.5}$$

where r is the radial distance $r = \sqrt{x^2 + y^2}$.
The coefficients $F_1(e)$ and $A_1(e)$ are plotted in Fig.1.3. For high values of e, these coefficients affect clearly the force and contact area, indeed, using the formulas for circular contact may lead to overestimating contact area and to underestimating the total force.

1.2.2 Contact models for rough surfaces

The basic idea behind the classical contact models, such as [Greenwood and Williamson(1966), Bush *et al.*(1975)], is to relate quickly and easily the surface response to a few statistical parameters issued from surface measurements. However, those models neglect interaction effects and their results depend strongly on the choice of the statistical parameters. Furthermore, a numerical accurate analysis of rough contact becomes rapidly expensive since a high number of contact points is needed to efficiently simulate the problem [Pei(2005), Yastrebov *et al.*(2011)].
In what follows, two contact models are proposed. Globally, the surface description came from the classical statistical contact models. In both of them, the surface is seen as a discrete system of elliptic or circular

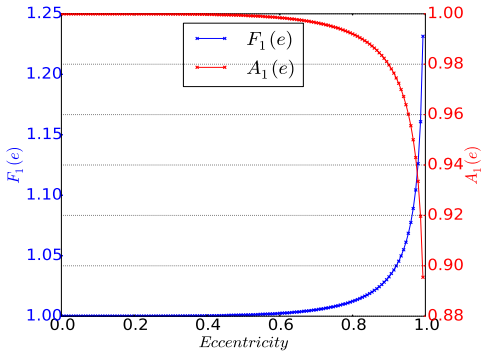

Figure 1.3: Evolution of the coefficients $F_1(e)$ and $A_1(e)$ in terms of the contact eccentricity e

asperities and the summit of each of them has a specific height and radius of curvature. Thus, the response of the surface is given by a discrete summation over all the contacting asperities.
The first model neglects interaction effects, and hence the asperities deform independently. In the second model, the displacement of each asperity depends on the Hertzian pressures applied in the other contacting asperities, thus a nonlinear system of equations is obtained and is solved using an iterative scheme. This approach was proposed first by [Ciavarella *et al.*(2006)]. They consider a circular contact over asperities and they solved the problem using an incremental correction. However, in real surfaces, the asperities are not symmetric, and as shown in Fig.1.3, the symmetric assumption may mislead to a wrong estimation of contact area and force. Hence, the model is generalized to consider the elliptic contact and the resolution is performed with a truncated Newton algorithm [Nash(2000)].

1.2.2.1 Discrete model without interaction

Considering a rigid flat surface which is moved vertically with a motion δ against a rough surface of an elastic body. Let us denote z_M the maximum height of the rough surface and z_i the height of the i^{th} asperity, the displacement of the i^{th} asperity is given by:

$$w_i = \langle \delta - (z_M - z_i) \rangle \tag{1.6}$$

where $< . >$ is the positive part of its operand.
The total force and the real contact area are obtained by adding the contribution of all the contacting asperities, hence they are respectively given by:

$$F = \frac{4}{3} E^* \sum_i^N R_i^{\frac{1}{2}} F_1(e_i) \, w_i^{\frac{3}{2}} \tag{1.7}$$

$$A = \pi \sum_i^N R_i A_1(e_i) \, w_i \tag{1.8}$$

where N is the total number of the asperities.
The average normal separation between the two faces is:

$$g_n = (z_M - \bar{z}) - \delta \tag{1.9}$$

where $\bar{z}$ is the height of the mean plane ($\bar{z} = \frac{1}{N}\sum_{1}^{N} z_i$). The simple version of this model is to consider that asperities are symmetric, hence the coefficients A_1 and F_1 are both considered equal to 1.

1.2.2.2 Discrete circular contact with interaction

The main idea of this approach is to consider that the displacement of each asperity is a consequence of all the contact strengths applied on asperities. If the surface is supposed to be approximately flat out of asperities domain and that the contact is Hertzian, the normal displacement in every point of the surface is given by [Johnson(1987)]

$$U_z(r) = \begin{cases} \frac{1}{R}\left(a^2 - \frac{r^2}{2}\right) & \text{if } r \leq a \\ \frac{1}{\pi R}\left[\left(2a^2 - r^2\right)\arcsin\left(\frac{a}{r}\right) + a\sqrt{r^2 - a^2}\right] & \text{else.} \end{cases}$$

Thus, the displacement of each asperity is obtained by summing the displacements due to the contacting asperities. If n is the number of the supposed contacting asperities and w_k the displacement of the k^{th} asperity, then w_k reads

$$w_k = \sum_{i=1}^{n} G_i(r_{ik}) \tag{1.10}$$

where

$$G_i(r_{ik}) = \begin{cases} \frac{a_i^2}{R_i} & \text{if } i = k \\ \frac{1}{\pi R_i}\left[\left(2a_i^2 - r_{ik}^2\right)\arcsin\left(\frac{a_i}{r_{ik}}\right) + a_i\sqrt{r_{ik}^2 - a_i^2}\right] & \text{else} \end{cases}$$

and r_{ik} is the horizontal distance between the k^{th} and the i^{th} asperity.
Furthermore, the displacement should satisfy this kinematic conditions:

$$w_k \geq \delta - (z_M - z_k) \tag{1.11}$$

The equality in Eq.1.11 means that the asperity is in contact (see the k^{th} asperity in Fig.1.4), while the strict inequality signifies that the asperity is not in contact (see the j^{th} asperity), and in this case, the height of this asperity has changed due to interaction effects. Hence, it is not known if an asperity is in contact or not, unlike the previous model(i.e without interaction) where the number of contacting asperities depends only on the vertical motion δ.
Solving the problem is to find a distribution of contact dimensions $\mathbf{a} = (a_1, a_2, ..., a_n)$ satisfying contact conditions (Eq.1.11). The obtained system of equations is non linear and is solved using a suitable iterative scheme.
Practically, we write the objective function defined by

$$\mathrm{O}(\mathbf{a}) = \sum_{k=1}^{n} \left(w_k - \delta + (z_M - z_k)\right)^2 \tag{1.12}$$

The resolution of the contact problem is equivalent to the minimization of the objective function provided that contact dimensions respect contact kinematics. The function O is bounded and twice continuously differentiable. The minimization is performed using a Newton algorithm:

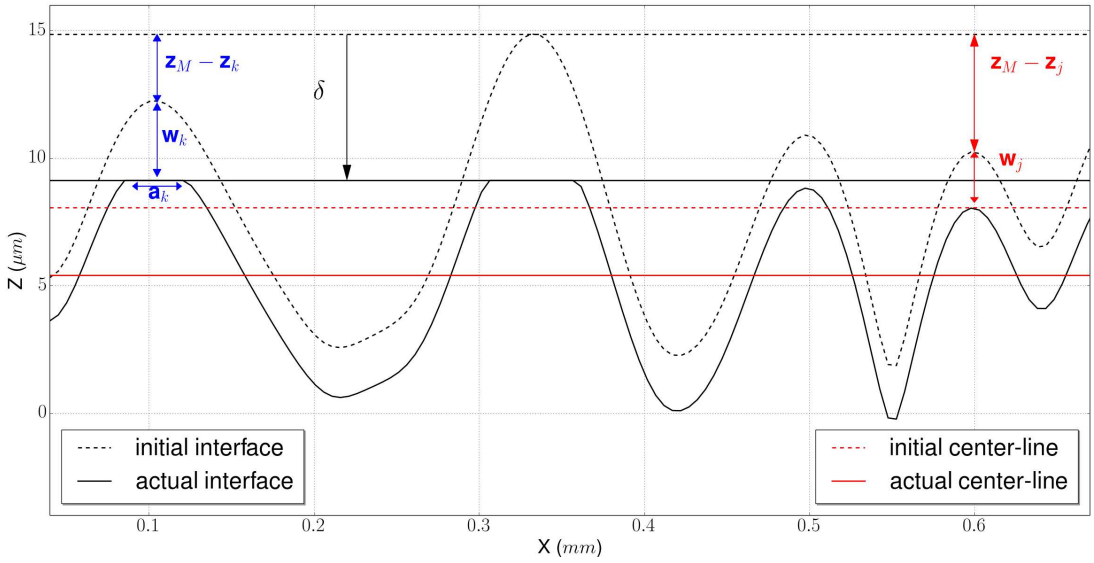

Figure 1.4: Geometry of a rough interface, only asperities are in contact and the gap distance between the interface center line and the rigid flat surface decreases while the vertical motion δ is increasing

- The solution $\mathbf{a}$ verify $\mathbf{J}(\mathbf{a}) = \mathbf{0}$, where $\mathbf{J}$ is the gradient vector of O,
- The function O is approximated by

$$\mathrm{O}(\mathbf{a} + \delta\mathbf{a}) = \mathrm{O}(\mathbf{a}) + \mathbf{J}.\delta\mathbf{a} + \frac{1}{2}\,\delta\mathbf{a}^t \underline{\underline{H}}(\mathbf{a})\,\delta\mathbf{a} \tag{1.13}$$

  where $\underline{\underline{H}}$ is the Hessian matrix,

- From an initial guess $\mathbf{a}_0$, the iterates are consecutively computed by

$$\mathbf{a}_{i+1} = \mathbf{a}_i + \delta\mathbf{a} \tag{1.14}$$

  where $\delta\mathbf{a}$ is the solution of the linear system of equations

$$\underline{\underline{H}}(\mathbf{a}_i)\,\delta\mathbf{a} = -\mathbf{J}(\mathbf{a}_i) \tag{1.15}$$

The convergence of the algorithm is quadratic as long as the initial guess $\mathbf{a}_0$ is near to the solution. However, the resolution of the linear system (Eq.1.15) may be very costly, especially when the number of asperities increases. An alternative solution consists in using one of the truncated-Newton methods [Nash(2000), Nash(1985)]. In this case, an iterative method is used to approximately solve the Newton equations (Eq.1.15). Indeed, the matrix $\underline{\underline{H}}^{-1}$ is not exactly computed but just estimated with a variable tolerance. Hence, the resolution of the global problem falls into two loops: an outer iteration for the non-linear optimization problem, and an inner iteration for the Newton equations.
In order to solve Eq.1.15, the linear conjugate-gradient method [Powell(1977)] is usually used. The use of this method is justified because the Hessian matrix is always symmetric, and is definite positive at a local minimizer of the problem.
Once the contact dimensions vector $\mathbf{a}$ has been calculated, the force and contact area are computed automatically using a discrete sum. Then, the normal gap is estimated by subtracting the vertical displacement of every point from the rigid body motion of the flat surface. In what follows, an extension to the case of elliptic contact is presented.

1.2.2.3 Discrete elliptic contact with interaction

The general structure of the algorithm remains unchanged. However, the displacement field must be recalculated in order to take into account the elliptical shape of contact area.
From the theory of [Boussinesq(1885)], the normal displacement of the surface reads

$$U_z(x,y) = \frac{1}{\pi E^*} \int \frac{p_n(\zeta,\eta)}{\rho} \mathrm{d}\zeta \mathrm{d}\eta \tag{1.16}$$

where p_n is the normal pressure and $\rho = \sqrt{(x-\zeta)^2 + (y-\eta)^2}$
It then follows from the potential theory [Johnson(1987)] that the surface normal displacement due to an ellipsoidal distribution of pressure (see Eq.1.4) applied to an elliptic region is given by

$$U_z(X,Y) = \frac{p_0 ab}{2E^*} \int_{\lambda_1}^{\infty} \left(1 - \frac{X^2}{a^2+w} - \frac{Y^2}{b^2+w}\right) \frac{\mathrm{d}w}{\left[(a^2+w)(b^2+w)w\right]^{1/2}} \tag{1.17}$$

where p_0 is the pressure at the center of the loaded region, a and b are loaded region dimensions and λ_1 is the positive root of the equation

$$\frac{X^2}{a^2+\lambda} + \frac{Y^2}{b^2+\lambda} = 1 \tag{1.18}$$

within the loaded area λ_1 is taken to be zero;
X and Y are the local relative coordinates in the principal directions.
From Eq.1.17, the surface displacement may be written

$$U_z(X,Y) = \frac{2}{\pi R}. \left(\frac{\pi}{2} \frac{1}{K(e) F_1(e)^{2/3}}\right)^3 \left(L - MX^2 - NY^2\right) \tag{1.19}$$

where $K(e)$ and $F_1(e)$ are specified in Eq.1.1, and

$$L = \frac{a^3}{2} \int_{\lambda_1}^{\infty} \frac{\mathrm{d}w}{\left[(a^2+w)(b^2+w)w\right]^{1/2}}$$

$$M = \frac{a^3}{2} \int_{\lambda_1}^{\infty} \frac{\mathrm{d}w}{\left[(a^2+w)^3(b^2+w)w\right]^{1/2}}$$

$$N = \frac{a^3}{2} \int_{\lambda_1}^{\infty} \frac{\mathrm{d}w}{\left[(a^2+w)(b^2+w)^3 w\right]^{1/2}}$$

Using integration by substitution, these integrals may be expressed in term of elliptic integrals

$$L = a^2 \left[K(e) - F(\phi_1, e)\right] \tag{1.20}$$

$$M = \frac{1}{e^2} \left[\left(K(e) - F(\phi_1, e)\right) - E\left(\frac{\pi}{2} - \phi_2, e\right)\right] \tag{1.21}$$

$$N = \frac{1}{e^2} \left[\frac{1}{1-e^2} \left(E(e) - E(\phi_1, e)\right) - \left(K(e) - F(\phi_1, e)\right)\right] \tag{1.22}$$

where $F(\phi, e)$ and $E(\phi, e)$ are respectively the incomplete elliptic integrals of the first and the second kind;

and $\phi_1 = \tan^{-1}\left(\frac{\sqrt{\lambda_1}}{b}\right)$, $\phi_2 = \tan^{-1}\left(\frac{\sqrt{\lambda_1}}{a}\right)$;
Within contact area, ϕ_1 and ϕ_2 are taken to be zero, and in that case, the expressions are the same as those given by Johnson[Johnson(1987)],i.e.

$$L = a^2 K(e)\ ,\ M = \frac{1}{e^2}\left[K(e) - E(e)\right]\ ,\ N = \frac{1}{e^2}\left[\frac{1}{1-e^2}E(e) - K(e)\right]$$

The displacement field corresponding to an elliptic contact is plotted in Fig.1.5 and is compared to the circular contact solution. The difference between the two fields is more important in the major axis direction, and decreases far from the contact zone. Nevertheless, the main difference between the two assumptions is the contact area size.
From Hertz theory, it is known that the eccentricity e depends only on the geometry of the contacting bodies (see Eq.1.2). If the major semi axis a is known, the minor one can be deduced automatically according to the relation $b = a\sqrt{1-e^2}$.

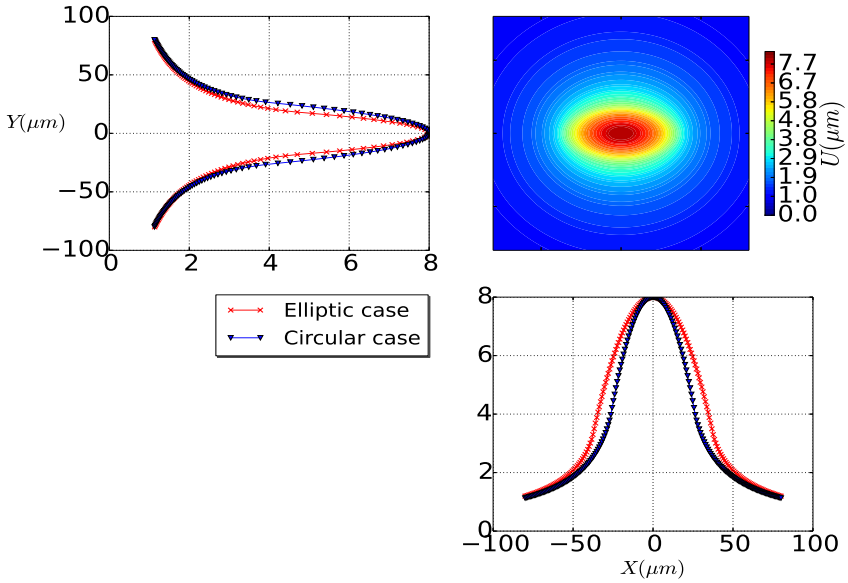

Figure 1.5: Graphical representation of the vertical displacement for a given elliptic contact area. The asymmetry of this field decreases far from the center of contact area

Let us now consider the contact of a rough surface, similarly to the case of the circular contact, the normal displacement at the k^{th} asperity is

$$w_k = \sum_{i=1}^{n} G_i\left(\Delta X_{ik}, \Delta Y_{ik}\right) \tag{1.23}$$

where

$$G_i\left(\Delta X_{ik}, \Delta Y_{ik}\right) = \begin{cases} \frac{1}{R_i}.\left(\frac{\pi}{2}\frac{a_i}{K(e_i)F_1(e_i)}\right)^2 & \text{if } i = k \\ \frac{2}{\pi R_i}.\left(\frac{\pi}{2}\frac{1}{K(e_i)F_1(e_i)^{2/3}}\right)^3\left(L_i - M_i\Delta X_{ik}^2 - N_i\Delta Y_{ik}^2\right) & \text{else} \end{cases}$$

and $\Delta X_{ik} = X_i - X_k$, $\Delta Y_{ik} = Y_i - Y_k$, and the triplet (L_i, M_i, N_i) is computed according to Eqs.1.20, 1.21 and 1.22.
The solution scheme is exactly the same as the one used for the circular contact case. The vector $\mathbf{a}$ of major semi-axis of contact zones is the only unknown of the problem.

1.3 Example

In order to illustrate the results obtained with the proposed contact models, some calculations were performed on 3D numerical rough surfaces. These surfaces were generated using fractal techniques. Here their geometrical parameters are presented and the evolution of some relevant quantities like contact area and contact mean pressure are analyzed.

1.3.1 Surfaces

Many rough surfaces are approximately self-affine fractals, which means that their statistical properties are unchanged if a scale change is made. One of the most useful tools to characterize a self-affine surface is the spectral density. One can show that for that kind of surfaces, this quantity reads approximately (see [Persson *et al.*(2005)])

$$\mathcal{S}(\mathbf{k}) = \mathcal{S}_0 |k|^{-2(H+1)} \tag{1.24}$$

where $\mathcal{S}_0$ is a constant and H is the Hurst exponent which is related to the fractal dimension $D_f = 3 - H$. A randomly rough surface can be generated with any given spectral density [Persson *et al.*(2005)]

$$h(\mathbf{x}) = \sum_{\mathbf{k}} B(\mathbf{k}) e^{i.\left(\frac{2\pi}{L}\mathbf{k}.\mathbf{x} + \phi(\mathbf{k})\right)} \tag{1.25}$$

where $B(\mathbf{k}) = 2\pi \left(\frac{\mathcal{S}(\mathbf{k})}{A_0}\right)^{1/2}$, A_0 is the surface area, L is the root square of A_0 and $\phi(\mathbf{k})$ are independent random variables which are uniformly distributed in the interval $[0, 2\pi[$.
In this section, the contact analysis is made on a square surface with dimensions of 1mm×1mm. Roughness is generated according to Eq.1.25. Two sets of parameters are used. In the first one, Set 1, the surface have the same characteristics in both directions. In the second one, Set 2, the cut-off wave vectors are modified so that the asperities are highly eccentric.
The spectral density used in this study is plotted in Fig.1.6(a). Its parameters were computed basing on surface measurements of a brake pad (see [Naidoo(2014)]). An example of a possible realization of roughness using the parameters presented in Tab.1.1 is shown in Fig.1.6(b).

	Area A_0 (mm^2)	H	upper wave-vector k_{max}	lower wave-vector k_{min}
Set 1	1	0.95	10	2
Set 2	1	0.95	$k_{x,max} = 7$	2
			$k_{y,max} = 12$	2

Table 1.1: Fractal rough surfaces parameters

The next step is to compute the geometrical properties of asperities summits. These points are identified as local maxima, where each summit is higher than the neighboring points, of which there are eight. Then, principal radius of curvature are calculated as the inverse of Hessian matrix eigenvalues. This matrix is computed on the summit and is given approximately means of the finite difference method. Subsequently,

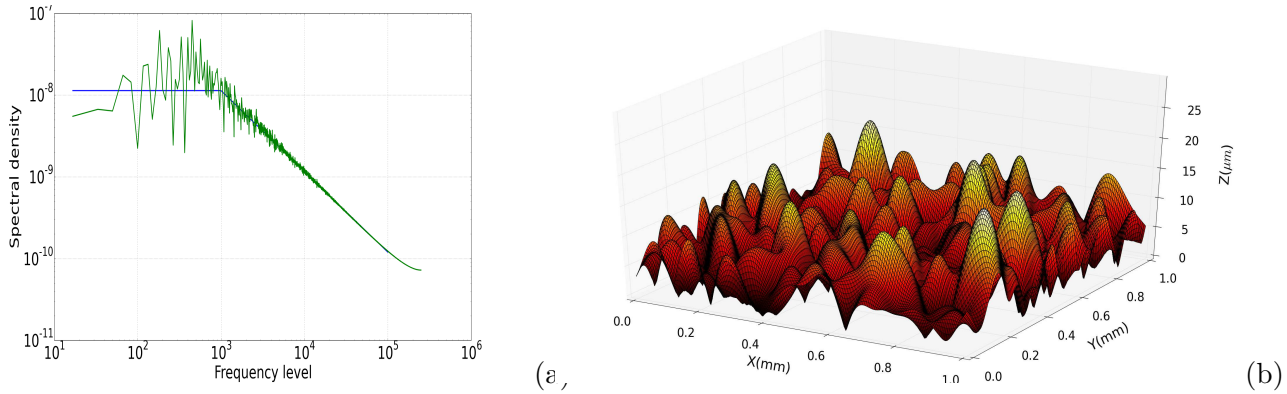

(a) (b)

Figure 1.6: (a) Power spectral density of a rough surface (b) Example of a generated rough surface for the parameters specified in Tab.1.1 (Set 1)

the principal directions are also computed as the eigenvectors of this matrix. Then, this geometrical data and the elastic parameters ($E = 4\,GPa$ and $\nu = 0.15$) are taken as models input data.

1.3.2 Results

Considering that one of those surfaces is in contact with a rigid flat plan. The rigid face is moved normally against the elastic surface with a given motion δ. In this paragraph, results from the various models described in section 1.2.2 are presented. Specifically, the analysis concerns the evolution of

- The fraction of the real contact area defined by :A/A_0;
- The contact mean pressure p_n defined by: F/A_0;
- The surface separation g;

where A is the real contact area and F the total force.
In Fig.1.7 and Fig.1.9, the results obtained with four different models are presented. The curves show a typical result for a realization issued from Set 1 and from Set 2. The four models are

- (1) Discrete elliptic contact, i.e the elliptic model with interaction;
- (2) Discrete circular contact, i.e the circular model with interaction;
- (3) Elliptic contact without interaction;
- (4) Circular contact without interaction

Obviously, the concern here is how the elliptic hypothesis and the interactions affect the predicted values of the contact interface properties. First of all, let us consider the first set (Set 1); it is clear that the elliptic shape of contact does not change the response of the surface. This was quite predictable because in this set, the surface has the same properties in both directions thus the eccentricity is not sufficiently high to influence the pressure distribution and the contact dimensions.
With regard to the evolution of contact mean pressure against the rigid motion and the separation (see Fig.1.7: i and ii), the models neglecting interaction, overestimate the mean pressure and hence contact area. This is due to the fact that the consideration of interactions reduce the number of the contacting asperities.
Otherwise, an interesting behavior can be seen in Fig.1.7(iii); the contact area- mean pressure relationship is almost linear for the four models and it seems that this behavior is preserved despite the

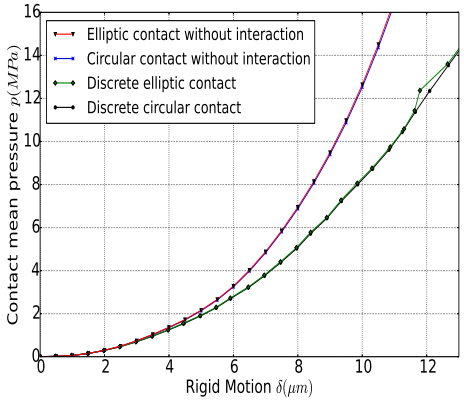

(i) Rigid motion vs mean pressure

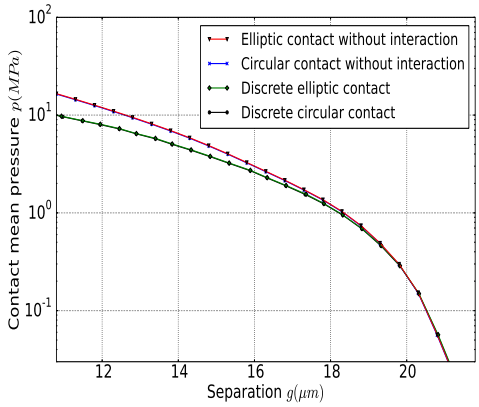

(ii) Separation vs mean pressure

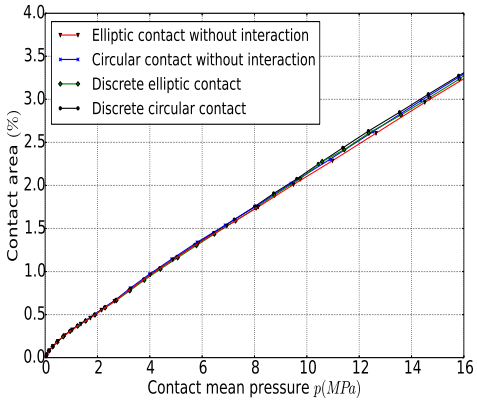

(iii) Mean pressure vs contact area

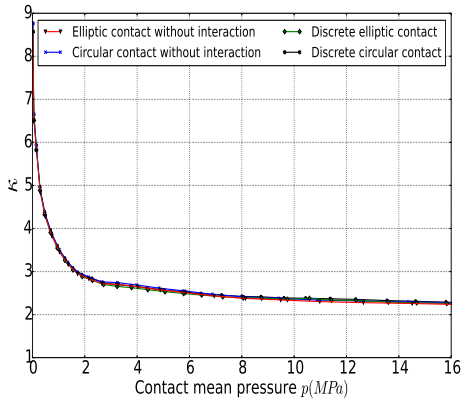

(iv) Evolution of the parameter κ

Figure 1.7: Results obtained for a surface from Set 1 using four different models

non-consideration of interactions. The coefficient of proportionality κ is plotted in Fig.1.7 (iv). Note that this parameter is defined by $A/A0 = \kappa(\langle|\nabla h|^2\rangle)^{-1/2} p_n/E^*$, where $\langle|\nabla h|^2\rangle$ is the average square slope of the surface. As shown in that figure, all the models predict the same law. For a contact area fraction less than 1.5%, there is no proportionality because there are a few contacting asperities and hence the non-linear Hertzian behavior is still predominant. When contact pressure exceeds $6MPa$, which corresponds to an area fraction equal to 1.5%, the parameter κ is roughly equal to 2.2. This value is not far from some theoretical predictions such as in the theory of [Bush *et al.*(1975)] ($\kappa = 2.5$), and some recent numerical works [Putignano *et al.*(2012), Yastrebov *et al.*(2015)].

Another interesting point is that the linearity between the mean pressure and contact area covers a wide range of areas that extend from 1.5% to 3.5%. With regards to the literature, this behavior can be analyzed by calculating Nayak's parameter which is defined by $\alpha = m_0\, m_4/m_2^2$, where m_i is the moment of the i^{th} order of the spectral density. Here, the value of this parameter is 2.6 which is a small value comparing to real surfaces; nevertheless the linearity should be limited to very small contact area, i.e less than 1% (see [Putignano *et al.*(2012), Yastrebov *et al.*(2015)]) which is not the case here.

Hence, it seems that this non-conventional result tend to confirm that the consideration of interactions does not play a major role in the prediction of linearity between contact area and mean pressure. Indeed, some calculations were achieved on 20 different realizations using the same parameters considered for Set 1. In Fig.1.8, the evolution of contact mean pressure versus contact area fraction, and the parameter κ

are plotted for the models which does not include the interaction effect. Once again the elliptic assumption does not affect the results. Also we clearly see that for the different realizations, the parameter κ converges towards values ranging between 2.34 and 2 for a fraction of contact area higher than 5% which is not far from the predictions of [Bush *et al.*(1975)] theory. Once more, the linearity is not valid for small contact area.

Now, regarding the second set (Set 2), a different observations can be made. In Fig.1.9 ((*i*) and (*ii*)), it

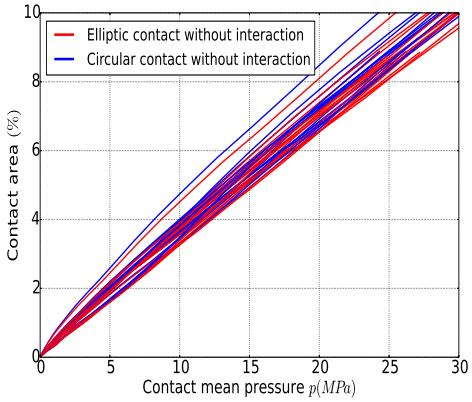

(i) Mean pressure vs contact area

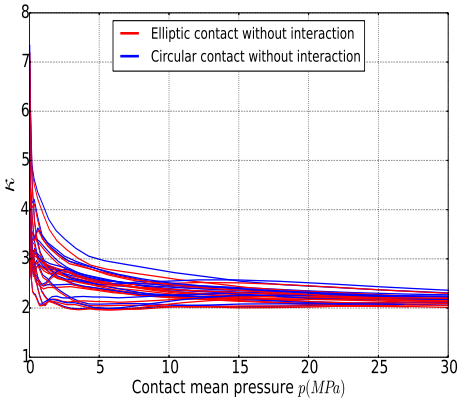

(ii) Evolution of the parameter κ

Figure 1.8: Results obtained for 20 realizations from Set 1 using two different models

can be seen that the consideration of the elliptic shape affects only slightly the prediction of the surface behavior. This is due to the fact that the distances between asperities are much bigger than contact dimensions, hence the displacements are quasi symmetric (see Fig.1.5). Indeed, if a point is located far from an asperity center(i.e $a, b << X, Y$), the variable λ_1 can be approximated by

$$\lambda_1 \simeq X^2 + Y^2 \tag{1.26}$$

Therefore, the solution is quasi-symmetric far from the center of contact zone, and this can be easily seen in Fig.1.5. Furthermore, the consideration of interactions changes drastically the rigid motion - mean pressure relationship. Again, the slope of this curve has decreased because interactions reduce the number of contacting asperities.

As regards the evolution of contact area versus the mean pressure (see Fig.1.9 (*iii*)), interactions do not change the results and there is not a clear linearity between the two quantities. For this sample, Nayak's parameter is equal to 3, which is slightly higher than the previous one (Set 1) but remains small comparing to real surfaces.

On the other hand, the influence of the elliptic hypothesis is remarkable. Indeed, as mentioned above, the circular assumption overestimates the area and underestimates the pressure. Thus, as shown in that figure, the slope of the predicted curves issued from the circular models is bigger than the elliptic models one. The parameter κ is plotted in Fig.1.9. Comparing to the first set (Set 1), κ converges slowly. The predicted values for the elliptic models are between 2 and 3 for a fraction of contact area higher than 1.5%.

From this example, it is clear that the consideration of the elliptic geometry affects strongly the contact area estimation when a surface has a highly eccentric asperities. Furthermore, the linearity between contact area and pressure is clearly not predicted.

As summary, we can see that the results obtained with the different presented models are in good accordance with many classical results. The most important point is that interactions affect clearly the slope

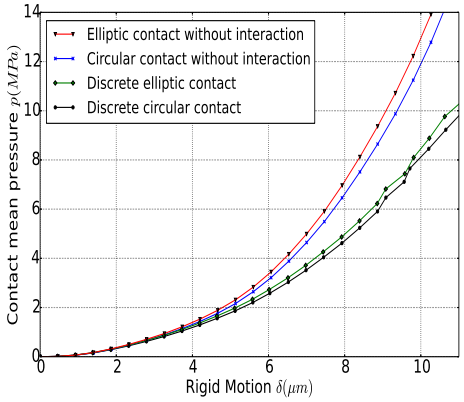

(i) Rigid motion vs mean pressure

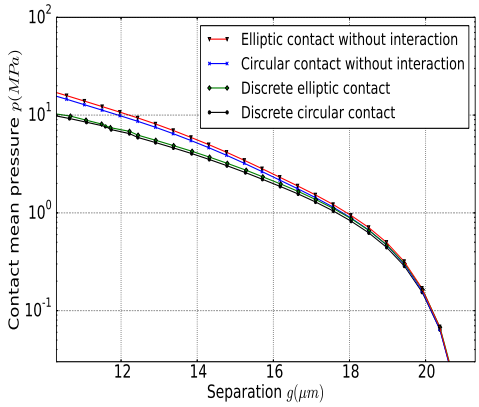

(ii) Separation vs mean pressure

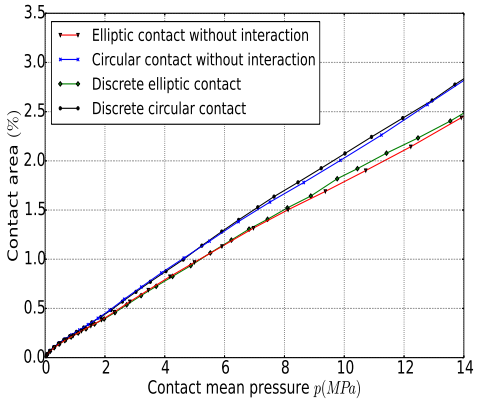

(iii) Mean pressure vs contact area

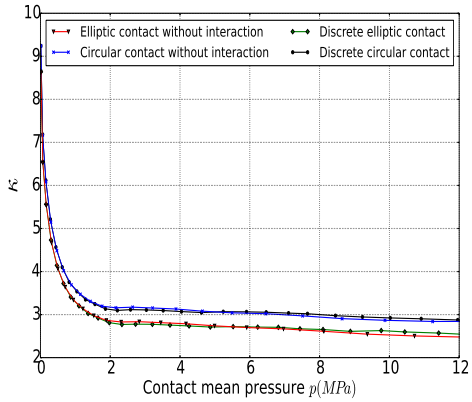

(iv) Evolution of the parameter κ

Figure 1.9: Results obtained for a surface from Set 2 using four different models

of the pressure-motion curve, and hence must be considered. The consideration of elliptic contact is only necessary when a surface contains a highly eccentric asperities. In the second part of this paper, one of the discrete models considering interactions is selected to embed a numerical model. In particular, the pressure-motion curve is used to define a contact law representing roughness effect. The main steps of the methodology are presented in the next section.

1.4 A numerical interface embedding strategy

The aim of this work is to integrate the microscopic behavior of the contact interface in a macroscopic numerical model. Indeed, roughness will not be represented physically in the model but only included via contact laws. Hence, we obtain an embedded/homogenized numerical model where roughness is implicitly present.
In this section, some basic principles of the numerical modeling of a frictionless contact problem are recalled, then the principle behind this strategy and its different steps will be detailed.

1.4.1 A brief overview on the numerical treatment of frictionless contact problem

Different topics are involved when contact problems have to be simulated numerically. The first is to formulate the geometrical contact conditions. In detail, it concerns the normal gap distance of the

(a) (b)

Figure 1.10: Graphical representation of contact laws: Penetration is not allowed in Kuhn tucker condition (a) while in the penalty method (b) contact constraints are violated and penetration depends on contact pressure

interface g_n and p_n the normal contact pressure. Indeed, in a continuum model, it is not allowed that two different points occupy the same position in space. It comes that for two contacting bodies, no boundary point of the first body penetrates in the other. Moreover, there is no contact pressure where there is no contact. These constraints lead to the following statement

$$g_n \geq 0,\ p_n \geq 0,\ p_n.g_n = 0 \tag{1.27}$$

which is well known as Kuhn-tucker condition for frictionless contact problems (see Fig.1.10 (a)).

Within the finite element framework, solving the contact problem goes through the derivation of the weak form of equilibrium including contact, and the minimization of a variational problem which is constrained to Kuhn-tucker condition [Wriggers(1995)]. The virtual work of contact forces can be expressed in terms of contact kinematics and surface tractions. The kinematics of contact surfaces are related directly to the displacements of the contacting bodies while the tractions are unknown.

Several methods are used to compute surface tractions and solve contact problem, with respect to the impenetrability constraint. In this paper we shall focus on regularization methods and more exactly the penalty method [Kikuchi and Song(1981)]. This technique pairs up the contact normal pressure with the gap distance with a law of proportionality

$$p_n = k_n < -g_n > \tag{1.28}$$

where k_n is the penalty coefficient (see Fig.1.10 (b)) .

Hence it comes that the virtual work of contact forces depends only on the displacements field.

In this formulation a penalty term due to constraint condition is added to the weak form and the contact problem becomes unconstrained. The global scheme of resolution is performed by choosing a suitable discretization of contact surface, and an iterative algorithm to minimize the virtual work[Kikuchi and Song(1981), Wriggers(2006)].

The penalty method leads to a solution letting the violation of contact constraints (Eq.1.27). To avoid large penetrations, the penalty coefficient has to be chosen enough large. However, this choice may lead to an ill-conditioning of the global matrix.

1.4.2 Embedding strategy principle

Let us consider a large-scale numerical model of two bodies which are in contact. One of them is rigid and the other one is elastic (see Fig.1.11-(a)). The penalty method is used to enforce contact constraints

and the contact interface is divided into a complementary set of patches, where each patch represents the roughness standing inside it (see Fig.1.11-(b)). Since surface roughness is described only by asperities, each patch corresponds to a discrete subset of asperities.
Following one of the contact models described before, the mean contact pressure in each patch can be related to the local vertical motion. The strategy that we propose, is to consider that the large scale model's interface is flat and smooth for each patch, and to use the contact laws instead of the penalty method. Indeed, this yields to a modified penalty term which represent roughness effect, and hence, the penalty coefficient is not chosen arbitrary but is depending on contact pressure (see Fig.1.11-(c)). This approach was proposed first in many works (e.g [Zavarise *et al.*(1992), Bandeira *et al.*(2004)]). Comparing to these works, the interface laws are defined considering the geometry of each patch and its interacting asperities. Indeed, these points were not considered in the mentioned works and are definitely important to preserve the same behavior in micro and macro contact models.
Following this strategy, for a given motion of the rigid body, the total force calculated in the large-scale model must be the same as the one calculated in the microscopic model, and to ensure this, it is necessary to define a convenient gap-contact pressure law for each patch.

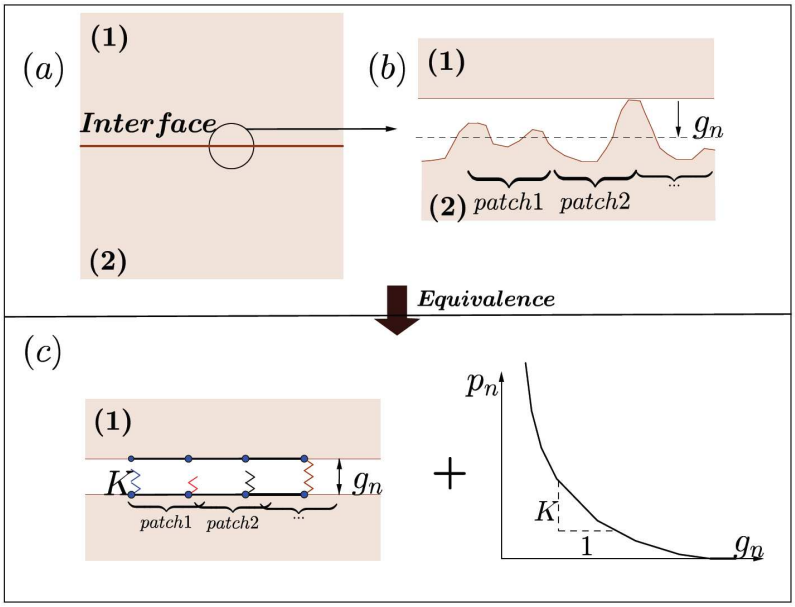

Figure 1.11: Schema of the proposed strategy: (a) the large scale problem, (b) the real interface geometry and patches distribution, and (c) the embedded model where the interface is embedded with contact laws

For example, let us take a rectangular patch (of dimensions $2a$ and $2b$) and suppose that this patch is embedded by a law linking the contact mean pressure to the normal gap. For a given motion of the rigid body, making contact over that patch is equivalent to apply a uniform pressure p_n on it (Fig.1.12), thus it follows from Love model[Love(1929)] that the vertical displacement of the elastic body surface reads approximately

$$U(x,y) = L(a,b,x,y)\,\frac{p_n}{\pi E^*} \tag{1.29}$$

where

$$\begin{aligned} L(a,b,x,y) &= (x+a)\ln\left(\frac{(y+b)+\sqrt{(y+b)^2+(x+a)^2}}{(y-b)+\sqrt{(y-b)^2+(x+a)^2}}\right) \\ &+ (y+b)\ln\left(\frac{(x+a)+\sqrt{(y+b)^2+(x+a)^2}}{(x-a)+\sqrt{(y+b)^2+(x-a)^2}}\right) \\ &+ (x-a)\ln\left(\frac{(y-b)+\sqrt{(y-b)^2+(x-a)^2}}{(y+b)+\sqrt{(y+b)^2+(x-a)^2}}\right) \\ &+ (y-b)\ln\left(\frac{(x-a)+\sqrt{(y-b)^2+(x-a)^2}}{(x+a)+\sqrt{(y-b)^2+(x+a)^2}}\right) \end{aligned} \tag{1.30}$$

With respect to the rigid motion δ, the normal gap distance reads

$$g_n(x,y) = \delta - U(x,y) = \delta - L(a,b,x,y)\,\frac{p_n}{\pi E^*} \tag{1.31}$$

From this equation and with respect to the contact law $p_n = f(g_n)$, the contact pressure is iteratively computed. However, it is not guaranteed to find the same contact pressure associated to the motion δ, because the Eq.1.31 might be different from the contact law linking g_n to p_n. In other words, for a given motion δ, if the contact model predicts a gap evolution which is different from the one given in Eq.1.31, the pressure will be different, and hence, the total force will not be the same.

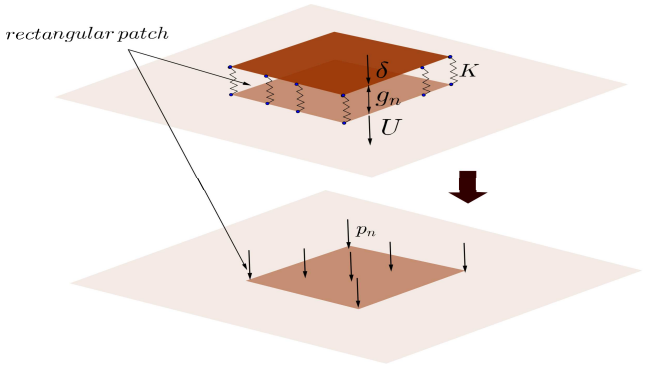

Figure 1.12: Analogy between the effect of a contact law defined on a patch and a uniform pressure applied on it. The contact stresses act like a uniform pressure p_n and the elastic displacements U in the elastic body are given from Love model

In order to get the equivalence between the two models, the law which links the contact pressure with the rigid motion δ must be respected. So it is necessary to compute a new gap according to Eq.1.31. Therefore, the strategy proposed here read as follows:

- For a given δ, the corresponding force F is computed using one of the micro mechanical models (see section 1.2.2) and then the normal contact pressure read $p_n = F/A$, where A is the patch area,

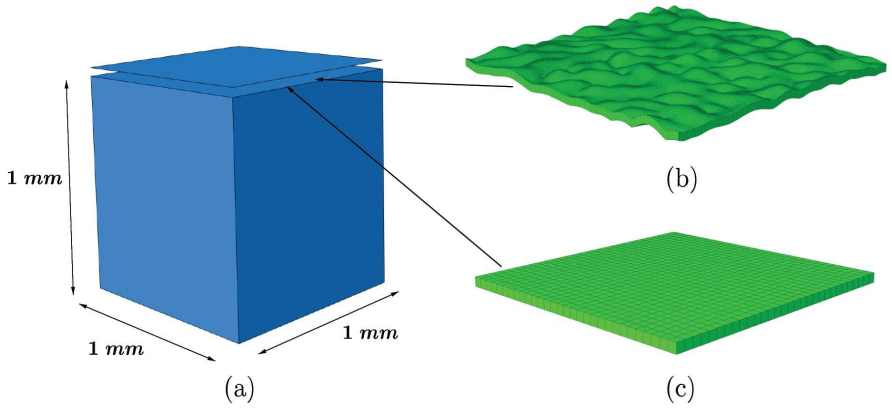

Figure 1.13: Numerical models : (a) Geometry of the problem, (b) the surface mesh in the numerical reference model (6.10^5 hexahedron elements) and (c) the flat surface mesh in the embedded numerical models(4.10^4 hexahedron elements).

- Following Love model[Love(1929)], the gap g_n is computed according to Eq.1.31, and the contact law is then defined by the couple (g_n, p_n)

As stated before, this step is crucial since it makes possible the consideration of patch's geometry. The procedure is done zone by zone so that an interface law is defined for each patch of the surface. Comparing to numerical approaches, the operation is very fast since the semi-analytic contact model is used. The Love solution is only valid when the patches geometry is rectangular and when their size are much smaller than the total surface dimensions. The procedure can be generalized to cover the general case of quadrilateral and triangular contact elements, without any difficulty. In the latter case, Boussinesq solution for normal load over a triangular area is used.

1.5 Numerical examples

1.5.1 Numerical models

Considering an elastic cube and a rigid flat surface (Fig.1.13-(a)). The rigid surface is moved normally against the cube with a given motion. Two numerical models are proposed:

- (1) Numerical reference model: A first model where roughness is explicitly (or finely) meshed. In order to get an accurate solution, the model contains 6.10^5 hexahedron elements and the Augmented Lagrangian formulation is used to enforce the contact constraints. This method is more accurate and is less dependent on the choice of its parameters. The contact elements are of the type surface to surface (see Fig.1.13-(b)).

- (2) Embedded/Homogenized numerical model: In the second model, the interface is flat. The surface is divided into $N_x \times N_y$ square patches. For each patch, the contact interface is embedded with a contact law using the discrete circular model with interaction and the strategy described above. Furthermore, surface to surface discretization type is used and the mesh density is very small compared to the first model (4.10^4 hexahedron elements, see Fig.1.13-(c)).

1.5.2 Results

All the numerical analysis are performed with the commercial Finite Element code Abaqus/Standard 6.13. We compare both analytic and numerical results. In the embedded model, three simulations are performed considering various number of patches.
In Fig.1.14, the evolution of contact mean pressure versus the motion of the rigid plan is presented. It is clear that the solution without interaction overestimates the mean pressure. The discrete analytic results (with interaction) match with the numerical model predictions. With regard to the embedded models, the results are consistent with those predicted by the numerical reference model.
The size of patches has a little influence on the total surface behavior. Indeed, there is small differences varying from 0% to 3%. This is due to the way the interface laws are defined. Indeed, each patch represents the asperities that are inside it, and the interaction between the asperities coming from various patches is slightly different from interactions between patches.

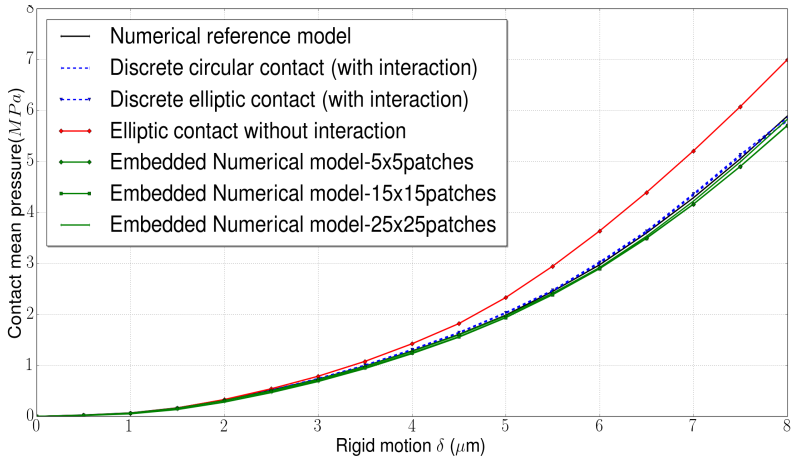

Figure 1.14: Numerical and analytic predictions of the contact mean pressure versus the vertical motion of the rigid body

In Fig.1.15, the distribution of contact normal stresses corresponding to $\delta = 8\mu m$, is shown for the different models. In Fig.(a), (b) and (c), it is clear that the number of the contacting asperities is the same. In the elliptic model, the shape and the orientation of contact zones are consistent with the numerical reference model.
The real contact area is very small compared to the apparent one (approximately 4%). In the numerical model, contact area is slightly larger due to the mesh size effect.
On the other hand, the distribution of contact stresses, in the three embedded models (Fig.1.15: (d), (e) and (f)), depends on the patch size. The higher the number of patches, the more precise the contact stresses distribution is. The contacting patches correspond to the zones where asperities are in contact hence, each patch describes macroscopically the micro mechanical behavior of the asperities standing inside it. The mean pressure remains approximatively the same as shown in Fig.1.14, despite the differences in contact stresses distribution.
As regards the computational time, It has been reduced significantly. For the numerical reference model, the computational time is 3 hours whereas it does not exceed 15 minutes for the embedded models and 10 minutes for the semi-analytic models.

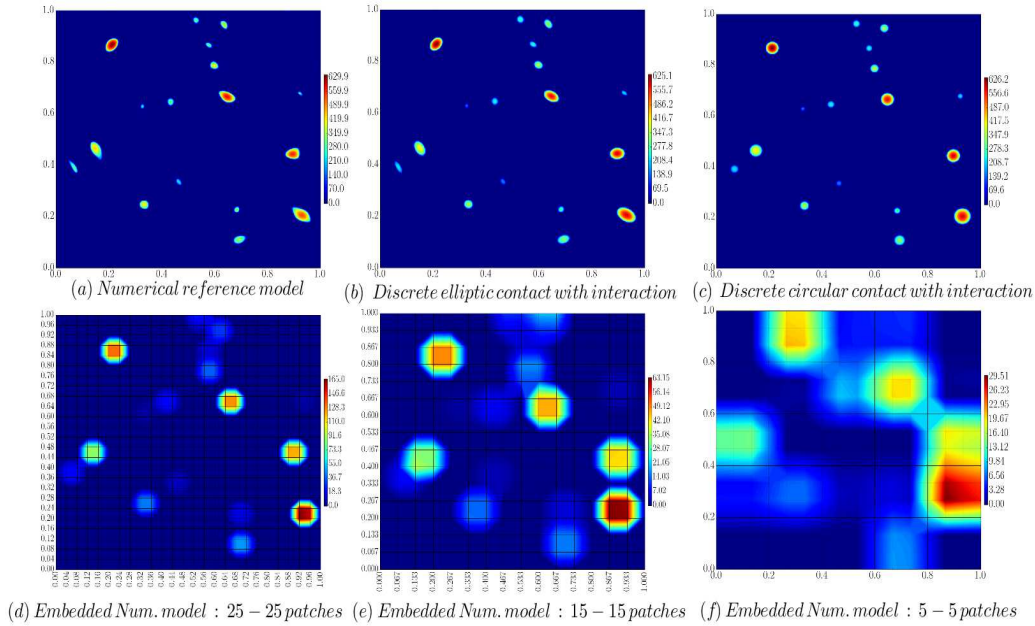

(a) *Numerical reference model* (b) *Discrete elliptic contact with interaction* (c) *Discrete circular contact with interaction*

(d) *Embedded Num. model* : $25-25$ *patches* (e) *Embedded Num. model* : $15-15$ *patches* (f) *Embedded Num. model* : $5-5$ *patches*

Figure 1.15: Contact normal stresses (MPa) distribution for different models: (a) the numerical reference model, (b) and (c) the analytic models, and (d) and (e) and (f) the embedded numerical models where roughness is modeled by contact laws

Conclusion

In this work, various contact models of rough surfaces have been presented. Using Hertz theory, an elliptic contact approximation of non symmetric asperities has been proposed which provides a more realistic description of contact stresses distribution. The results show that the predictions of the model are quite similar to the circular model one's for isotropic surfaces. But when this is not the case, the symmetric circular models overestimate contact area.
Interactions play a key role in the prediction of the surface behavior. Indeed, the results obtained with the model including interactions shows a good correlation with a highly meshed finite element model. However, regarding contact area, interactions seem to not affect its evolution versus the contact pressure.
In the second part, a useful simulation tool to model macroscopically a rough contact, has been proposed. Indeed, the surface is divided into patches each one representing the asperities which are inside it. Then an interface law is defined for each patch using a specific strategy which involves Love solution for elastic half spaces.
The numerical analysis shows consistent results. The size of patches does not affect the global surface response but has an influence on the contact stresses distribution. Such a strategy allows to integrate roughness effect in a large scale contact model and gives approximately the same global response as a highly meshed model, with a very reduced computational time.

Acknowledgments

The present research work has been supported by the International Campus on Safety and Intermodality in Transportation, the Hauts-de-France Region, the European Union, the Regional Delegation for Research and Technology, the Ministry of Higher Education and Research, the French National Research Agency (ANR COMATCO), and the National Center for Scientific Research. The authors gratefully acknowledge these institutions for their support.

Bibliography

[Abbot and Firestone(1933)] Abbott, E & Firestone, F. *Specifying surface quality: a method based on accurate measurement and comparison.* Journal of Mechanical Engineering, No. 55, 1933, 569-572.

[Björklund and Andersson(1994)] Björklund, S. & Andersson, Sö. *A numerical method for real elastic contacts subjected to normal and tangential loading.* Wear, 1994, 179, 117-122.

[Bandeira *et al.*(2004)] Bandeira, A., Wriggers, P. & de Mattos Pimenta, P. *Numerical derivation of contact mechanics interface laws using a finite element approach for large 3D deformation.* International Journal for numerical methods in Engineering, Wiley Online Library, 2004, 59, 173-195

[Bigerelle *et al.*(2004)] Bigerelle, M., Nianga, J.M., Najjar, D., Iost, A., Hubert, C. & Kubiak, K.J. *Roughness signature of tribological contact calculated by a new method of peaks curvature radius estimation on fractal surfaces.* Tribology International, 2013, 65, 235–247

[Boussinesq(1885)] Boussinesq, J. *Application des potentiels á l'étude de l'équilibre et du mouvement des solides élastiques: principalement au calcul des déformations et des pressions que produisent, dans ces solides, des efforts quelconques exercés sur une petite partie de leur surface ou de leur intérieur: mémoire suivi de notes étendues sur divers points de physique, mathématique et d'analyse.* Gauthier-Villars, 1885

[Bush *et al.*(1975)] Bush, A., Gibson, R. & Thomas, T. *The elastic contact of a rough surface.* Wear, Elsevier, 1975, 35, 87-111

[Ciavarella *et al.*(2006)] Ciavarella, M., Delfine, V. & Demelio, G. *A re-vitalized Greenwood and Williamson model of elastic contact between fractal surfaces.* Journal of the Mechanics and Physics of Solids, 2006, 54, 2569-2591

[Ciavarella *et al.*(2008)] Ciavarella, M., Greenwood, J. & Paggi, M. *Inclusion of interaction in the Greenwood and Williamson contact theory.* Wear, 2008, 265, 729-734

[Dapp *et al.*(2002)] Dapp, W. B., Lücke, A., Persson, B. N., & Müser, M. H. *Self-affine elastic contacts: percolation and leakage.* Physical review letters, 108(24), 244301.

[De Lorenzis and Wriggers(2013)] De Lorenzis, L. & Wriggers, P., *Computational homogenization of rubber friction on rough rigid surfaces.* Computational Materials Science, 2013, 77, 264-280

[Eriksson *et al.*(2002)] Eriksson, M., Bergman, F. & Jacobson, S. *On the nature of tribological contact in automotive brakes.* Wear, 2002, 252, 26-36

[Gallego *et al.*(2010)] Gallego, L., Nelias, D. & Deyber, S. *A fast and efficient contact algorithm for fretting problems applied to fretting modes I, II and III.* Wear, 2010, 268, 208–222.

[Greenwood and Williamson(1966)] Greenwood, J. & Williamson, J. *Contact of nominally flat surfaces*. Proceedings of the Royal Society of London. Series A. Mathematical and Physical Sciences, The Royal Society, 1966, 295, 300-319

[Hetzler and Willner(2012)] Hetzler, H. & Willner, K. *On the influence of contact tribology on brake squeal*. Wear, 2012, 46, 237-246

[Heussaff *et al.*(2012)] Heussaff, A., Dubar, L., Tison, T., Watremez, M. & Nunes, R.F. *A methodology for the modelling of the variability of brake lining surfaces*. Wear, Elsevier, 2012, 289, 145-159

[Hyun *et al.*(2004)] Hyun, S., Pei, L., Molinari, J.-F. & Robbins, M. *Finite-element analysis of contact between elastic self-affine surfaces*. Phy. Rev. E, 2004, 70, 026117

[Johnson(1987)] Johnson, K. L. *Contact mechanics*. Cambridge university press, 1987

[Kikuchi and Song(1981)] Kikuchi, N. & Song, Y. J. *Penalty finite element approximations of a class of unilateral problems in linear elasticity*. Quarterly of Applied Mathematics, 1981, 39, 1-22

[Leroux *et al.*(2010)] Leroux, J., Fulleringer, B. & Nelias, D. *Contact analysis in presence of spherical inhomogeneities within a half-space*. International Journal of Solids and Structures, 2010, 47, 3034–3049.

[Longuet-Higgins(1957)] Longuet-Higgins, M. S. *The statistical analysis of a random, moving surface*. Philosophical Transactions of the Royal Society of London. Series A, Mathematical and Physical Sciences, 1957, 321-387

[Lorenz *et al.*(2010)] Lorenz, B., Carbone, G. & Schulze, C. *Average separation between a rough surface and a rubber block: Comparison between theories and experiments*. Wear, 2010, 268, 984–990

[Love(1929)] Love, A. E. H. *The stress produced in a semi-infinite solid by pressure on part of the boundary*. Philosophical Transactions of the Royal Society of London. Series A, Containing Papers of a Mathematical or Physical Character, 1929, 377-420

[Magnier *et al.*(2014)] Magnier, V., Brunel, J.F. & Dufrénoy, P. *Impact of contact stiffness heterogeneities on friction-induced vibration*. International Journal of Solids and Structures, 2014, 51, 1662–1669

[Naidoo(2014)] Naidoo R., D. *Influence of friction material & test sequence on disc brake squeal*. Université Lille-1 , 2014

[Nash(2000)] Nash, S. G. *A survey of truncated-Newton methods*. Journal of Computational and Applied Mathematics, 2000, 124, 45-59

[Nash(1985)] Nash, S. G.*Preconditioning of truncated-Newton methods*. SIAM Journal on Scientific and Statistical Computing, SIAM, 1985, 6, 599-616

[Nayak(1971)] Nayak, P. R. *Random process model of rough surfaces*. Journal of Tribology, American Society of Mechanical Engineers, 1971, 93, 398-407

[Patewska *et al.*(1992)] Pastewka, L., Prodanov, N., Lorenz, B., Müser, Martin H., Robbins, Mark O & Persson, Bo NJ *Finite-size scaling in the interfacial stiffness of rough elastic contacts*. Physical Review E, APS, 2013, 87, 062809

[Pei *et al.*(2005)] Pei, L., Hyun, S., Molinari, J. F. & Robbins, M. O.*Finite element modeling of elasto-plastic contact between rough surfaces*. Journal of the Mechanics and Physics of Solids, 2005, 53, 2385-2409

[Persson *et al.*(2002)] Persson, B., Bucher, F. & Chiaia, B. *Elastic contact between randomly rough surfaces: comparison of theory with numerical results*. Physical Review-Series B-, American Physical Society, 2002, 65, 184106

[Persson *et al.*(2005)] Persson, B., Albohr, O., Tartaglino, U., Volokitin, A. & Tosatti, E. *On the nature of surface roughness with application to contact mechanics, sealing, rubber friction and adhesion*. Journal of Physics: Condensed Matter, IOP Publishing, 2005, 17, R1-R62

[Powell(1977)] Powell, M. J. D. *Restart procedures for the conjugate gradient method*. Mathematical programming, Springer, 1977, 12, 241-254

[Putignano *et al.*(2012)] Putignano, C., Afferrante, L., Carbone, G. & Demelio, G. *A new efficient numerical method for contact mechanics of rough surfaces*. International Journal of Solids and Structures, Elsevier, 2012, 49, 338-343

[Willner(2008)] Willner, K. *Fully coupled frictional contact using elastic halfspace theory*. Journal of Tribology, American Society of Mechanical Engineers, 2008, 031405, 1–8.

[Wriggers(1995)] Wriggers, P. *Finite element algorithms for contact problems*. Archives of Computational Methods in Engineering, Springer, 1995, 2, 1-49

[Wriggers(2006)] Wriggers, P. *Computational contact mechanics*. 2nd ed., Springer, 2006.

[Wriggers and Reinelt(2009)] Wriggers, P. & Reinelt, J., *Multi-scale approach for frictional contact of elastomers on rough rigid surfaces*. Computer Methods in Applied Mechanics and Engineering, 2009, 198, 1996-2008

[Yastrebov *et al.*(2011)] Yastrebov, V. A., Durand, J., Proudhon, H. & Cailletaud, G. *Rough surface contact analysis by means of the Finite Element Method and of a new reduced model*. Comptes Rendus Mécanique, 2011, 339, 473-490

[Yastrebov *et al.*(2015)] Yastrebov, V. A., Anciaux, G. & Molinari, J.-F. *From infinitesimal to full contact between rough surfaces: evolution of the contact area*. International Journal of Solids and Structures, 2015, 52, 83-102.

[Zahouani *et al.*(2009)] Zahouani, H., Mezghani, S., Pailler-Mattei, C. & Elmansori, M. *Effect of roughness scale on contact stiffness between solids*. Wear, 2009, 266, 589-591

[Zavarise *et al.*(1992)] Zavarise, G., Wriggers, P., Stein, E. & Schrefler, BA. *Real contact mechanisms and finite element formulation - a coupled thermomechanical approach*. International Journal for Numerical Methods in Engineering, Wiley Online Library, 1992, 35, 767-785

Transition

The first chapter was devoted to the analysis of the normal contact of rough surfaces between homogeneous solids. However, the material beneath the surface is subjected to thermal and mechanical loads which induce within it a gradient of material properties. This gradient is normal to the contact surface. Consequently, the material can be considered as a multi-layered system where each layer is homogeneous. Thus, this chapter is dedicated to the modeling of rough contact of multi-layered solids.
To do that, an asperity based model is developed using the Hankel transform and the transfer matrix technique. The obtained results are verified with the Finite Element Method calculations and the effects of solid layers are highlighted.
Hence, this chapter complements the micro-contact model developed in the first chapter by introducing the effect of a gradient of properties.

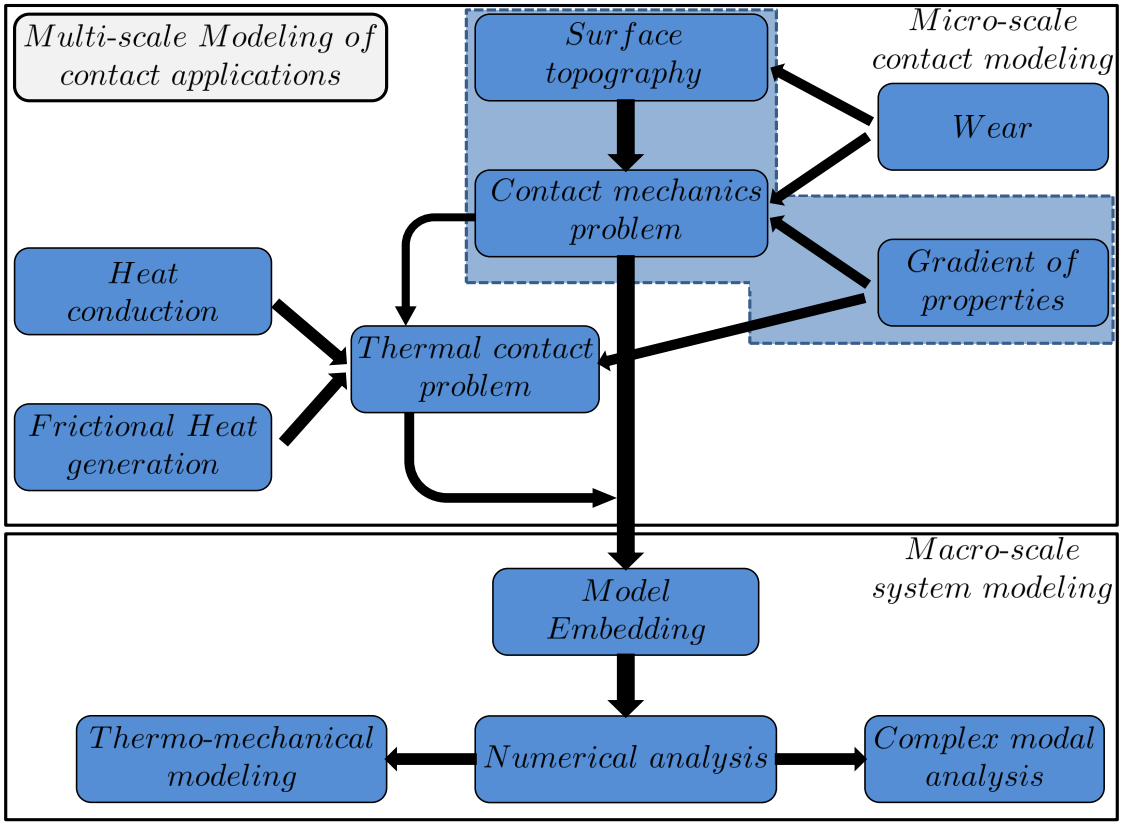

This figure presents the complete plan of this thesis. This chapter position is highlighted by a blue box in the background.

Chapter 2

A new contact model for multi-layered solids with rough surfaces

Contents

A new contact model for multi-layered solids with rough surfaces

Y. Waddad, V. Magnier, P. Dufrénoy, G. De Saxcé

Université de Lille Nord de France, F-59000 Lille, France
Lille1-LML, F-59655 Villeneuve d'Ascq, France
CNRS, FRE 8107, F-59655 Villeneuve d'Ascq, France

Abstract

A new numerical model is proposed to investigate the normal contact of multi-layered solids with rough surfaces. The Hankel transform and the transfer matrix technique are used to solve the problem of the deformation of a multi-layered solid. Then, the normal contact of an asperity is solved with Abel transform. Using this solution, an asperity-based contact model of rough surfaces is developed considering interactions between asperities. Numerical results are presented and compared to finite element calculations. The present model provides good results. The effects of interactions and the solid layers properties are discussed.

keywords : Contact analysis, surface roughness, multi-layered solid, Hankel transform, transfer matrix technique.

2.1 Introduction

Contact mechanics is of high interest in many engineering systems. For many of them, if two solids are in contact the real contact area is much smaller than the apparent one due to surface roughness. The interface behavior and the contact area has a great effect on system performance [Hetzler and Willner(2012)]. Naturally, the contact interface behavior depends on the roughness of the contacting solids and their mechanical properties. A contact model considering surface roughness goes first through the description of surface roughness. For this purpose, the random process theory is commonly used to compute some relevant statistical parameters [Longuet-Higgins(1957), Nayak(1971)] and fractal techniques are often used to characterize the multi-scale nature of rough surfaces [Majumdar and Tien(1990), Persson *et al.*(2005)]. There is a wide range of normal contact theories with rough surfaces. The classical contact theories are based on the concept of asperity which was first introduced by [Archard(1957)]. The basic idea of these theories is that contact occurs only on the top of these asperities. The well-known theory of [Greenwood and Williamson(1966)] represents the basis of all the asperity-based models. This theory assumes that roughness can be described as a spatial distribution of spherical asperities having the same curvature radius and a randomly distributed heights. The asperities deform according to Hertz theory. An improvement of this theory has been proposed by [Bush *et al.*(1975)]. They consider that each asperity is approximated by a paraboloid having the same geometric parameters as the asperity. The basic idea is to consider a random process of asperity heights and curvatures.
These models have achieved many results of great interest and have been successful for many years. However there is some weaknesses arising from the dependency on the statistical parameters and the non-consideration of interactions between asperities. Nevertheless, many improvements have been proposed by different authors. For instance, interactions have been included using semi-analytic approaches [Ciavarella *et al.*(2006), Waddad *et al.*(2016)]. Considering interactions is in particular important for the cases close to full contact situation.

The contact problem can also be solved by means of numerical methods. Using the finite element method, the problem is solved with optimization techniques and the region near to contact surfaces has to be finely meshed to guarantee a good accuracy [Pei(2005), Wriggers(2006)]. In return, the method is very costly in terms of CPU time which might be restrictive.
Another method is to consider the solid as a half space and solve the problem using the so-called influence coefficients [Johnson(1987), Willner(2008)]. Following this approach, only the surface is discretized which saves considerably CPU time. Using the Fast Fourier Transform (FFT), a fast version of this method, has been developed in [Gallego *et al.*(2010)].
The various existing models are focused on the contact surface geometry and consider that the solid is elastic and homogeneous, which is obviously not always true. Solids could be heterogeneous and could undergo several transformations under thermal and mechanical loadings and notably the subsurface material is the most exposed to these loadings. Hence, the bulk material properties change constantly and could affect the contact interface behavior. In several works, the material properties effect have been investigated. The plastic contact have been analyzed in [Wang *et al.*(2013)] using the influence matrix coefficients, and in [Kogut and Etsion(2002)] with the finite element method. Material heterogeneities have been considered in [Leroux *et al.*(2010)] to model fretting problems.
In many problems, the material beneath the surface can be considered as multi-layered, such as coating and composites. Moreover, in braking applications and hot forging tools, there is material transformations leading to the appearance of a gradient of material properties near to contact interfaces. Thus, these properties vary in the direction normal to the contact surface. Consequently, in some way, the material can be considered as a multi-layered system where each layer is homogeneous and perfect continuity is assumed at the interface layers.
To the best of our knowledge, the contact problem involving rough surfaces with multi-layered solids has so far received a few attention. The contact between an ellipsoid and a layered half space has been studied numerically in [Plumet and Dubourg(1998)]. In [Mao *et al.*(1997), Cole and Sayles(1992)], a Green function approach has been used to analyze a 2D sliding contact problem including friction. In [Peng and Bhushan(1996), Cai and Bushan(2005)], Papkovich-–Neuber potentials with a Fast Fourier Transform scheme (FFT), have been used to study the rough contact problem of elastic and plastic solids. These studies were carried on solids having a maximum of three layers. The problem is solved using the influence matrix method of which the coefficients are obtained by solving a linear system of equations. This system is obtained from the continuity conditions at the interface layers. Under such an approach, it is very complicated to extend the technique to cover the general case of multi-layers.
An interesting approach has been proposed by [Yue(1996)] who has investigated the contact problem of a multi-layered solid submitted to the indentation of a rigid circular plate using the transfer matrix technique([Singh(1986), Ernian(1996)]) and both the Fourier transform and Hankel transform properties [Sneddon(1995)] to obtain a Fredholm integral equation which is solved to obtain a closed-form solution for the contact problem. The main advantage of this technique is the ability to relate directly surface stresses to surface displacements which is very useful in solving contact and surface loading problems.
In this paper, a rough contact model of multi-layered solids is proposed based on the transfer matrix technique [Ernian(1996)] and the works of [Sneddon(1965), Yue(1996)]. First, by making use of the transfer matrix technique, the surface displacements are expressed in terms of surface stresses for a multi-layer problem. Second, a contact model of an axially symmetric asperity is developed by extending the solutions proposed by [Sneddon(1965), Yue(1996)]. Subsequently, by considering the classical multi-asperity surface description, the contact asperity model is used to solve the rough contact problem including interactions between asperities. Finally, typical results are presented and compared to Finite Element calculations. In particular, the effect of the solid layers elastic properties and the asperities interactions are discussed.

2.2 Surface loading of multi-layered elastic solid : the transfer matrix technique

2.2.1 General framework

Considering an isotropic elastic medium ($z \geq 0$) laterally unbounded. There is no body forces, the static equilibrium of the solid can be written as follows

$$\sigma_{ij,j} = 0 \tag{2.1}$$

where σ is the Cauchy stress tensor.
The deformation in the solid is assumed to be infinitesimal, thus, the strains ϵ_{ij} are related to the displacements u_i by

$$\epsilon_{ij} = \frac{1}{2}\left(u_{i,j} + u_{j,i}\right) \tag{2.2}$$

The constitutive based material has elastic properties varying with depth z. Thus, one can consider the solid as a multi-layered system of unbounded horizontal layers, where each layer has its own local properties (see Fig.2.1).
For the k^{th} layer, the constitutive equation between stresses σ_{ij} and strains ϵ_{ij} is expressed by Hooke's law

$$\sigma_{ij} = 2\,\mu_k \left(\varepsilon_{ij} + \frac{\nu_k}{1-2\nu_k}\varepsilon_{qq}\delta_{ij}\right) \tag{2.3}$$

where μ_k is the shear modulus, ν_k is the Poisson's ratio and δ_{ij} is the Kronecker symbol.
Solving the contact problem is to express the displacements and the stresses in the contacting regions of the top surface of the solid ($z = 0$). For that issue, the problem is solved through the Hankel integral transform and the transfer matrix technique.

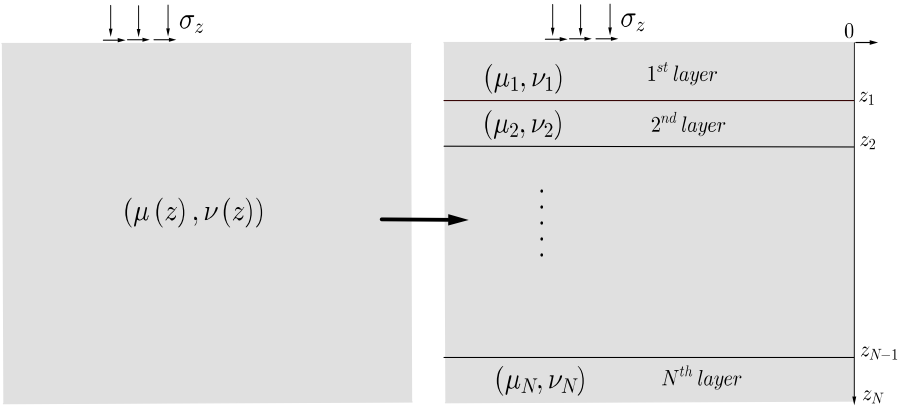

Figure 2.1: Schematic of a multi-layered elastic solid under surface loads

2.2.2 The transfer matrix technique

Let us consider the axis of symmetry of an isotropic elastic medium as the z-axis. The governing equations are presented as follows in cylindrical coordinates (r, θ, z). The problem is solved in the case of axially symmetric deformation and all field variables are independent of θ.

Considering the stress vector defined by $\mathbf{T}_z = [\sigma_{rz}, \sigma_{\theta z}, \sigma_{zz}]^t$ and the displacements vector $\mathbf{u} = [u_r, u_\theta, u_z]^t$. Let us introduce the following set of solution representation using the Hankel integral transform

$$\mathbf{w} = \begin{bmatrix} w_\xi \\ w_\eta \\ w_z \end{bmatrix} = \int_0^{+\infty} \begin{bmatrix} -J_1(\rho r)/\rho & 0 & 0 \\ 0 & J_1(\rho r)/\rho & 0 \\ 0 & 0 & J_0(\rho r) \end{bmatrix} . \mathbf{u}\, r\mathrm{d}r$$

$$\boldsymbol{\tau} = \begin{bmatrix} \tau_\xi \\ \tau_\eta \\ \tau_z \end{bmatrix} = \int_0^{+\infty} \begin{bmatrix} -J_1(\rho r)/\rho & 0 & 0 \\ 0 & J_1(\rho r)/\rho & 0 \\ 0 & 0 & J_0(\rho r) \end{bmatrix} . \mathbf{T}_z\, r\mathrm{d}r$$

It is well known that this set of variables satisfies the two decoupled first order differential equations

$$\frac{\mathrm{d}}{\mathrm{d}z} \begin{bmatrix} w_\eta \\ \tau_\eta \end{bmatrix} = \begin{bmatrix} 0 & \dfrac{1}{\mu} \\ \mu\rho^2 & 0 \end{bmatrix} \begin{bmatrix} w_\eta \\ \tau_\eta \end{bmatrix}$$

$$\frac{\mathrm{d}}{\mathrm{d}z} \begin{bmatrix} w_z \\ \rho w_\xi \\ \tau_z/\rho \\ \tau_\xi \end{bmatrix} = \begin{bmatrix} 0 & \dfrac{\nu\rho}{1-\nu} & \dfrac{(1-2\nu)\rho}{2\mu(1-\nu)} & 0 \\ -\rho & 0 & 0 & \dfrac{\rho}{\mu} \\ 0 & 0 & 0 & \rho \\ 0 & \dfrac{2\mu\rho}{1-\nu} & -\dfrac{\nu\rho}{1-\nu} & 0 \end{bmatrix} \begin{bmatrix} w_z \\ \rho w_\xi \\ \tau_z/\rho \\ \tau_\xi \end{bmatrix}$$

The global solution of this system is an eigenvalue extraction problem and can be written in the following form

$$\begin{bmatrix} w_\eta \\ \tau_\eta \end{bmatrix} = \mathbf{Z}_1 \begin{bmatrix} A_\eta \\ B_\eta \end{bmatrix} \text{ and } \begin{bmatrix} w_z \\ \rho w_\xi \\ \tau_z/\rho \\ \tau_\xi \end{bmatrix} = \mathbf{Z}_2 \begin{bmatrix} A_z \\ A_\xi \\ B_z \\ B_\xi \end{bmatrix}$$

where A_z , A_η, B_η, B_z, A_ξ and B_ξ are constants and the matrices $\mathbf{Z}_1$ and $\mathbf{Z}_2$ are given in Appendix A. Considering that the medium is an unbounded horizontal layer of which the thickness is h. The superscript $^{(+)}$ (resp. $^{(-)}$) is used for the top layer surface variables (resp. the bottom one). One can show that

$$\begin{bmatrix} w_\eta^{(+)} \\ \tau_\eta^{(+)}/\rho \end{bmatrix} = \mathbf{T}_\eta \begin{bmatrix} w_\eta^{(-)} \\ \tau_\eta^{(-)}/\rho \end{bmatrix} \text{ and } \begin{bmatrix} w_z^{(+)} \\ \rho w_\xi^{(+)} \\ \tau_z^{(+)}/\rho \\ \tau_\xi^{(+)} \end{bmatrix} = \mathbf{T}_{z\xi} \begin{bmatrix} w_z^{(-)} \\ \rho w_\xi^{(-)} \\ \tau_z^{(-)}/\rho \\ \tau_\xi^{(-)} \end{bmatrix} \tag{2.4}$$

where $\mathbf{T}_{z\xi}$ and $\mathbf{T}_\eta$ are the transfer matrices of the layer and are given in Appendix A.
Now let us consider a multi-layered body made of N horizontal layers. The 1^{st} layer is on the top of the solid and the N^{th} layer lies on a homogeneous half space that can be either rigid or elastic. Considering the perfect continuity between the parallel layers, then the displacement field $\mathbf{u}$ and the stress vector $\mathbf{T}_z$ are both continuous. Using the transfer matrices, one can obtain the following set of equations

$$\begin{bmatrix} w_\eta^{(0)} \\ \tau_\eta^{(0)}/\rho \end{bmatrix} = \underbrace{\mathbf{T}_\eta^{(1)} \ldots \mathbf{T}_\eta^{(N)}}_{\mathbf{R}} \begin{bmatrix} w_\eta^{(N)} \\ \tau_\eta^{(N)}/\rho \end{bmatrix} \text{ and } \begin{bmatrix} w_z^{(0)} \\ \rho w_\xi^{(0)} \\ \tau_z^{(0)}/\rho \\ \tau_\xi^{(0)} \end{bmatrix} = \underbrace{\mathbf{T}_{z\xi}^{(1)} \ldots \mathbf{T}_{z\xi}^{(N)}}_{\mathbf{S}} \begin{bmatrix} w_z^{(N)} \\ \rho w_\xi^{(N)} \\ \tau_z^{(N)}/\rho \\ \tau_\xi^{(N)} \end{bmatrix}$$

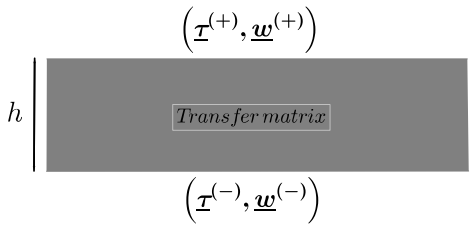

Figure 2.2: Schematic of an elastic layer of which the deformations and the stresses are given by the transfer matrix technique

From these equations, it can be seen that the transformed stresses and displacements of the top surface of the 1^{st} layer can be related directly to those of the bottom surface of the N^{th} layer by the mean of the matrices $\mathbf{S}$ and $\mathbf{R}$. These matrices are given by a simple product of the transfer matrices of the intermediate layers as shown in these equations.
In order to solve the problem, the boundary conditions in the bottom face are used. Following many algebraic operations, one can show that

$$\begin{bmatrix} w_z^{(0)} \\ \rho w_\xi^{(0)} \\ w_\eta^{(0)} \end{bmatrix} = \mathbf{F} \begin{bmatrix} \tau_z^{(0)}/\rho \\ \tau_\xi^{(0)} \\ \tau_\eta^{(0)}/\rho \end{bmatrix} \text{ , where } \mathbf{F} = \begin{bmatrix} F_{11} & F_{12} & 0 \\ F_{21} & F_{22} & 0 \\ 0 & 0 & F_{33} \end{bmatrix} \tag{2.5}$$

The matrix $\mathbf{F}$ is called the transfer matrix of the body. The matrix coefficients depend on the bottom surface boundary conditions and are given in Appendix B.
In Eq.2.5, one can see that surface displacements are related directly to surface loads using the matrix $\mathbf{F}$. More clearly, if a general surface loading is applied to the top surface $z = 0$, one can compute the real displacements automatically using the inverse Hankel transform of Eq.2.5.
At last, it has to be noticed that the transfer matrix can also be formulated in Cartesian coordinates with the use of Fourier integral transform.
In what follows, the normal elastic contact problem of an axially symmetric asperity is solved by making use of the transfer matrix and integral transforms.

2.3 Elastic contact of an axially symmetric asperity

2.3.1 General contact problem

Considering a multi-layered solid, the top surface shape of the solid contains an asperity which is described by a function $z = f(r)$. The small-slope approximation is considered. The asperity is compressed normally against a rigid plan with a vertical motion δ. Just as in Hertz theory, a circular contact zone appears and has a radius a. Also, no shear stresses are considered.
The boundary conditions of the problem are :

- Inside the contact: $u_z(r) = \delta - f(r)$, $0 \leq r \leq a$
- Outside the contact: $\sigma_{zz}(r) = 0$, $a \leq r$

As shown in the previous section, using the transfer matrix technique, one can show that

$$w_z = F_{11}(\rho)(\tau_z/\rho)$$

Using inverse Hankel transform, the boundary conditions can be written as follows

- Inside contact:
$$u_z(r) = \delta - f(r) = \int_0^{+\infty} F_{11}(\rho)\,\tau_z(\rho)\,J_0(\rho r)\,\mathrm{d}\rho \ , \ 0 \le r \le a \tag{2.6}$$
- Outside contact:
$$\int_0^{+\infty} \tau_z(\rho)\,J_0(\rho r)\,\rho \mathrm{d}\rho = 0 \ , \ a \le r$$

Let us denote
$$\alpha = \lim_{\rho\to\infty} \frac{1}{F_{11}(\rho)}$$
One can show that for any given boundary conditions, we have
$$\alpha = \frac{\mu_1}{\nu_1 - 1}$$
where μ_1 et ν_1 are the elastic parameters of the first layer.
Consequently, we introduce the kernel k_z defined by
$$k_z(\rho) = \alpha\, F_{11}(\rho) - 1$$
Then Eq.(2.6) becomes
$$\alpha(\delta - f(r)) = \int_0^{+\infty} \tau_z(\rho)\,J_0(\rho r)\,\mathrm{d}\rho + \int_0^{+\infty} k_z(\rho)\ \tau_z(\rho)\,J_0(\rho r)\,\mathrm{d}\rho\,, 0 \le r \le a \tag{2.7}$$
In order to solve this singular integral equation, we will refer to the earlier works of [Sneddon(1965), Yue(1996)]. Therefore, the auxiliary function ϕ is introduced by
$$\tau_z(\rho) = \int_0^a \phi(x)\cos(\rho x)\,\mathrm{d}x \tag{2.8}$$
We also introduce the Abel transform $\mathcal{A}$ defined by
$$\mathcal{A}(f(x), r) = \frac{2}{\pi}\int_0^r \frac{f(x)}{\sqrt{r^2 - x^2}}\,\mathrm{d}x$$
Knowing that
$$J_0(\rho r) = \mathcal{A}(\cos(\rho x), r)$$
then
$$\int_0^{+\infty} \tau_z(\rho)\,J_0(\rho r)\,\mathrm{d}\rho = \mathcal{A}\left(\frac{\pi}{2}\phi(x), r\right)$$
and
$$\int_0^{+\infty} k_z(\rho)\ \tau_z(\rho)\,J_0(\rho r)\,\mathrm{d}\rho = \mathcal{A}\left(\int_0^{+\infty}\int_0^a k_z(\rho)\ \phi(x)\cos(\rho x)\cos(\rho r)\,\mathrm{d}x\mathrm{d}\rho, r\right)$$
Hence equation (2.7) may be written as an Abel integral equation
$$\mathcal{A}\left(\frac{\pi}{2}\phi(x) + \int_0^{+\infty}\int_0^a k_z(\rho)\ \phi(x)\cos(\rho x)\cos(\rho r)\,\mathrm{d}x\mathrm{d}\rho, r\right) = \alpha(\delta - f(r))$$

Making use of the inverse Abel transform $\mathcal{A}^{-1}$ and the integration by parts, one can obtain

$$\frac{\pi}{2}\phi(r)+\int_0^{+\infty}\int_0^a k_z(\rho)\ \phi(x)\cos(\rho x)\cos(\rho r)\,\mathrm{d}x\mathrm{d}\rho=\alpha\left(\delta-f(0)-\int_0^r\frac{r\,f'(x)}{\sqrt{r^2-x^2}}\mathrm{d}x\right)$$

After normalization, a Fredholm equation of the second order is obtained

$$\phi_a(s)+\int_0^1 K_a(s,t)\,\phi_a(t)\,\mathrm{d}t=G(s) \tag{2.9}$$

where

$$K_a(s,t)=\frac{2}{\pi}\int_0^{+\infty}k_z(\rho/a)\cos(\rho s)\cos(\rho t)\,\mathrm{d}\rho$$

and

$$\phi_a(u)=\frac{\pi}{2}\phi(a.u)$$

and

$$G(s)=\alpha\left(\delta-f(0)-a\int_0^s\frac{s\,f'(at)}{\sqrt{s^2-t^2}}\mathrm{d}t)\right)$$

Solving Eq.(2.9) is done numerically by a quadrature technique. Indeed, by choosing an interpolation base, the equation can be written in a matrix format

$$\boldsymbol{\phi}+\mathbf{K}.\boldsymbol{\phi}=\mathbf{G}$$

and then

$$\boldsymbol{\phi}=(\mathbf{I}+\mathbf{K})^{-1}\mathbf{G}$$

Once the auxiliary function ϕ_a is computed, one can calculate the total normal force P by

$$P=-4a\int_0^1\phi_a(t)\,\mathrm{d}t \tag{2.10}$$

At last, all surface stresses and displacements can be deduced using Hankel transform properties. In particular, we have

- The normal stress

$$\sigma_{zz}(s)=\frac{2}{\pi a}\left(\frac{\phi_a(1)}{\sqrt{1-s^2}}-\int_s^1\frac{\phi_a'(t)}{\sqrt{t^2-s^2}}\mathrm{d}t\right)\ ...\ s=r/a\leq 1$$

  If f is smooth, contact stress vanishes at the edge of contact zone ($r=a$), hence, it comes that $\phi_a(1)=0$ and

$$\sigma_{zz}(s)=-\frac{2}{\pi a}\int_s^1\frac{\phi_a'(t)}{\sqrt{t^2-s^2}}\mathrm{d}t\ ...\ s=r/a\leq 1 \tag{2.11}$$

- Contact radius a in the case where f is smooth

$$\delta=f(0)+a\int_0^1\frac{f'(at)}{\sqrt{(1-t^2)}}\mathrm{d}t+\frac{1}{\alpha}\int_0^1 K_a(1,t)\,\phi_a(t)\,\mathrm{d}t \tag{2.12}$$

- The normal displacement outside contact area

$$u_z(s)=\frac{2}{\alpha\pi}\int_0^1\phi_a(t)\left(\frac{1}{\sqrt{s^2-t^2}}+\int_0^\infty k_z(\rho/a)\cos(\rho t)J_0(\rho s)\,\mathrm{d}\rho\right)\mathrm{d}t$$

  where $s=r/a>1$

It is important to state that the solution of [Sneddon(1965)] of elastic half spaces can be deduced by considering $k_z=0$, whereas the solution given by [Yue(1996)] can be retrieved by choosing $f=0$, which corresponds to the flat contact case. In other words, the proposed solution is an extension of both solutions to cover the axially symmetric frictionless contact problem of multi-layered solids.

2.3.2 Contact solution for a parabolic asperity

Considering the case of an asperity of parabolic shape. In this case, by taking the origin on the symmetry axis, the function f is given by

$$f(r) = \frac{r^2}{2R}$$

Hence the Fredholm equation (2.9) becomes

$$\phi_a(s) + \int_0^1 K_a(s,t)\,\phi_a(t)\,\mathrm{d}t = \alpha\left(\delta - \frac{(as)^2}{R}\right) \tag{2.13}$$

In this equation, the unknown is the contact radius a. Eq.(2.13) is solved iteratively starting from an initial trial value which can be chosen for instance from Hertz theory $a_0 = \sqrt{R.\delta}$.
In order to illustrate the results obtained with this model, some calculations have been performed on a single asperity model of a two-layered solid (see Fig.2.3). The asperity is in contact with a rigid flat plan that is moved vertically against the asperity with a given displacement δ.

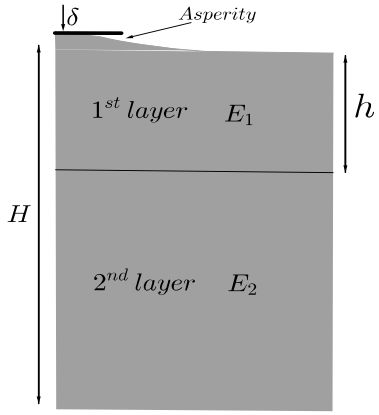

Figure 2.3: Schematic of the single asperity model. The asperity is compressed vertically with a displacement δ. The solid is composed of two elastic layers.

The total height of the solid is $H = 1mm$ and the elastic modulus of the first layer is $E_1 = 4GPa$. Both of these quantities are fixed in this study, while the first layer thickness h is varied as well as the second layer modulus E_2. The Poisson ratio $\nu = 0.15$ is the same for both layers.
The obtained results are compared to finite element calculations and Hertz theory. The latter corresponds to the case of a homogeneous half space. The idea is to evaluate the accuracy of the model comparing to FEM calculations and to enhance the role of the sub-layers parameters.
The evolution of the total force P with the displacement is presented in Figs.2.4 -2.6. In Fig.2.4, the elastic modulus ratio E_2/E_1 is varied from 1 to 10 and the thickness h is fixed at $100\mu m$. As we can see, the predicted force deviates from Hertz theory predictions when the ratio E_2/E_1 increases. For the unit ratio, there is a slight difference which is due to boundary conditions effect. Moreover, comparing the model predictions with finite element results (marked by FEM in the figure and drawn by dashed lines) show a good consistency.
In Fig.2.5, the effect of the first layer thickness is highlighted. The predicted results match FEM results. The less the thickness is, the more the results deviate from Hertz theory. Additionally, the curve plotted in Fig.2.6 shows the predicted values for different values of asperity radius and fixed elastic parameters.

Once again, there is a good consistency between the obtained results and FEM values.
As summary, the proposed contact solution is in good accordance with FEM calculations and the force-displacement evolution is affected by the layers properties and thicknesses. In the following, the contact solution is simplified and used to model the normal contact of rough surfaces considering solid layers.

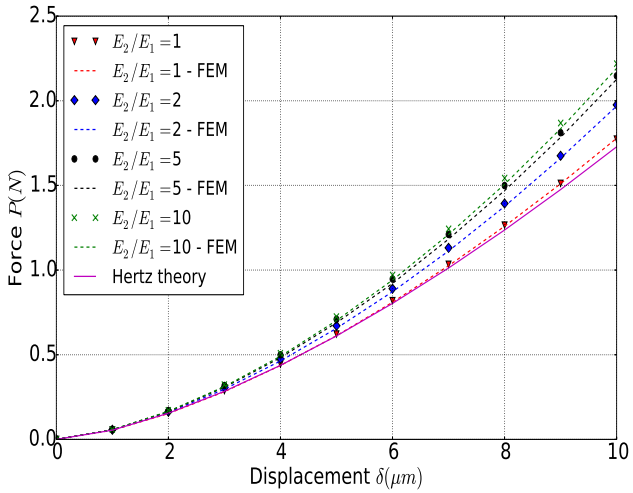

Figure 2.4: Variation of the total force with the vertical displacement for the parameters : $h = 100\mu m$ and $R = 100\mu m$

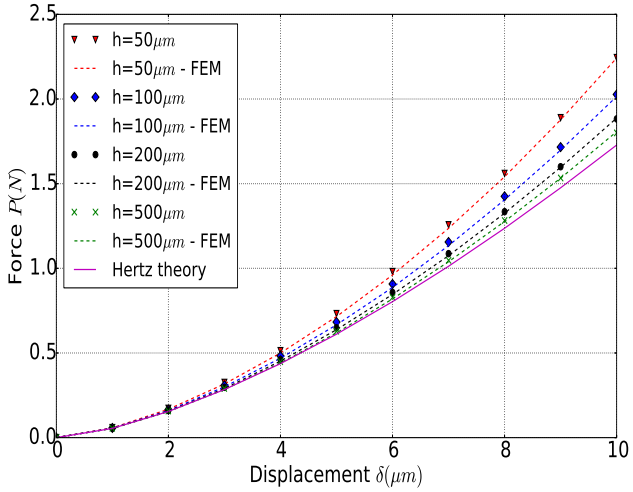

Figure 2.5: Variation of the total force with the vertical displacement for the parameters : $E_2 = 10GPa$ and $R = 100\mu m$

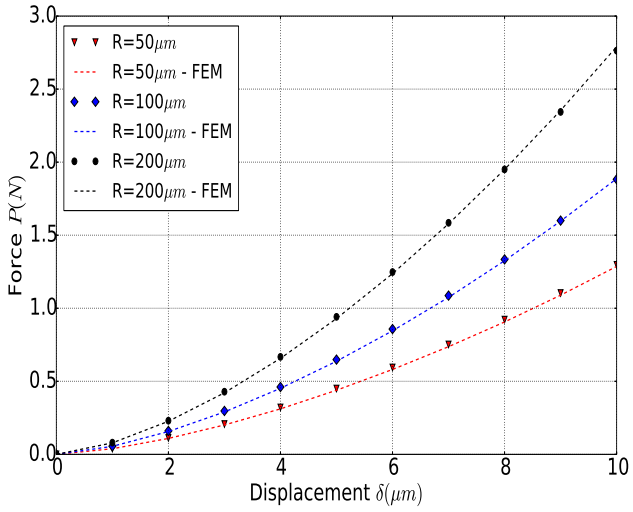

Figure 2.6: Variation of the total force with the vertical displacement for the parameters : $E_2 = 10GPa$ and $h = 100\mu m$

2.4 Contact of rough surfaces

2.4.1 An approximate asperity contact model

In the previous section, a contact model of asperities has been presented. In order to make use of this model, some simplifications are proposed. First, let us consider a parabolic asperity. The derivation of the Fredholm integral equation 2.9 gives

$$\frac{\mathrm{d}\phi_a}{\mathrm{d}s}(s) + \int_0^1 \frac{\partial K_a}{\partial s}(s,t)\,\phi_a(t)\,\mathrm{d}t = -\alpha\frac{2a^2 s}{R}$$

Since $\dfrac{\partial K_a}{\partial s}(0,t) = 0$, one can deduce that $\dfrac{\mathrm{d}\phi_a}{\mathrm{d}s}(0) = 0$
Hence, by considering that the function ϕ_a is a 2^{nd} order polynomial, one can write

$$\phi_a(s) = \phi_a(0)\left(1 - s^2\right)$$

Using this simplified form and based on Eq.(2.9), $\phi_a(0)$ and δ are respectively given by

$$\phi_a(0) = \frac{\alpha\delta}{1 + \displaystyle\int_0^1 K_a(0,t)\left(1 - t^2\right)\mathrm{d}t} \tag{2.14}$$

$$\delta = \frac{a^2}{R} + \frac{\phi_a(0)}{\alpha}\int_0^1 \left(1 - t^2\right) K_a(1,t)\,\mathrm{d}t \tag{2.15}$$

Making use of the two last equations, one can write

$$\phi_a(0) = \frac{\alpha a^2}{R}\chi(a) \text{ and } \delta = \frac{a^2}{R}\zeta(a)$$

where ζ and χ are functions of a

$$\chi(a) = \frac{1}{1 + \int_0^1 \left(1 - t^2\right) \left(K_a(0,t) - K_a(1,t)\right) \mathrm{d}t}$$

$$\zeta(a) = \left(1 + \int_0^1 \left(1 - t^2\right) K_a(0,t)\, \mathrm{d}t\right) \chi(a)$$

Finally, the following approximated expressions are deduced:

- The total normal force P

$$P = -\frac{8}{3}\, \alpha\, \chi(a)\, \frac{a^3}{R} \tag{2.16}$$

- The normal stress σ_{zz}

$$\sigma_{zz}(r) = \frac{4\,\alpha}{\pi R} \chi(a) \sqrt{a^2 - r^2} \quad \text{if } r \leq a \tag{2.17}$$

- The normal displacement is then given by

$$u_z(r) = \begin{cases} \dfrac{1}{2R}\left(2a^2 \zeta(a) - r^2\right) & \text{if } r \leq a \\ \dfrac{\chi(a)}{\pi R}\left[\left(2a^2 - r^2\right) \arcsin\left(\dfrac{a}{r}\right) + a\sqrt{r^2 - a^2} + g(a,r)\right] & \text{else.} \end{cases} \tag{2.18}$$

where $g(a,r) = 4 \int_0^\infty k_z(\rho)\, J_0(\rho r)\, \dfrac{\sin(a\rho) - a\rho\cos(a\rho)}{\rho^3} \mathrm{d}\rho$

By using this simplified form, one can express all the variables as a function of the contact radius a, which is very helpful for the case of rough surfaces as it will be presented in the next section. But before tackling the problem of rough surfaces, the parameters χ and ζ are plotted in Figs.2.7-2.8 for the same configurations studied in the previous section. For small values of contact radius a, these parameters are close to 1. In this case, the predicted values of the total force is almost the same as those predicted by Hertz theory.
Increased ratio E_2/E_1 and or decreased h/H both lead to too much small values of ζ corresponding to too much large contact radius for a given displacement, and to too much large values of χ which results in more important force values.
These parameters can be seen, in a certain manner, as sub-layer impact coefficients. Indeed, if the sub-layers have elastic parameters that are very different from those of the first one or if the first layer is very thin, these coefficients will influence strongly the contact behavior, which is the case in the predicted curves shown in Figs.2.4-2.6.
As stated before, this approximate solution is obtained using a 2nd order approximation of the auxiliary function. In Fig.2.9, the relative error between the total force predicted using the approximate solution and the one issued from the theory is drawn for the same tested configurations. As we can see, the maximum relative error does not exceed 1% except for the case of the thinnest layer ($h = 50\mu m$) where the value of 4% is reached, which is still acceptable.
The approximation introduced in this paragraph is of great importance because it significantly simplifies the asperity contact model. Using this approximation a multi-asperity contact model is presented in the following section.

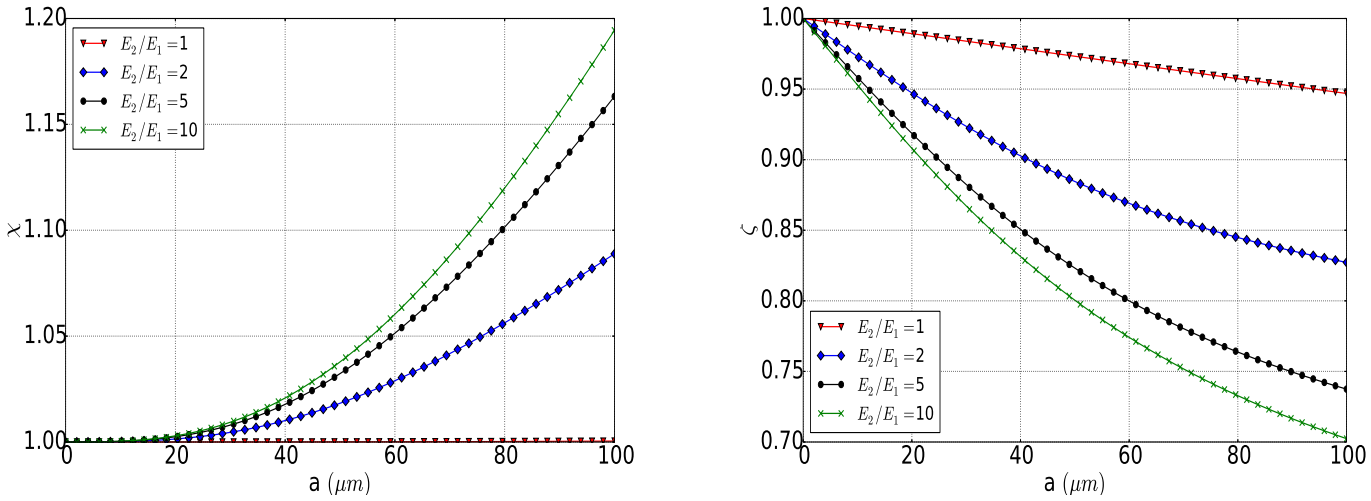

Figure 2.7: Evolution of the functions χ and ζ for the case of $h = 100\mu m$

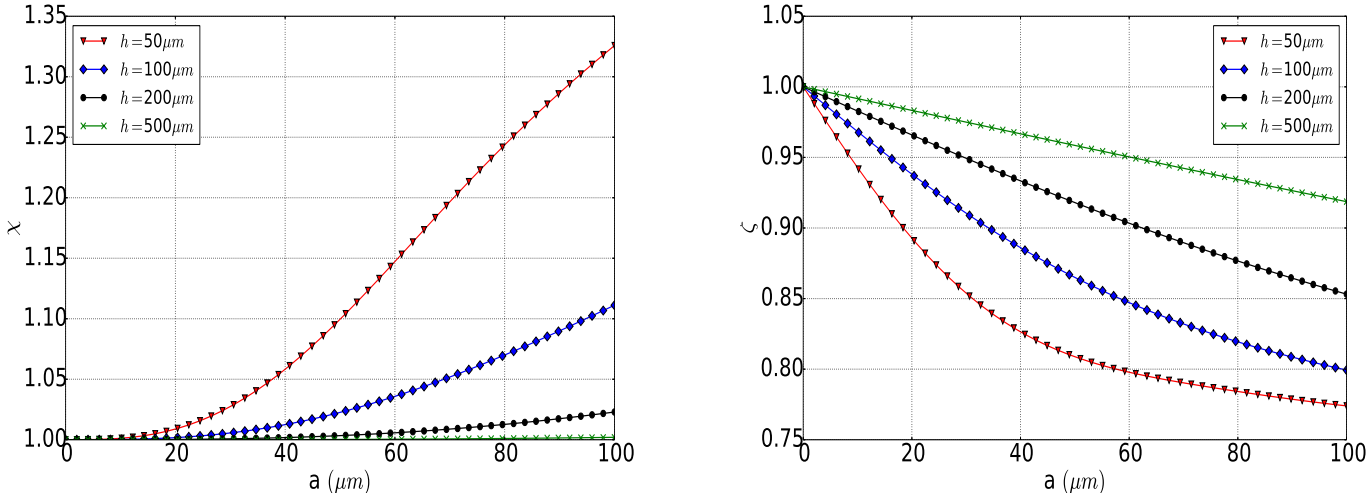

Figure 2.8: Evolution of the functions χ and ζ for the case $E_2 = 10GPa$

2.4.2 A multi-asperity contact model

In this section, we are dealing with the contact problem between a rough surface and a flat one. The following geometric description is similar to the ones given in [Ciavarella *et al.*(2006), Waddad *et al.*(2016)]. The body containing the rough surface is elastic and is considered as a multi-layered solid. The flat surface is rigid and is moved normally with a displacement δ with respect to the rough surface. Within the framework of a multi-asperity approach, the normal displacement in every point is a consequence of all the contact strengths applied on surface asperities. Taking into account the interactions between asperities, the displacement of each asperity is obtained by summing the displacements due to all the contacting asperities.

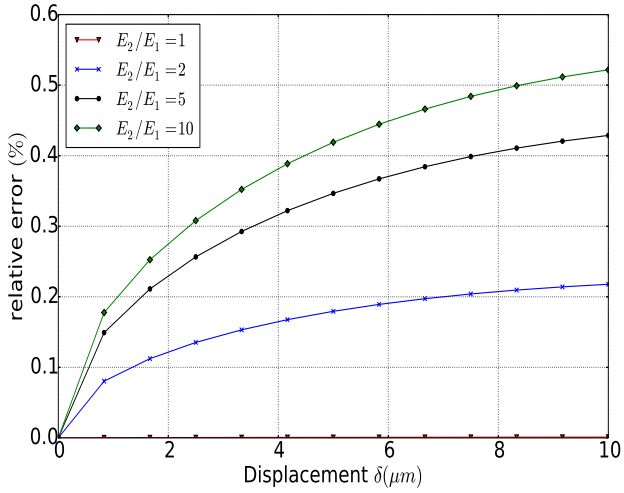

(i) $h = 100\mu m$, $R = 100\mu m$

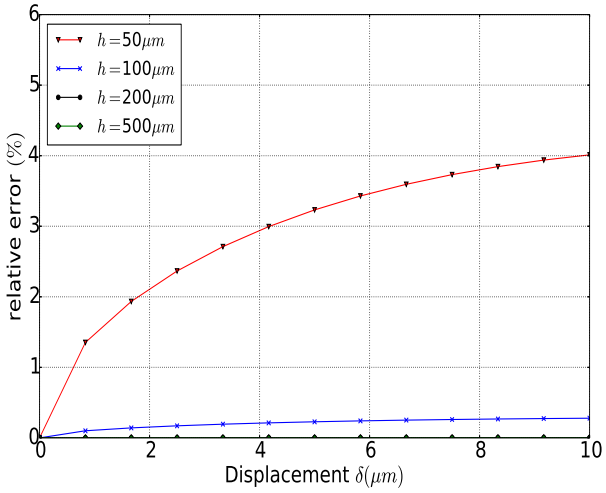

(ii) $E_2 = 10GPa$, $R = 100\mu m$

Figure 2.9: The relative error between the theoretical predictions of the total force and those of the approximated model for two considered configurations

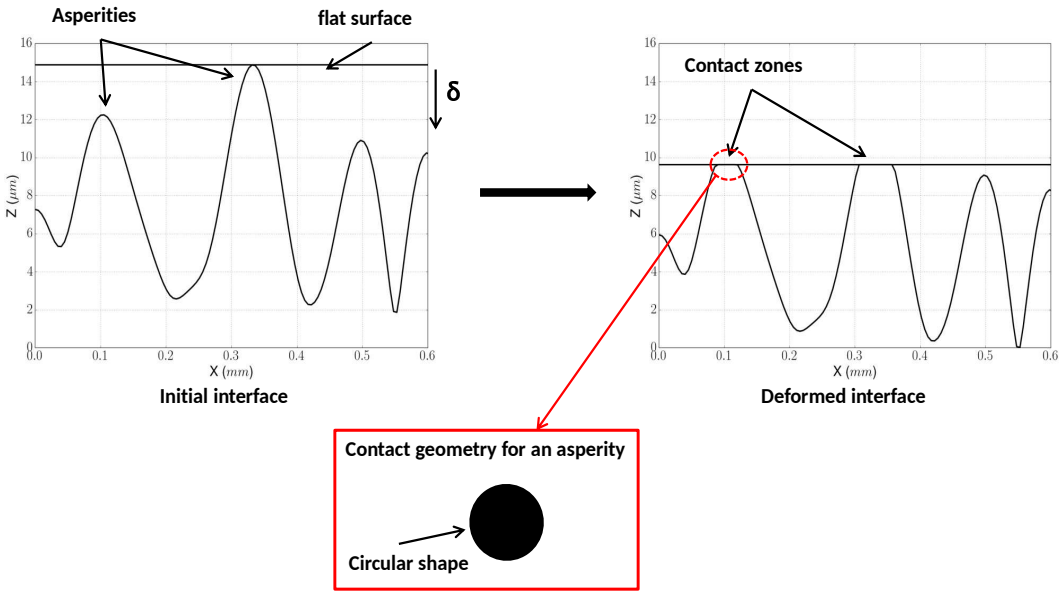

Figure 2.10: Geometry of rough contact problem within a multi-asperity approach. Contact occurs only on asperities and the contact area shape in an asperity is circular.

If N is the number of the supposed contacting asperities, the displacement w_k of the k^{th} asperity reads

$$w_k = \sum_{i=1}^{N} G_i\left(r_{ik}\right) \tag{2.19}$$

where

$$G_i\left(r_{ik}\right)=\begin{cases}\dfrac{a_i^2}{R_i}\,\zeta\left(a_i\right) & \text{if } i=k\\ \dfrac{\chi\left(a_i\right)}{\pi R_i}\left[\left(2a_i^2-r_{ik}^2\right)\arcsin\left(\dfrac{a_i}{r_{ik}}\right)+a_i\sqrt{r_{ik}^2-a_i^2}+g\left(a_i,r_{ik}\right)\right] & \text{else}\end{cases}$$

where r_{ik} is the horizontal distance between the k^{th} and the i^{th} asperity.
Let us denote z_M the maximum height of the rough surface and z_i the height of the i^{th} asperity, the prescribed displacement of the i^{th} asperity is given by:

$$\delta_k=\langle\delta-\left(z_M-z_k\right)\rangle \tag{2.20}$$

where $<.>$ is the positive part of its operand.
Solving the problem is to find a distribution of contact dimensions $\mathbf{a}=(a_1,a_2,...,a_N)$ satisfying contact conditions : $w_k\geq\delta_k$.
The equality means that the asperity is in contact while the strict inequality signifies that the asperity is not in contact, and in this case, the change of the asperity height is due to interaction effects.
Unlike our previous work [Waddad *et al.*(2016)], where the problem has been solved using a direct method based on the minimization of an objective function based on contact kinematic conditions, the present problem is solved with a variational method consisting in minimizing of the total complementary energy of the solid [Johnson(1987)]

$$U_E=\frac{1}{2}\int_{\Gamma_c}p.u_z\;dS-\int_{\Gamma_c}p.\delta\;dS \tag{2.21}$$

where Γ_c is the contact zone, p is the contact pressure field and δ is the prescribed displacement field.
For a given asperity, the internal energy is given by

$$\begin{aligned}\int_{\Gamma_j}p.u_z\;dS&=\frac{-4\,\alpha\chi\left(a_j\right)}{\pi R_j}\int_{\Gamma_j}\sqrt{a_j^2-r^2}\sum_l^N G_l\left(r_{lj}\right)\;dS\\&=\frac{-8\,\alpha}{3}\frac{\chi\left(a_j\right)\;a_j^3}{R_j}\left(\sum_{l\neq j}^N G_l\left(r_{lj}\right)+\frac{a_j^2}{R_j}\left(\zeta\left(a_j\right)-\frac{1}{5}\right)\right)\end{aligned}$$

and the prescribed displacements work is

$$\begin{aligned}\int_{\Gamma_j}p.\delta\;dS&=\frac{-8\,\alpha}{R_j}\,\chi\left(a_j\right)\int_{\Gamma_j}\sqrt{a_j^2-r^2}\left(\delta_j-\frac{r^2}{2R_j}\right)\;rdr\\&=\frac{-8\,\alpha}{3}\frac{\chi\left(a_j\right)\;a_j^3}{R_j}\left(\delta_j-\frac{1}{5}\frac{a_j^2}{R_j}\right)\end{aligned}$$

Hence the total complementary energy on all the asperities is given by

$$U_E=\frac{-4\,\alpha}{3}\sum_j^N\frac{\chi\left(a_j\right)\;a_j^3}{R_j}\left(\sum_{l\neq j}^N G_l\left(r_{lj}\right)+\frac{a_j^2}{R_j}\left(\zeta\left(a_j\right)+\frac{1}{5}\right)-2\delta_j\right) \tag{2.22}$$

For the special case of a homogeneous half space $\xi=\zeta=1$, this energy reads

$$U_E=\frac{-4\,\alpha}{3}\sum_j^N\frac{a_j^3}{R_j}\left(\sum_{l\neq j}^N G_l\left(r_{lj}\right)+\frac{2}{5}\frac{a_j^2}{R_j}-2\delta_j\right) \tag{2.23}$$

The problem is solved by minimizing the system total energy under the constraints $a \geq 0$. A Newton likewise method is used to minimize this quantity [Nash(2000)].
Once the optimal contact radius distribution is found, the total force and the real contact area are obtained by adding the contribution of all the contacting asperities, hence they are respectively given by

$$P = -\frac{8}{3}\alpha \sum_{i}^{N} \chi(a_i) \frac{a_i^3}{R} \tag{2.24}$$

$$A = \pi \sum_{i}^{N} a_i^2 \tag{2.25}$$

The normal separation between the two faces is

$$g_n = (z_M - \bar{z}) - \delta \tag{2.26}$$

where $\bar{z}$ is the height of the mean plane.
As stated before, this model considers the interactions between asperities. A simple form can be proposed to cover the case where interactions are not considered. Indeed, by neglecting the interaction terms G_j, the contact radius for each asperity can be computed from the following equation

$$\delta_i = \frac{a_i^2}{R_i} \zeta(a_i)$$

This formula can be obtained directly from contact kinematic conditions.

2.5 Results

As an example, the normal contact of a two-layered elastic solid with a rigid plan is investigated. The surface of the solid is rough (see Fig.2.11). For instance, surface roughness is kept fixed while the solid layer parameters are varied. For each configuration, the obtained results are compared to finite element calculations in the same manner as it was done for the single asperity problem (see section 2.3.2). Moreover, the effect of the solid parameters and interactions is discussed.
The dimensions of the surface sample are $1mm \times 1mm$. Roughness is generated numerically using numerical techniques based on surface spectral density [Persson *et al.*(2005)]. The surface asperities are identified as local maxima. Their geometrical properties are computed using finite difference method.
In the finite element model (FEM model), illustrated in Fig.2.12, the solid is meshed with 6.10^5 hexahedron elements. The convergence of the numerical models has been checked and the number of the considered elements is high enough to capture all surface details. The contact problem is solved using Augmented Lagrangian formulation [Wriggers(2006)]. All the numerical analysis are performed with Abaqus/Standard 6.13.
The results from various models are shown in Fig.2.13 and Fig.2.14. The first layer thickness is $h = 100\mu m$, its modulus is fixed at $E_1 = 4\,GPa$ and the ratio E_2/E_1 is varied from 1 to 10.
The variation of the dimensionless contact pressure p_n/E_1^* (where $E_1^* = -2\alpha$ is the equivalent elastic modulus of the first layer) with normal separation g_n is shown in Fig.2.13. At first sight, there is a good accordance between the proposed model predictions and finite element results. One also can see that the impact of the sub-layer properties is considerable. It is also noticeable that the evolution between the logarithm of p_n/E_1^* and g_n is almost linear except for the case of small loadings, and this for the different tested configurations.

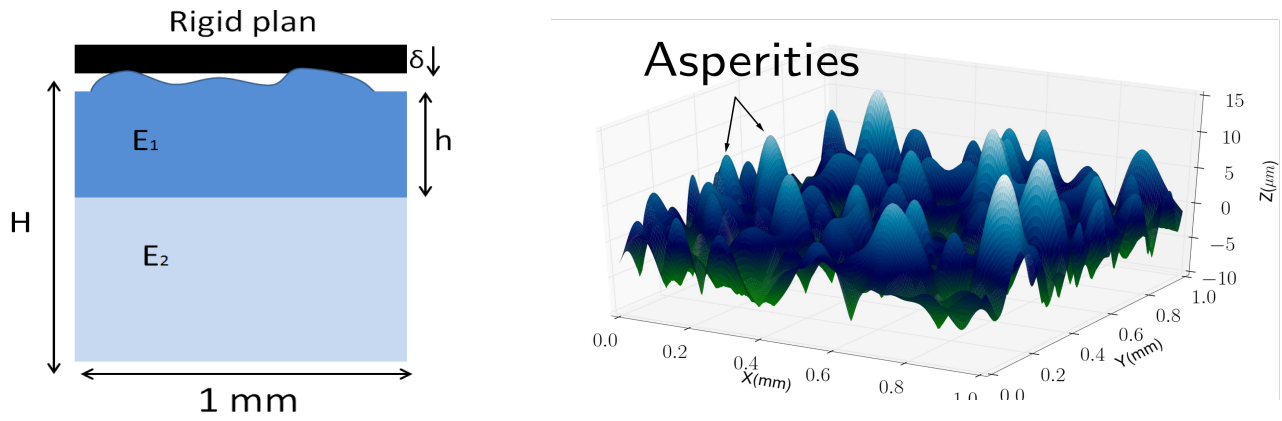

Figure 2.11: Schematic of the model. On the left, the surface roughness is illustrated and on the right, the solid geometry is shown. The following parameters are considered : $H = 1mm$ and $E_1 = 4GPa$

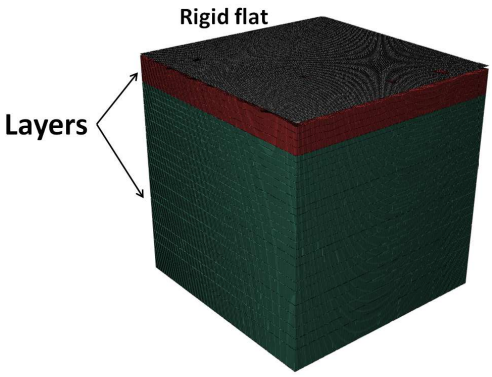

Figure 2.12: Schematic of the finite element model. The two-layered solid is meshed with 6.10^5 hexahedron elements. The first layer thickness is $h = 100\mu m$.

In Fig.2.14, the evolution of the real contact area fractions A/A_0 with the quantity p_n/E_1^* is presented. The numerical predictions are in good agreement with the model results. The contact area - mean pressure relationship is almost linear except for the case of very small fractions of contact area ($A/A_0 \leq 0.5\%$). However, the most interesting observation that can be made is that this evolution is marginally affected by the sub-layer modulus. Indeed, the first layer modulus is the same for all the considered configurations and the introduced function χ is equal to 1 (see Figs.2.7- 2.8), independently of the sub-layer modulus. Therefore, the pressure level which is controlled by function χ (see Eq.2.17), is kept fixed with respect to contact area. Thus, this evolution is mainly affected by roughness and the first layer modulus.
From these examples, it is clear that the elastic properties of the sub-layers have a considerable influence on the separation-load relation but little affect on the contact area-load evolution. It seems that this relationship depends only on the first layer modulus which was fixed in this study.
Another interesting point to be investigated is the interaction effect on the system response. Up to now, the complete model considering interactions has been tested and results are in good accordance with FEM calculations. In what follows, the results from the complete model (that is indicated as " I model ") are compared to the simplified model which does not consider interaction (indicated as " N model ").
The evolution of p_n/E_1^* with normal separation g_n is shown for both models in Fig.2.15. As we can

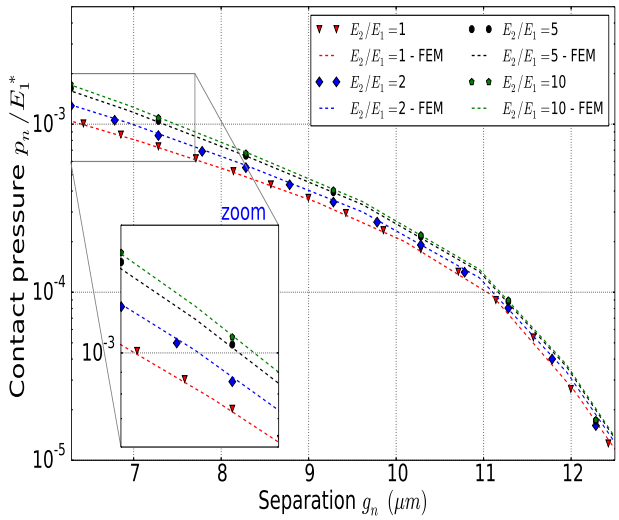

Figure 2.13: Evolution of the dimensionless contact pressure with the normal separation. Comparison between FEM results and the model predictions.

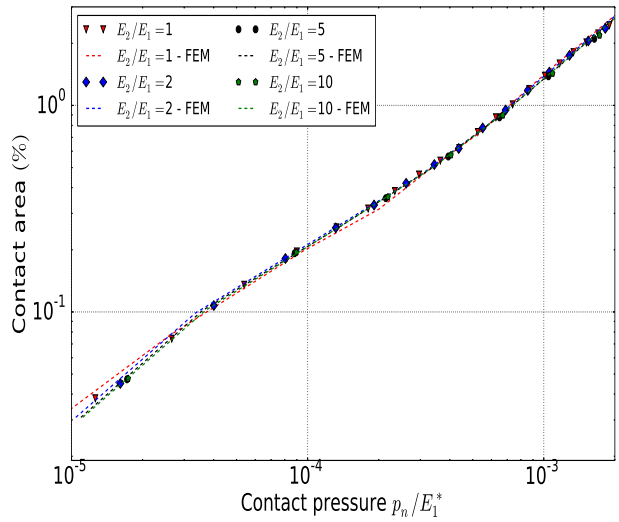

Figure 2.14: Evolution of the fraction of the contact real area with the dimensionless contact pressure. Comparison between FEM results and the model predictions.

see, the contribution of interactions depends on the solid parameters, and in this example, it is the ratio E_2/E_1. For the homogeneous case ($E_2/E_1 = 1$), interactions affect clearly the curve. Regarding the other cases ($E_2/E_1 > 1$), interactions has little effect on the studied curve. Thus, the consideration of interactions has an insignificant effect on the load-separation curve in the latter cases. Indeed, for these cases, function g introduced in Eq.2.18 has a great effect on interaction terms. For instance, for the case

where $E_2/E_1 = 10$, these terms are almost equal to 0 and there is no need to consider interactions.
Hence one can conclude that the major influence of the sub-layers properties on the interface behavior lies in the interactions between asperities. This conclusion is only valid for the case of small loads and contact areas. It is also worth to notice that the influence of interactions is not only dependent on the sub-layers properties but also on the first layer thickness.
Regarding the evolution of the real contact area with loading (see Fig.2.16), we observe that interactions do not affect this evolution. This remark have been already made in many works studying the effect of interactions on loading-area evolution (see [Ciavarella *et al.*(2006), Waddad *et al.*(2016)]).
With regard to the computational time, the new contact model provides results within few minutes. The fully discretized solution obtained with the finite element method is more computationally expensive. Thus the present model is numerically efficient.

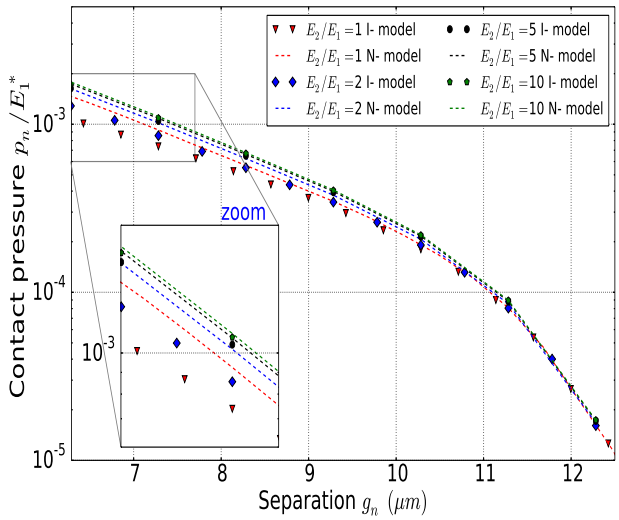

Figure 2.15: Evolution of the dimensionless contact pressure with the normal separation. Comparison between the complete model and the one which does not consider interactions

Conclusion

In this work, a contact model of rough surfaces and multi-layered solids has been proposed. The model is based on a multi-asperity surface description. The transfer matrix technique has been used to express surface displacements as functions of the surface loads. Then, making use of Abel and Hankel transforms, a contact model of parabolic asperities has been developed. At the asperity scale, results show that the sub-layer properties affect clearly the load-displacement curve.
By making use of a second order approximation of the asperity model, a contact model of rough surfaces has been developed. The obtained results have been compared to finite element calculations. A good agreement has been observed between the two methods.
As an example, a two-layered solid with a rough surface has been studied. Results show that the sub-layer properties strongly affect the contact interface stiffness but much less the load-area evolution. The latter depends essentially on surface roughness and the first layer properties. With regard to stiffness, the sub-

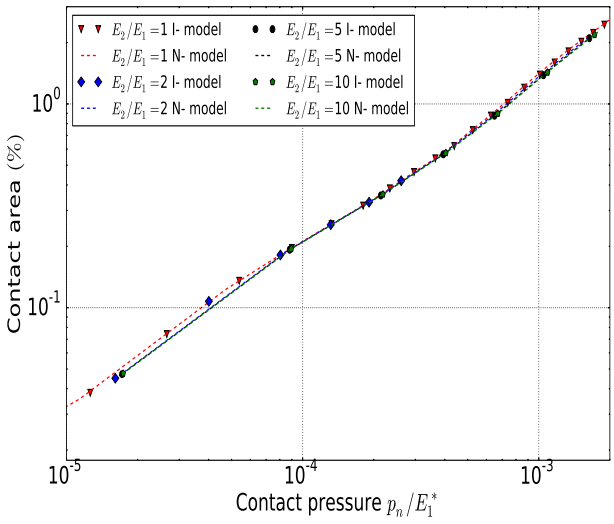

Figure 2.16: Evolution of the fraction of the contact real area with the dimensionless contact pressure. Comparison between the complete model and the one which does not consider interactions.

layers properties have a great influence on interaction terms which affects the load-separation evolution. Indeed, it has been shown that in some cases, the interactions between asperities can be neglected, while in the homogeneous case, interactions must be considered even in the case of small loads and contact areas.
Finally, this model can be used to embed large scale numerical models with the aim to consider the effect of roughness and a normal gradient of properties using the approach presented in our first work [Waddad *et al.*(2016)].

Acknowledgments

The present research work has been supported by the International Campus on Safety and Intermodality in Transportation, the Hauts-de-France Region, the European Union, the Regional Delegation for Research and Technology, the Ministry of Higher Education and Research, the French National Research Agency (ANR COMATCO), and the National Center for Scientific Research. The authors gratefully acknowledge these institutions for their support.

Bibliography

[Archard(1957)] Archard, J. F. *Elastic deformation and the laws of friction*. Proceedings of the Royal Society of London. Series A. Mathematical, Physical and Engineering Sciences, The Royal Society, 1957, 243, 190-205

[Bush *et al.*(1975)] Bush, A., Gibson, R. & Thomas, T. *The elastic contact of a rough surface*. Wear, 1975, 35, 87-111

[Cai and Bushan(2005)] Cai, Shaobiao & Bhushan, Bharat *A numerical three-dimensional contact model for rough, multilayered elastic/plastic solid surfaces*. Wear, 2005, 259, 1408-1423.

[Ciavarella *et al.*(2006)] Ciavarella, M., Delfine, V. & Demelio, G. *A re-vitalized Greenwood and Williamson model of elastic contact between fractal surfaces*. Journal of the Mechanics and Physics of Solids, 2006, 54, 2569-2591

[Cole and Sayles(1992)] Cole, S. J., & Sayles, R. S. *A numerical model for the contact of layered elastic bodies with real rough surfaces*. Journal of tribology, 1992, 114(2), 334-340.

[Ernian(1989)] Ernian, Pan *Static response of a transversely isotropic and layered half-space to general surface loads*. Physics of the Earth and Planetary Interiors, 1989, 54, 353–363.

[Gallego *et al.*(2010)] Gallego, L., Nelias, D. & Deyber, S. *A fast and efficient contact algorithm for fretting problems applied to fretting modes I, II and III*. Wear, 2010, 268, 208–222.

[Greenwood and Williamson(1966)] Greenwood, J. & Williamson, J. *Contact of nominally flat surfaces*. Proceedings of the Royal Society of London. Series A. Mathematical and Physical Sciences, The Royal Society, 1966, 295, 300-319

[Hetzler and Willner(2012)] Hetzler, H. & Willner, K. *On the influence of contact tribology on brake squeal*. Wear, 2012, 46, 237-246

[Johnson(1987)] Johnson, K. L. *Contact mechanics*. Cambridge university press, 1987

[Kogut and Etsion(2002)] Kogut, L., & Etsion, I. *Elastic-plastic contact analysis of a sphere and a rigid flat*. Journal of applied Mechanics, 2002, 69(5), 657-662

[Leroux *et al.*(2010)] Leroux, J., Fulleringer, B. & Nelias, D. *Contact analysis in presence of spherical inhomogeneities within a half-space*. International Journal of Solids and Structures, 2010, 47, 3034–3049.

[Longuet-Higgins(1957)] Longuet-Higgins, M. S. *The statistical analysis of a random, moving surface*. Philosophical Transactions of the Royal Society of London. Series A, Mathematical and Physical Sciences, 1957, 321-387

[Majumdar and Tien(1990)] Majumdar, A., & Tien, C. L. *Fractal characterization and simulation of rough surfaces*. Wear, 1990, 136(2), 313-327

[Mao *et al.*(1997)] Mao, K., Bell, T., Sun, Y., & Sayles, R. S. *Effect of sliding friction on contact stresses for multi-layered elastic bodies with rough surfaces*. Journal of tribology, 1997, 119(3), 476-480.

[Nash(2000)] Nash, S. G. *A survey of truncated-Newton methods*. Journal of Computational and Applied Mathematics, 2000, 124, 45-59

[Nayak(1971)] Nayak, P. R. *Random process model of rough surfaces*. Journal of Tribology, American Society of Mechanical Engineers, 1971, 93, 398-407

[Pei *et al.*(2005)] Pei, L., Hyun, S., Molinari, J. F. & Robbins, M. O.*Finite element modeling of elasto-plastic contact between rough surfaces*. Journal of the Mechanics and Physics of Solids, 2005, 53, 2385-2409

[Peng and Bushan(1996)] Peng, Wei & Bhushan, Bharat *Three-dimensional contact analysis of layered elastic/plastic solids with rough surfaces*. Wear, 2001, 249, 741-760.

[Persson *et al.*(2002)] Persson, B., Bucher, F. & Chiaia, B. *Elastic contact between randomly rough surfaces: comparison of theory with numerical results*. Physical Review-Series B-, American Physical Society, 2002, 65, 184106

[Persson *et al.*(2005)] Persson, B., Albohr, O., Tartaglino, U., Volokitin, A. & Tosatti, E. *On the nature of surface roughness with application to contact mechanics, sealing, rubber friction and adhesion*. Journal of Physics: Condensed Matter, IOP Publishing, 2005, 17, R1-R62

[Plumet and Dubourg(1998)] Plumet, S. & Dubourg, M. C. *A 3-D model for a multilayered body loaded normally and tangentially against a rigid body: Application to specific coatings*. Journal of tribology, 1998, 120(4), 668-676.

[Singh(1986)] Singh, Sarva Jit *Static deformation of a transversely isotropic multilayered half-space by surface loads*. Physics of the earth and Planetary Interiors, 1986, 4, 263–273.

[Sneddon(1965)] Sneddon, I. N. *The relation between load and penetration in the axisymmetric boussinesq problem for a punch of arbitrary profile*. International Journal of Engineering Science, 1965, 3(1):47-57.

[Sneddon(1995)] Sneddon, I. N. *Fourier transforms*. Courier Corporation, 1995.

[Waddad *et al.*(2016)] Waddad, Y. , Magnier, V. , Dufrénoy, P. & De Saxcé, G. *A multiscale method for frictionless contact mechanics of rough surfaces*. Tribol. int., 2016, 96, 109-121.

[Wang *et al.*(2013)] Wang, Z., Jin, X., Liu, S., Keer, L. M., Cao, J., & Wang, Q. *A new fast method for solving contact plasticity and its application in analyzing elasto-plastic partial slip*. Mechanics of Materials, 2013, 60, 18-35.

[Willner(2008)] Willner, K. *Fully coupled frictional contact using elastic halfspace theory*. Journal of Tribology, American Society of Mechanical Engineers, 2008, 031405, 1–8.

[Wriggers(2006)] Wriggers, P. *Computational contact mechanics*. 2nd ed., Springer, 2006.

[Yue(1996)] Yue, Z. Q. *Elastic field for eccentrically loaded rigid plate on multilayered solids*. International Journal of Solids and Structures, 1996, 33, 4019-4049.

Appendix A

- Elastic matrices

$$\mathbf{Z}_1 = \exp(\rho z)\,.\begin{bmatrix} 1 & \exp(-2\rho z) \\ \mu\,\rho & -\mu\,\rho\exp(-2\rho z) \end{bmatrix}$$

and

$$\mathbf{Z}_2 = \begin{bmatrix} \frac{1}{2\mu}\exp(\rho z) & \frac{1}{2\mu}\exp(-\rho z) & \frac{1}{2\mu}\left(z - \frac{2(1-\nu)}{\rho}\right)\exp(\rho z) & \frac{1}{2\mu}\left(z + \frac{2(1-\nu)}{\rho}\right)\exp(-\rho z) \\ \frac{1}{2\mu}\exp(\rho z) & -\frac{1}{2\mu}\exp(-\rho z) & \frac{1}{2\mu}\left(z + \frac{(1-2\nu)}{\rho}\right)\exp(\rho z) & \frac{1}{2\mu}\left(-z + \frac{(1-2\nu)}{\rho}\right)\exp(-\rho z) \\ \exp(\rho z) & -\exp(-\rho z) & \left(z - \frac{1}{\rho}\right)\exp(\rho z) & \left(-z - \frac{1}{\rho}\right)\exp(-\rho z) \\ \exp(\rho z) & \exp(-\rho z) & z\exp(\rho z) & z\exp(-\rho z) \end{bmatrix}$$

- Transfer matrices of a layer

$$\mathbf{T}_\eta = 0.5\,\exp(\rho h)\,.\begin{bmatrix} 1+\exp(-2\rho h) & -\frac{1}{\mu}\left(1-\exp(-2\rho h)\right) \\ -\mu\left(1-\exp(-2\rho h)\right) & 1+\exp(-2\rho h) \end{bmatrix}$$

and

$$\mathbf{T}_{z\xi} = \frac{\mu}{1-\nu}\left(\mathbf{T}_1\cosh(\rho h) + \mathbf{T}_2\sinh(\rho h)\right) \tag{2.27}$$

where

$$\mathbf{T}_1 = \begin{bmatrix} \frac{1-\nu}{\mu} & -\frac{\rho h}{2\mu} & \frac{\rho h}{4\mu^2} & 0 \\ \frac{\rho h}{2\mu} & \frac{1-\nu}{\mu} & 0 & -\frac{\rho h}{4\mu^2} \\ \rho h & 0 & \frac{1-\nu}{\mu} & -\frac{\rho h}{2\mu} \\ 0 & -\rho h & \frac{\rho h}{2\mu} & \frac{1-\nu}{\mu} \end{bmatrix} \;\&\; \mathbf{T}_2 = \begin{bmatrix} -\frac{\rho h}{2\mu} & \frac{1-2\nu}{\mu} & -\frac{3-4\nu}{4\mu^2} & \frac{\rho h}{4\mu^2} \\ \frac{\rho h}{2\mu} & \frac{\rho h}{2\mu} & -\frac{\rho h}{4\mu^2} & -\frac{1-\nu}{2\mu^2} \\ -1 & \rho h & -\frac{\rho h}{2\mu} & -\frac{\rho h}{2\mu} \\ -\rho h & -1 & -\frac{1-2\nu}{\mu} & \frac{\rho h}{2\mu} \end{bmatrix}$$

Appendix B

The transfer matrix that relates surface displacements to surface loads can be expressed as follows

$$\mathbf{F} = \begin{bmatrix} F_{11} & F_{12} & 0 \\ F_{21} & F_{22} & 0 \\ 0 & 0 & F_{33} \end{bmatrix}$$

The matrix coefficients are obtained from boundary conditions. Two cases are examined here :

- Case of an elastic half space

The multi-layered solid lies on an elastic half space. Thus, the half space parameters $A_\eta^{(N+1)}$, $A_z^{(N+1)}$ and $B_z^{(N+1)}$ vanish. It follows that

$$\begin{bmatrix} F_{11} & F_{12} \\ F_{21} & F_{22} \end{bmatrix} = \frac{1}{N_{44}N_{32} - N_{34}N_{42}} \begin{bmatrix} N_{12} & N_{14} \\ N_{22} & N_{24} \end{bmatrix} \begin{bmatrix} N_{44} & -N_{34} \\ -N_{42} & N_{32} \end{bmatrix}$$

and

$$F_{33} = \frac{M_{12}}{M_{22}}$$

where $\mathbf{N} = \mathbf{S}.\mathbf{Z}_2^{(N+1)}(Z_N)$ and $\mathbf{M} = \mathbf{R}.\mathbf{Z}_1^{(N+1)}(Z_N)$

- Case of a rigid half space

If the multi-layered solid lies on a rigid half space, the displacements $w_\eta^{(N)}$, $w_\xi^{(N)}$ and $w_z^{(N)}$ are set to be zero. One can deduce that

$$F_{33} = \frac{R_{12}}{R_{22}}$$

and

$$\begin{bmatrix} F_{11} & F_{12} \\ F_{21} & F_{22} \end{bmatrix} = \frac{1}{S_{44}S_{33} - S_{34}S_{43}} \begin{bmatrix} S_{13} & S_{14} \\ S_{23} & S_{24} \end{bmatrix} \begin{bmatrix} S_{44} & -S_{34} \\ -S_{43} & S_{33} \end{bmatrix}$$

Transition

The two first chapters of this part were dedicated to the modeling of the normal contact using an asperity based model. In the following chapter, we are interested in wear modeling.
In comparison to the previous chapters, the contact problem is solved here by discretizing the contact surface into square elements. This choice is motivated by the fact that this approach is less dependent on the shape of asperities and can be accelerated using the FFT technique, regardless the high number of degrees of freedom comparing to mutli-asperity approaches. Besides, this approach is of practical use for wear modeling because it avoids the complexity and the non-linearity of asperities models.
Thus, in this chapter we propose a different approach to solve the contact problem considering both roughness and a gradient of properties. As regards wear modeling, the Archard's model is used.
Note that friction forces are calculated directly using Coulomb's law and that they are assumed not to affect the contact area.

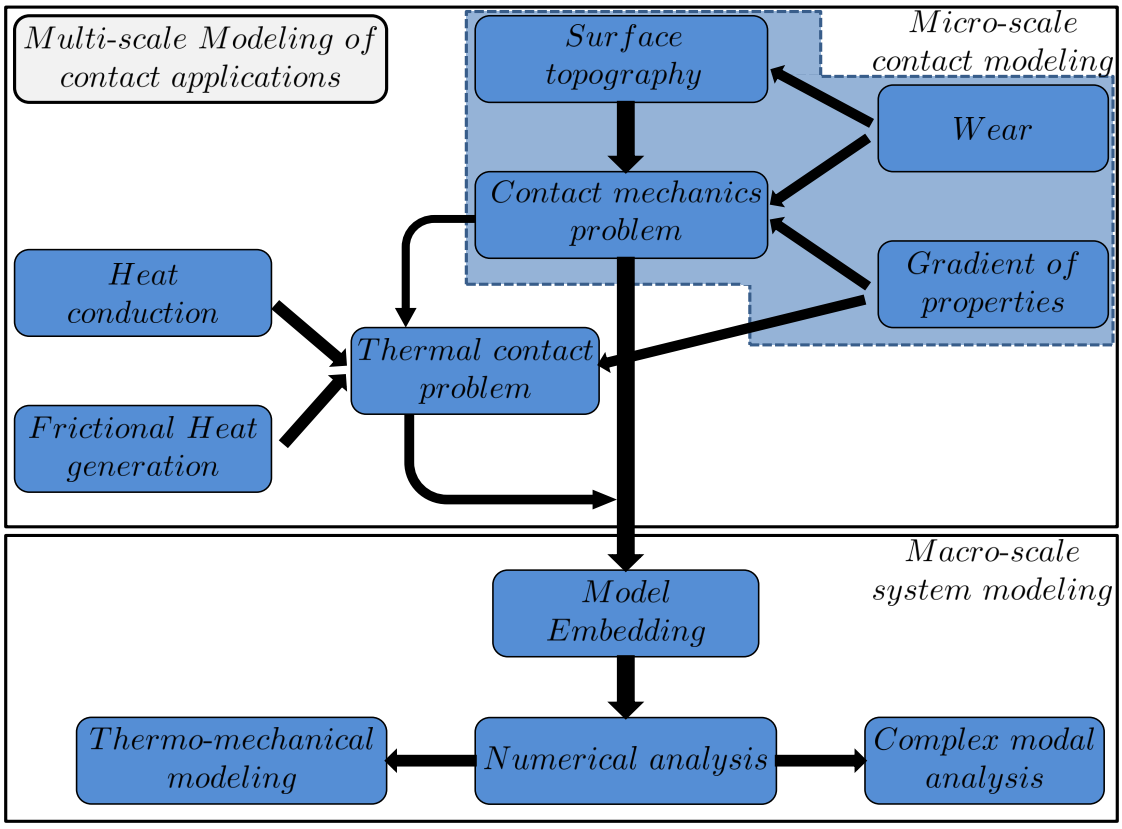

This figure presents the complete plan of this thesis. The position of this chapter is highlighted by a blue box in the background.

Chapter 3

Numerical analysis of wear in a rough contact for multi-layered solids

Contents

Numerical analysis of wear in a rough contact for multi-layered solids

Y. Waddad, V. Magnier, P. Dufrénoy, G. De Saxcé

Université de Lille Nord de France, F-59000 Lille, France
Lille1-LML, F-59655 Villeneuve d'Ascq, France
CNRS, FRE 8107, F-59655 Villeneuve d'Ascq, France

Abstract

The present work aims to analyze the wear process of rough surfaces for homogeneous and multi-layered solids. First, the contact problem is solved numerically with a variational approach based on the influence matrix technique. The terms of this matrix are obtained with Fourier transform and the transfer matrix technique for multi-layered solids. Wear modeling is performed using Archard's law and the total surface wear is obtained by micro-contact. Finally some examples are presented. The effect of wear on a rough surface is presented and the effect of surface layers on wear is highlighted.

keywords : Contact analysis, surface roughness, wear, multi-layered solid, Fourier transform, transfer matrix technique

3.1 Introduction

In sliding contact systems, the knowledge of the real contact area is of high importance since it affects the global behavior of the system [Dufrénoy *et al.*(2016), Hetzler and Willner(2012)]. As is well known, the contact area depends on the mating surfaces roughness. Yet the initial surface roughness is affected by contact loads and wear. In fact, a progressive damage and material removal is caused by frictional interactions between the contacting surfaces. Thus, surface wear affects the real contact area which consequently may harm the efficiency and the durability of the global process.
There are several types of wear : abrasive, adhesive, corrosive, etc. Wear types are conditioned by many physical phenomena such as micro-fractures, melting or chemical effects. The dominant wear mode depends on the sliding distance, a lubricated or a dry contact, friction conditions, material properties and environmental parameters, which affect the amount of wear volume[Kato(2000), Kato(2002)].
Wear modeling has been the subject of many works. A large variety of wear models are described in [Meng(1995)] based on theoretical and experimental works existing in the literature. From these models, the amount of the worn volume can be expressed as a function of contact load, sliding distance and a coefficient depending on material properties and wear mode. Concerning rough surfaces, a micro-contact model of abrasive wear has been proposed by [Masen(2005)] by considering that micro-contact spots act as abrasive entities. The abrasive action of a single micro-contact is based on experimental investigations. Therefore, the macroscopic wear volume is found by summing the volumetric wear of each individual micro-contact zone.
The difficulty in wear modeling is that there is no universal model that can be applicable to all situations[Williams(1999)]. Most of the existing models are empirical. Nevertheless, it appears that most of wear mechanisms (e.g. abrasive and adhesive modes) can be described, using simplified description of the considered mechanism, by a linear law defining a steady wear volume with sliding and characterized by a constant wear rate [Archard(1953), Kato(2002)]. In this case, wear volume is proportional to the normal load and the sliding distance. Yet, wear rate depends on the governing mechanisms of wear and has to be

identified with appropriate experiments. For instance, wear rate corresponding to adhesive wear of metals have been quantified, by [Archard(1953)], depending on the operating conditions and material properties. In this work, our interest is focused on the contact between a disk brake and a composite material. Our aim is to analyze the evolution of surface roughness with wear process. For this, we use a linear law, like Archard's one, which is based on a wear rate coefficient issued from the literature. The real challenge is to solve the contact mechanics problem for a given surface roughness. To do this, we simplify the study by considering that the tangential behavior is rigid. This means that the tangential deformations are not considered and that the contact area depends only on the normal ones. This hypothesis have been made to simplify the resolution of the contact problem. Moreover, from several works like [Gallego *et al.*(2010), Willner(2008)], it appears that the effect of the tangential behavior, on wear and contact area, is very limited comparing to the normal one. Furthermore, it is assumed that the contact is fully sliding, thus the shear stresses are obtained directly for normal stresses using a friction coefficient. So, the current issue here is to solve the normal contact problem and find the pressure distribution.

The normal contact mechanics of rough surfaces have been extensively studied using the classical asperity based models of [Greenwood and Williamson(1966), Bush *et al.*(1975)]. In the same framework, interaction between asperities have been considered by [Ciavarella *et al.*(2006), Waddad *et al.*(2016)]. The finite element method has been also used by [Pei(2005), Waddad *et al.*(2016)] but remains very costly. An interesting approach is to consider the solid as a half space and solve the problem using the so-called influence coefficients [Johnson(1987), Willner(2008)]. Following this approach, only the surface is discretized which saves considerably CPU time. Using the Fast Fourier Transform (FFT), a fast version of this method has been developed in [Gallego *et al.*(2010)]. Note that the frictional contact has been considered in [Gallego *et al.*(2010), Willner(2008)], and from the obtained results, it appears that the frictional forces have little effect on the pressure and the contact area distribution.

In the above cited models, the studied solids were considered as homogeneous half spaces. However, in many problems, the material beneath the surface can be considered as multi-layered, such as coating and composites. Moreover, in braking applications, there are material transformations leading to the appearance of a gradient of material properties near to the contact interface. Thus, these properties vary in the direction normal to the contact surface (see Fig.3.1). Consequently, in some way, the material can be considered as a multi-layered system where each layer is homogeneous and perfect continuity is assumed at the interface layers.

To the best of our knowledge, the contact problem involving rough surfaces with multi-layered solids has so far received a few attention. In [Peng and Bhushan(1996), Cai and Bhushan(2005)], Papkovich–Neuber potentials with a Fast Fourier Transform scheme (FFT), have been used to study the rough contact problem of elastic and plastic solids. These studies were carried on solids having a maximum of three layers. The problem is solved using the influence matrix method of which the coefficients are obtained by solving a linear system of equations. However, under such an approach, it is very complicated to extend the technique to cover the general case of multi-layers. An interesting approach has been proposed in [Yue(1996)] who has investigated the contact problem of a multi-layered solid submitted to the indentation of a rigid circular plate using the transfer matrix technique [Singh(1986), Ernian(1996)] and both the Fourier transform and Hankel transform properties to obtain a Fredholm integral equation which is solved to obtain a closed-form solution for the contact problem. Based on this concept, we recently developed a contact model [Waddad *et al.*(2017^a)] considering surface asperities and solid layers.

In this work, we aim to investigate the effect of wear on a rough surface of a multi-layered solid. As is aforementioned, wear is modeled with Archard's law using a constant wear rate. Moreover, wear volume is obtained by summing the volumetric wear of each individual micro-contact [Masen(2005)]. In order to solve the contact problem, the approach based on influence coefficients and FFT technique is used [Gallego *et al.*(2010)]. These coefficients are obtained with the transfer matrix technique [Singh(1986), Er-

nian(1996)]. Finally, a contact analysis is performed to highlight the effects of solid layers.

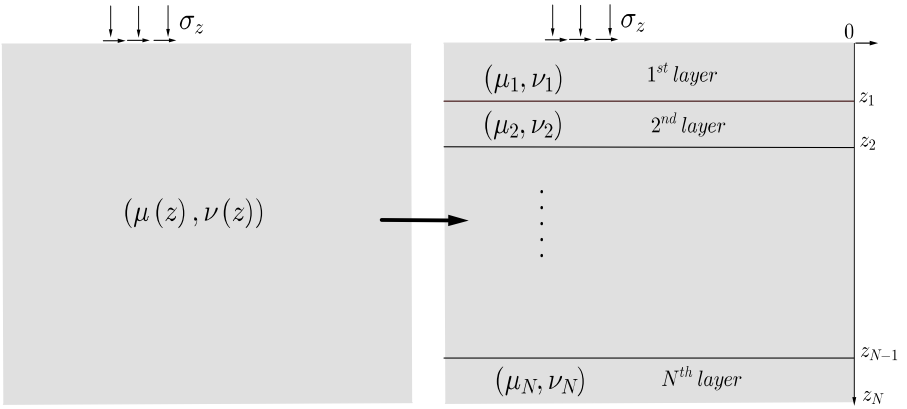

Figure 3.1: Schematic of a multi-layered elastic solid under surface loads

3.2 Global framework and general assumptions

Considering two solids in a sliding frictional contact, the first solid is rigid and its surface is smooth and plane. For the second one, a linear elastic behavior is considered and the contact surface is rough. Moreover, a general normal load P is applied to enforce contact, and the first solid is sliding with a predefined velocity while the other one is static (see Fig.3.2).
In this work, many simplifications have been considered : The contact zone is small with respect to the dimensions of both solids. Also, there is no coupling between the normal contact problem and the tangential one and the complete sliding regime is considered in all the contact points. Thus, the contact area is not affected by shear stresses and tangential deformations are neglected. Moreover, the Coulomb's friction law is adopted with a fixed friction coefficient.
Initially, the contact surface contains only asperities. Due to wear, the contacting asperities break down and a new contact zones are formed. The worn zones are relatively flat comparing to the asperities curvature. These zones are namely called "plateaus". Therefore, the contact is made on the plateaus and the asperities which remain intact.
When contact occurs, the surface deforms. The normal displacement u_z in every surface point depends on the contact normal stresses p on asperities and plateaus. These stresses fulfill the balance equation $P = \int_{\Gamma_c} p\, dS$, where Γ_c is the contact zone. Furthermore, a prescribed displacement δ occurs automatically in every contact point. This displacement differs from a point to an other depending on surface topography.
To solve the contact problem, we use a variational approach consisting in minimizing the total complementary energy of the solid [Willner(2008), Gallego *et al.*(2010)]

$$U_E = \frac{1}{2}\int_{\Gamma_c} p.u_z\, dS - \int_{\Gamma_c} p.\delta\, dS \tag{3.1}$$

Solving the contact problem leads to find the contact pressure field minimizing U_E subject to contact constraints and balance equation. To achieve this, an iterative scheme is used and a motion-driven strategy is considered. Indeed, starting from a test motion δ_r prescribed to the first solid, the prescribed

displacement δ of the surface is deduced from the surface geometry, and the contact problem can be solved considering contact constraints. Then, the equilibrium balance is checked. If the equilibrium is fulfilled, the problem is solved. If not, the prescribed motion δ is changed consequently. This operation is repeated until the balance equilibrium is reached.
Up to now, the basic elements of the strategy have been presented. The expression of the energy has been given in a continua way. The next section presents the discretized form of the problem. Two cases are considered : The first one concerns homogeneous solids while the second one is dealing with multi-layered solids.

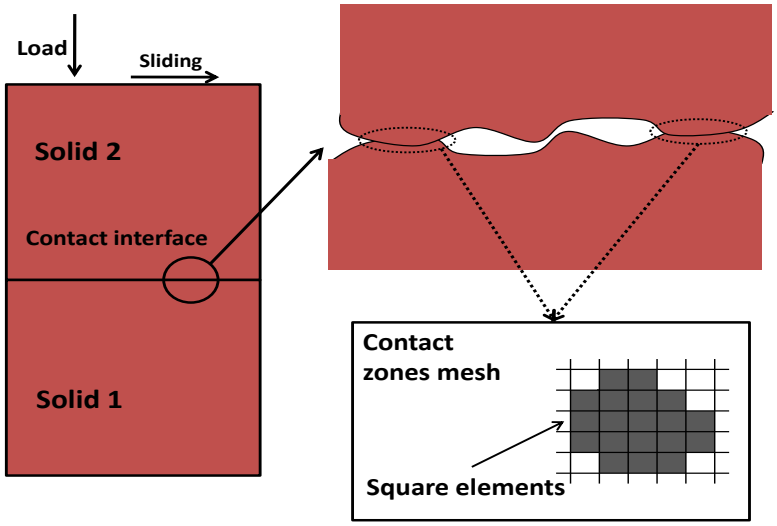

Figure 3.2: Real contact interface. The contact surface is discretized into square elements of the same size.

3.3 Modeling of the contact mechanics problem

3.3.1 Discretization of the contact problem

The contact surface is discretized into small squares of uniform size. Within a single square, the pressure field is assumed to be constant. The normal displacement for any surface point (x, y) reads

$$u_z(x, y) = \sum_{k=1}^{N_p} p_k L(x, y, x_k, y_k) \tag{3.2}$$

where N_p is the number of surface squares, p_k is the pressure applied on the k^{th} square, (x_i, y_i) are the coordinates of the centers of squares, and L is the interaction term (or influence coefficient). $L(x, y, x_k, y_k)$ corresponds to the normal displacement of the point (x, y) induced by a unit pressure applied on the k^{th} square element. For homogeneous solids, this function is derived from the classical potential theory [Johnson(1987)]. More exactly, interaction terms for squares are given by Love theory. For multi-layered solids, these terms are obtained with the transfer matrix technique [Singh(1986), Ernian(1996)].

Now, let us denote z_M the maximum height of the surface and z_i the height of the i^{th} contact point. The prescribed displacement of the i^{th} contact point reads

$$\delta_i = \langle \delta_r - (z_M - z_i) \rangle \tag{3.3}$$

where δ is the rigid solid motion induced by the total load P, and $< . >$ is the positive part of its operand. Using the expressions of interaction terms, the discretized form of the energy reads

$$U_E = \frac{1}{2} \sum_{i}^{N_p} \sum_{k}^{N_p} p_i p_k A_i L_{ki} - \sum_{i}^{N_p} p_i A_i \delta_i \tag{3.4}$$

where p_i is the pressure, A_i is the square area and L_{ki} is the interaction terms (or the influence coefficients). The total load P reads then

$$P = \sum_{i}^{N_p} p_i A_i \tag{3.5}$$

The contact problem is solved if the pressure field minimizes the energy and satisfies the constraints of the problem: $p_i \geq 0$.

3.3.2 Interaction terms for homogeneous solids

In this case, interaction terms are derived from the classical potential theory [Johnson(1987)]. More exactly, these coefficients have been obtained by Love and are expressed by

$$L_{ik} = G\left(x_{ik}, y_{ik}, l_i\right) + G\left(y_{ik}, x_{ik}, l_i\right) - G\left(-x_{ik}, y_{ik}, l_i\right) - G\left(-y_{ik}, x_{ik}, l_i\right)$$

where l_i is the square half width, (x_{ik}, y_{ik}) are the relative coordinates of the k^{th} element in the basis located at the i^{th} element and d_{ik} is the corresponding distance and the function G reads

$$G\left(x, y, l\right) = \frac{(x+l)}{\pi\, E^*} \ln \left(\frac{(y+l) + \sqrt{(y+l)^2 + (x+l)^2}}{(y-l) + \sqrt{(y-l)^2 + (x+l)^2}} \right)$$

where E^* is the equivalent modulus of the solid.

3.3.3 Interaction terms for multi-layered solids

In this case, the transfer matrix technique is used to compute interaction terms. This technique consists in the construction of a matrix linking surface displacements to surface loads using Fourier integral transforms. In this paragraph, we present only some key points of this method.
Let us consider an isotropic medium ($z \geq 0$) laterally unbounded. The material which forms the solid have an elastic properties which vary with depth z. Using the Fourier integral transform, we introduce the transformed variables of the stress vector defined by $\mathbf{T}_z = [\sigma_{xz}, \sigma_{yz}, \sigma_{zz}]^t$ and the displacements vector $\mathbf{u} = [u_x, u_y, u_z]^t$

$$\mathbf{w} = \begin{bmatrix} w_\xi \\ w_\eta \\ w_z \end{bmatrix} = \int_0^{+\infty} \begin{bmatrix} i\xi/\rho^2 & i\eta/\rho^2 & 0 \\ i\eta/\rho^2 & -i\xi/\rho^2 & 0 \\ 0 & 0 & 1 \end{bmatrix} . \exp\left[i\left(\xi x + \eta y\right)\right] \mathbf{u}\, \mathrm{d}x\, \mathrm{d}y$$

$$\boldsymbol{\tau} = \begin{bmatrix} \tau_\xi \\ \tau_\eta \\ \tau_z \end{bmatrix} = \int_0^{+\infty} \begin{bmatrix} i\xi/\rho^2 & i\eta/\rho^2 & 0 \\ i\eta/\rho^2 & -i\xi/\rho^2 & 0 \\ 0 & 0 & 1 \end{bmatrix} . \exp\left[i\left(\xi x + \eta y\right)\right] \mathbf{T}_z \, \mathrm{d}x \, \mathrm{d}y$$

where $\rho^2 = \xi^2 + \eta^2$.
The transformed variables are a solution of an eigenvalue problem. If the medium is an unbounded horizontal layer we can show that these variables satisfy the following equations

$$\begin{bmatrix} w_\eta^{(-)} \\ \tau_\eta^{(-)}/\rho \end{bmatrix} = \mathbf{T}_\eta \begin{bmatrix} w_\eta^{(+)} \\ \tau_\eta^{(+)}/\rho \end{bmatrix} \text{ and } \begin{bmatrix} w_z^{(-)} \\ \rho w_\xi^{(-)} \\ \tau_z^{(-)}/\rho \\ \tau_\xi^{(-)} \end{bmatrix} = \mathbf{T}_{z\xi} \begin{bmatrix} w_z^{(+)} \\ \rho w_\xi^{(+)} \\ \tau_z^{(+)}/\rho \\ \tau_\xi^{(+)} \end{bmatrix} \tag{3.6}$$

where the superscript $^{(+)}$ (resp. $^{(-)}$) is used for the top layer surface variables (resp. the bottom one) and $\mathbf{T}_{z\xi}$ and $\mathbf{T}_\eta$ are the matrices of the layer.
Now let us consider a multi-layered solid formed by N horizontal layers. Considering the perfect continuity between layers, the displacement field $\mathbf{u}$ and the stress vector $\mathbf{T}_z$ are both continuous. Using the layers matrices, one can obtain the following set of equations

$$\begin{bmatrix} w_\eta^{(0)} \\ \tau_\eta^{(0)}/\rho \end{bmatrix} = \underbrace{\mathbf{T}_\eta^{(1)} \ldots \mathbf{T}_\eta^{(N)}}_{\mathbf{R}} \begin{bmatrix} w_\eta^{(N)} \\ \tau_\eta^{(N)}/\rho \end{bmatrix} \text{ and } \begin{bmatrix} w_z^{(0)} \\ \rho w_\xi^{(0)} \\ \tau_z^{(0)}/\rho \\ \tau_\xi^{(0)} \end{bmatrix} = \underbrace{\mathbf{T}_{z\xi}^{(1)} \ldots \mathbf{T}_{z\xi}^{(N)}}_{\mathbf{S}} \begin{bmatrix} w_z^{(N)} \\ \rho w_\xi^{(N)} \\ \tau_z^{(N)}/\rho \\ \tau_\xi^{(N)} \end{bmatrix}$$

where the superscript $^{(0)}$ (resp. $^{(N)}$) is used for the top solid surface variables (resp. the bottom one).
These equations relate the transformed stresses and displacements of the top surface of the 1^{st} layer to those of the bottom surface of the N^{th} layer by means of the matrices $\mathbf{S}$ and $\mathbf{R}$.
In order to solve the problem, the boundary conditions in the bottom face are used. Indeed, the N^{th} layer lies on a half space which can be either rigid or elastic. Following many algebraical operations, one can show that

$$\begin{bmatrix} w_z^{(0)} \\ \rho w_\xi^{(0)} \\ w_\eta^{(0)} \end{bmatrix} = \mathbf{F} \begin{bmatrix} \tau_z^{(0)}/\rho \\ \tau_\xi^{(0)} \\ \tau_\eta^{(0)}/\rho \end{bmatrix} \text{ , where } \mathbf{F} = \begin{bmatrix} F_{11} & F_{12} & 0 \\ F_{21} & F_{22} & 0 \\ 0 & 0 & F_{33} \end{bmatrix} \tag{3.7}$$

The matrix $\mathbf{F}$ coefficients depend on the bottom surface boundary conditions and are given in Appendix B.
By ignoring the tangential components, one can deduce from Eq.3.7 that

$$w_z^{(0)} = F_{11}\left(\rho\right) \tau_z^{(0)} \tag{3.8}$$

Using this equation, interaction terms can be deduced by inverse integral transforms. Indeed, the interaction term corresponds to the case of a unit pressure applied on the square. By defining a grid of the surface, one can obtain the interaction terms by reversing Eq.3.8

$$L = \mathrm{IFFT}\left(F_{11}\right)$$

where IFFT is the Inverse Fast Fourier transform.
Note that L is not computed analytically but only computed numerically in the grid points.

3.3.4 Numerical solving of the contact problem

Now that interaction terms have been expressed, the discretized form of the energy can be written in a matrix format

$$U_E = \frac{1}{2}\,{}^t\boldsymbol{p}\,\mathbf{L}\,\boldsymbol{p} - {}^t\boldsymbol{p}\,\boldsymbol{\delta} \tag{3.9}$$

Using an iterative method, for example Newton or the conjugate gradient, the minimization problem is performed and pressure can be calculated. For more details about optimization, the reader may refer to these works ([Peng and Bhushan(1996)],[Gallego *et al.*(2010)]).
Otherwise, it is interesting to note that the normal displacement is a discrete convolution of the pressure field and the operator of interactions $u_z = L * p$. Thus, the matrix product can be replaced by the convolution equation. Furthermore, convolution can be accelerated with the FFT technique which is of practical interest comparing to a matrix product.
Now that the different key points of the contact problem solving method have been presented, the next section is devoted to wear modeling strategy.

3.4 Wear modeling

As is aforementioned, wear is modeled with Archard's law. At the scale of a contact point, the wear depth $\mathrm{d}h$ corresponding to a small sliding distance is

$$\mathrm{d}h = k_w\,\mu\,p\,\mathrm{d}S \tag{3.10}$$

where k_w is the wear rate coefficient and $\mathrm{d}S$ is the sliding distance.
By considering N slide increments, the wear depth h^N for a given contact point is

$$h^N = \sum_{j=1}^{N} \mathrm{d}h^j = \sum_{j=1}^{N} k_w\,\mu\,p^j\,\mathrm{d}S^j$$

Here the friction coefficient and the wear rate are assumed to be constant.
The total slide is

$$S^N = \sum_{j=1}^{N} \mathrm{d}S^j$$

The total wear volume is obtained by summing all the elementary wear volumes

$$W^N = \sum_{i=1}^{N_p} A_i h_i^N$$

3.5 Numerical analysis of the evolution of a rough surface under wear process

In this section, a numerical analysis is performed on a rough surface with the aim of investigating the effect of wear. This surface is generated with fractal technique which is based on the spectral density [Persson *et al.*(2005)]. Here, the spectral density is a power law, of which the fractal dimension is 0.8. The cutoff wave vectors are 2 and 10. The studied surface is shown in Fig.3.5. For information, its root mean square (RMS) is 6 μm.

3.5.1 Wear step effect on the model predictions

As an example, we consider the sliding contact between two homogeneous solids S_1 and S_2. The material properties of both solids are presented in Tab.3.1. The normal pressure is fixed at $p = 1\ MPa$. The friction coefficient is $\mu = 0.4$ and the total sliding distance is $S = 10\ mm$. Besides, we consider that only S_1 is worn. The wear rate k_w of S_1 is $10^{-12}\ Pa^{-1}$.

	$E\ (GPa)$	ν
Solid S_2	220	0.33
Solid S_1	4	0.15

Table 3.1: Elastic and thermal properties of Solid S_2

In this part, we analyze the effect of wear step on the total wear process. To do this, the sliding distance is divided into N small increments (=wear steps), ranging from 200 to 600. Fig.3.3 shows the evolution of the contact area with the sliding distance for different wear steps. Besides, wear depth evolution is shown in Fig.3.4. One can see that beyond $N = 300$, there is no effect of wear step on the predicted contact area. This number is high enough to get a good convergence of the obtained results. For $N = 200$, the contact area is underestimated and wear depth is overestimated.
Furthermore, the slope of the wear depth evolution decreases as the sliding distance increases. This is quite predictable since contact area increases, the concentration of contact stresses decreases in contact zones. This affects consequently the wear depth intensity but not the volume which remains constant according to the wear model equation.

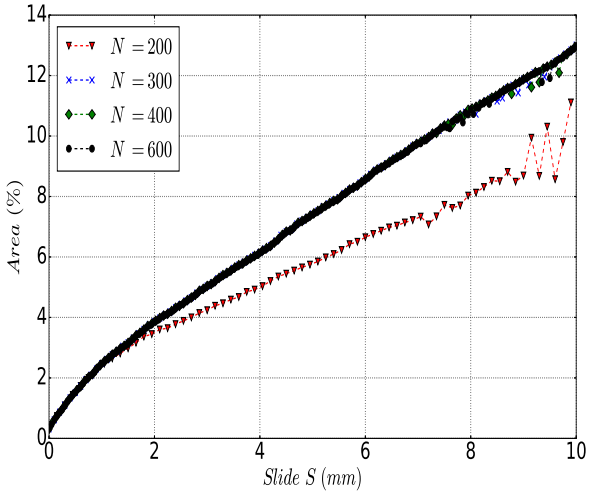

Figure 3.3: Evolution of contact area with sliding distance for various wear increments

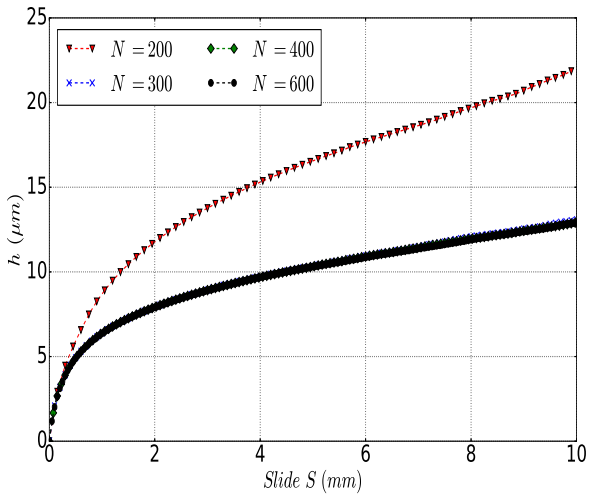

Figure 3.4: Evolution of wear depth with sliding distance for various wear increments

The evolution of surface roughness is illustrated through Figs.3.5-3.6. In the first one, the initial roughness is shown. The associated displacement field and pressure field are shown below it. In the second one, the final surface is presented. On can remark the presence of some flat zones corresponding to the worn asperities of the surface. The growth of contact area is also considerable as illustrated also in Fig.3.3. Indeed for the same prescribed pressure, the contact area has increased from 1% to 13% at the final state.

As regarding the local pressure distribution and the normal displacement, their maximum level decreases drastically. As a direct consequence, the stiffness will certainly increases considerably.
In this part, the evolution of a rough surface under wear process has been analyzed. The effect of wear step has been highlighted. The two contacting solids were homogeneous. In the following part, the contact between a two-layered solid and a homogeneous solid is considered. In particular, the effect of the solid layer is studied.

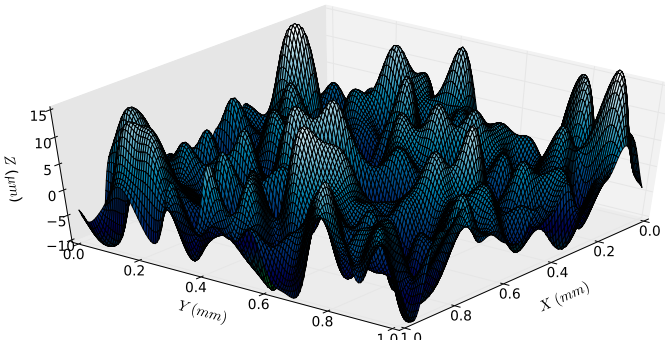

Initial surface roughness

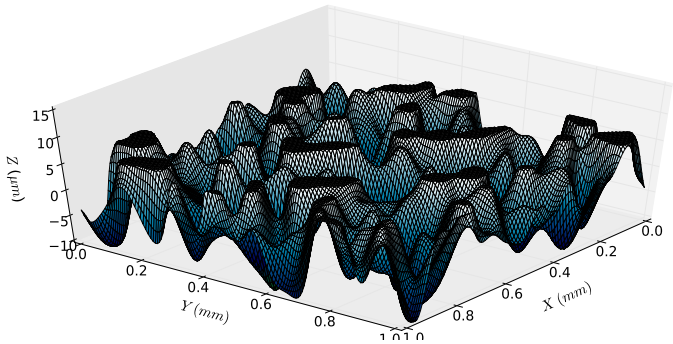

Surface roughness at the end of the simulation

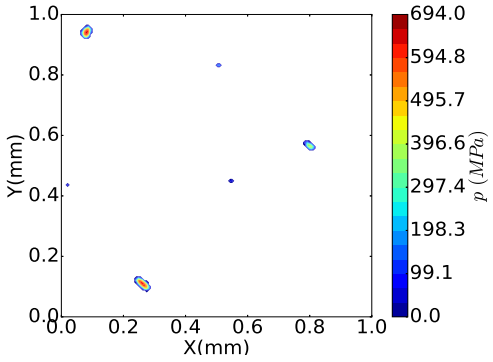

Initial contact pressure distribution

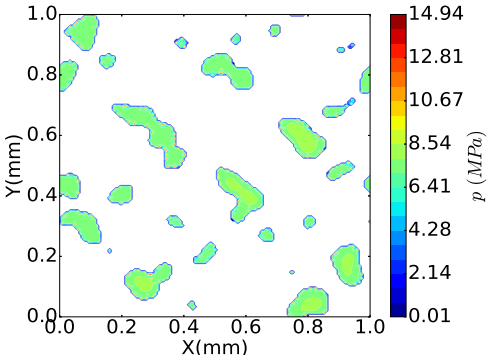

Final contact pressure distribution

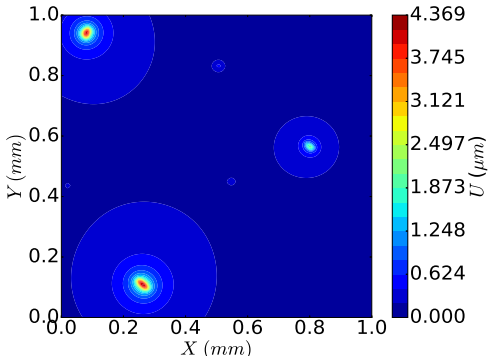

Initial vertical displacement field

Figure 3.5: Surface data for the initial surface

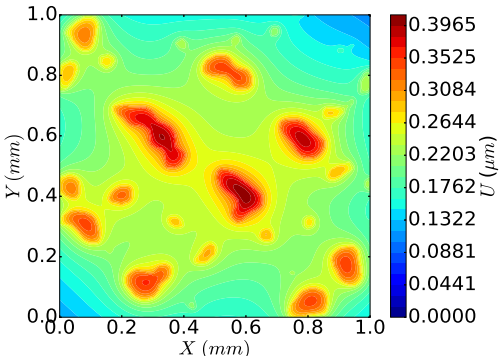

Final vertical displacement field

Figure 3.6: Surface data at the end of the simulation

3.5.2 Case of a two-layered solid

In this section, we consider the same elastic properties for S_2. The solid S_1 contains two layers. The first layer is the one on the top of the solid. Its thickness is fixed at $200\,\mu m$ while its modulus E_1 is varied from 4 to 1 GPa. The second layer one is $E_2 = 4\ GPa$. Moreover, 400 wear steps have been considered so that the wear process is not affected by this variable. This section aims to highlight the effect of the surface layer modulus on the wear process.
The evolution of the contact area with the sliding distance is shown in Fig.3.7. The contact area is higher for the case of $E_2/E_1 = 4$. The wear depth evolution is presented in Fig.3.8. As can be seen, the slope of its evolution decreases progressively. The wear depth decreases while E_2/E_1 increases. This can be explained by the fact that the local pressure level decreases with E_2/E_1, which corresponds to the case of a compliant surface layer ($E_1 < E_2$). In Fig.3.9, is shown the wear volume evolution. Since the wear rate has been maintained constant in this example, the wear volume is unaffected by the surface layer modulus. However, one should expect that this coefficient value depends certainly on the surface layer modulus, which consequently may affect the amount of wear volume. Nevertheless, the case of a compliant surface layer could be beneficial by reducing the amount of wear and increasing the contact area. In that sense, increasing the thickness of a compliant surface layer will lead to the same conclusions as the studied example.
The contact stiffness is also affected by wear. In Fig.3.10, is shown the evolution of the contact pressure p_n with the gap g_n for different worn state of the surface, and for the case of $E_2/E_1 = 1$. One can see that the slope of this evolution increases with sliding. This corresponds to an expansion of the contact area with sliding, and has been clearly illustrated in Figs.3.5-3.6.

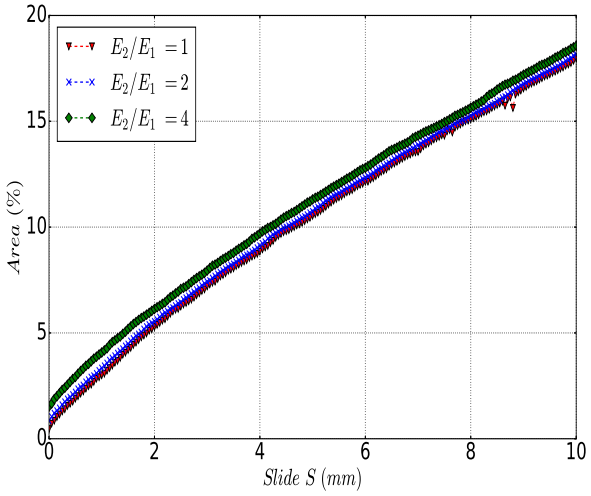

Figure 3.7: Evolution of the contact area with sliding

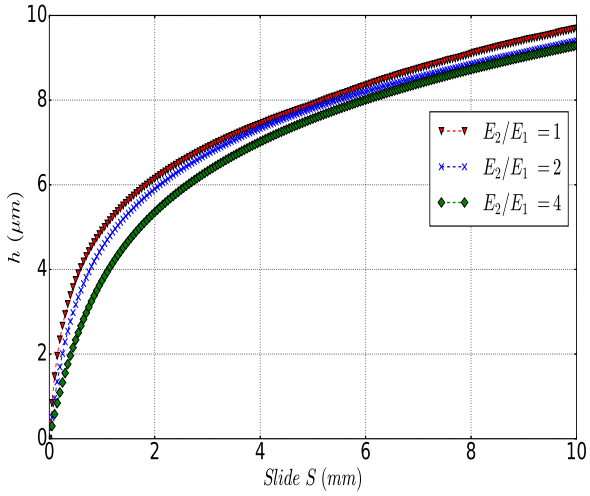

Figure 3.8: Evolution of the maximal wear depth with sliding

Conclusion

In this work, surface evolution under wear process has been analyzed for both homogeneous and multi-layered solids. First of all, contact analysis has been performed, considering surface roughness, with an approach based on influence coefficients method and the FFT technique. For homogeneous solid bodies,

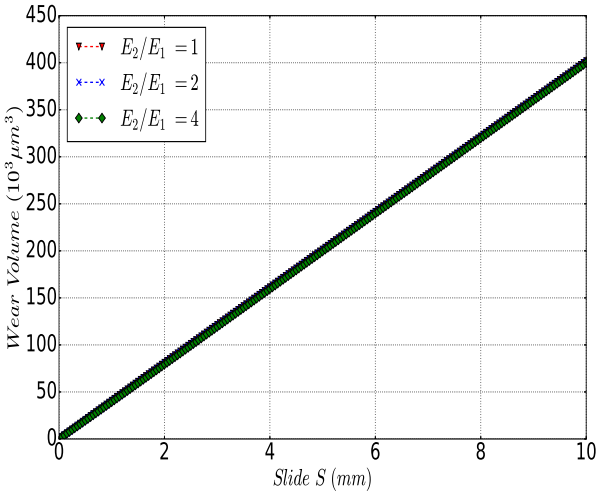

Figure 3.9: Evolution of the wear volume with sliding

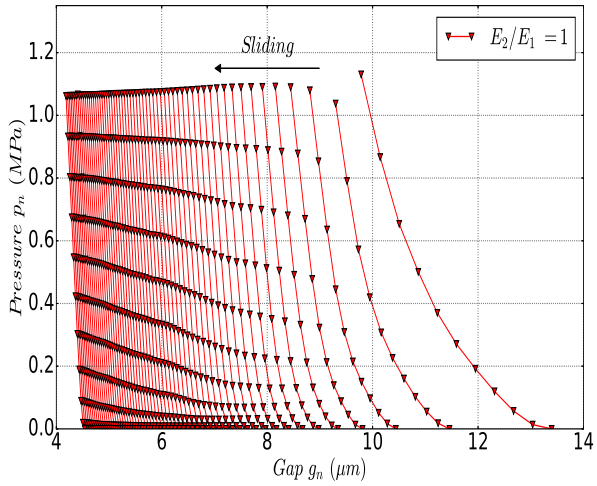

Figure 3.10: The evolution of the curve relating the mean pressure to the normal gap with sliding

the influence coefficients are obtained from Love theory, while for multi-layered solids, these coefficients are calculated with Fourier transform and the transfer matrix technique. Within this framework, the contact problem is solved with a variational approach consisting in minimizing the elastic potential energy. Once the contact problem is solved, wear is modeled based on Archard's law. The total wear volume is obtained by summing all the elementary wear volumes. These volumes are calculated from the local contact pressure field, frictional sliding parameters and a wear rate coefficient.
The results of the model focused on the effect of the wear step increment and the presence of solid layers. For the first parameter, it has been shown that choosing an adequate wear step the process of wear is unaffected. This parameter depends certainly on the wear rate coefficient with respect to friction coefficient and sliding distance. As regards the influence of solid layers, it has been shown that a compliant surface layer decreases the local pressure, stiffness and the amount of wear, and increases the contact area.
Finally, it should be noted that some improvements of the present work can be done, in particular by considering temperature rise due to frictional sliding and a wear model based on surface temperature. Indeed, the high temperatures encountered in sliding systems could accelerate the process of wear which undoubtedly will affect the model results. Furthermore, an appropriate wear coefficient should be considered for multi-layered solids when compared to homogeneous solids. Indeed, this coefficient depends, among other factors, on the stiffness of the surface layer.

Bibliography

[Archard(1953)] Archard, J. F. *Contact and rubbing of flat surfaces*. Journal of Applied Physics, 1953, 24(8), 981-988.

[Bush *et al.*(1975)] Bush, A., Gibson, R. & Thomas, T. *The elastic contact of a rough surface*. Wear, 1975, 35, 87-111

[Cai and Bhushan (2005)] Cai, Shaobiao & Bhushan, Bharat *A numerical three-dimensional contact model for rough, multilayered elastic/plastic solid surfaces*. Wear, 2005, 259, 1408-1423.

[Ciavarella *et al.*(2006)] Ciavarella, M., Delfine, V. & Demelio, G. *A re-vitalized Greenwood and Williamson model of elastic contact between fractal surfaces*. Journal of the Mechanics and Physics of Solids, 2006, 54, 2569-2591

[Dufrénoy *et al.*(2016)] Dufrénoy, P., Magnier, V., Waddad, Y., Brunel, J. F., & De Saxcé, G. *A Multiscale Model of a Disc Brake Including Material and Surface Heterogeneities*. SAE Int. J. of Passenger Cars-Mechanical Systems, 2016, 9, 1136-1143.

[Ernian(1996)] Ernian, Pan *Static response of a transversely isotropic and layered half-space to general surface loads*. Physics of the Earth and Planetary Interiors, 1989, 54, 353–363.

[Gallego *et al.*(2010)] Gallego, L., Nelias, D. & Deyber, S. *A fast and efficient contact algorithm for fretting problems applied to fretting modes I, II and III*. Wear, 2010, 268, 208–222.

[Greenwood and Williamson(1966)] Greenwood, J. & Williamson, J. *Contact of nominally flat surfaces*. Proceedings of the Royal Society of London. Series A. Mathematical and Physical Sciences, The Royal Society, 1966, 295, 300-319

[Hetzler and Willner(2012)] Hetzler, H. & Willner, K. *On the influence of contact tribology on brake squeal*. Wear, 2012, 46, 237-246

[Johnson(1987)] Johnson, K. L. *Contact mechanics*. Cambridge university press, 1987

[Kato(2000)] Kato, K. *Wear in relation to friction—a review*. Wear, 2000, 241(2), 151-157.

[Kato(2002)] Kato, K. *Classification of wear mechanisms/models*. Proceedings of the Institution of Mechanical Engineers, Part J: Journal of Engineering Tribology, 2002, 216(6), 349-355.

[Masen(2005)] Masen, M. A., De Rooij, M. B., & Schipper, D. J. *Micro-contact based modelling of abrasive wear*. Wear, 2005, 258(1), 339-348.

[Meng(1995)] Meng, H. C., & Ludema, K. C. *Wear models and predictive equations: their form and content*. Wear, 1995, 181, 443-457.

[Pei(2005)] Pei, L., Hyun, S., Molinari, J. F. & Robbins, M. O.*Finite element modeling of elasto-plastic contact between rough surfaces.* Journal of the Mechanics and Physics of Solids, 2005, 53, 2385-2409

[Peng and Bhushan(2001)] Peng, Wei & Bhushan, Bharat *Three-dimensional contact analysis of layered elastic/plastic solids with rough surfaces.* Wear, 2001, 249, 741-760.

[Persson *et al.*(2005)] Persson, B., Albohr, O., Tartaglino, U., Volokitin, A. & Tosatti, E. *On the nature of surface roughness with application to contact mechanics, sealing, rubber friction and adhesion.* Journal of Physics: Condensed Matter, IOP Publishing, 2005, 17, R1-R62

[Singh(1986)] Singh, Sarva Jit *Static deformation of a transversely isotropic multilayered half-space by surface loads.* Physics of the earth and Planetary Interiors, 1986, 4, 263–273.

[Waddad *et al.*(2016)] Waddad, Y., Magnier, V., Dufrénoy, P. & De Saxcé, G. *A multiscale method for frictionless contact mechanics of rough surfaces.* Tribol. Int., 2016, 96, 109-121.

[Waddad *et al.*(2017)] Waddad, Y., Magnier, V., Dufrénoy, P. & De Saxcé, G. *A new contact model for multi-layered solids with rough surfaces.* In preparation.

[Willner(2008)] Willner, K. *Fully coupled frictional contact using elastic halfspace theory.* Journal of Tribology, American Society of Mechanical Engineers, 2008, 031405, 1–8.

[Williams(1999)] Williams, J. A. *Wear modelling: analytical, computational and mapping: a continuum mechanics approach.* Wear, 1999, 225, 1-17.

[Yue(1996)] Yue, Z. Q. *Elastic field for eccentrically loaded rigid plate on multilayered solids.* International Journal of Solids and Structures, 1996, 33, 4019-4049.

Transition

Micro-contact modeling has been addressed in the previous chapters. This chapter comes as an application of the multi-scale strategy proposed in this thesis. Indeed, the contact interface behavior is integrated into a macroscopic numerical model of a braking system. The objective here is to evaluate the impact that could have the interface roughness on the dynamic behavior of the system (i.e complex modal analysis).

In this way, the contact model and the embedding methodology, both developed in the first chapter, are used in this work. Note that the micro-contact model conserves the same methodology as the first chapter, except for the solving method which is performed here by minimizing the complementary energy instead of the kinematic objective function introduced in the first chapter. Several surface samples are analyzed and the link between the interface behavior and the modal coupling is highlighted.

At last, this work can be enriched by considering also the effect of a gradient of properties and/or wear. Two features that were discussed in the previous chapters.

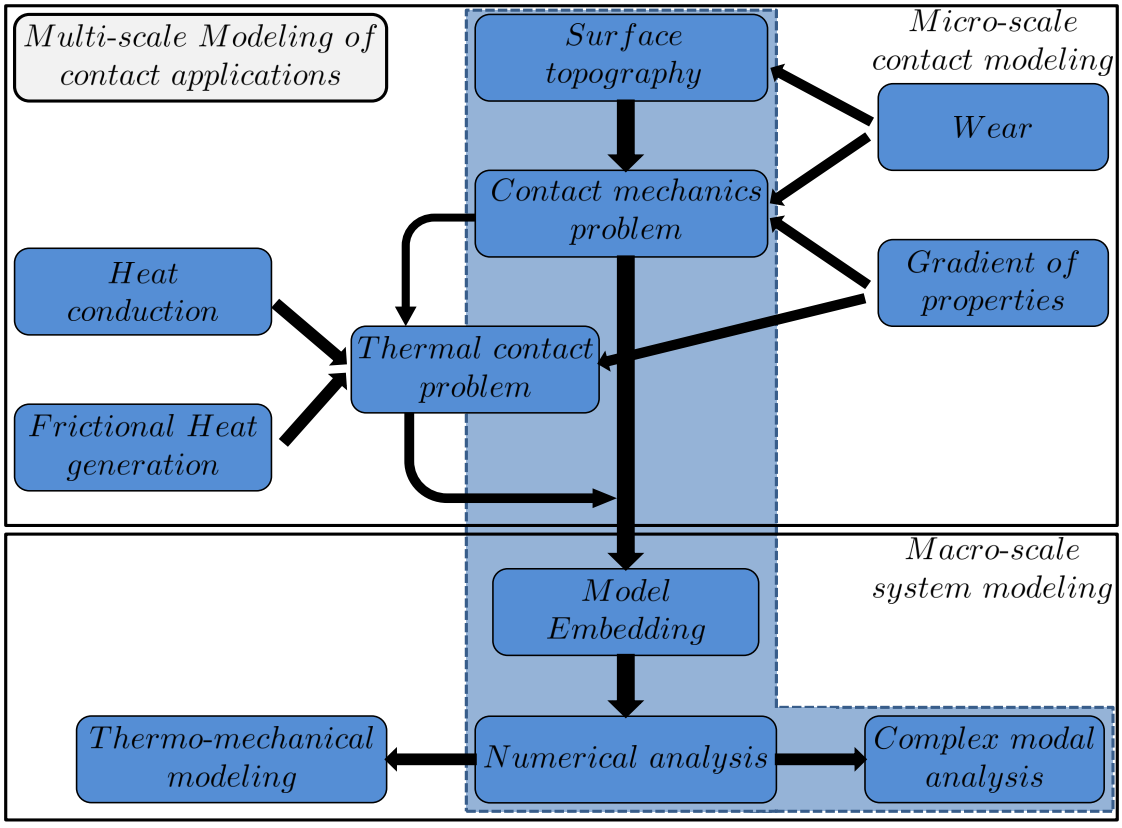

This figure presents the complete plan of this thesis. This chapter position is highlighted by a blue box in the background.

Chapter 4

Influence of roughness on mode Lock-in in a brake system

Contents

Influence of roughness on mode Lock-in in a brake system

Y. Waddad, V. Magnier, P. Dufrénoy, G. De Saxcé

Université de Lille Nord de France, F-59000 Lille, France
Lille1-LML, F-59655 Villeneuve d'Ascq, France
CNRS, FRE 8107, F-59655 Villeneuve d'Ascq, France

Abstract

During friction it is well known that the real contact area is much lower to the theoretical one and that it evolves constantly during braking. This can influence drastically the system performance. Conversely the system behavior modifies the loading conditions and consequently the contact surface area. This interaction between scales is well-known for the problematic of vibrations induced by friction but also for the thermo-mechanical behavior. Indeed, it is necessary to develop models combining a fine description of the contact interface and a model of the whole brake system. This is the aim of the present work.
A multi-scale strategy is proposed to integrate the microscopic behavior of the interface in a macroscopic numerical model. Semi-analytical resolution is done on surface patches at the contact scale while FEM solution with contact parameters embedded the solution at the micro-scale is used. Surface asperities are considered at the contact interface. As an example, the multi-scale model is used to perform a complex value analysis with the aim of identifying modal coupling in NVH simulations. With this model the interaction between non uniform surface and the system dynamic behavior is clearly shown. The contact surface variations clearly affect the modal coupling and therefore noise propensity.

keywords : Disc Brake, Surface Roughness, Finite Element Modeling, Complex Modal Analysis, NVH Analysis

4.1 Introduction

Braking performance simulation is a huge challenge as it needs to consider coupling between several physics (mechanics, thermal, tribology, etc.) and between several scales. It is now well known that there is a strong interaction between phenomena at the contact interface and the global system behavior. For instance, recent works about friction-induced vibration for braking applications have shown that the contact distribution plays a key role in the determination of unstable frequencies leading to squeal [Heussaff *et al.*(2012), Magnier *et al.*(2014)]. In particular, experimental works[Bergman *et al.*(1999), Renault *et al.*(2012)] have shown that the topography of the pad/disc interface has a major influence on brake squeal generation.
From a numerical point of view, considering micro-scale contact phenomena and the macro-scale global system with many components, is a complex challenge especially for braking analysis as the problem varies during the application. Usually only one scale is considered, the other one is simplified, for instance, in [Hetzler and Willner(2012)] with a rough contact model but a simplified discrete model of the system or in [Heussaff *et al.*(2012)] with a FEM model of the system but limited modeling of the interface. Therefore, it is necessary to develop an efficient multi-scale strategy to model this complex systems. This is the aim of the present work.
As regards the problem of micro-scale contact simulation between rough surfaces, the first models are based on the concept of asperity which was first introduced in [Archard(1957)]. Thus, the surface is described

by a statistical distribution of asperities and the contact occurs only on the top of these asperities. The asperities are spherical[Greenwood and Williamson(1966)] or approximated by a paraboloid[Bush *et al.*(1975)]. The contact problem is then solved by assuming that asperities deform according to Hertz theory. These models have achieved many results of great interest and have been successful for many years. However there is some weaknesses arising from their dependency on the statistical parameters and the non-consideration of interactions between asperities. Nevertheless, many improvements have been proposed by different authors. For instance, interactions have been included using semi-analytic approaches in [Ciavarella *et al.*(2006), Waddad *et al.*(2016)].
Numerical methods have been also used to solve the rough contact problem. With the finite element method, the problem has been solved with optimization techniques and the region near to contact surfaces has to be finely meshed to guarantee a good accuracy [Pei(2005), Hyun *et al.*(2004), Wriggers(1995)]. In return, the method is very costly in terms of CPU time which might be restrictive. Another method is to consider the solid as a half space and solve the problem using the so-called influence coefficients [Johnson(1987), Willner(2008)]. Following this approach, only the surface is discretized which saves considerably CPU time. Using the Fast Fourier Transform (FFT), a fast version of this method, has been developed in [Leroux *et al.*(2010)] to model the contact of heterogeneous half spaces, and in [Gallego *et al.*(2010)] to model the fretting problems.
In the present work, our interest is focused in friction brakes where contact status evolves continuously, and the size and distribution of contact zones influence drastically the global behavior of the surrounding components [Eriksson *et al.*(2002), Magnier *et al.*(2014)]. The main purpose is to propose a numerical strategy that allows to consider contact roughness in a large-scale model. As mentioned before, the explicit meshing of contact roughness in this kind of models is computationally expensive, so it is needed to define a multi-scale homogenization strategy allowing to consider roughness effects. For this aim, we use an approach developed in [Waddad *et al.*(2016)]. This multi-scale homogenization technique is done zone by zone, so that each zone has its local contact properties. The implementation of this technique allows to get a macroscopic contact localizations depending only on the size and the geometry of each homogenized zone. The strategy incorporates two mains steps. The first one is to analyze the micro-mechanical behavior of an interface involving rough surfaces. The second one aims to integrate this behavior in a macroscopic numerical model. An asperity based model inspired from [Ciavarella *et al.*(2006)] and improved in [Waddad *et al.*(2016)], is used to describe surface displacements under contact stresses at the micro-scale. This model is computationally efficient comparing to purely numerical models. At the macro-scale a flat interface is considered, and then enriched by contact laws taking into account the microscopic mechanical behavior. This strategy has been verified in [Waddad *et al.*(2016)] and its main steps are briefly described in this work.
With this multi-scale strategy, a complex modal analysis is performed on a complete braking system. By analyzing several surface topographies, the influence of the pad/disc interface behavior on the system dynamic behavior, is highlighted.

4.2 Multi-scale modeling of contact interface

4.2.1 Global strategy

Considering a rigid plan making contact with an elastic body represented by a cube in Fig.4.1. Let us take a zone from the contact interface. By zooming in on this zone, the real surface is rough. The aim of this work is to integrate the microscopic interface behavior in large scale numerical modeling. Since roughness scale is much smaller than the structure's one, modeling strategy will consider that the interface is perfect and embed it with a contact law that traduces its behavior (see Fig.4.2(a))

For that purpose, the strategy will build on the penalty method. this technique pairs up contact pressure p_n to the interface gap g_n by contact stiffness K_n, and we write: $p_n = K_n(g_n).g_n$. The objective here is to identify the contact law by choosing properly this parameter. The choice is made depending on surface roughness and its geometry.
Practically, contact surface is divided into many zones, where each zone has its proper geometry and roughness. For each zone, stiffness is computed using a micro-contact model that considers material properties and roughness. Indeed, on one hand, by choosing a convenient micro model, one can express the contact pressure p_n in terms of real displacement δ_r. On the other hand, one can calculate the elastic displacement δ_p corresponding to perfect contact situation (see Fig.4.2(b)). Thus, from the two situations, one can compute the gap by $g_n = \delta_r - \delta_p$, and from this equation, one can deduce the stiffness by a simple inversion and derivation operations.
Using this technique, the microscopic behavior of an interface is easily integrated in a large scale numerical model and a macroscopic accurate description of the interface is achieved in a relatively small computational time. In what follows, a micro-contact model is proposed to analyze the real interface evolution.

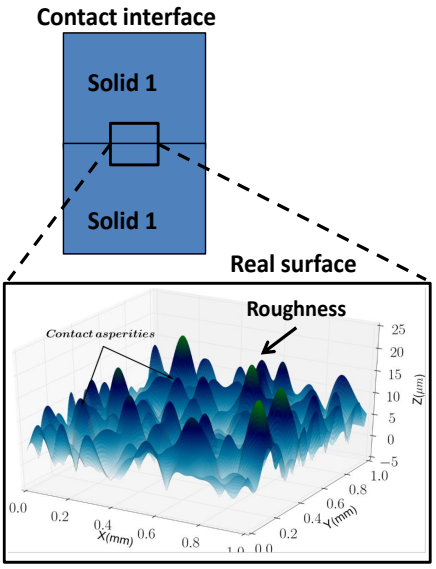

Figure 4.1: Real contact interface

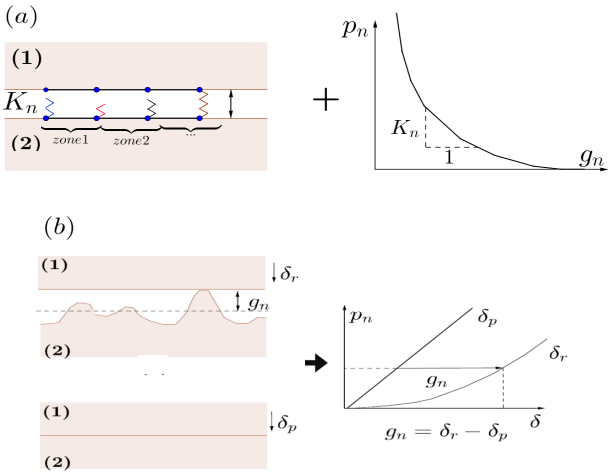

Figure 4.2: Schematic of the proposed strategy

4.2.2 Micro-contact model

Surface roughness can be seen as a random set of parabolic asperities (see Fig.4.3). When contact occurs, surface asperities deform elastically and an elliptic contact zones appear above them. The contact is mainly concentrated on the asperities. In order to solve the elastic contact problem considering surface asperities, we use a variational approach that consists in the minimization of the complementary potential energy U_E

$$U_E = \frac{1}{2}\int_{\Gamma_c} p.u_z \, dS - \int_{\Gamma_c} p.\delta \, dS \tag{4.1}$$

where Γ_c is the contact zone, u_z is the displacement field and p is the pressure field and δ is the prescribed displacement field.

Considering the solid body as an elastic homogeneous half space and using Hertz theory to describe the contact at the scale of an asperity, the potential energy reads

$$U_E = \frac{2E^*}{3} \sum_{j=1}^{N_a} \frac{a_j^3}{R_j} \left(\sum_{l \neq j}^{N_a} G_{lj} + \frac{6}{5} \frac{a_j^2}{R_j} - 2\delta_j \right)$$

where E^* is the equivalent modulus, a_j is the asperity contact radius, R_j is the asperity radii of curvature, δ_j is the prescribed displacement and the interaction term G_{lj} reads

$$G_{ik} = \begin{cases} \dfrac{a_i^2}{2R_i} \left(2 - \dfrac{d_{ik}^2}{a_i^2} \right) & \text{if } d_{ik} \leq a_i \\ \dfrac{a_i^2}{\pi R_i} \left[\left(2 - \dfrac{d_{ik}^2}{a_i^2} \right) \arcsin \left(\dfrac{a_i}{d_{ik}} \right) + \sqrt{\dfrac{d_{ik}^2}{a_i^2} - 1} \right] & \text{else} \end{cases}$$

where d_{ik} is the distance between the k^{th} and the i^{th} asperity.
In this model, the contact zones are considered circular. The elliptic shape can be considered using the same approach by introducing the eccentricity of the contact area and elliptic integrals [Waddad *et al.*(2016)]. Nevertheless, we consider that the circular shape is sufficient and enough precise to describe the contact geometry.
Solving the contact problem is to minimize U_E subject to $a_j \geq 0$. Once these variables are determined, the total load is expressed by

$$P = \frac{4}{3} E^* \sum_{j=1}^{N_a} \frac{a_j^3}{R_j}$$

Note that this model is slightly different from the original model proposed in [Waddad *et al.*(2016)]. Here the minimization is performed on the potential energy while in the first model, the minimization is done for the objective function defined on a purely kinematic contact conditions. Nevertheless, the two approaches provide approximately the same results.
The couple (P, δ) gives a full description of the interface behavior considering asperities and is used to embed the large scale numerical model as explained before.

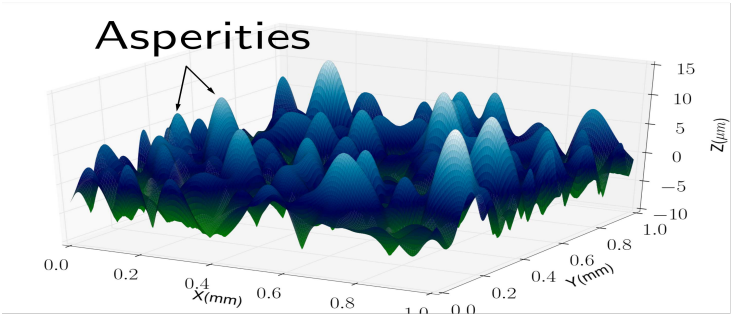

Figure 4.3: A rough surface is formed by asperities which are approximated by elliptic paraboloids

4.3 Multi-scale modeling of a braking system including contact interface behavior

The aim of this section is to present the numerical model of a braking system which considers the contact interface behavior using the multi-scale strategy aforementioned. The global objective of this model is to investigate numerically the influence of contact interface modeling on the dynamic behavior of the braking system.

4.3.1 Numerical model presentation

A 3D finite element model is adopted for the braking system. This model is composed from many structural elements. Essentially, there is a knuckle, a caliper, a piston, an anchor, a disc and two pads maintained by two backplates (see Fig.4.4). The action of braking consists in making into contact the two pads with the rotating disc in order to create friction that retards the rotation. For this to happen, a hydraulic system is used to transfer a pressurized fluid into the caliper-piston system inter-area. Thus, the pressure applied on the piston and the caliper is used to squeeze the two backplate-pad systems against the disc. The pressure that is considered in this work is $P = 10\ bar$. The disc is rotating with a constant velocity $\omega = 5\ rad.s^{-1}$ which corresponds to braking at low velocity (see Fig.4.4). As regards the boundary conditions, the displacements are blocked in the knuckle extremities and the disc inner annular face. With regard to material properties, the disc is made from cast iron, the braking pads are made from composite materials. For the other components, different types of steel are used. The whole model is composed from 229000 elements (tetrahedral and hexahedron elements) and 359000 nodes. The mesh element size is of 10 mm for the disk, the anchor, the knuckle and the caliper. For the other components, which are relatively small, the mesh size is comprised between 2 mm and 5 mm.

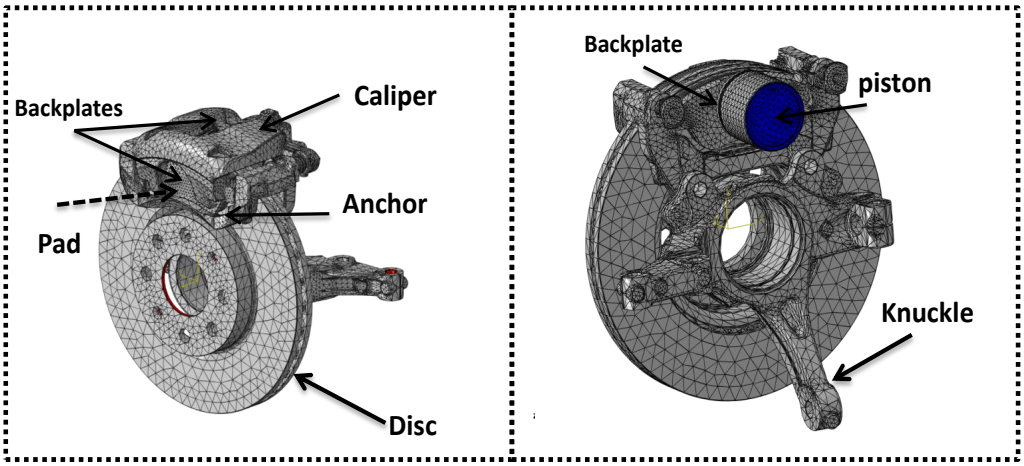

Figure 4.4: Braking system numerical model

The numerical analysis is divided into two major steps: the first one is a quasi-static analysis which consists in applying progressively the load P while the disc is rotating. At the end of this step, a steady state braking situation is achieved. The second step is to realize a complex modal analysis under contact conditions with sliding friction. The objective here is to extract the complex eigenvalues and the complex mode shapes of the entire system. A special attention is devoted to the study of unstable modes. Indeed,

due to friction contribution, two neighboring modes, which are close to each other in frequency range, can merge together and one of them becomes unstable, and the system components " are said to be locking in to each other "[Tuchinda *et al.*(2001)].
As the model contains several components, the connection between a component and an other have to be defined appropriately. Thus, tie elements are introduced between each pad and its backplate to ensure the perfect adherence between them. Additionally, contact elements are introduced between the other components connections. A frictional contact is considered and the penalty method is used to enforce contact constraints (e.g. Signorini law) except for the two contact zones between the disc and the two pads. These zones are the main object of this study and their modeling is presented in the following section.

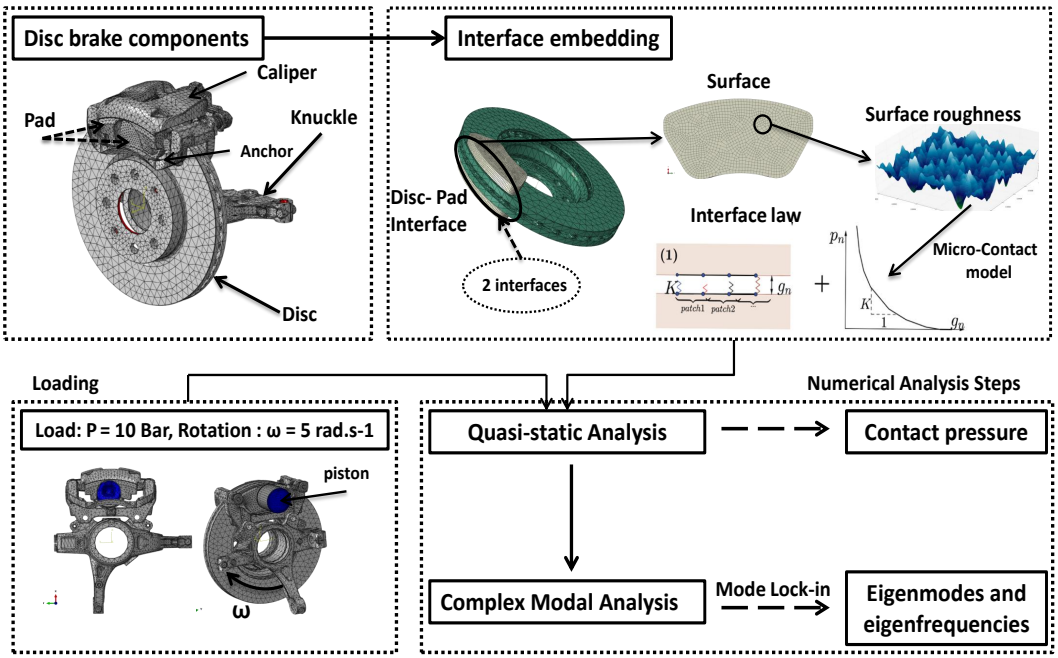

Figure 4.5: Braking system multi-scale modeling strategy

4.3.2 Pad/disc interfaces modeling

The main issue of this work is the braking pad/disc interfaces modeling. In order to highlight the effect of these interfaces, two kind of models are proposed. In the first one, the contact is assumed to be perfect and the penalty method is chosen for this purpose. The contact is frictional and the friction coefficient is set at 0.4. Thus, the interface normal behavior is not considered in this model.
The second kind considers the interface behavior. In this case, the interface is assumed to be rough. To simplify the study, only the roughness of the friction pads are considered and the disc surface is flat. Basing on the multi-scale strategy presented in the first section (see Fig.4.5), the interface behavior is integrated into the model. Moreover, a frictional behavior is also considered with the same friction coefficient used for the first model. Besides, it is important to note that it is assumed that the interface normal behavior does not account of the frictional effect.

Otherwise, roughness profile can differ from a pad to another depending on many factors such as the manufacturing process or the wear process. In order to evaluate the effect of roughness on the system's response, several surface samples are considered. These surfaces have been generated numerically using fractal techniques[Persson *et al.*(2005)]. Therefore, 6 cases are considered, and for each case, the two surface pads are different but have the same statistical parameters in terms of the root mean square σ and the quadratic mean R_q. The surface properties are summarized in Tab.4.1. Moreover, Figures 4.6-4.9 show a sample from 4 cases. As it can be seen, from the table and these figures, roughness amplitude decreases from $Case$ 0 to $Case$ 5.

	Case 0	Case 1	Case 2	Case 3	Case 4	Case 5
$R_q(\mu m)$	11.8	5.7	4.9	4.3	3.9	3.5
$\sigma(\mu m)$	5.5	2.7	2.3	2.0	1.8	1.6

Table 4.1: Statistical parameters of the studied surfaces

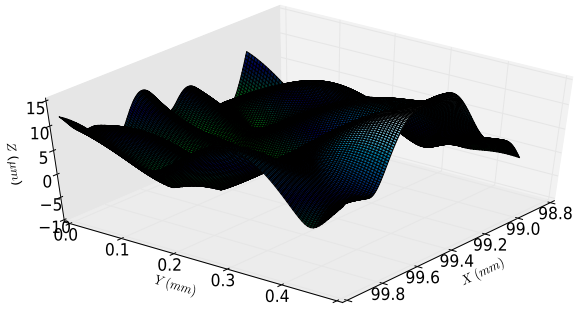

Figure 4.6: Case 0

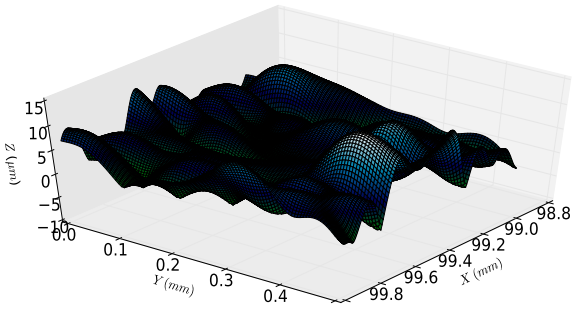

Figure 4.7: Case 1

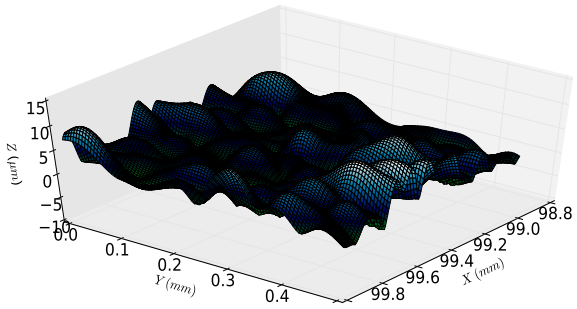

Figure 4.8: Case 3

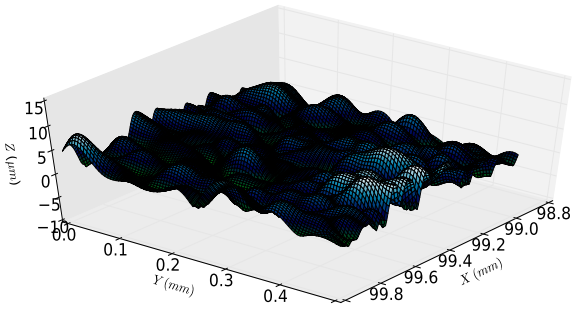

Figure 4.9: Case 5

In what follows, the results obtained with the model considering a perfect contact between pads and the disc, will be designed by " perfect contact ". The ones that are embedded by contact laws are named " case " followed by the number's case. Before proceeding to analyze the braking system dynamic behavior, we present a numerical compression test of the brake pads. This test has been carried out to evaluate the normal stiffness of the pad. To fulfill this task, the compression has been performed by prescribing a normal displacement to a rigid flat in contact with the top surface of the studied pad. Also, the bottom face is bonded to the backplate which is maintained fixed. Besides, the contact interface have been modeled using the main strategy of this work.

Fig.4.10 shows the displacement obtained, with the compression test, for one of the studied cases. Also, the mean contact pressure evolution with the normal displacement is presented in Fig.4.11. For each case, one can distinguish two curves : the dashed one corresponding to the outer pad and the continuous one for the inner pad.
The contact stiffness is identified as the slope of the plotted curves. From this figure, we can see that contact stiffness increases from case 0 to case 5. The perfect contact case corresponds to the maximal stiffness that can be reached. In the latter case, the evolution is linear while in the other cases is not. This non-linearity corresponds to a continuously growing contact area as the pressure increases. Moreover, the variation of stiffness from a case to another is mainly linked to the surface root mean square σ. Indeed, as σ increases, the real contact area and the stiffness decreases accordingly.
The following section presents the results obtained with the proposed multi-scale strategy. Results are illustrated and discussed with the aim of highlighting the interface role in the dynamic behavior of the global system.

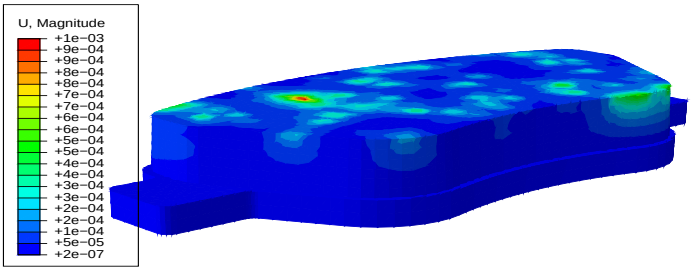

Figure 4.10: The displacement field (mm) in a braking pad and its backplate in a compression test

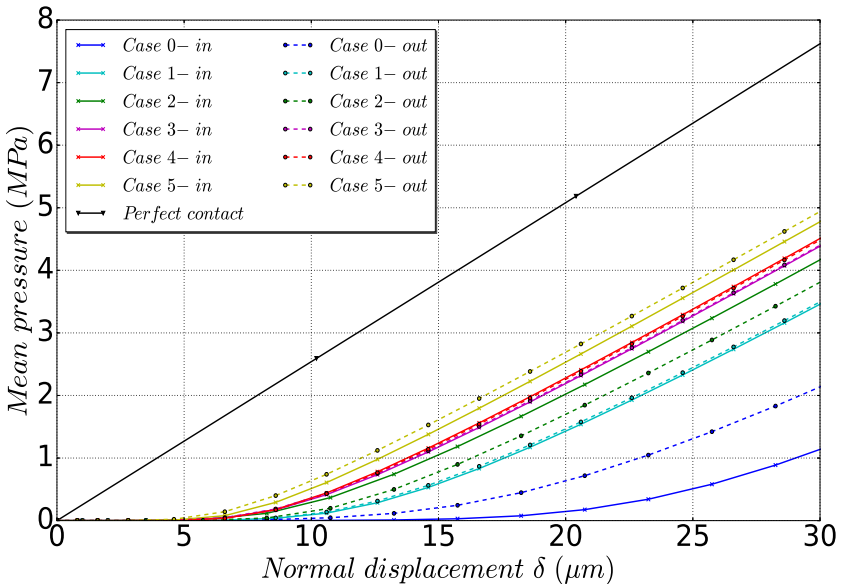

Figure 4.11: Evolution of the contact mean pressure with the prescribed displacement for the different studied cases

4.4 Results and discussion

In this section, the results issued from quasi-static analysis (first step) and complex modal analysis (second step) are presented. Beginning with the first step, Fig.4.4 shows the pressure distribution for both the inner and the outer pad and this for three configurations increasing roughness (perfect surface, case 5, case 0). One can see clearly how the pressure distribution varies from an interface to another one. For the embedded models, the pressure field is highly heterogeneous and this is a consequence of stiffness heterogeneity. Indeed, stiffness is defined for each surface element using the multi-scale strategy.

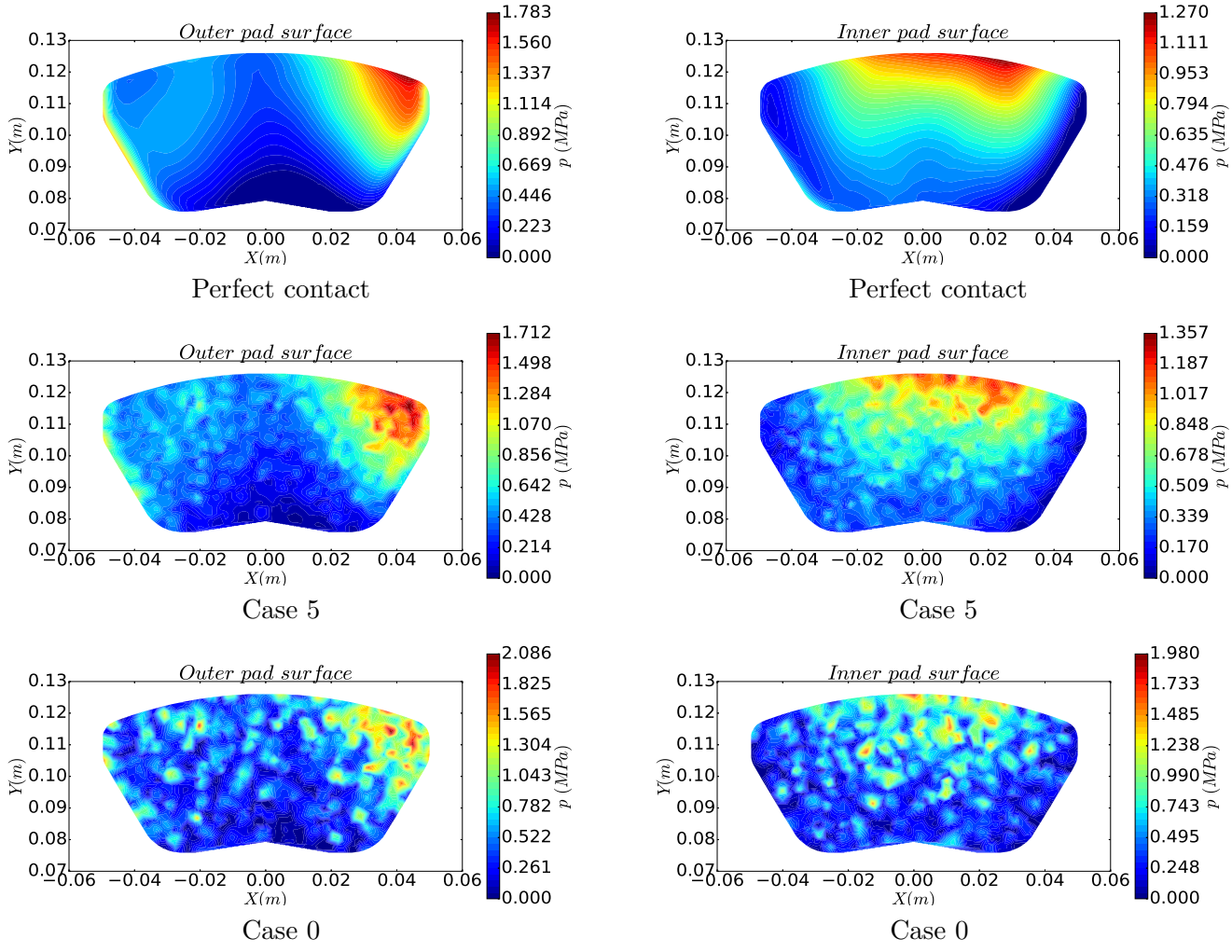

Figure 4.12: Contact pressure in both brake pads for the perfect contact case, case 5 and case 0

Additionally, we can observe that there is a macroscopic contact orientation. For the inner pad, the maximum pressure is obtained in the upper central zone, whereas, on the outer pad, the maximum pressure is reached in the upper right zone. Comparing to embedded models, this macroscopic distribution is globally conserved despite of stiffness heterogeneity. This can be explained by the fact that the backplate maintaining the inner pad is in contact with the piston in a centered zone, while the other one is in contact with the anchor in two remote zones. Moreover, considering the sliding effect, the pressure shape is distorted according to the sliding direction.

Finally, with regard to pressure intensity, we can see that the maximum value depends on roughness scale. For small standard deviations, the maximum pressure is not far from the one obtained with perfect contact simulations (around 1.5 MPa). For higher standard deviations, the pressure field is concentrated on few macroscopic zones and the maximum pressure is around 2 MPa.
Now, regarding complex modal analysis results, Fig.4.13 shows the real part of complex frequencies against the imaginary part for all the studied surfaces. At first sight, one can see that the eigenfrequencies are affected by the contact interface behavior. Furthermore, the predicted unstable modes differ from a case to another one. These modes are characterized by a strictly positive eigenfrequency real part.
In order to analyze the evolution of instability for the different cases, the unstable modes are highlighted in Fig.4.14. One can distinguish the unstable modes (illustrated by full bars), which are characterized by positive real parts, and the potentially unstable modes (corresponding to dashed bars), which are characterized by two neighboring modes that are very close in frequency range but remain stable. Roughness amplitude decreases from case 0 (see blue bars in the bottom part of the illustration) to the perfect contact (see black bars at the top part of the same figure). One can see a large variability of the distribution of the unstable and potentially unstable modes according to the surface.

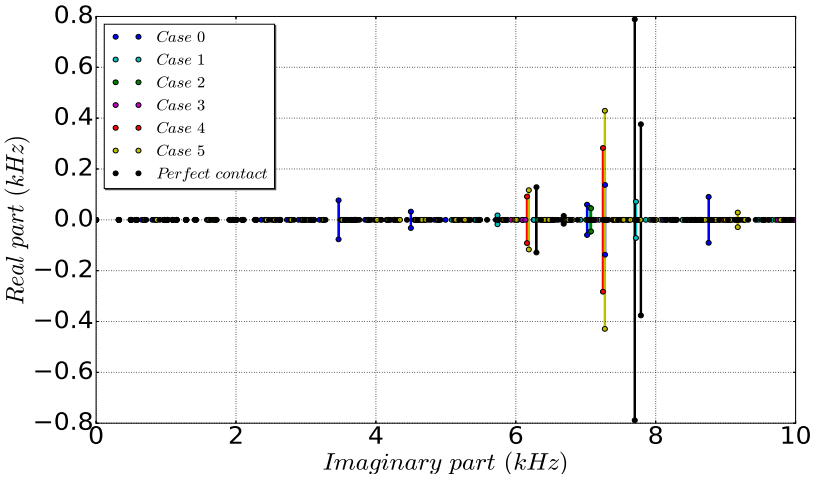

Figure 4.13: Eigenfrequency real part evolution with imaginary part

Globally the unstable modes are obtained in a high frequency range, for which the braking pads have generally more influence. Some of the potentially modes remains for all the studied cases such as mode 20 and mode 32. In these cases the pads have a global displacement with low deformation, and hence the coupling is not possible and the interface behavior has no influence. On the other hand, the instability of some modes is strongly affected by the interface behavior like modes 51 and 66 and many others. Some unstable modes are illustrated in Fig.4.15. These modes as can be seen in this figure correspond to bending vibrations of the pads which are often coupled to nodal diameter based modes of the disk. It has also to be noticed that some cases have a common number for an unstable eigenmode which does not correspond necessary to the same shape.
Results for perfect contact strongly differs from case 5 as between case 1 and case 0 to a lesser extent. It has to be related to contact stiffness effect. Indeed, contact stiffness of the perfect contact case and case 0 strongly differ to the other ones as illustrated in Fig.4.11. Moreover, contact stiffness controls contact forces which accordingly affect bending vibrations of the brake pads.
An example of surface roughness influence can be illustrated with the unstable modes close to 7 kHz.

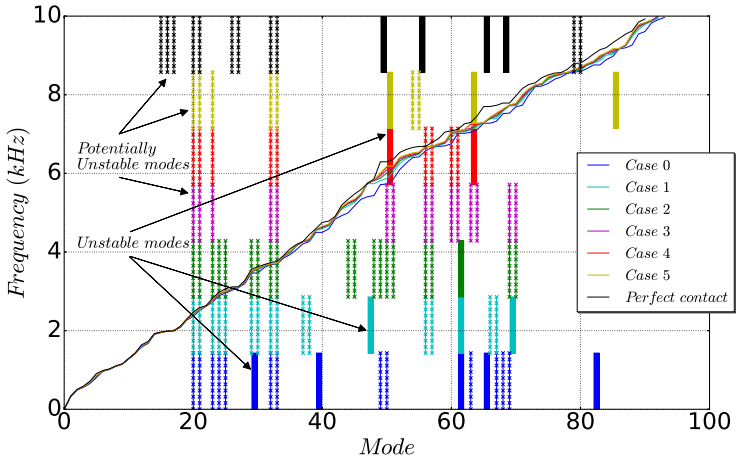

Figure 4.14: Unstable modes evolution across eigenmodes for the different studied cases

When increasing roughness, there is an unstable mode at a frequency close to 7.5 kHz (for perfect contact) which decreases when roughness increases until a value close to 7 kHz for cases 2 to 0. In fact the eigenmode differs from one case to another, as illustrated in Fig.4.15 showing mode 62 for case 1 and mode 64 for cases 4 and 5. Note that there is any unstable mode for case 3.

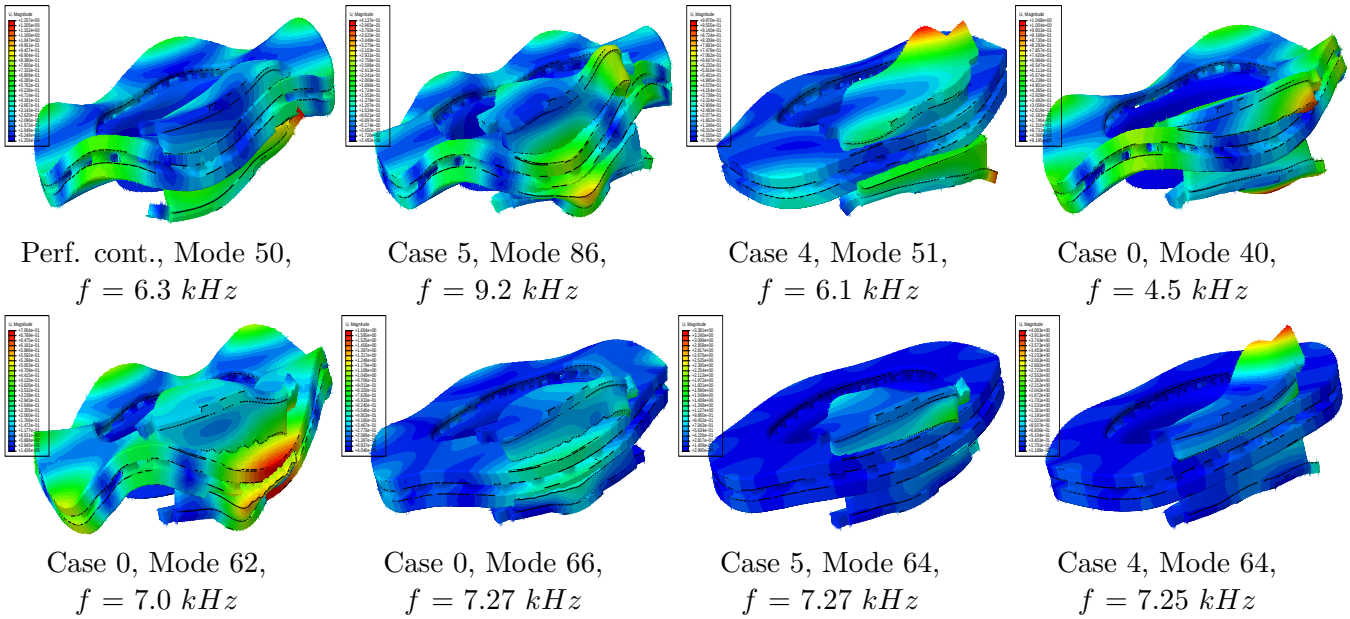

Perf. cont., Mode 50, $f = 6.3\ kHz$ | Case 5, Mode 86, $f = 9.2\ kHz$ | Case 4, Mode 51, $f = 6.1\ kHz$ | Case 0, Mode 40, $f = 4.5\ kHz$

Case 0, Mode 62, $f = 7.0\ kHz$ | Case 0, Mode 66, $f = 7.27\ kHz$ | Case 5, Mode 64, $f = 7.27\ kHz$ | Case 4, Mode 64, $f = 7.25\ kHz$

Figure 4.15: Some unstable modes for the different studied cases

In order to better appreciate the influence of roughness, an analysis of shape correlation between the different studied cases is done using the Modal Assurance Criterion (MAC) [Allemang(2003)]. The MAC

is a matrix of correlation where each term is given by

$$(MAC)_{i,j} = \frac{|\{y_i^1\}^T\{y_j^2\}|^2}{\{y_i^1\}^T\{y_i^1\}\{y_j^2\}^T\{y_j^2\}}$$

where $\{y_i^a\}$ is the eigenvector of the case a and mode i and ${}^T\{y\}$ is the conjugate transpose of y.
In Fig.4.16 and Fig.4.17, one can see that for small standard deviations (case 5) the eigenvectors are quite correlated to the ones with perfect contact surface. This correlation decreases remarkably for surface 0 corresponding to higher roughness standard deviation. Moreover, the correlation decreases for both cases as the frequency increases.
From the MAC matrix, the correlation coefficient $MMAC$ can be defined for the ith eigenvector by

$$(MMAC)_i = \max_j((MAC)_{i,j})$$

This coefficient gives an information on the jth eigenvector which is the most correlated to the ith eigenvector. Moreover, it is also of interest to study the evolution of $MMAC$ through the different modes. Indeed, it is interesting to evaluate this parameter in an averaging sense so that we can highlight the fluctuation and the trend of the considered parameter. For this purpose, the cumulative moving average of a series x_i is defined by

$$\bar{x}_n = \frac{1}{n}\sum_{k=0}^{n-1} x_{n-k}$$

In Fig.4.18, is shown the evolution of the $MMAC$ for the different modes. The correlation is computed by comparing the eigenmodes from the embedded models to the perfect contact one. From this figure, one can see that several modes have a weak correlation with the studied cases modes. The difference is more relevant for large standard deviations which is the case for case 0. Additionally, Fig.4.19 shows the corresponding cumulative moving average. As can be seen, the cumulative correlation is decreasing with modes for all these cases. Indeed, in the first 20 modes, modal shapes are almost similar to those obtained for perfect contact model.
Thus, the MAC analysis suggests that there is many eigenmodes without significant correlation with the perfect contact case. Therefore, this study tends to confirm that some new eigenvectors can be found by changing the surface parameters. However it is not sure that these new modes come from the two pads or the other components. In order to highlight the effect of the friction pads into the apparition of new eigenmodes, the strain energy distribution is presented in Fig.4.20. As is shown in this figure, the brake pads contains only a small part of the elastic strain energy and most of strain energy is stored in the disc and/or the other components. The part of energy that is stored into the pads increases with the frequency. The strain energy results are meaningless in terms of reported quantities. But its evolution through the different cases, gives us an information on how the interface behavior can affect the repartition of the energy. Fig.4.21 provides the strain energy distribution between the two pads for three cases. By analyzing the two figures, it seems that the energy contained in brake pads increases with frequency and more especially for some unstable modes of high frequency (e.g. mode 66 for perfect contact case, modes 64 and 86 in case 5, and modes 62 and 66 and 83 in case 0). Thus, the strain energy analysis confirms that the pads are involved in the instabilities and therefore the influence of contact pressure heterogeneity due to roughness.
By linking, the different results of the modal analysis with roughness parameters and stiffness values, one can remark that surfaces ranging from 1 to 5, have a quite similar parameters and thus their dynamic behavior is nearly the same, while surface 0 and perfect contact models had remarkably different behaviors. By decreasing the roughness amplitude, stiffness increases and the dynamic behavior is becoming increasingly similar to a perfect contact model.

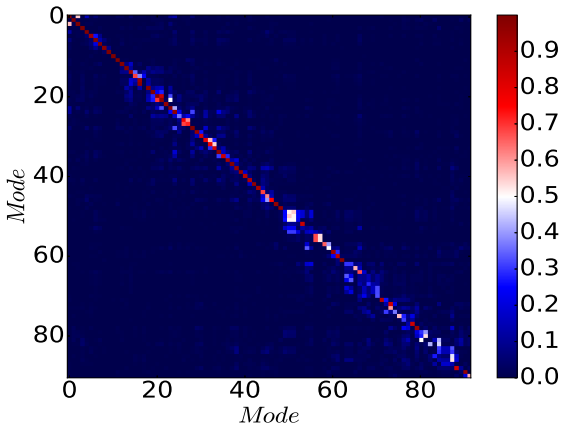

Figure 4.16: Mac between the perfect contact and case 5

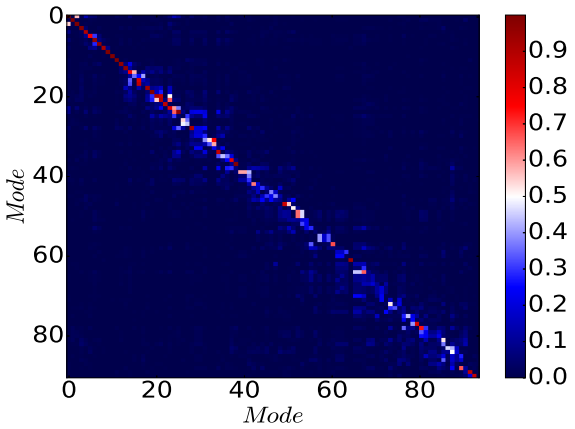

Figure 4.17: Mac between the perfect contact and case 0

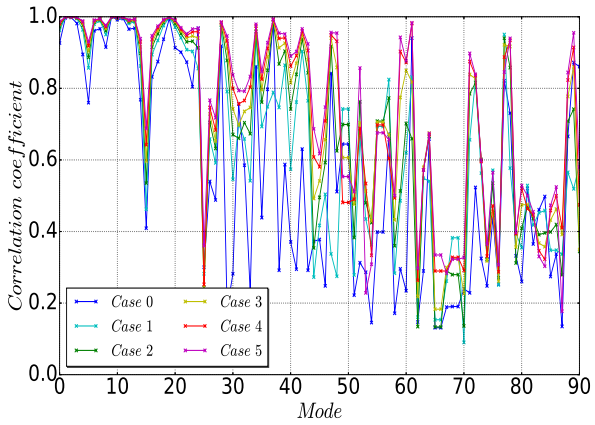

Figure 4.18: Maximum correlation coefficient

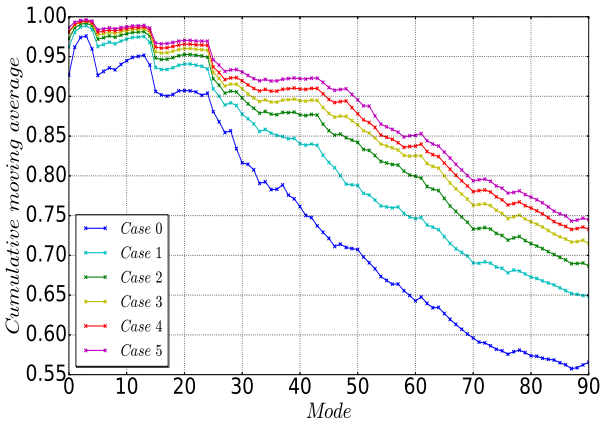

Figure 4.19: Mean cumulative coefficient

4.5 Conclusion

An efficient simulation tool has been proposed to describe a realistic contact surface at a micro scale in a macro model of a complete brake system. This multi-scale model combines a semi-analytical resolution of the contact on contact elements embedded in a FEM simulation of the macro model. At the surface, roughness asperities are considered in order to introduce realistic phenomenon of asperity deformation under contact forces. For the resolution at the micro-scale, the solid body is considered as an elastic homogeneous half space, potential theory is used to describe surface displacements under contact stresses. At the macro-scale a perfect interface is considered, enriched by the microscopic mechanical behavior.
An application to squeal noise propensity has been described on a disc braking system. A rough surface of asperities is introduced at the friction interface. Parametric analysis of topology has been done. Results show that braking system instabilities are strongly affected by the interface behavior. By changing the contact parameters, some unstable modes become stable, and some eigenvectors can emerge. Also it can be observed that surfaces with very small deviations had a similar dynamic behavior to a perfect contact situation. In the opposite case, the variability of the dynamic behavior is more relevant especially at high frequencies for which the pad behavior is more influent. The multi-scale strategy has been described here

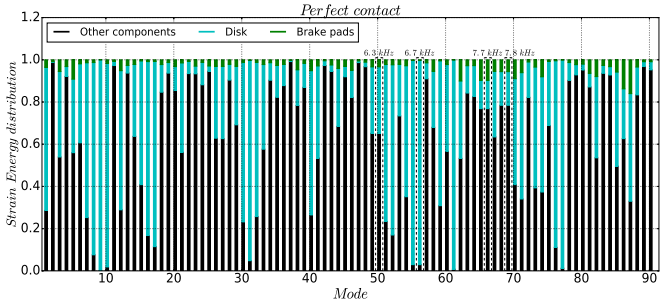

Perfect contact

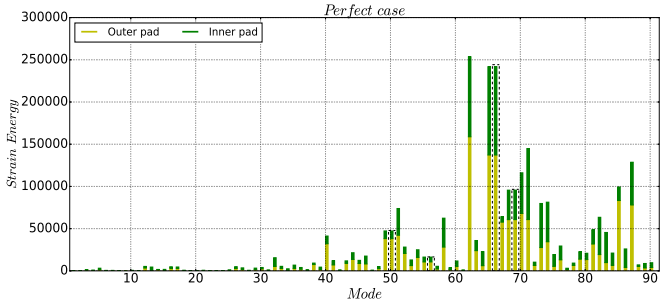

Perfect contact

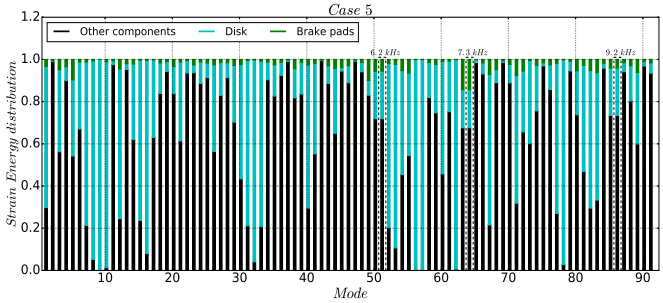

Case 5

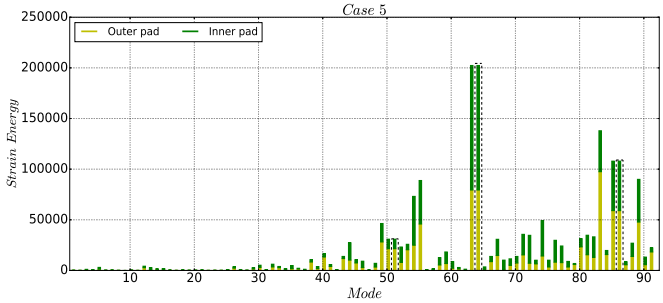

Case 5

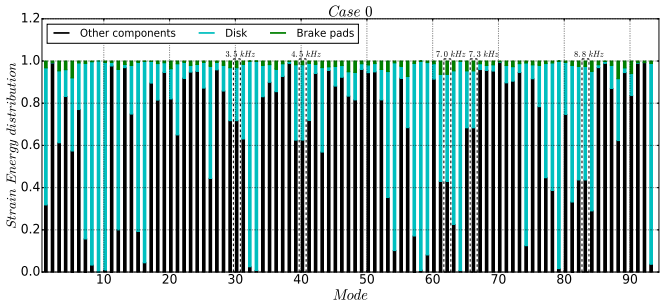

Case 0

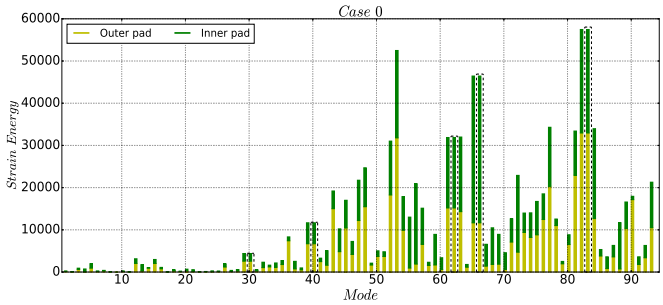

Case 0

Figure 4.20: Strain energy distribution

Figure 4.21: Strain energy in the two pads

for mechanical analysis but it can be extended to thermal analysis. Evolution of the interface can also be considered to introduce loading history effect and more complex mechanisms at the interface.

Acknowledgments

The present research work has been supported by the International Campus on Safety and Intermodality in Transportation, the Hauts-de-France Region, the European Union, the Regional Delegation for Research and Technology, the Ministry of Higher Education and Research, the French National Research Agency (ANR COMATCO), and the National Center for Scientific Research. The authors gratefully acknowledge these institutions for their support.

Bibliography

[Allemang(2003)] Allemang, Randal J. *The modal assurance criterion–twenty years of use and abuse.* Sound and Vibration, 2003, 37, 14-23.

[Archard(1957)] Archard, J. F. *Elastic deformation and the laws of friction.* Proceedings of the Royal Society of London. Series A. Mathematical, Physical and Engineering Sciences, The Royal Society, 1957, 243, 190-205

[Bergman *et al.*(1999)] Bergman, F., Eriksson, M., & Jacobson, S. *Influence of disc topography on generation of brake squeal.* Wear, 1999, 225, 621–628.

[Bush *et al.*(1975)] Bush, A., Gibson, R. & Thomas, T. *The elastic contact of a rough surface.* Wear, 1975, 35, 87-111

[Ciavarella *et al.*(2006)] Ciavarella, M., Delfine, V. & Demelio, G. *A re-vitalized Greenwood and Williamson model of elastic contact between fractal surfaces.* Journal of the Mechanics and Physics of Solids, 2006, 54, 2569-2591.

[Eriksson *et al.*(2002)] Eriksson, M., Bergman, F. & Jacobson, S. *On the nature of tribological contact in automotive brakes.* Wear, 2002, 252, 26-36

[Gallego *et al.*(2010)] Gallego, L., Nelias, D. & Deyber, S. *A fast and efficient contact algorithm for fretting problems applied to fretting modes I, II and III.* Wear, 2010, 268, 208–222.

[Greenwood and Williamson(1966)] Greenwood, J. & Williamson, J. *Contact of nominally flat surfaces.* Proceedings of the Royal Society of London. Series A. Mathematical and Physical Sciences, The Royal Society, 1966, 295, 300-319

[Hetzler and Willner(2012)] Hetzler, H. and Willner, K. *On the influence of contact tribology on brake squeal.* Wear, 2012, 46, 237-246

[Heussaff *et al.*(2012)] Heussaff, A., Dubar, L., Tison, T., Watremez, M. & Nunes, R.F. *A methodology for the modelling of the variability of brake lining surfaces.* Wear, 2012, 289, 145-159

[Hyun *et al.*(2004)] Hyun, S., Pei, L., Molinari, J.-F. & Robbins, M. *Finite-element analysis of contact between elastic self-affine surfaces.* Phy. Rev. E, 2004, 70, 026117

[Johnson(1987)] Johnson, K. L. *Contact mechanics.* Cambridge university press, 1987

[Leroux *et al.*(2010)] Leroux, J., Fulleringer, B. & Nelias, D. *Contact analysis in presence of spherical inhomogeneities within a half-space.* International Journal of Solids and Structures, 2010, 47, 3034–3049.

[Magnier *et al.*(2014)] Magnier, V., Brunel, J.F. & Dufrénoy, P. *Impact of contact stiffness heterogeneities on friction-induced vibration.* International Journal of Solids and Structures, 2014, 51, 1662–1669

[Pei(2005)] Pei, L., Hyun, S., Molinari, J. F. & Robbins, M. O.*Finite element modeling of elasto-plastic contact between rough surfaces.* Journal of the Mechanics and Physics of Solids, 2005, 53, 2385-2409

[Persson *et al.*(2005)] Persson, B., Albohr, O., Tartaglino, U., Volokitin, A. & Tosatti, E. *On the nature of surface roughness with application to contact mechanics, sealing, rubber friction and adhesion.* Journal of Physics: Condensed Matter, IOP Publishing, 2005, 17, R1-R62

[Renault *et al.*(2012)] Renault, A., Massa, F., Lallemand, B., & Tison, T. *Experimental investigations for uncertainty quantification in brake squeal analysis.* J. of Sound and Vibration, 2016, 367, 37-55

[Tuchinda *et al.*(2001)] Tuchinda, A., Hoffmann, N. P., Ewins, D. J., & Keiper, W. *Mode lock-in characteristics and instability study of the pin-on-disc system.* In IMAC-XIX: A Conference on Structural Dynamics, 2001, February, Vol. 1, 71-77.

[Waddad *et al.*(2016)] Waddad, Y., Magnier, V., Dufrénoy, P. & De Saxcé, G. *A multiscale method for frictionless contact mechanics of rough surfaces.* Tribol. int., 2016, 96, 109-121.

[Willner(2008)] Willner, K. *Fully coupled frictional contact using elastic halfspace theory.* Journal of Tribology, American Society of Mechanical Engineers, 2008, 031405, 1–8.

[Wriggers(1995)] Wriggers, P. *Finite element algorithms for contact problems.* Archives of Computational Methods in Engineering, Springer, 1995, 2, 1-49

Part II

Thermal contact of rough surfaces

Transition

The first part of this thesis aimed to investigate the contact mechanics problem of rough surfaces and the integration of the mechanical behavior into macro-scale numerical models using an embedding strategy developed in its first chapter. Besides, an application of the proposed strategy has been presented in the last chapter.
The second part of this thesis deals with the thermal features of rough contact modeling. Indeed, thermal exchanges are taking place in the contact interface. The presence of roughness and a change of material near to the interface modifies surely the heat conduction and the temperature field.
The idea of the following chapter is to study the steady heat conduction considering a static rough contact and the presence of a gradient of material properties near to the interface. The contact area is defined based on the contact mechanics model which has been presented in chapter 3. The obtained results are verified by Finite Element calculations. Also, a parametric study is performed to highlight the role of each physical parameter that could influence the process of heat conduction.
Note that the thermal expansion is not considered in this work.

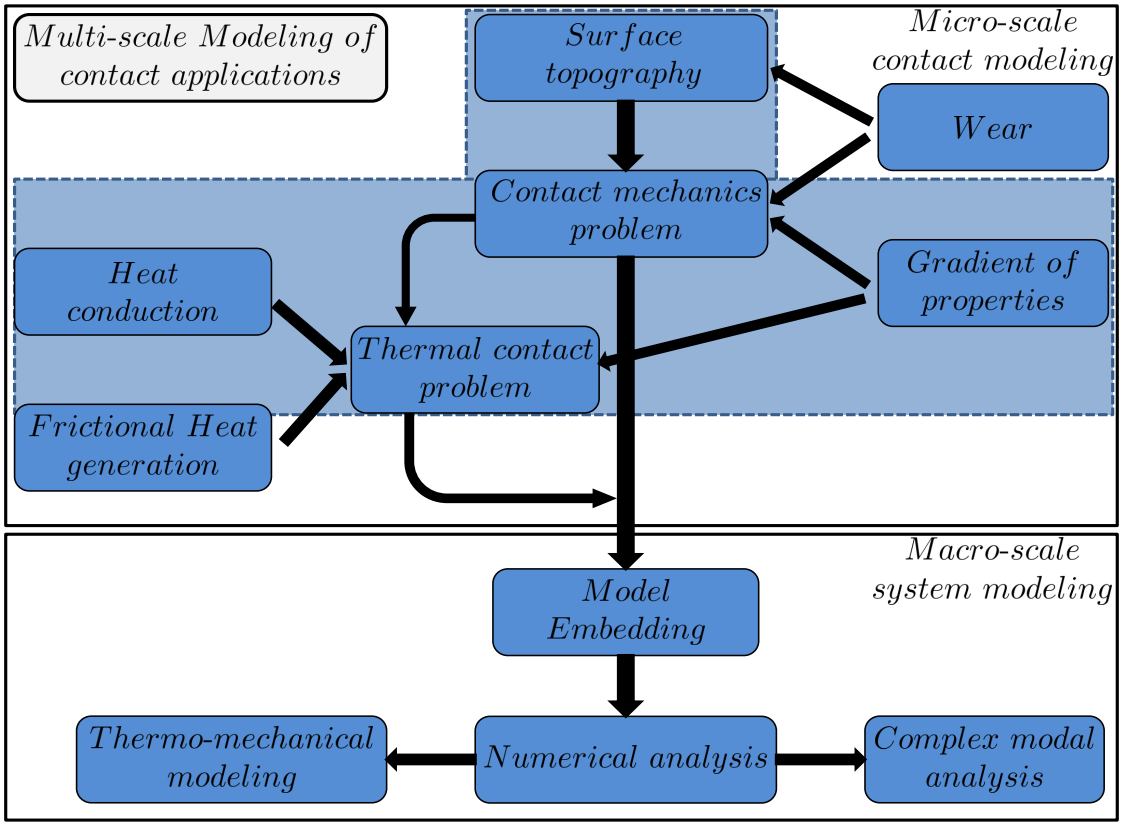

This figure presents the complete plan of this thesis. The position of this chapter is highlighted by a blue box in the background.

Chapter 5

Heat conduction in multi-layered solids with rough surfaces

Contents

Heat conduction in multi-layered solids with rough surfaces

Y. Waddad, V. Magnier, P. Dufrénoy, G. De Saxcé

Université de Lille Nord de France, F-59000 Lille, France
Lille1-LML, F-59655 Villeneuve d'Ascq, France
CNRS, FRE 8107, F-59655 Villeneuve d'Ascq, France

Abstract

The present study aims to investigate the heat conduction between multi-layered solids with rough surfaces. An efficient numerical method is proposed to predict the thermal conductance of this kind of materials considering surface roughness. The Fourier transform and transfer matrix technique are used to solve the problem of surface heating of multi-layered solids. Using the same techniques, the contact area is obtained by solving the problem of surface loading. Based on this framework, the heat flowing through the contact interface is computed by solving a linear system. The obtained results are fully discussed and compared to Finite Element results carried out in the present study. The efficiency of the method is also highlighted. The effects of many parameters such as layers physical properties, roughness and local thermal resistance are investigated.

keywords : Thermal contact conductance, surface roughness, multi-layered solid, Fourier transform, transfer matrix technique

5.1 Introduction

Heat conduction between solid bodies in contact is a challenge in many engineering fields. Experimental studies have shown that temperature of the mating surfaces are not equal. This is the direct consequence of contact interface roughness. Indeed, contact occurs only at a few discrete zones surrounded by interstitial gaps. Hence heat flows through these contact zones and the air contained in these gaps and radiation. The two latter mechanisms are generally of secondary significance and are not studied in this work.
The temperature jump at the interface is said to be a result of the presence of a thermal contact resistance. The inverse of this property is the thermal contact conductance. This quantity is equivalent to the amount of heat flowing per unit of area through the interface for a unit temperature jump.
The thermal contact conductance has been extensively investigated. The theoretical framework was firstly proposed in the pioneering works of [Cooper *et al.*(1969), Mikic(1974)]. Indeed, this property was evaluated considering surface roughness and the heat conduction problem was first solved by deriving a solution for the single contact problem and then extended to cover the case of multiple contact zones. The conducted studies aimed to evaluate the evolution of the contact pressure with the thermal conductance relationship considering surface parameters (distribution of surface height peaks, geometry of the profile, etc.) [Cooper *et al.*(1969)] and deformations modes (elastic and plastic deformations for both asperities and substrate) in [Mikic(1974)]. As a result of these studies, it has been shown that the influence of statistical surface parameters depends on the deformation mode considered and the thermal conductance depends strongly on the contact stiffness especially for the case of small loads. Therefore, contact mechanics is strongly involved in thermal conductance computation.
Contact mechanics of rough surfaces has been widely studied, starting with classical asperity-based models [Greenwood and Williamson(1966), Bush *et al.*(1975)] up to more improved models [Persson

et al.(2002), Ciavarella *et al.*(2006)] or numerical methods requiring just surface discretization [Willner(2008), Gallego *et al.*(2010)]. Within asperity-based models, the thermal contact was studied in [McWaid and Marschall(1992), Salgon *et al.*(1997)]. Asperity interactions was also considered in [Bahrami *et al.*(2005)] which is the missing key point of the oldest models. Indeed, asperities interactions reduce contact area and thus influence the thermal conductivity. Some improvements can also be consulted in a recent review paper [Yovanovich(2005)] such as the consideration of the elasto-plastic behavior, the presence of gas in the gap interface and phase evolution effect. The above-cited models deal with contact problems considering small contact areas. For high fractions of contact areas, an analytical model of thermal contact conductance have been proposed by [Sadowski *et al.*(2010)]. Their model expresses the contact conductance as a function of the real contact and the local thermal contact resistance. However, the contact area distribution has been obtained from purely geometric considerations which neglect the mechanical behavior of the surface.

In the last decades, there were many improvements in numerical simulations of contact between rough surfaces. In [Zavarise *et al.*(1992)], the thermal contact conductance was computed combining radiation and gas effects and surface roughness. The obtained contact conductance was integrated into a thermo-mechanical finite element model. Within the same framework, a thermo-mechanical computational homogenization technique of interfaces with rough surfaces was developed in [Temizer and Wriggers(2010)]. This approach was used in [Temizer(2011)] to study random rough surfaces and evaluate the interface temperature jump in relationship with contact pressure. Nevertheless, this kind of methods is expensive since a high number of contact points is needed to efficiently simulate the problem. Within a purely thermal point of view, the finite volume method was employed to compute the thermal contact resistance in a sliding contact [Salti and Laraqi(1999)], but with a simplified geometry.

The various existing models are focused on the contact surface geometry and consider that solids are homogeneous. Experimentally, it has been observed that, under thermal loadings, the contacting solids undergo several transformations especially near to contact interfaces. These solid transformations can be seen as a solid having a gradient of material properties. Thus, the appearance of a gradient of material properties has to be considered in the theoretical study of both thermal and mechanical contact problems. In this work, the gradient of properties is considered only in the normal direction to the interface. Thus, the material can be considered as a multi-layered solid where each layer has its local properties. The contact mechanics of multi-layered solids has been studied in few works (e.g. [Peng and Bhushan(1996), Cai and Bhushan(2005)]). Recently, a new contact model was proposed in [Waddad *et al.*(2017^a)] which is based on the transfer matrix technique developed in [Singh(1986), Ernian(1996)]. This method can be easily extended to study the thermal contact problem using the Fast Fourier transform (FFT).

The aim of this work is thus to propose an efficient modeling strategy of heat conduction in multi-layered solids with rough surfaces. First, the contact area is computed with a semi-analytic approach developed in [Waddad *et al.*(2017^a)] using the transfer matrix technique. Second, the transfer matrix technique is formulated for the thermal surface heating problem and the thermal contact is solved by meshing the surface and FFT technique. The effect of a local thermal resistance is also considered. Indeed, even at low scales, the continuity of temperature is not guaranteed. This is principally due to the presence of wear particles, oxides and lubricants, etc.[Sadowski *et al.*(2010)]. Notice that the thermal and the mechanical problems are considered to be decoupled, hence no thermoelastic deformations will be considered in this work. Finally, a parametric study is presented and the obtained results are compared to finite element calculations. In particular, the effects of solid layers, roughness and the local thermal resistance are highlighted.

5.2 Global framework

Considering two solids S_1 and S_2 in contact. The temperature of their extremities are fixed at θ_{l1} and θ_{l2} respectively. If $\theta_{l1} \neq \theta_{l2}$, heat flows from the hot solid to the cold one through the interface (see Fig.5.1). Therefore, for each of the two solids, the contact interface is considered as a source of heat acting on the superior face of each body.
Solving the thermal contact problem consists in finding the amount of heat flowing through the contact interface for a given contact area. If we assume that the surface is the only source of heat, the solid temperature θ is expressed as a function of surface heating ϕ. In order to solve the thermal contact problem, the surface heating problem has to be solved first.
For this aim, let us suppose that the surface is discretized into N_p small squares of the same size. The heat flux acting on each single square is assumed to be uniformly distributed on it. The solid temperature is then calculated as a combination of all variations of temperature due to all the fluxes acting on the surface

$$\theta(x,y,z) = \sum_{i=1}^{N_p} \phi_i T(x - x_i, y - y_i, z) \tag{5.1}$$

where ϕ_i is the heat flux on the square i, (x_i, y_i) are the coordinates of square centers and T is the temperature elevation at the solid point (x, y, z) that is due to the flux distributed over the i^{th} element. The temperature θ can be seen as a discrete convolution of the heat flux ϕ and the function T

$$\theta = T * \phi \tag{5.2}$$

By making use of the Fast Fourier transform FFT, one can show that the temperature field reads

$$\theta = \mathrm{IFFT}\left(\mathrm{FFT}(T).\mathrm{FFT}(\phi)\right) \tag{5.3}$$

where IFFT is the Inverse Fast Fourier transform.
Solving the thermal loading problem consists in expressing T as a function of the material properties and the heated zone geometry. T is the elementary solution corresponding to the case of heat supplied over a square area. In what follows, the surface heating problem of multi-layered solids is presented.

5.3 Surface heating of multi-layered solids

Let us begin by reminding the Heat equation for steady state heat transfer and the Fourier law which are expressed respectively by

$$\Delta\theta = 0 \tag{5.4}$$

and

$$\boldsymbol{\Phi} = -\kappa\, \boldsymbol{grad}\, \theta \tag{5.5}$$

We introduce the following set of solution representation using Fourier transform

$$V = \iint \theta(x,y,z) \exp\left[i\left(\xi x + \eta y\right)\right] \mathrm{d}\xi \mathrm{d}\eta$$

and

$$\phi = -\iint \Phi_z(x,y,z) \exp\left[i\left(\xi x + \eta y\right)\right] \mathrm{d}\xi \mathrm{d}\eta$$

From Heat equation we found

$$\frac{\partial^2 V}{\partial z} = \rho^2 V$$

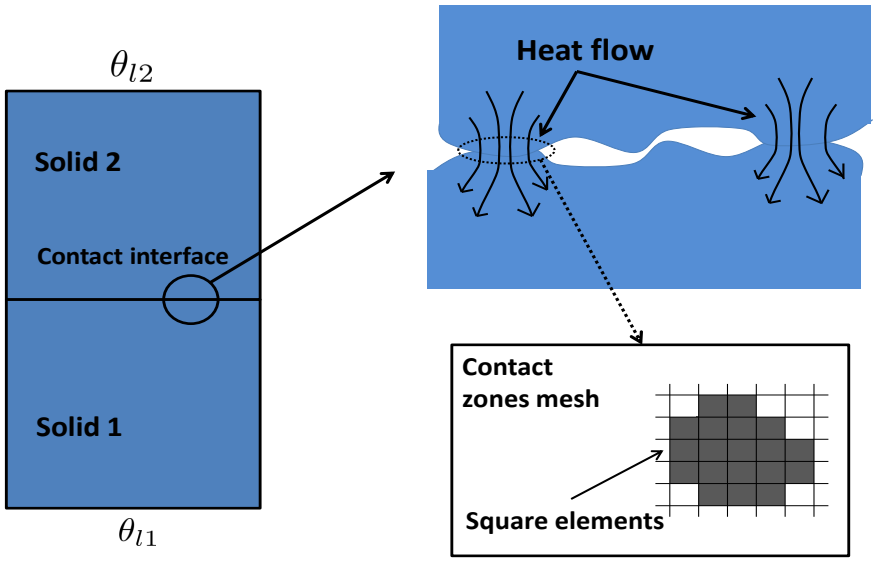

Figure 5.1: Schematic of a contact interface. Heat flows through the micro-contact zones. These zones are discretized into square elements with the same size. Heat flowing through the air contained in the interface is neglected.

where $\rho = \sqrt{\xi^2 + \eta^2}$ and from Fourier law

$$\phi = \kappa \frac{\partial V}{\partial z}$$

The global solution of this problem is an eigenvalue extraction problem and can be written in the following form

$$\begin{bmatrix} V \\ \phi/\rho \end{bmatrix} = \mathbf{Z} \begin{bmatrix} Y_1 \\ Y_2 \end{bmatrix}$$

where Y_1 and Y_2 are constants and the matrix $\mathbf{Z}$ reads

$$\mathbf{Z} = \exp(\rho z) \cdot \begin{bmatrix} 1 & \exp(-2\rho z) \\ \kappa & -\kappa \exp(-2\rho z) \end{bmatrix}$$

Considering that the solid is an unbounded horizontal layer of which the thickness is h. The superscript $^{(+)}$ is used for the top surface variables while $^{(-)}$ is for the bottom ones. One can prove that

$$\begin{bmatrix} V^{(-)} \\ \phi^{(-)}/\rho \end{bmatrix} = \mathbf{R} \begin{bmatrix} V^{(+)} \\ \phi^{(+)}/\rho \end{bmatrix} \tag{5.6}$$

where $\mathbf{R}$ is the transfer matrix of the layer and is given by

$$\mathbf{R} = 0.5 \exp(\rho h) \cdot \begin{bmatrix} 1 + \exp(-2\rho h) & -\frac{1}{\kappa}(1 - \exp(-2\rho h)) \\ -\kappa(1 - \exp(-2\rho h)) & 1 + \exp(-2\rho h) \end{bmatrix}$$

Now let us consider a multi-layered body formed by N horizontal layers. The 0^{th} layer is on the top of the solid and the N^{th} layer is on the bottom part of the solid. Considering the perfect continuity between the

parallel layers, the temperature field θ and the flux ϕ are both continuous. Using the transfer matrices, one can deduce that

$$\begin{bmatrix} V^{(0)} \\ \phi^{(0)}/\rho \end{bmatrix} = \underbrace{\mathbf{R}^{(1)}...\mathbf{R}^{(N)}}_{\mathbf{M}} \begin{bmatrix} V^{(N)} \\ \phi^{(N)}/\rho \end{bmatrix}$$

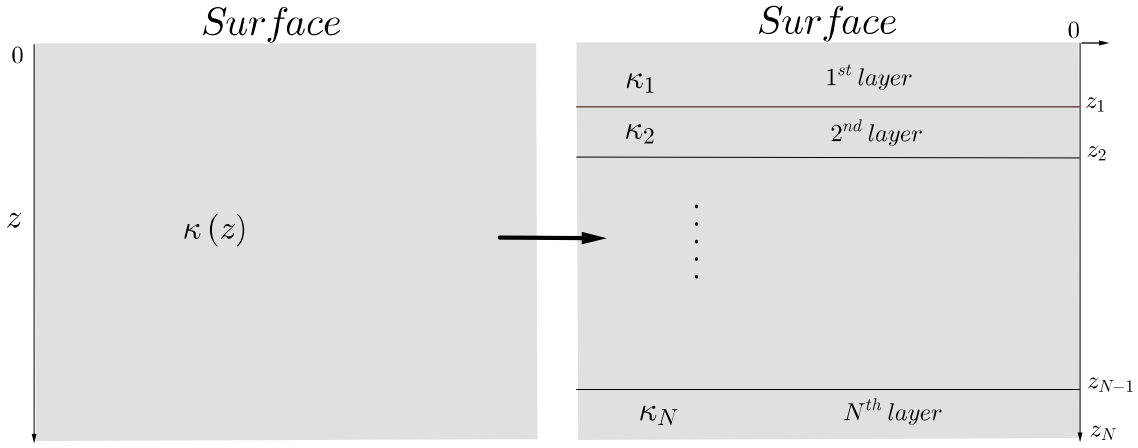

Figure 5.2: Schematic of a multi-layered system

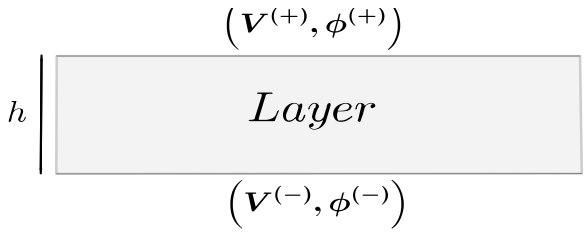

Figure 5.3: Schematic of a layer

To solve the thermal loading problem, one has to make use of boundary conditions at the bottom surface. For instance, we suppose that $\theta^{(N)} = 0$, which corresponds to zero temperature at the bottom surface of the solid, and we obtain

$$V^{(0)} = \frac{M_{12}}{M_{22}} \left(\phi^{(0)}/\rho\right)$$

Thus, one can finally write

$$V^{(0)} = F(\rho)\, \phi^{(0)}$$

where F is the solid transfer function.
Using the inverse Fourier transform, the temperature field can be obtained for any given thermal loading and especially for the case of heat acting over a square area. Indeed, the transfer function F is the Fourier transform of the function T mentioned in Eq.5.2. Finally, to reduce the computation time, the FFT technique is used and only the transfer function is computed instead of the function T.
As an example, a two-layered solid is illustrated in Fig.5.4. The solid height is fixed to $1mm$ and the first (resp. second) layer conductivity is equal to $\kappa_1 = 10\, Wm^{-1}K^{-1}$ (resp. $\kappa_2 = 50\, Wm^{-1}K^{-1}$). The

first layer thickness h varies from 100 to 500 μm. About boundary conditions, a heat flux ϕ_0 is applied to a square zone whose size is $a = 200\mu m$ and centered at the top surface. Fig.5.5 shows the surface temperature profile for $Y = 0$, $Z = 0$ and X ranging from $-100\mu m$ to $100\mu m$. One can see in this figure, the perfect accordance between results obtained from the present method and those of the Finite Element Method (FEM). One can also notice the increase of temperature with the increase of the first layer thickness.
Figs 5.6-5.7 show the temperature field in depth for $h = 100$ μm and $h = 200$ μm. One can see the differences in temperature levels especially in the near-surface zone. The corresponding flux lines are also shown in Figs 5.8-5.9.

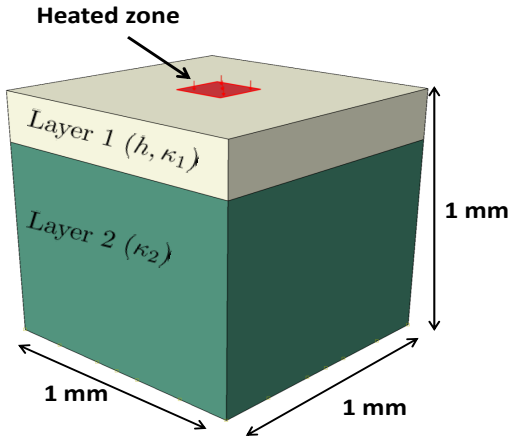

Figure 5.4: Schematic of surface heating problem. The solid contains two layers.

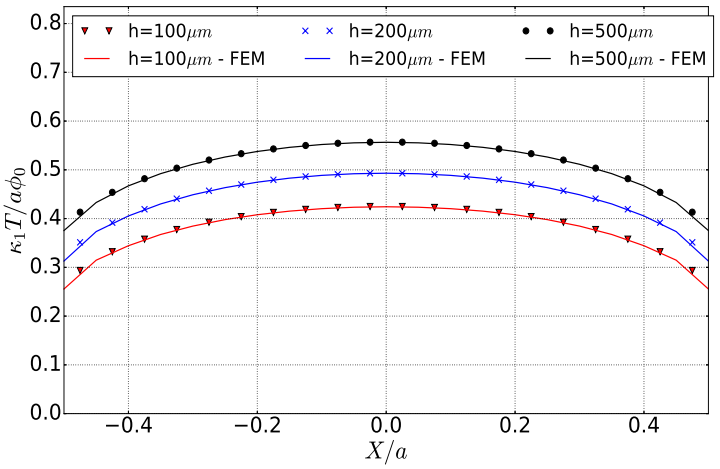

Figure 5.5: Temperature profile for the case : $\kappa_1 = 10\,Wm^{-1}K^{-1}$, $\kappa_2 = 50\,Wm^{-1}K^{-1}$ - Comparison with FEM calculations

Now that the surface heating solving technique has been detailed, the thermal contact problem solving

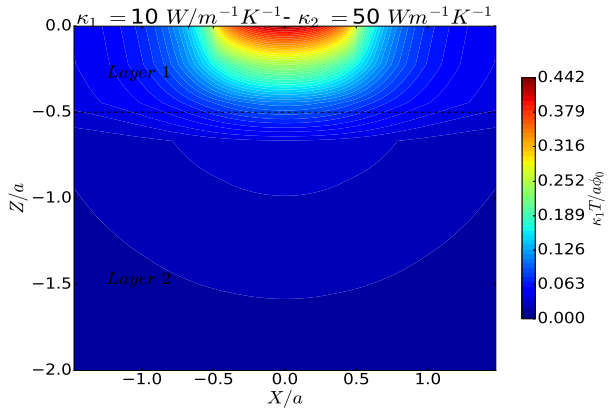

Figure 5.6: Sub-surface temperature field for $h = 100\mu m$

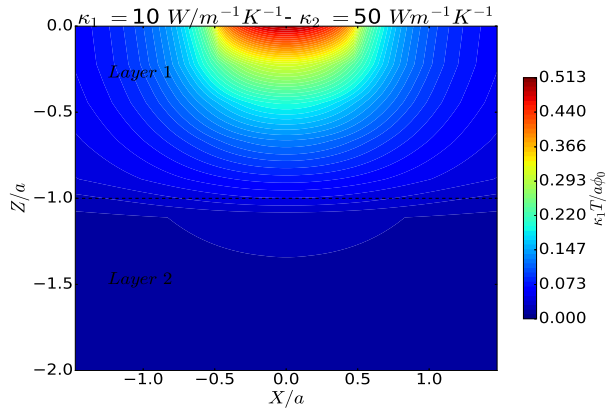

Figure 5.7: Sub-surface temperature field for $h = 200\mu m$

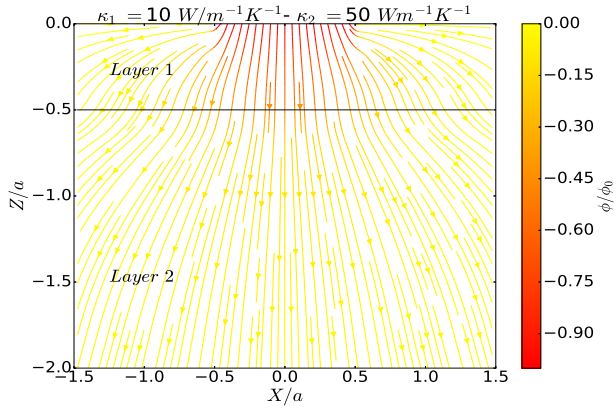

Figure 5.8: Heat flux lines for $h = 100\mu m$

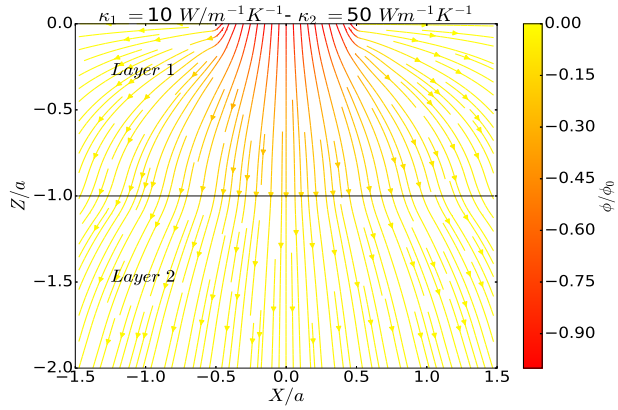

Figure 5.9: Heat flux lines for $h = 200\mu m$

strategy is presented in the next section.

5.4 Thermal contact of multi-layered solids

5.4.1 Contact area definition

Before tackling the thermal contact problem, we would first give a brief insight of contact area definition. The real contact area depends on the mechanical loads maintaining solids in contact and their elastic properties. The transfer matrix technique has been used to solve the loading problem of multi-layered solids [Singh(1986), Ernian(1996), Waddad *et al.*(2017[a])] in a similar way to the thermal problem. Within this framework, the normal displacement U is expressed as a discrete convolution of the contact pressure p and a special function L which is obtained from the Fourier transform of the transfer function.
Solving the contact mechanics problem is to solve an equation of the type

$$p * L = \delta$$

where δ is the prescribed displacement field which depends on surface roughness and boundary conditions. The contact pressure must satisfy the condition $p \geq 0$ for all the assumed contacting points. Once found,

the contact area can be defined.

5.4.2 Thermal contact problem

Considering ϕ_1 (resp. ϕ_2) the heat flowing through the solids S_1 (resp. S_2), we have

$$\phi_1 + \phi_2 = 0$$

Assuming the small-slope hypothesis, the contact surfaces can be simplified to flat surfaces with multiple contact spots. As we have presented in the earlier sections, the surface temperature of both solids are expressed as a discrete convolution of the applied heat, thus we have

$$\theta_1 = T_1 * \phi_1 + \theta_{l1}$$

$$\theta_2 = T_2 * \phi_2 + \theta_{l2}$$

where θ_i is the surface temperature and T_i is the temperature function of S_i $(i = 1, 2)$.
In order to solve the contact problem, an assumption have to be made on the continuity of the temperature field at the interface. Indeed, the continuity of temperature means that temperatures are equal in the contact zone $\theta_1 = \theta_2$, leading to the following equation

$$(T_1 + T_2) * \phi_1 = \theta_{l2} - \theta_{l1} \tag{5.7}$$

However, it is well known that, even at this scale, the temperature is not continuous. Indeed, by looking at much smaller scales, a contact zone is composed from multiple contact zones and also wear debris that are circulating at the interface. The discontinuity of temperature can be inserted in the model by defining a local contact resistance expressed by a function f that relies the gap between surface temperatures θ_1 and θ_2 to the flux ϕ_1

$$\theta_2 - \theta_1 = f(\phi_1)$$

Thus, we have in this case

$$(T_1 + T_2) * \phi_1 + f(\phi_1) = \theta_{l2} - \theta_{l1} \tag{5.8}$$

Solving the thermal contact problem consists in finding the heat flux ϕ_1 flowing in the solid S_1 and satisfying Eq.(5.8). Once calculated, the total thermal contact conductance per unit area is given by

$$K_t = \frac{\Phi_1}{S \,.\, (\theta_{l2} - \theta_{l1})} \tag{5.9}$$

where S is the surface area and Φ_1 is the total heat flowing through the surface of S_1

$$\Phi_1 = \iint_S \phi_1 \mathrm{d}S$$

The interface thermal conductance K_i can thus be deduced from K_t by

$$K_i = \frac{1}{\frac{1}{K_t} - \frac{1}{K_p}}$$

where K_p is the thermal conductance which corresponds to the perfect contact case.
With regard to the function f, the simplest way is to consider it linear $f(\phi_1) = R\,\phi_1$, with R the local thermal resistance. The value of R depends on many parameters such as material properties, friction and wear rate. In this study, we will consider it as a parametric coefficient which will be varied to evaluate its effect on the total thermal conductance.

5.4.3 Solving method

The convolution Eq.(5.8) is equivalent to a matrix equation that can reads

$$\mathbf{T}\boldsymbol{\Phi}_1 = \boldsymbol{\Theta} \tag{5.10}$$

In order to solve Eq.(5.10), the contact problem is transformed into a minimization problem by defining the objective function F

$$F\left(\boldsymbol{\Phi_1}\right) = \frac{1}{2}\,{}^t\boldsymbol{\Phi}_1\mathbf{T}\boldsymbol{\Phi}_1 - {}^t\boldsymbol{\Phi}_1\boldsymbol{\Theta} \tag{5.11}$$

Besides, from the contact area, an additional equation is obtained, which is of the type

$$\mathbf{P}\boldsymbol{\Phi}_1 = \mathbf{0} \tag{5.12}$$

The matrix $\mathbf{P}$ defines the contact constraints prescribed by the real contact area geometry. The shape of $\mathbf{P}$ is (N_p, Nr), with N_r the number of surface squares which are in contact. In this matrix, the entry 1 corresponds to a non-contacting point while the entry 0 is for those in contact. This additional equation defines the contact constraints.
Using an iterative method, for example Newton or the conjugate gradient, the minimization problem is performed and heat and surface temperature can be calculated. It should be noted that the same technique is used to solve the contact mechanics problem. For more details, the reader may refer to these works [Peng and Bhushan(1996), Cai and Bhushan(2005), Gallego *et al.*(2010)].
In the following, results of this approach are illustrated and compared to finite element calculations. A parametric study is also performed so that the impact of contact interface and solid layers is shown.

5.5 Numerical example

5.5.1 Model presentation

In this section, we consider two elastic solid cubes in normal contact (see Fig.5.10). A rough interface is considered between the two cubes and their volume is $1mm^3$. The contact surface is discretized into 150×150 elements. Hence, the unit square dimensions are $6.66 \times 6.66\mu m^2$. This size is sufficient for the considered scale of roughness. Indeed, a comparison has been performed with this size and a coarser one ($10 \times 10\mu m^2$) and the results were the same.
The first solid is made from a highly conductive material, noted here S_2, and its properties are summarized in Tab.5.1. The other one, noted her S_1, is a two-layered solid of which the physical properties are varied in this study. Indeed, several case studies are done with the purpose of analyzing the influence of solid layers on the thermal conductance.
Roughness is obtained from numerical surface generation techniques which are based on surface spectrum[Persson *et al.*(2002)]. Indeed, a random rough surface can be generated with any given spectral density. Here, the spectral density is a power law, of which the fractal dimension is 0.8. The cutoff wave vectors are 2 and 10. In this work, the roughness profile has been fixed for the first case studies. The root mean square (RMS) of the considered surface is 6 μm. The effect of roughness will be investigated later.
In this simulation, the solid S_2 is moved normally against the other cube with a motion δ_2. The bottom face of the second cube is fixed $\delta_1 = 0$. Once contact occurs, different temperatures are prescribed at both solids extremities (see Fig.5.10). For instance, in this study, we choose $\theta_{l1} = 0°C$ and $\theta_{l2} = 1°C$. The lateral bounds are free from any prescribed heat conditions, thus no heat goes through these faces. Thermal dilations are not considered in this study.

Two procedures are compared : The first one is the present model strategy and the second one is the Finite Element Method (FEM). In what follows, several case studies are presented. The local thermal resistance is not considered except if we clearly mention it in the case study description. In the FEM model, 5.10^5 elements are used to discretize the multi-layered solid.

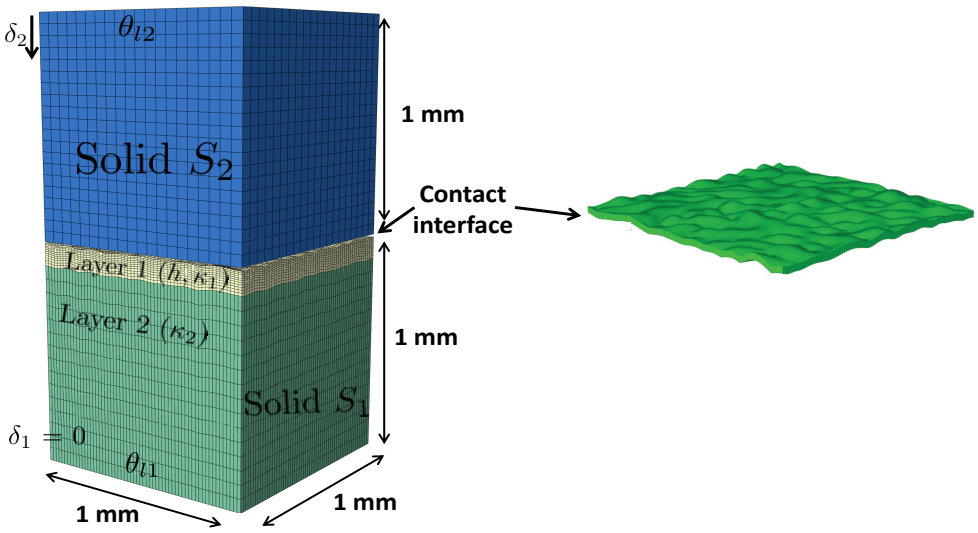

Figure 5.10: Schematic of the studied configuration. Two solid cubes in contact and surface roughness is generated numerically

	$E_s\ (GPa)$	ν_s	$\kappa_s\,(Wm^{-1}K^{-1})$
Solid S_2	220	0.33	50

Table 5.1: Elastic and thermal properties of Solid S_2

5.5.2 An illustrative case study

An illustrative example is presented in this paragraph. The considered solid properties are summarized in Tab.5.2. As we can see, it is the case where the two layers have the same physical properties.

$E_1\ (GPa)$	$E_2\ (GPa)$	$\kappa_1\,(Wm^{-1}K^{-1})$	$\kappa_2\,(Wm^{-1}K^{-1})$	$h\,(\mu m)$
4	4	10	10	500

Table 5.2: Elastic and thermal properties of the two-layered solid in the first study

Before analyzing the results of the thermal contact study, a brief overview is provided to highlight the contact mechanics results. For $\delta_2 = 10\ \mu m$, the contact pressure (resp. the normal displacement) are presented in Fig.5.11 (resp. Fig.5.12). From these figures, we can see the distribution and the geometry of contact zones. The contact is mainly concentrated on some asperities. At the scale of an asperity, the

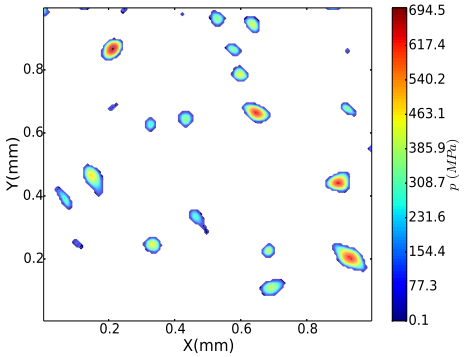

Figure 5.11: Contact pressure distribution for solid S_1 and $\delta_2 = 10\mu m$

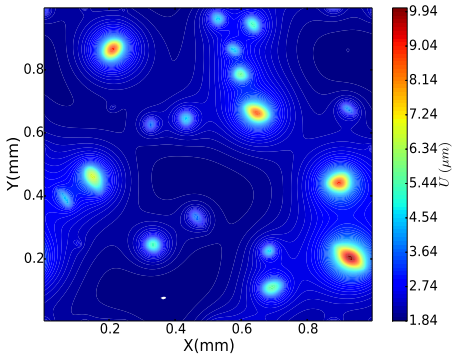

Figure 5.12: Normal displacement for solid S_1 and $\delta_2 = 10\mu m$

contact shape is almost elliptic. The real contact area is very small compared to the apparent one (less than 2%).
With regard to the thermal contact, the evolution of the total conductance with contact pressure is shown in Fig.5.13 for the two considered procedures (Finite Element Method "FEM" and the "present model"). The two predicted curves are in good agreement. The curve slope decreases while the pressure is increasing. A high slope corresponds to the case of small contact pressures and contact area. In this case, there is few contacting asperities and thus the heat is concentrated on these asperities. Increasing the contact area leads to a decrease in heat concentration.

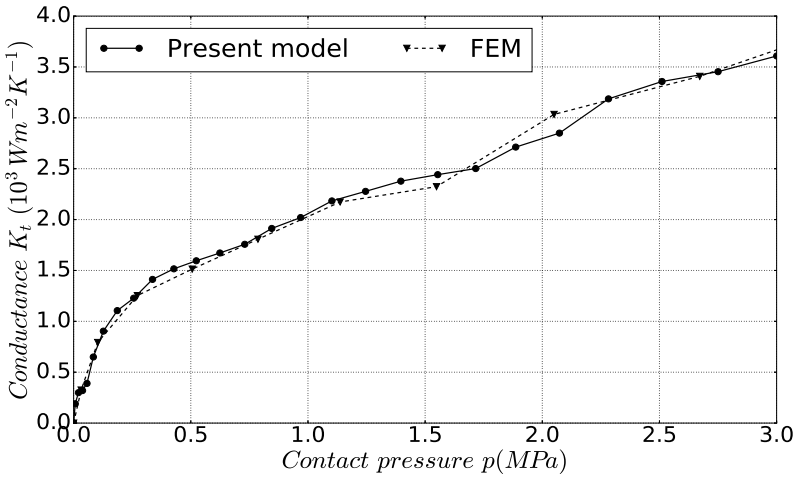

Figure 5.13: Real contact area evolution with contact pressure for the illustrative case study : $\kappa_1 = \kappa_2 = 10\,Wm^{-1}K^{-1}$

The temperature distribution for this case study is illustrated in Fig.5.15 for the two-layered solid and Fig.5.14 for solid S_2. The temperature is constant within contact zones and is equal to 0.83. Also, since solid S_2 is the hot one, contact zones are thus the coldest ones within it, and inversely, contact zones in the other cube are the hottest ones. Between the two surfaces, we can also see the discrepancy in the temperature gradient. Indeed, the temperature in solid S_2 is varying from 0.90 to 0.83 $°C$ which is much

smoother than the second solid where temperature is ranging between 0.83 and 0.53 $°C$. This difference is essentially due to the relatively weak conductivity of the second solid.
Now, let us take a look at the sub-surface temperature and heat flux lines. Fig.5.16 shows the temperature field for the plane associated to axis 1 (see Figs.5.14-5.15 to see the localization of this axis). This plane cuts the surface at two contact zones. As we can see, the same remark concerning the gradient of temperature is observable in this figure. In this plane, contact is made only in two zones. On the left of the figure ($X \leq 0.1mm$), a temperature elevation is observed at the surface. This elevation is due to another contact zone which is not visible in this cut plane. In Fig.5.17, flux lines are shown for the same cut plane. Heat is flowing, in the direction normal to surface, through contact zones from the hottest solid to the coldest one. The constriction of the flux lines is also observable near to contact zones. Far from the two contact zones, we can also see the curved flux lines from the other contact zones which are not visible in this plane.
As regards the computational time, it has been reduced considerably. The FEM calculations are very slow comparing to the present model strategy. Indeed, the thermal problem resolution has been done within few minutes for both strategies because the contact area is fixed for this step. But the contact mechanics problem has been solved within 5 hours with the FEM strategy whereas this time was approximately 20 min for the present model.
Now that the illustrative case has been presented, the following presents a parametric study with the aim to study the effect of solid layers, surface roughness and local thermal resistance on the total thermal conductance. In most cases, results from the present model are compared to FEM results with the aim to evaluate the efficiency of the model.

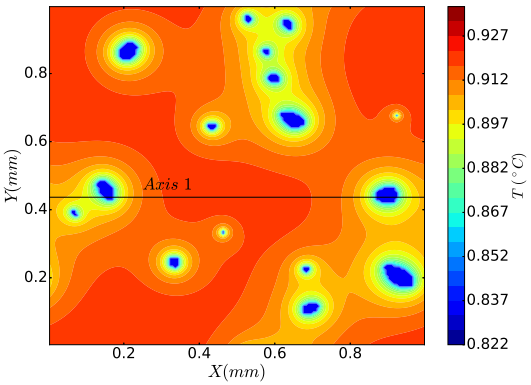

Figure 5.14: Surface temperature of solid S_2

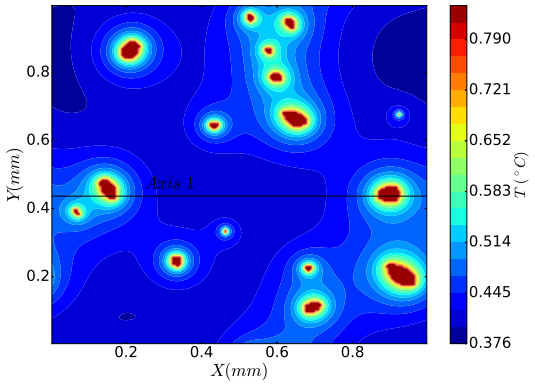

Figure 5.15: Surface temperature of the two-layered solid S_1

5.5.3 Parametric study

- Influence of the first layer thermal properties

In this case study, the thermal properties are varied while the elastic parameters are kept fixed. Tab.5.3 presents the considered parameters for this study. As we can see, the first layer conductivity is decreased from 10 to 2.5 $Wm^{-1}K^{-1}$ while the second layer conductivity is fixed at 10 $Wm^{-1}K^{-1}$. The result analysis is devoted to the contact pressure p relationship with the total thermal conductance K_t (see Fig.5.18).
At first sight, FEM results fit well with the present model predictions. Also, the decrease of the first layer

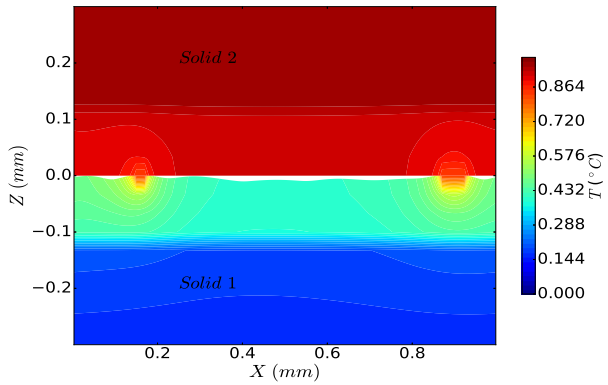

Figure 5.16: Temperature field in the cross-section: axis 1

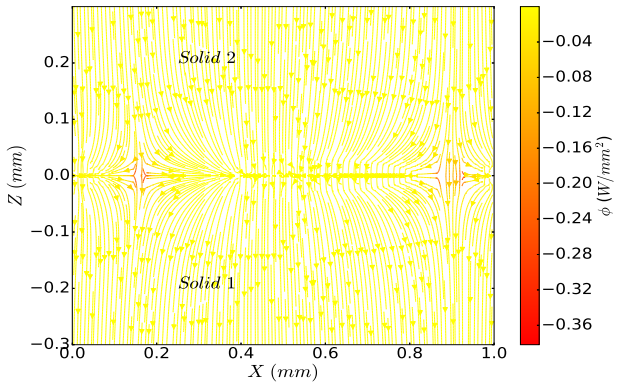

Figure 5.17: flux lines in the cross-section: axis 1

	$E_1\ (GPa)$	$E_2\ (GPa)$	$\kappa_1\,(Wm^{-1}K^{-1})$	$\kappa_2\,(Wm^{-1}K^{-1})$	$h\,(\mu m)$
Case 1	4	4	10	10	-
Case 2	4	4	5	10	500
Case 3	4	4	2.5	10	500

Table 5.3: Elastic and thermal properties of the two-layered solid in the first study

conductivity leads to the decrease of the thermal conductance. In Tab.5.4, K_t values for a pressure equal to $3MPa$ are presented for the 3 cases. The decrease of the conductance is followed by an increase of surface temperature T_s. This temperature corresponds to the one reached in contact zones and is constant. Comparing T_s to T_p the surface temperature of the perfect contact, we can see that the temperature reached in contact zones remains the same despite roughness. This is due to the fact that temperature is prescribed at both solids extremities.
It is of interest to compare K_t to the thermal conductance corresponding to the perfect contact case K_p which is independent of the pressure. As we can see, the ratio K_t/K_p is decreasing from 0.45 to 0.33. Thus we can deduce from this study that the thermal conductance is mainly influenced by the conductivity of the first layer.

	κ_1/κ_2	$K_t\ (10^3\,Wm^{-2}K^{-1})$	$T_s\ (°C)$	$K_p\ (10^3\,Wm^{-2}K^{-1})$	$T_p\ (°C)$	K_t/K_p
Case 1	1	3.75	0.83	8.33	0.83	0.45
Case 2	0.5	2.24	0.88	5.88	0.88	0.38
Case 3	0.25	1.24	0.93	3.70	0.93	0.33

Table 5.4: Summarized results for the present case study : the effect of the first layer thermal properties is highlighted.

- Influence of the first layer thermal and elastic properties

In the last paragraph, only thermal properties were changed from one case to another. In the present case, both thermal and elastic properties of the first layer are decreased in such a way that the ratios

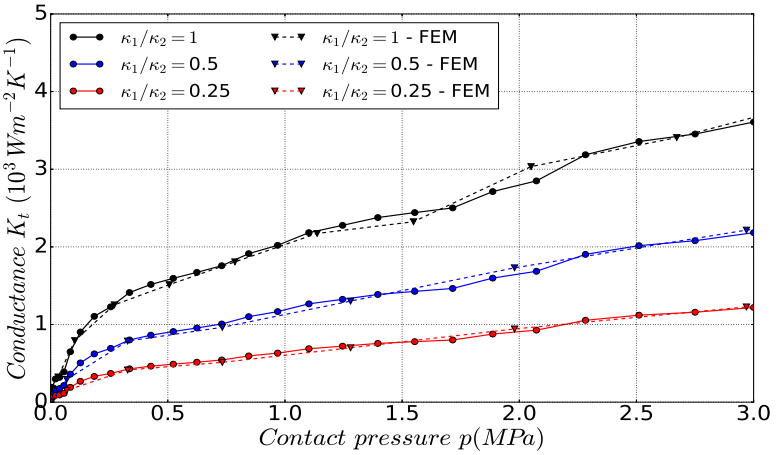

Figure 5.18: Thermal conductance evolution with contact pressure for the present case study : $\kappa_2 = 10\,Wm^{-1}K^{-1}$, $h = 500\mu m$ and $E_2 = E_1 = 4GPa$

κ_1/κ_2 and E_1/E_2 are kept equal. The different parameters are summarized in Tab.5.5.

	$E_1\ (GPa)$	$E_2\ (GPa)$	$\kappa_1\,(Wm^{-1}K^{-1})$	$\kappa_2\,(Wm^{-1}K^{-1})$	$h\,(\mu m)$
Case 1	4	4	10	10	-
Case 2	2	4	5	10	500
Case 3	1	4	2.5	10	500

Table 5.5: Elastic and thermal properties of the two-layered solid in the first study

As is shown in Fig.5.19, the reduction of κ_1/κ_2 leads to a decrease of K_t. Comparing to the last case study, the reduction of K_t is less but is still significant. This different behavior is mainly due to the variation of the first layer elastic modulus E_1. Indeed, the contact pressure with real contact area evolution has been modified and thus the contact area is not the same for the three cases. In Fig.5.20, this evolution is shown for the three cases. One can see that the slope of this evolution is almost constant and increases while the first layer modulus is decreasing (from 1% to 4.5%). Moreover, this evolution-slope is almost inversely proportional to the first layer modulus. In other words, with respect to contact area, the pressure level is fully controlled by the first layer modulus.
Therefore, the ratio K_t/K_p was affected by the mechanical properties of the first layer(see Tab.5.6). Comparing to the last study, we can see how these properties influenced drastically the thermal conductance by affecting the contact area. Additionally, as regards surface temperature within contact zones, the latter is only affected by boundary conditions and material thermal properties.
At last, one have to keep in mind that ratios κ_1/κ_2 and E_1/E_2 are kept equal in this study. One should expect different behaviors if these ratios were different.

- Influence of the first layer thickness

In the two last studies, the influence of material properties has been studied. In this case study, thermal and elastic properties are kept fixed and the first layer thickness h is varied from 100 to 500 μm (see Tab.5.7). Also the ratios κ_1/κ_2 and E_1/E_2 are both kept fixed at 0.25.

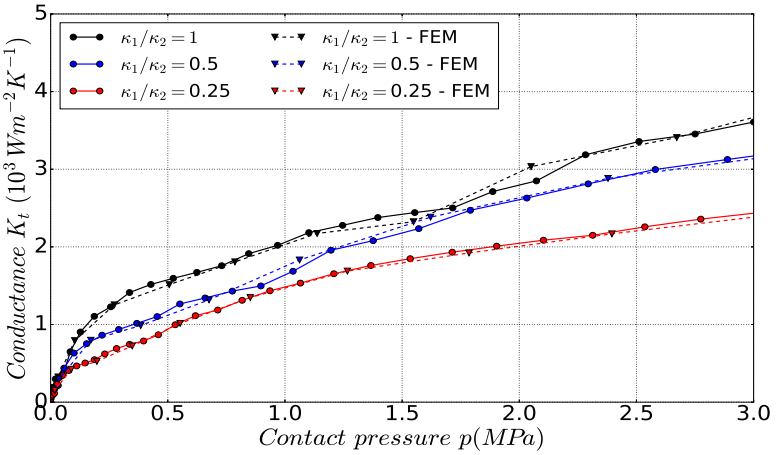

Figure 5.19: Thermal conductance evolution with contact pressure for the present case study : $\kappa_2 = 10\,Wm^{-1}K^{-1}$, $h = 500\mu m$ and $\kappa_1/\kappa_2 = E_1/E_2$

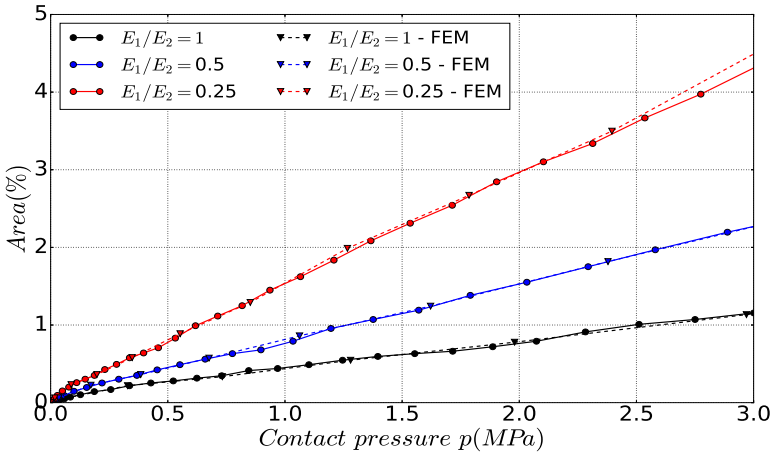

Figure 5.20: Real contact area evolution with contact pressure for the present case study : $\kappa_2 = 10\,Wm^{-1}K^{-1}$, $h = 500\mu m$ and $E_1/E_2 = \kappa_1/\kappa_2$

Similarly to the last cases, the evolution of K_t with pressure p is illustrated in Fig.5.21. Once again, FEM results match the present model results. Tab.5.8 shows different results for the three considered thicknesses. One can see that with increasing h, the conductance K_t is decreasing and surface temperature is increasing. This evolution was expected since the first layer conductivity is weaker than that of the second layer. The ratio K_t/K_p is also increasing with h. This behavior is totally linked to solids elastic properties and the first layer thickness.
From these studies, we can see how the properties and the thickness of the solid layers affect the thermal conductance. With respect to contact pressure, elastic properties have an impact on the real contact area which subsequently affects the conductance.

	$\kappa_1/\kappa_2\ (=E_1/E_2)$	$K_t\ (10^3\,Wm^{-2}K^{-1})$	$T_s\ (°C)$	$K_p\ (10^3\,Wm^{-2}K^{-1})$	$T_p\ (°C)$	K_t/K_p
Case 1	1	3.75	0.83	8.33	0.83	0.45
Case 2	0.5	3.20	0.88	5.88	0.88	0.54
Case 3	0.25	2.46	0.93	3.70	0.93	0.66

Table 5.6: Summarized results for the second case study : the effect of the first layer properties is highlighted.

	$E_1\ (GPa)$	$E_2\ (GPa)$	$\kappa_1\,(Wm^{-1}K^{-1})$	$\kappa_2\,(Wm^{-1}K^{-1})$	$h\,(\mu m)$
Case 1	1	4	2.5	10	100
Case 2	1	4	2.5	10	200
Case 3	1	4	2.5	10	500

Table 5.7: Elastic and thermal properties of the two-layered solid in the second study

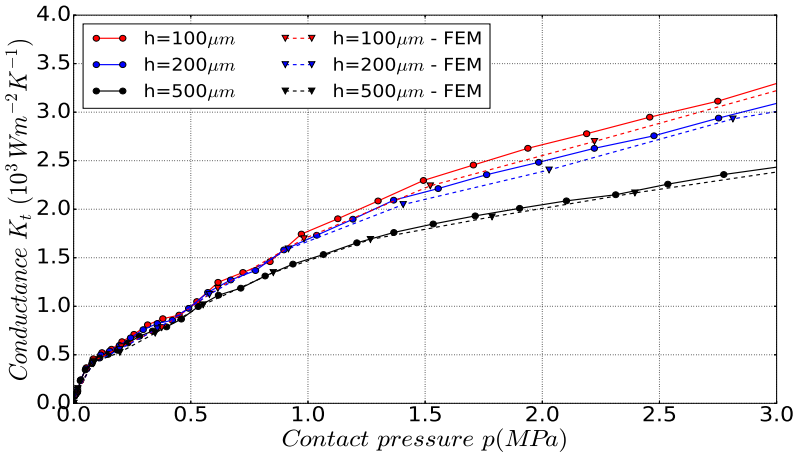

Figure 5.21: Thermal conductivity evolution with contact pressure for the case : $\kappa_1 = 2.5\,Wm^{-1}K^{-1}$, $E_1 = 1\,GPa$ and $E_1/E_2 = \kappa_1/\kappa_2 = 0.25$

	$h(\mu m)$	$K_t\ (10^3\,Wm^{-2}K^{-1})$	$T_s\ (°C)$	$K_p\ (10^3\,Wm^{-2}K^{-1})$	$T_p\ (°C)$	K_t/K_p
Case 1	100	3.27	0.87	6.67	0.87	0.49
Case 2	200	3.10	0.89	5.55	0.89	0.55
Case 3	500	2.46	0.93	3.70	0.93	0.66

Table 5.8: Summarized results for the present case study : the effect of the first layer thickness is highlighted.

- Influence of roughness

The present paragraph presents results concerning 10 random rough surfaces considering 2 configurations (see Tab.5.9). The elastic properties have been fixed at $4GPa$ for both layers. The surfaces have been generated with fractal techniques [Persson *et al.*(2002)]. The fractal dimension has been slightly varied

from one sample to another and the same cutoff wave vectors have been conserved (2 and 10). Thus, the scale of asperities does not change for all the studied samples while the root mean square (RMS) varies from one case to another. The main objective of this case study is to evaluate the influence of solid layers on the thermal conductance through many surface topographies.
In Fig.5.22, are shown the evolution of K_t for different surface samples. For both cases, the continuous line corresponds to the averaged response, which is computed with a linear interpolation. The gap between the two lines is conserved for the different samples. For $p = 3MPa$, the evolution of K_t with the RMS of the studied samples is shown in Fig.5.23. One can see that, for both cases, the conductance decreases slightly with the increase of surface RMS. This is essentially due to the fact that the real contact area decreases with the increase of the RMS, with respect to contact pressure (see Fig.5.24).

	$E_1\ (GPa)$	$E_2\ (GPa)$	$\kappa_1\,(Wm^{-1}K^{-1})$	$\kappa_2\,(Wm^{-1}K^{-1})$	$h\,(\mu m)$
Case 1	4	4	10	10	500
Case 2	4	4	5	10	500

Table 5.9: Elastic and thermal properties of the two-layered solid considered is this case study

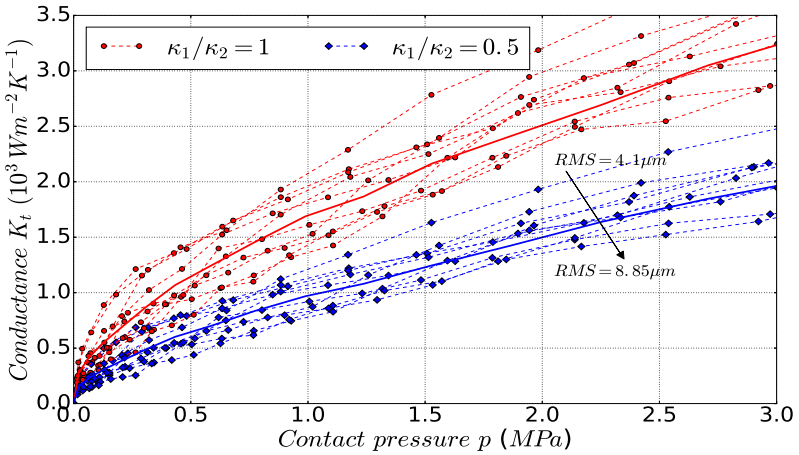

Figure 5.22: Thermal conductance evolution with contact pressure for 10 surface samples. Material properties are those of cases 1 and 2

- Influence of the local thermal resistance

Now that the effect of solid layers and roughness have been discussed, it is interesting to investigate the influence of a local thermal resistance. For this purpose, the first illustrative case study is considered (see section 5.5.2) and a thermal resistance R, ranging from 0 to $10^{-6}\,m^2K/W$, is added. Note that a local resistance equal to $10^{-6}\,m^2K/W$ corresponds to a local conductance equal to $10^6\,Wm^{-2}K^{-1}$. This value is 1000 times higher than the effective conductance of the bulk material, as can be seen in the first case study (see Fig.5.13). In Fig.5.25 the evolution of the total conductance with contact pressure is presented. One can see that the impact of the resistance is significant. The increase of R leads undoubtedly to a decrease of the total conductance. At this point of the study, we cannot link the value of this resistance to a real contact state. The objective here was only to introduce a gap between the contacting solids

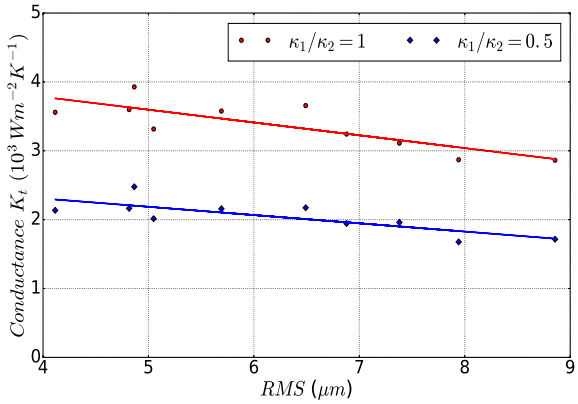

Figure 5.23: Evolution of the thermal conductance with RMS for $p = 3MPa$ using 10 surface samples. The continuous lines represent the interpolation between the different points

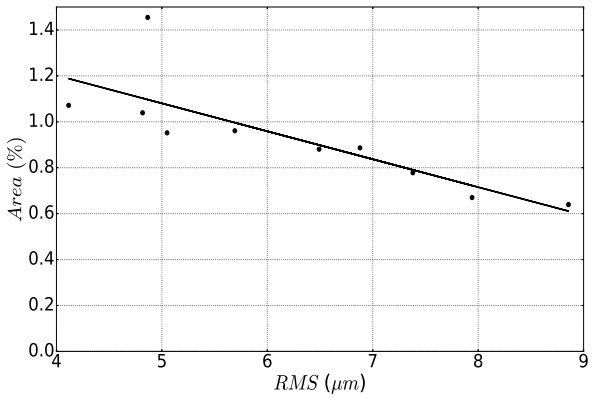

Figure 5.24: Evolution of the contact area with RMS σ for $p = 3MPa$ using 10 surface samples. The continuous line represents the interpolation between the different points

surface temperatures and identify its effect on heat conduction. This gap could be a consequence of a lower scale imperfect conduction which, for instance, can result from the presence of wear debris. As we can see in the last figure, the impact of the local resistance can be no less important than the presence of a thin layer near to the interface.

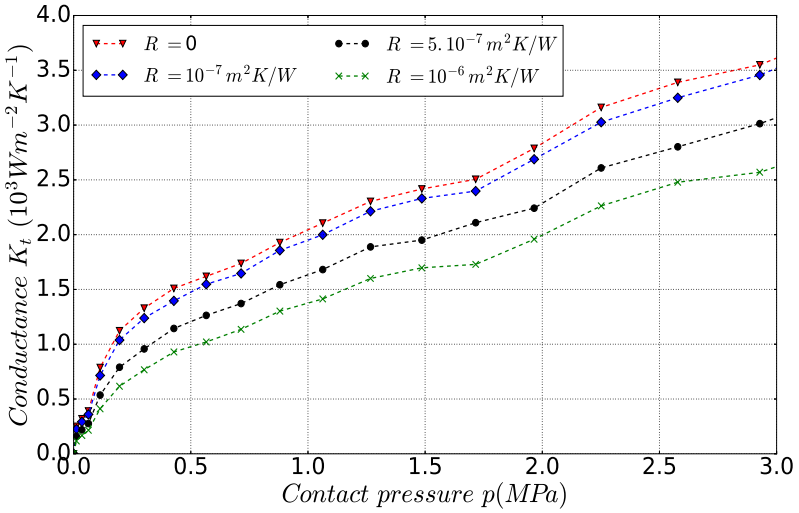

Figure 5.25: Evolution of the thermal conductance with contact pressure for different values of the local thermal resistance.

Conclusion

In this work, the heat conduction between multi-layered solids considering roughness has been studied. For this purpose, the Fourier transform has been used to express surface temperature as a function of

surface heating. Using the same technique, the contact area is defined by solving the contact mechanics problem. Afterwards, the thermal contact problem is expressed as a linear system of which the unknown is the heat flowing through the contact interface. This system is numerically solved with optimization techniques and the obtained results provide surface temperature and thermal conductance considering roughness and solid layers.
As a case example, the contact of a two-layered solid with a layered one has been studied. Through various illustrations, the results of the present model have been compared to Finite Element calculations and a good agreement has been found between the two methods. Furthermore, the computational time has been reduced significantly. For the FEM calculations, the computational time is about $5h$ whereas it does not exceed 30 min for the present model.
Moreover, the studied cases demonstrate the great impact of roughness, solid-layers and local thermal resistance on the thermal conductance. It is shown that the elastic properties and roughness define the contact area distribution. Therefore, in addition to layers conductivities, the thermal behavior is affected by all of this parameters. In particular, reducing the first layer elastic modulus leads to an increase of both the contact area and the thermal conductance. However, if the modulus decrease is followed by a conductivity decrease, the thermal conductance can decrease depending on the ratio between layers modulus and conductivities.
Furthermore, several surface samples have been studied. The effect of roughness, quantified by the standard deviation, has been presented. It has been shown that increasing the standard deviation leads to a diminution of contact area and thermal conductance, with respect to contact pressure.
Concerning the local thermal resistance, its effect has been highlighted. From a physical point of view, more tools are needed to quantify properly this quantity.
Finally, it should be noted that some improvements of the present model can be done, in particular by considering thermoelastic deformations which can affect contact area. Furthermore, the quantification of the local thermal resistance has to be addressed in future works. Also, the consideration of interface convection will also represent an interesting perspective for this work.

Acknowledgments

The present research work has been supported by the International Campus on Safety and Intermodality in Transportation, the Hauts-de-France Region, the European Union, the Regional Delegation for Research and Technology, the Ministry of Higher Education and Research, the French National Research Agency (ANR COMATCO), and the National Center for Scientific Research. The authors gratefully acknowledge these institutions for their support.

Bibliography

[Bahrami *et al.*(2005)] Bahrami, M., Yovanovich, M. M., & Culham, J. R. *Thermal contact resistance at low contact pressure: Effect of elastic deformation.* International Journal of heat and mass transfer, 2005, 48(16), 3284-3293.

[Bush *et al.*(1975)] Bush, A., Gibson, R. & Thomas, T. *The elastic contact of a rough surface.* Wear, Elsevier, 1975, 35, 87-111

[Cai and Bhushan(2005)] Cai, Shaobiao & Bhushan, Bharat *A numerical three-dimensional contact model for rough, multilayered elastic/plastic solid surfaces.* Wear, Elsevier, 2005, 259, 1408-1423.

[Carslaw and Jaeger(1959)] Carslaw, H. S., & Jaeger, J. C.*Conduction of heat in solids.* Oxford: Clarendon Press, 1959

[Ciavarella *et al.*(2006)] Ciavarella, M., Delfine, V. & Demelio, G. *A re-vitalized Greenwood and Williamson model of elastic contact between fractal surfaces.* Journal of the Mechanics and Physics of Solids, Elsevier, 2006, 54, 2569-2591

[Cooper *et al.*(1969)] Cooper, M. G., Mikic, B. B., & Yovanovich, M. M. *Thermal contact conductance.* International Journal of heat and mass transfer, 1969, 12(3), 279-300.

[Fieberg and Kneer(2008)] Fieberg, C., & Kneer, R. *Determination of thermal contact resistance from transient temperature measurements.* International Journal of heat and mass transfer, 2008, 51(5), 1017-1023.

[Ernian(1996)] Ernian, Pan . *Static response of a transversely isotropic and layered half-space to general surface loads.* Physics of the Earth and Planetary Interiors, 1989, 54, 353–363.

[Gallego *et al.*(2010)] Gallego, L., Nelias, D. & Deyber, S. *A fast and efficient contact algorithm for fretting problems applied to fretting modes I, II and III.* Wear, 2010, 268, 208–222.

[Greenwood and Williamson(1966)] Greenwood, J. & Williamson, J. *Contact of nominally flat surfaces.* Proceedings of the Royal Society of London. Series A. Mathematical and Physical Sciences, The Royal Society, 1966, 295, 300-319

[Johnson(1987)] Johnson, K. L. *Contact mechanics.* Cambridge university press, 1987

[McWaid and Marschall(1992)] McWaid, T., & Marschall, E. *Thermal contact resistance across pressed metal contacts in a vacuum environment.* International Journal of heat and mass transfer, 1992, 35(11), 2911-2920.

[Mikic(1974)] Mikić, B. B. *Thermal contact conductance; theoretical considerations.* International Journal of heat and mass transfer, 1974, 17(2), 205-214.

[Peng and Bhushan(1996)] Peng, Wei & Bhushan, Bharat *Three-dimensional contact analysis of layered elastic/plastic solids with rough surfaces*. Wear, Elsevier, 2001, 249, 741-760.

[Persson *et al.*(2002)] Persson, B., Bucher, F. & Chiaia, B. *Elastic contact between randomly rough surfaces: comparison of theory with numerical results*. Physical Review-Series B-, American Physical Society, 2002, 65, 184106

[Sadowski and Stupkiewicz(2010)] Sadowski, P., & Stupkiewicz, S. *A model of thermal contact conductance at high real contact area fractions*. Wear , 2010, 268(1), 77-85.

[Salgon *et al.*(1997)] Salgon, J. J., Robbe-Valloire, F., Blouet, J., & Bransier, J. *A mechanical and geometrical approach to thermal contact resistance*. International Journal of heat and mass transfer, 1997, 40(5), 1121-1129.

[Salti and Laraqi(1999)] Salti, B., & Laraqi, N. *3-D numerical modeling of heat transfer between two sliding bodies: temperature and thermal contact resistance*. International Journal of Heat and Mass Transfer, 1999, 42(13), 2363-2374.

[Singh(1986)] Singh, Sarva Jit *Static deformation of a transversely isotropic multilayered half-space by surface loads*. Physics of the earth and Planetary Interiors, Elsevier, 1986, 4, 263–273.

[Temizer and Wriggers(2010)] Temizer, I., & Wriggers, P. *Thermal contact conductance characterization via computational contact homogenization: a finite deformation theory framework*. International journal for numerical methods in engineering, 2010, 83(1), 27-58.

[Temizer(2011)] Temizer, I., *Thermomechanical contact homogenization with random rough surfaces and microscopic contact resistance*. Tribology International, 2011, 44(2), 114-124.

[Waddad *et al.*(2016)] Waddad, Y. , Magnier, V. , Dufrénoy, P. & De Saxcé, G. *A multiscale method for frictionless contact mechanics of rough surfaces*. Tribol. int., 2016, 96, 109-121.

[Waddad *et al.*(2017)] Waddad, Y. , Magnier, V. , Dufrénoy, P. & De Saxcé, G. *A new contact model for multi-layered solids with rough surfaces*. In preparation.

[Willner(2008)] Willner, K. *Fully coupled frictional contact using elastic halfspace theory*. Journal of Tribology, American Society of Mechanical Engineers, 2008, 031405, 1–8.

[Yovanovich(2005)] Yovanovich, M. M. *Four decades of research on thermal contact, gap, and joint resistance in microelectronics*. IEEE transactions on components and packaging technologies, 2005, 28(2), 182-206.

[Yue(1996)] Yue, Z. Q. *Elastic field for eccentrically loaded rigid plate on multilayered solids*. International journal of solids and structures, 1996, 33, 4019-4049.

[Zavarise *et al.*(1992)] Zavarise, G., Wriggers, P., Stein, E. & Schrefler, BA. *Real contact mechanisms and finite element formulation - a coupled thermomechanical approach*. International Journal for Numerical Methods in Engineering, Wiley Online Library, 1992, 35, 767-785

[Zheng *et al.*(2014)] Zheng, J., Li, Y., Wang, L., & Tan, H. *An improved thermal contact resistance model for pressed contacts and its application analysis of bonded joints*. Cryogenics, 2014, 61, 133-142.

Transition

In the previous chapter, stationary heat conduction has been analyzed in a static contact. The role of roughness and a gradient of properties has been highlighted.
In braking systems, the contact interface is the place where kinetic energy is transformed into frictional heat energy. Subsequently, high temperatures are reached within the interface. Hence, the aim of this chapter is to investigate the effect of surface roughness on this process.
This problem is solved using a transient approach based on the heat source method and the FFT method. The contact area is defined by the contact mechanics model presented in chapter 3. With this model, several case studies are presented.
Furthermore, heat conduction between remote temperatures is also considered in the steady version of the proposed model. The effects of heat conduction are also discussed.
Like the previous chapter, the thermal expansion is not considered in this work.

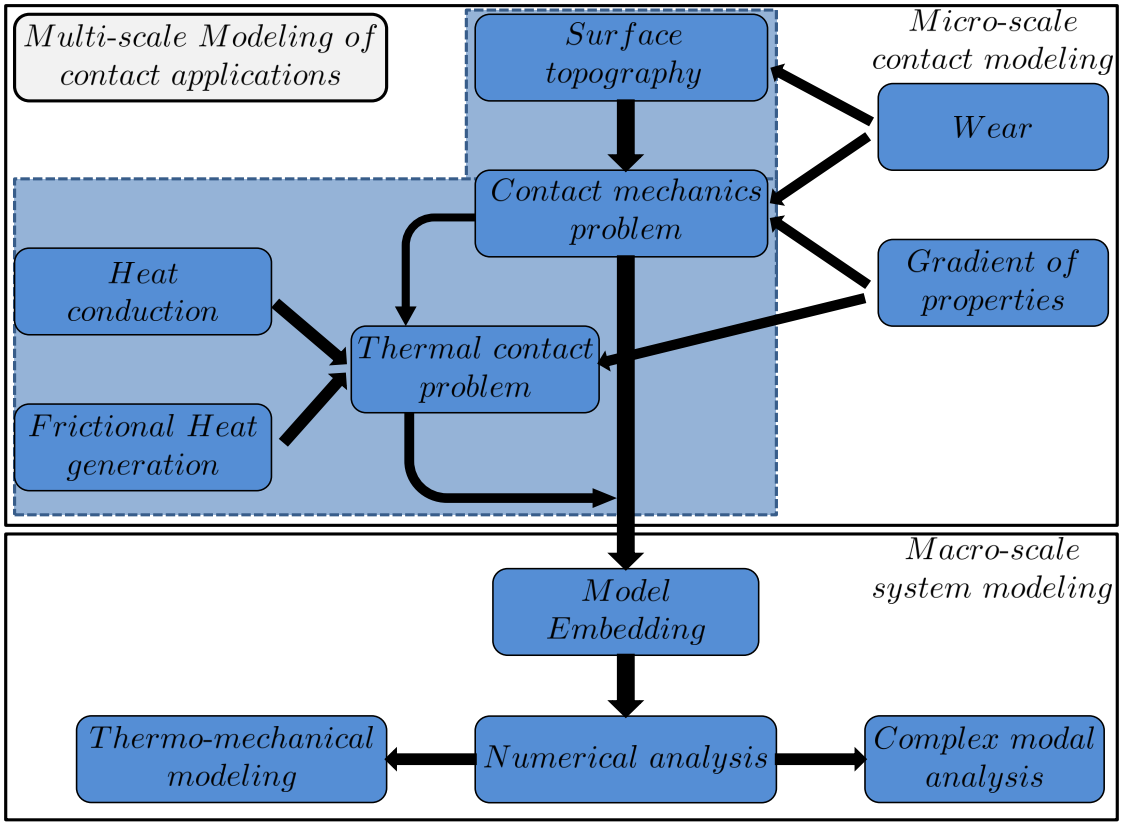

This figure presents the complete plan of this thesis. The placing of this chapter is highlighted by a blue box in the background.

Chapter 6

Heat partition and surface temperature in sliding contact problems

Contents

Heat partition and surface temperature in sliding contact problems

Y. Waddad, V. Magnier, P. Dufrénoy, G. De Saxcé

Université de Lille Nord de France, F-59000 Lille, France
Lille1-LML, F-59655 Villeneuve d'Ascq, France
CNRS, FRE 8107, F-59655 Villeneuve d'Ascq, France

Abstract

Knowledge of surface temperature is of high interest in the study of sliding contact problems. Indeed, it is largely accepted that the frictional energy is transformed into heat, which in turn lead to a rise of temperature in the contact interface that can influence the system performances. The aim of this article is to present a thermal contact model allowing to study the rise of temperature in sliding contact problems. The transient frictional heating problem is analyzed using the heat source method and discrete convolution method. The produced heat is computed based on a contact mechanics model which considers surface roughness. Heat is generated either within the surface or within a thin interface layer. The continuity of the temperature field is enforced within the interface layer. From this, a linear system is obtained and solved with optimization techniques. Moreover, the Fast Fourier Transform is used to accelerate the computational process. Several case studies are presented with the aim to investigate the effects of many parameters on surface temperature such as roughness, velocity, contact area, properties of the interface layer and boundary conditions.

keywords : Sliding contact, Heat partition, Transient analysis, Surface temperature, Roughness, Heat source method, Fourier transform

6.1 Introduction

In sliding contact systems, the largest part of the frictional energy is transformed into heat. It is commonly agreed that this phenomenon is linked to plastic deformations occurring at the sub-surface zone near to contact interface[Furey(1964), Kennedy(1984)]. However, others claim that heat production takes its origins from the atomic-scale interactions within the top atomic layers of the contacting surfaces[Landman *et al.*(1993)]. Thus, the exact location of heat production is not known for sure and depends most likely on the sliding situation.

Since real contact occurs only on some randomly distributed small zones, severe temperatures, resulting from frictional energy, are reached within these zones. These temperatures are a source of wear and local damages which could affect the tribological behavior of contact interface [Archard(1959)]. The reader may refer to the survey paper written by [Blok(1963)] for further details on this phenomena, and also a recent review paper of [Denape and Laraqi(2000)] which details modeling methods and experimental techniques for surface temperature measurement.

Most of the theoretical models of temperature rise in sliding contact are based on heat source method which was developed in the pioneering works of [Blok(1937), Carslaw and Jaeger(1959)]. From this method, several analytic solutions were proposed to study stationary and moving heat sources of different geometries [Zeng *et al.*(1997), Hou and Komanduri(2000)].

Using this technique, single contact problems have been widely studied. In [Tian and Kennedy(1994)], analytical and approximate solutions of maximum and average surface temperatures were obtained for

several geometries. The contact problem has been solved using [Blok(1937)] postulate which considers that the maximum surface temperature is equal for the two solids. In [Laraqi(1996)], the thermal contact resistance, considering the solid velocities, has been formulated for a rectangular contact area. Within the same framework, steady temperatures of circular and elliptic contact have been obtained by matching the surface temperature of both solids in [Bos and Moes(1995)]. In [Komanduri and Hou(2001)], a functional analysis approach has been used to solve the problem of a sliding system modeled as an infinite long band heat source. Using Hankel transform, a pin-on-disc contact has been analyzed in [Laraqi *et al.*(2009)] and the obtained results have been compared to analytical results from [Tian and Kennedy(1994)].
The above cited works consider a perfect contact geometry which is not convenient for studying heat generation in real tribological systems. Several works have used the concept of multiple asperities. Heat flows into solids through these asperities. In most of these works, these zones are uniformly distributed within the interface and are of rectangular shape. The temperature rise in each asperity is calculated using the heat source method considering its shape. For well separated contact spots, this technique has been used by [Chao and Trigger(1956)] to study the tool chip interface during metal cutting. In [Barber(1970)], general solutions of conduction between sliding solids have been addressed considering many configurations such as large scale cooling effects and sub-surface heat generation. In [Vick(2001)], the thermal contact was studied considering two rectangular zones. More recently, the same concept has been used in [Coulibaly *et al.*(2014)] by considering a uniformly distributed contact zones. In the two last works, a Green function has been computed using analytical solutions taking into account the thermal interactions between surface asperities.
Numerical methods have been also used for the contact problem. In [Salti and Laraqi(1999)], the finite volume method and a relaxation iterative method were employed to study the contact considering solid velocities and roughness using a uniformly distributed rectangular contact cells. In [Sadowski *et al.*(2010)], the Finite Element Method has been used to evaluate the contact thermal resistance for a static contact and realistic surface topographies.
The real challenge in studying the thermal contact for sliding systems is to be able to compute the real transient temperature distribution within an acceptable computational time. The main issues that have to be studied are the maximal surface temperatures and heat partition between the two solids. These issues are naturally affected by the contacting solids velocities, properties and boundary conditions. In this work, the effect of the real contact area and the interface conditions are also studied. Indeed, even if the exact location of heat generation is not known, in this work, two modes of heat generation are considered. In the first one, a surface heat generation is considered and the perfect continuity between both solids surface temperature is supposed. In the second one, heat is generated within a very small fictive layer that is modeled as a system of many thermal resistances and capacitances. Thus a gap of temperature can emerge between the two solids. The reason that is behind this approach is that even at the scale of the real contact area, the conduction of heat can be disturbed by wear particles and oxides, etc. The thermal properties of these elements are not known experimentally, so they will be considered as computational parameters.
In order to address the above-cited issues, the thermal contact study is conducted, in this work, based on heat source method. Indeed, using the Fast Fourier transform (FFT) and the discrete convolution technique, the transient contact problem is solved by matching surface temperatures point by point and using optimization techniques. The process of matching temperatures depends on the profile of heat generation (volume or surface heat). The studied surfaces are realistic fractal samples and are generated numerically using a power-law spectral density. The contact area is obtained using an asperity-based contact mechanics model developed in [Waddad *et al.*(2016)]. The amount of heat is obtained from the work of frictional forces which is determined from the friction coefficient, the velocity and the contact pressure.

As is aforementioned, several case studies are performed to show the effect of all the cited issues on heat partition and the rise of surface temperature. First results are focused on the thermal contact without consideration of boundary conditions. The latter corresponds to heat flowing through the two solids which can be caused by remote prescribed temperatures. In the last section, the steady conduction induced by these remote temperatures will be considered.
The originality of this work is the ability to consider a realistic thermal contact problem. Comparing to the existing approaches, this work makes use of the classical heat source method and extends it to cover the rough contact case. Moreover, the FFT technique makes the problem resolution very fast comparing to numerical methods such as the Finite Element Method. Furthermore, many interesting features have been considered such as the interface parameters, the volumetric profiles of heat generation and the consideration of non-zero infinity temperatures. The obtained results are of high interest as they are used in wear modeling and thermo-mechanical simulations for instance.

6.2 Analytic solutions for thermal loading of moving and static homogeneous solids

6.2.1 Surface heating of a fixed semi-infinite region

Let us consider an infinite solid, initially at zero temperature and an instantaneous point source of heat at time $t = 0$. The temperature field T that satisfies heat equation is given by [Carslaw and Jaeger(1959)]

$$T(r,t) = \frac{Q\,\chi}{8\kappa\,(\pi\chi)^{3/2}}\,\frac{1}{t^{3/2}}\exp\left(-\frac{r^2}{4\chi t}\right)$$

where Q is the quantity of heat liberated, χ is the thermal diffusivity, κ is the thermal conductivity and r is the distance from the source (see Fig.6.1).
Now considering that there is no heat flow across a diametrical plane of the solid ($z = 0$), which is the case of a semi infinite solid, the temperature with an instantaneous point source reads

$$T(r,t) = \frac{Q\,\chi}{4\kappa\,(\pi\chi)^{3/2}}\,\frac{1}{t^{3/2}}\exp\left(-\frac{r^2}{4\chi t}\right)$$

In this case all the heat is directed into one side.
If heat is supplied to the semi-infinite solid at a steady rate q distributed over a finite area S, the temperature distribution is then given by

$$T(x,y,z,t) = \frac{q\chi}{4\kappa\,(\pi\chi)^{3/2}}\int_0^t \frac{\mathrm{d}t'}{(t-t')^{3/2}}\iint_S \exp\left(-\frac{r^2}{4\chi\,(t-t')}\right)\mathrm{d}\xi\mathrm{d}\eta \tag{6.1}$$

where q is the heat flux density liberated per unit of time and space and $r = \sqrt{(x-\xi)^2+(y-\eta)^2+z^2}$.
If heat is introduced over a rectangular area $2a \times 2b$, the temperature is

$$T(x,y,z,t) = \frac{q\chi}{4\kappa\,(\pi\chi)^{3/2}}\int_0^t \frac{\mathrm{d}t'}{(t-t')^{3/2}}\int_{-a}^{a}\int_{-b}^{b} \exp\left(-\frac{(x-\xi)^2+(y-\eta)^2+z^2}{4\chi\,(t-t')}\right)\mathrm{d}\xi\mathrm{d}\eta \tag{6.2}$$

By making a substitution, we found

$$\begin{aligned}\frac{T(x,y,z,t)}{\frac{q}{4\kappa\pi^{1/2}}} =& I\left(x+a,y+b,z,\frac{1}{2\sqrt{\chi t}},\infty\right)+I\left(x-a,y-b,z,\frac{1}{2\sqrt{\chi t}},\infty\right)\\ &-I\left(x-a,y+b,z,\frac{1}{2\sqrt{\chi t}},\infty\right)-I\left(x+a,y-b,z,\frac{1}{2\sqrt{\chi t}},\infty\right)\end{aligned}$$

where

$$I(\alpha,\beta,\gamma,l,L)=\int_l^L \exp\left(-\gamma^2v^2\right)\operatorname{erf}(\alpha v)\operatorname{erf}(\beta v)\frac{\mathrm{d}v}{v^2}$$

Using integration by parts, The integral I reads for the case of steady state temperature

$$I(\alpha,\beta,\gamma,0,\infty)=\frac{\alpha}{\sqrt{\pi}}\ln\left(\frac{\beta+\left(\alpha^2+\beta^2+\gamma^2\right)^{1/2}}{-\beta+\left(\alpha^2+\beta^2+\gamma^2\right)^{1/2}}\right)+\frac{\beta}{\sqrt{\pi}}\ln\left(\frac{\alpha+\left(\alpha^2+\beta^2+\gamma^2\right)^{1/2}}{-\alpha+\left(\alpha^2+\beta^2+\gamma^2\right)^{1/2}}\right)$$
$$-2\frac{\gamma}{\sqrt{\pi}}\tan^{-1}\left(\frac{\alpha\beta}{\gamma\left(\alpha^2+\beta^2+\gamma^2\right)^{1/2}}\right)$$

From this solution, the integral I can be calculated for the transient case by subtraction

$$I\left(\alpha,\beta,\gamma,\frac{1}{2\sqrt{\chi t}},\infty\right)=I(\alpha,\beta,\gamma,0,\infty)-I\left(\alpha,\beta,\gamma,0,\frac{1}{2\sqrt{\chi t}}\right) \tag{6.3}$$

and the transient term is estimated numerically.

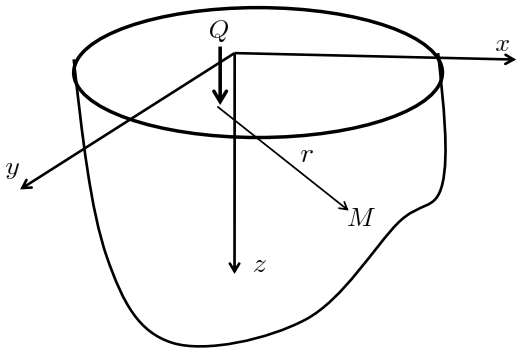

Figure 6.1: Schematic of the point source of heat in a half space

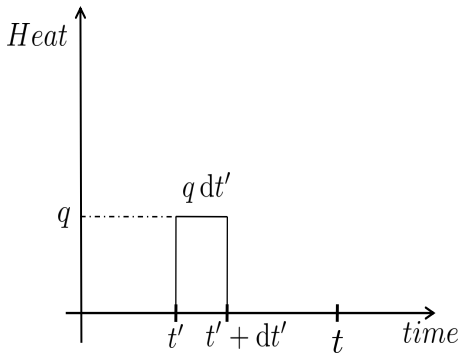

Figure 6.2: The amount of heat $q\mathrm{d}t'$ is emitted at time t'

6.2.2 Surface heating of a rotating semi-infinite region

Now let us consider that heat is produced at a fixed point by which a uniformly moving medium flows (see Fig.6.3). Suppose that a quantity $q\mathrm{d}t'$ of heat was emitted at time t' at the fixed point of space $(x_c, y_c, 0)$ (see Fig.6.2). We calculate the temperature at the fixed point (x, y, z) at time t.
Considering the solid rotation, the position of any point of the solid at time t is given by

$$X(t)=R\cos(s(t)+\phi)$$

$$Y(t)=R\sin(s(t)+\phi)$$

where R is the distance from the center of rotation, $s(t)$ is the angular position which is time dependent and ϕ is an arbitrary fixed angle.
Assume that the point (x, y, z) was at time t' at (x', y', z), we have

$$x'=x\,\cos\left(s(t)-s(t')\right)+y\,\sin\left(s(t)-s(t')\right)$$

$$y' = y\,\cos\left(s(t) - s(t')\right) - x\,\sin\left(s(t) - s(t')\right)$$

Hence, the temperature at time t at the point (x, y, z) with the heat $q\mathrm{d}t'$ emitted at t' is [Carslaw and Jaeger(1959)]

$$\mathrm{d}T = \frac{q\chi \mathrm{d}t'}{4\kappa\left(\pi\chi(t-t')\right)^{3/2}} \exp\left(-\frac{(x'-x_c)^2 + (y'-y_c)^2 + z^2}{4\chi(t-t')}\right)$$

Therefore, the temperature elevation due to heat emitted between 0 and t is given by

$$T\left(x, y, z, t\right) = \frac{q\chi}{4\kappa\left(\pi\chi\right)^{3/2}} \int_0^t \frac{\mathrm{d}t'}{(t-t')^{3/2}} \exp\left(-\frac{(x'-x_c)^2 + (y'-y_c)^2 + z^2}{4\chi(t-t')}\right)$$

Using a substitution, we obtain

$$T\left(x, y, z, t\right) = \frac{q}{\kappa\pi^{3/2}} \int_0^{\sqrt{4\chi t}} \frac{\mathrm{d}v}{v^2} \exp\left(-\frac{(x'-x_c)^2 + (y'-y_c)^2 + z^2}{v^2}\right)$$

where

$$x' = x\,\cos\left(s\left(t - \frac{v^2}{4\chi}\right) - s\left(t\right)\right) - y\,\sin\left(s\left(t - \frac{v^2}{4\chi}\right) - s\left(t\right)\right)$$

$$y' = y\,\cos\left(s\left(t - \frac{v^2}{4\chi}\right) - s\left(t\right)\right) + x\,\sin\left(s\left(t - \frac{v^2}{4\chi}\right) - s\left(t\right)\right)$$

If heat is distributed over a rectangular area $2a \times 2b$, the temperature field is then

$$T\left(x, y, z, t\right) = \frac{q}{\kappa\pi^{3/2}} \int_0^{\sqrt{4\chi t}} \frac{\mathrm{d}v}{v^2} . \int_{-a}^{a} \mathrm{d}\xi . \int_{-b}^{b} \mathrm{d}\eta \exp\left(-\frac{(x'-x_c-\xi)^2 + (y'-y_c-\eta)^2 + z^2}{v^2}\right) \tag{6.4}$$

which is equivalent to

$$\begin{aligned} T\left(x, y, z, t\right) = & \frac{q}{4\kappa\pi^{1/2}} \int_0^{\sqrt{4\chi t}} \mathrm{d}v \exp\left(-\frac{z^2}{v^2}\right) . \left(\mathrm{erf}\left(\frac{x'-x_c+a}{v}\right) - \mathrm{erf}\left(\frac{x'-x_c-a}{v}\right)\right) \\ & . \left(\mathrm{erf}\left(\frac{y'-y_c+b}{v}\right) - \mathrm{erf}\left(\frac{y'-y_c-b}{v}\right)\right) \end{aligned} \tag{6.5}$$

From this formula, the temperature field is calculated using numerical integration techniques (for e.g. Gaussian quadrature).
In the following, the analytic formulas are illustrated and the effect of velocity is highlighted.

6.2.3 Illustration of the analytic solutions

Before tackling the contact problem, we propose some illustrations of the presented-above equations. In this paragraph, we consider the case where the angular velocity ω either decreases linearly or remains constant with time. These cases are the most encountered in sliding contact applications, for e.g. friction brakes, where braking is applied to maintain the speed or to slow it.
Thus, the angular velocity reads

$$\omega(t) = \frac{\mathrm{d}s}{\mathrm{d}t}\left(t\right) = \begin{cases} \dfrac{\omega_1 - \omega_0}{t_0}\, t + \omega_0 & \text{if } t \leq t_0 \\ \omega_1 & \text{else.} \end{cases} \tag{6.6}$$

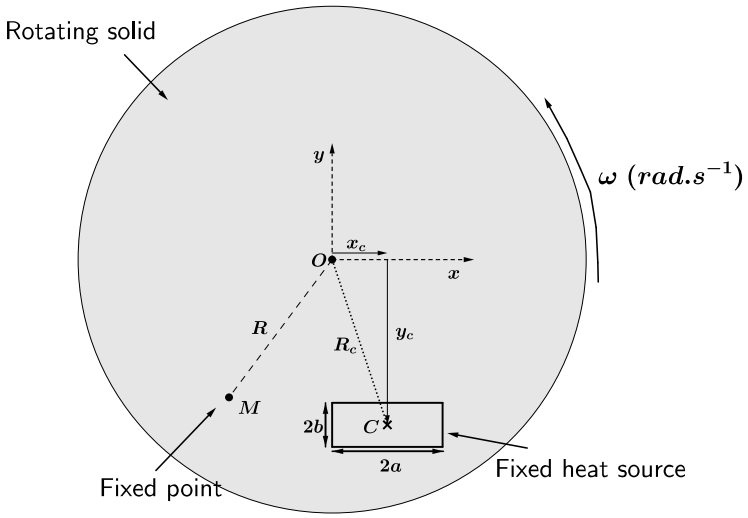

Figure 6.3: Schematic of a rotating solid heated through a fixed source on its surface

By integration, the angular position reads

$$s\,(t) = \begin{cases} \dfrac{\omega_1 - \omega_0}{2t_0}\, t^2 + \omega_0\, t & \text{if } t \leq t_0 \\ \omega_1\, t + \dfrac{\omega_0 - \omega_1}{2}\, t_0 & \text{else.} \end{cases} \tag{6.7}$$

and by derivation, the angular acceleration is

$$\frac{\mathrm{d}\omega}{\mathrm{d}t}\,(t) = \begin{cases} \dfrac{\omega_1 - \omega_0}{t_0} & \text{if } t \leq t_0 \\ 0 & \text{else.} \end{cases} \tag{6.8}$$

These formulas correspond to a linear variation of velocity from ω_0 to ω_1 within the interval time $[0, t_0]$. Beyond t_0, the velocity is fixed at ω_1. In Fig.6.4, several profiles of the angular position s are presented for different cases. For all of these cases, t_0 is fixed at $10s$ and the velocity ω_1 is varied from ω_0 to 0. In the same figure, we can also see the case where the velocity remains constant (i.e $\omega_1 = \omega_0$). In Fig.6.5, the impact of the velocity profile on the time evolution of the abscissa X is highlighted.

For the present study, the chosen parameters are summarized in Tab.6.1. The heat density q is introduced over a rectangular zone of which the dimensions are $2a \times 2b$. This quantity is assumed to be constant in this part. Note that, in real applications, this quantity depends on the velocity which is not the case here. Figures 6.6-6.15 present the evolution of the dimensionless temperature, defined by $\dfrac{\kappa T}{a\, q}$, for the different studied cases. Additionally, the dimensionless velocity, commonly named Peclet number, defined by $\mathrm{Pe} = \dfrac{R\,\omega\,a}{\chi}$, is indicated in the different curves.

In Fig.6.6, the evolution with time of the temperature in the center of the heated zone is shown. The velocity ω is fixed at $100\,rad.s^{-1}$ and the radius is varied from 0 to 20 cm. The surface temperature at $t = 1\,ms$ is plotted in Fig.6.7 for Y/a ranging from -2 to 8. As can be seen in both figures, the temperature level decreases with the increase of R_c. Also, the shape of the temperature profile is deformed by the solid velocity. Subsequently, the maximal temperature is not reached in the center of the heated zone ($y = y_c$),

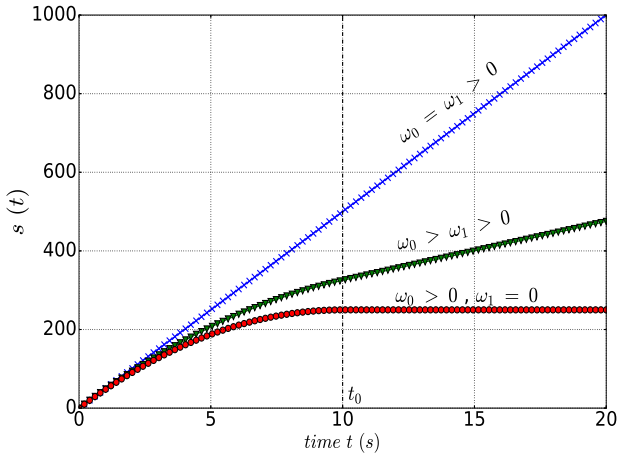

Figure 6.4: Time profile of the angular position

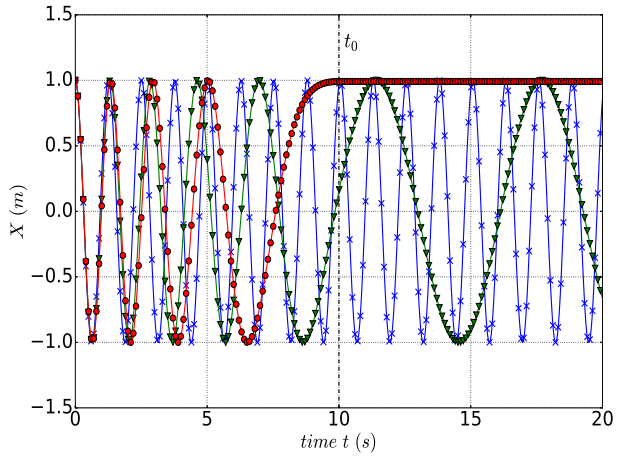

Figure 6.5: Evolution of the abscissa X with time.

Diffusivity $\chi\ (m^2/s)$	$a\ (\mu m)$	$b\ (\mu m)$	$y_c\ (mm)$	$t_0\ (ms)$
10^{-5}	100	100	0	100

Table 6.1: The considered parameters of the study

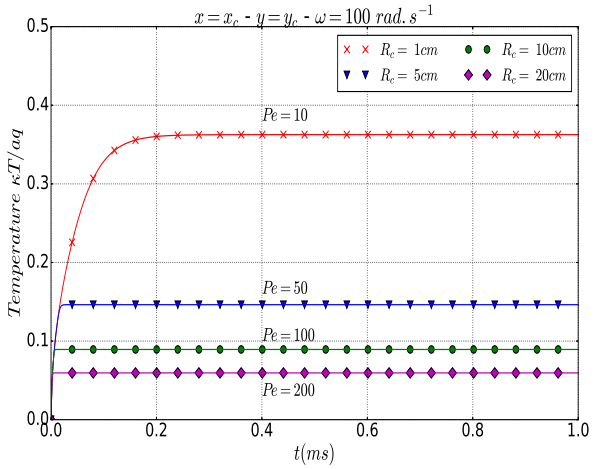

Figure 6.6: Effect of the radius on the time evolution of temperature in the heated zone center

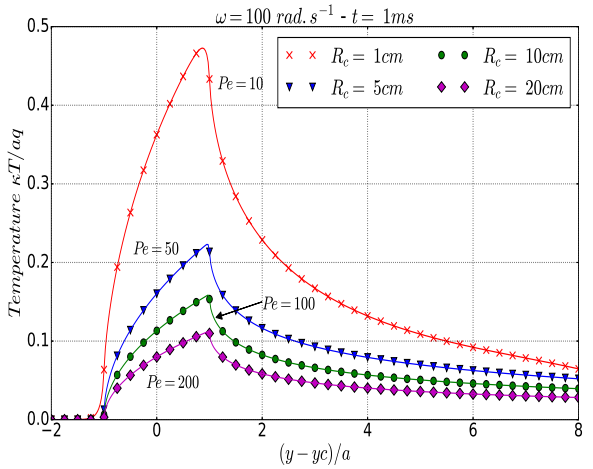

Figure 6.7: Effect of the radius on the spatial distribution of temperature at $t = 1ms$

but rather at the exit of the heated zone.
In Figs 6.8-6.9, the radius is fixed at $10cm$ and the angular velocity ω is fixed at time but varied from 0 to $100\,rad.s^{-1}$. Just like the previous paragraph, the same remarks can be made here. Indeed, by increasing the radius or the angular velocity, the Peclet number increases, the level of temperature decreases and the position of the maximal temperature deviates from the center of the heated zone. Moreover, it is well known that the steady temperature is reached rapidly for high velocities. This can be seen in Figs 6.6-

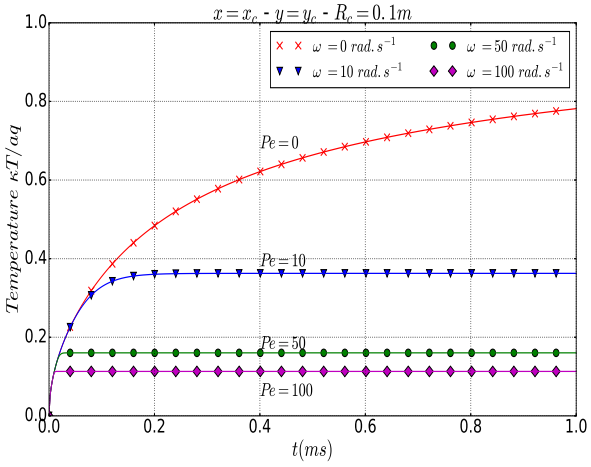

Figure 6.8: Effect of the rotation velocity on the time evolution of temperature in the heated zone center

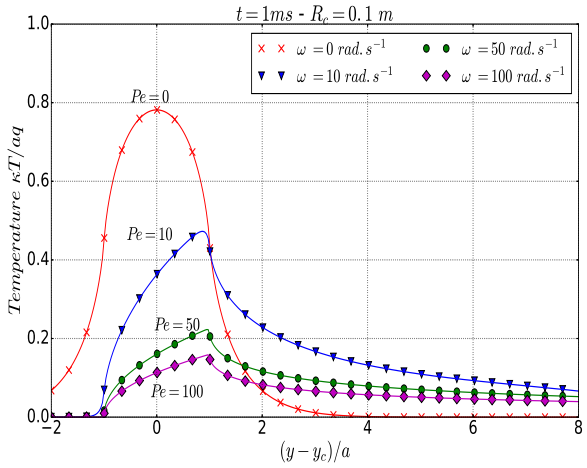

Figure 6.9: Effect of the rotation velocity on the spatial distribution of temperature at $t = 1ms$

6.8.

In Figs 6.10-6.13, are shown the temperature levels for the cases where the angular velocity is time-dependent. Here, the initial velocity is fixed at $\omega_0 = 10\,rad.s^{-1}$, the radius at $R_c = 10cm$ and $t_0 = 100ms$. The final velocity ω_1 is varied from 10 to 0 $rad.s^{-1}$. The last case corresponds to a deceleration of $-10m.s^{-2}$ which corresponds to the maximal deceleration that can be reached in automotive braking systems for instance. For the different cases, the angular position is plotted in Fig.6.10. The temperature evolution with time of the center point is plotted in Fig.6.11. As can be seen, the reached temperature level is almost the same for $t \leq 10\,ms$. As the velocity decreases, the temperature increases. The maximum level of temperature is the one reached for the static case. The temperature profile is shown for $t = 6\,ms$ (resp. $t = 100\,ms$) in Fig.6.12 (resp.6.13). As the velocity increases, the shape of the temperature profile becomes less distorted.

Furthermore, as an example, the temperature spatial distribution is shown in Figs 6.14-6.15 for a constant velocity $\omega = 100\,rad.s^{-1}$ and a $2\,ms$ of steady heating. The surface temperature is presented in Fig.6.14. The curvature of the temperature profile corresponds to the angular position of the heated zone which is placed here in the axis $y = 0$. In Fig.6.15 is shown the temperature distribution beneath the heated zone. From this figure we see that the temperature decreases very rapidly as $z \leq 0$. Thus, the heat entering the moving body beneath the heat source is concentrated in a thin zone.

In this section, the analytical solution obtained with heat source method have been presented. In the following, this method is used to study the transient surface temperature in sliding contact problems.

6.3 The transient temperature and heat distribution in sliding contact problems

6.3.1 General equations

The frictional heat is generated at the interface and its distribution depends on the physical nature of contact interactions. The contact interface is considered as a source of heat which is distributed over the

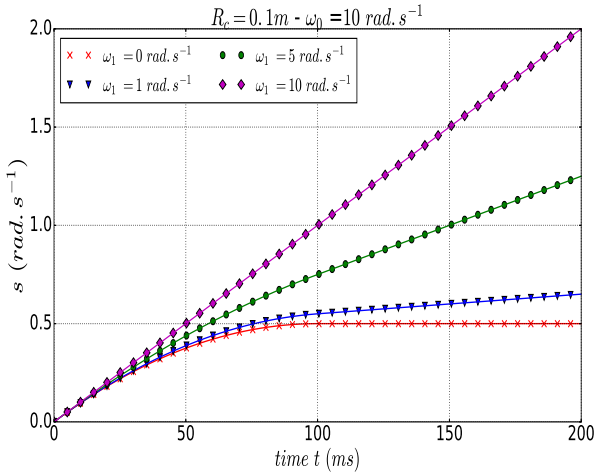

Figure 6.10: Evolution of the angular position for the different velocity profiles

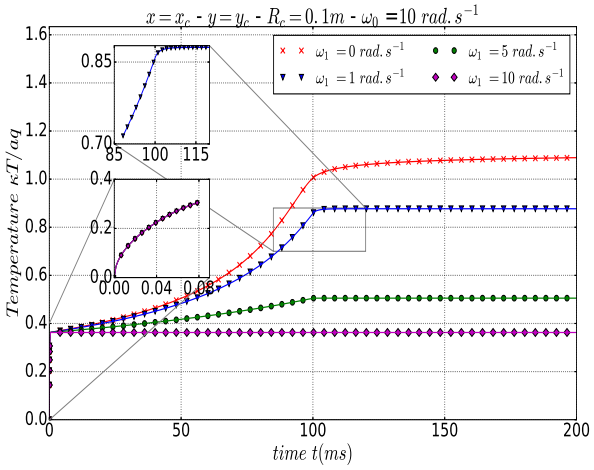

Figure 6.11: Time evolution of the temperature in the heated zone center

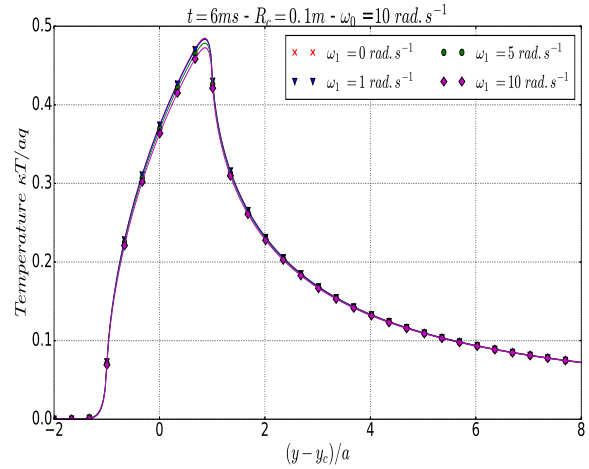

Figure 6.12: Spatial distribution of the temperature at $t = 6ms$

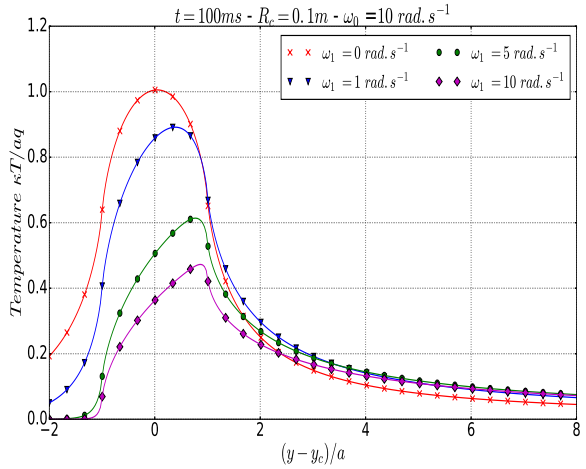

Figure 6.13: Spatial distribution of the temperature at $t = 100ms$

superior face of each body

$$\phi = \phi_1 + \phi_2$$

where ϕ is the total rate of heat generated at the interface and ϕ_1 and ϕ_2 are the rates of heat flowing through the solids S_1 and S_2.
The real contact area is small compared to the contacting bodies dimensions, thus it is possible to approximate the system to two semi-infinite regions. The surface temperature of each of the two solids (θ_1 and θ_2) can be related to the heat flowing into them by the functions F_1 and F_2

$$\theta_1 = F_1(\phi_1)$$

$$\theta_2 = F_2(\phi_2)$$

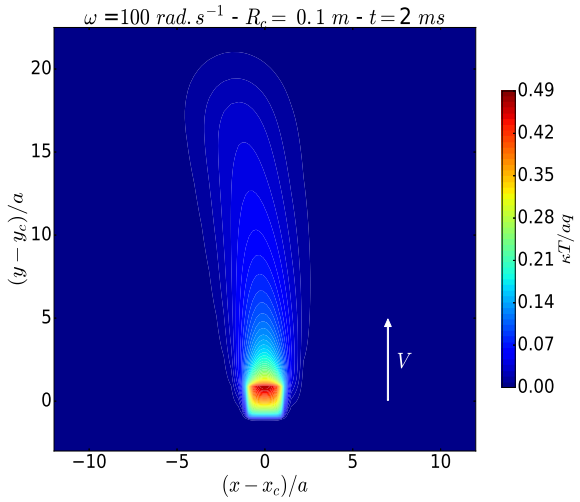

Figure 6.14: Surface temperature for $\omega = 100\,rad.s^{-1}$ and $t = 2\,ms$

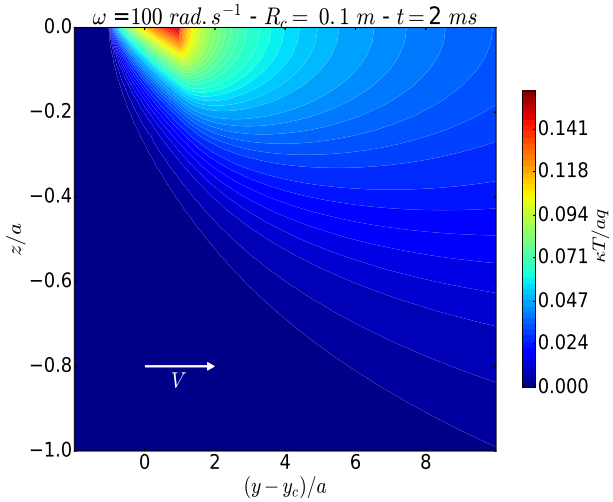

Figure 6.15: Temperature field beneath the heated zone for $\omega = 100\,rad.s^{-1}$ and $t = 2\,ms$

where F_1 and F_2 depend on the physical properties of the contacting solids.
In this work, we consider that there is a gap between the surface temperature of the contacting solids. This gap of temperature corresponds to the presence of an interface layer made from surface debris. Moreover, heat can be generated inside this zone as its exact generation place is not known exactly. Also, we suppose that the functions F_1 and F_2 are linear. Thus, one can deduce the following equation

$$(F_1 + F_2)(\phi_1) = (F_2)(\phi) + \theta_1 - \theta_2 \tag{6.9}$$

The temperature gap $\theta_1 - \theta_2$ will be expressed later as a function of ϕ_1 and ϕ. The obtained expressions will depend on the physical properties of the interface zone and the mode of heat generation. The unknown of this equation is ϕ_1.
This equation is spatial and temporal. In order to solve it, we propose a strategy that transforms it into a spatial equation which is more easy to resolve. For this aim, we propose the following strategy :
We consider the time step $t = t_N$ and we introduce λ defined by

$$\lambda(t) = \phi_1(t) \quad \text{if} \quad t \leq t_N \quad \text{and} \quad \lambda(t) = \phi_1(t_N) \quad \text{else.}$$

This means that λ is equal to ϕ_1 in space and time except for the case where time t exceeds t_N, where λ remains constant. Besides, we introduce ψ defined by $\psi = \phi_1 - \lambda$, then

$$\psi(t) = 0 \quad \text{if} \quad t \leq t_N \quad \text{and} \quad \psi(t) = \phi_1(t) - \phi_1(t_N) \quad \text{else.}$$

Hence ψ corresponds to the flux increment applied from time $t = t_N$.
From Eq.6.9, we obtain

$$(F_1 + F_2)(\lambda) + (F_1 + F_2)(\psi) = F_2(\phi) + \theta_1 - \theta_2 \tag{6.10}$$

Hence

$$(F_1 + F_2)(\psi) = F_2(\phi) - (F_1 + F_2)(\lambda) + \theta_1 - \theta_2 \tag{6.11}$$

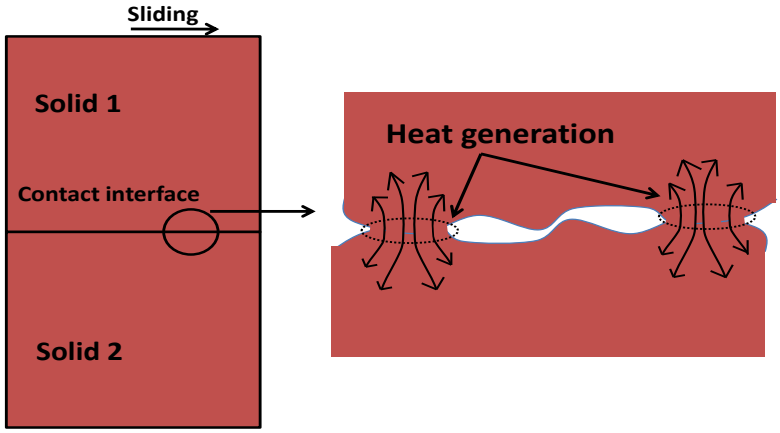

Figure 6.16: Schematic of the real contact interface. Heat is generated within the real contact zones

This equation relates the flux ψ applied from time $t = t_N$ to the total flux ϕ and λ. If the flux ϕ_1 is known for $t \leq t_N$, λ will be also known and we can compute from Eq.(6.11) the flux ψ and deduce ϕ_1 at time $t > t_N$.
Following this reasoning, ϕ_1 is assumed to be known for $t \leq t_N$ and ψ is constant within the time interval $[t_N, t]$. Therefore, the problem is solved incrementally, where at each time increment, the flux ψ is computed and the flux ϕ_1 is updated so that the flux λ can be computed for the next time step, and so on.
The total flux acting on the surface of the solid S_i $(i = 1, 2)$ reads then

$$\Phi_i = \int_S \phi_i \mathrm{d}S$$

Therefore, the coefficient of heat partition reads

$$p_i = \frac{\Phi_i}{\Phi}$$

where $\Phi = \Phi_1 + \Phi_2$ is the total heat generated at the interface.
Now that the key elements of the solving strategy have been presented, the discretized form of the problem is presented and more details about the gap of temperature are given in the following.

6.3.2 Discretization of the contact problem

Considering one of the contacting solids. Suppose that the surface is heated at many regions. The surface temperature θ is expressed as a function of surface heating ϕ

$$\theta(x, y, t) = F(\phi(x, y, t))$$

In order to solve the thermal contact problem, the surface is discretized into $N_{xy} = N_x \times N_y$ small squares of the same size (see Fig.6.17). The studied interval of time $[0, t]$ is also discretized into N_t equal small

intervals (see Fig. 6.18). The heat flux acting on each single square is assumed to be uniformly distributed on it. Thus, the flux ϕ reads

$$\phi(x,y,t) = \sum_{i=1}^{N_{xy}} \sum_{k=1}^{N_t} \mathbf{1}_i(x,y)\, \mathbf{1}_k(t)\, \phi_{ik}$$

where $\mathbf{1}_i$ is the indicator function of the space domain $[x_i - d, x_i + d] \times [y_i - d, y_i + d]$, (x_i, y_i) are the coordinates of the i^{th} surface element center, d is the half dimension of the element, $\mathbf{1}_k$ is the indicator function of the time interval $[t_k, t]$ and ϕ_{ik} is the flux increment applied on the i^{th} square and emitted steadily from the instant t_k.
The solid temperature is then calculated as a combination of all the temperature variations due to all the fluxes acting on the surface

$$F(\phi(x,y,t)) = \sum_{i=1}^{N_{xy}} \sum_{k=1}^{N_t} \mathbf{1}_k(t)\, T(x - x_i, y - y_i, t - t_k)\ \phi_{ik} \tag{6.12}$$

where $T(x - x_i, y - y_i, t - t_k)$ is the temperature elevation at the surface point (x, y) which is due to the unit flux applied over the i^{th} element from time t_k to t. Relative expressions of T have been presented in section 6.2.1 for fixed solids and in section 6.2.2 for moving solids.
The total heat flux applied on the surface at time t reads then

$$\Phi(t) = \sum_{i=1}^{N_{xy}} \sum_{k=1}^{N_t} \mathbf{1}_k(t)\, \phi_{ik} \tag{6.13}$$

In what follows, T_1 (resp. T_2) corresponds to the solid S_1 (resp. S_2).

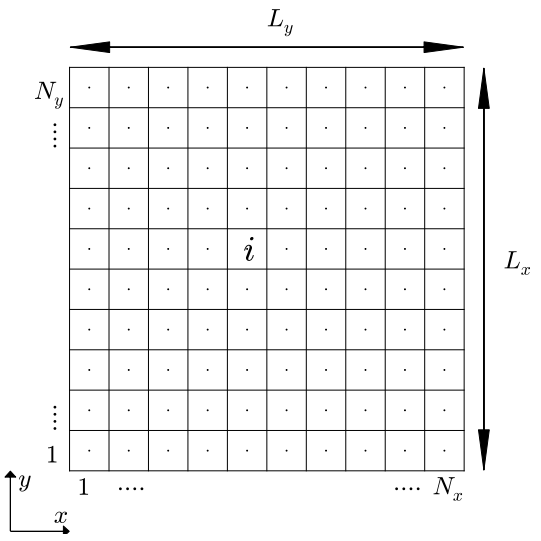

Figure 6.17: Surface grid used to solve the thermal contact problem

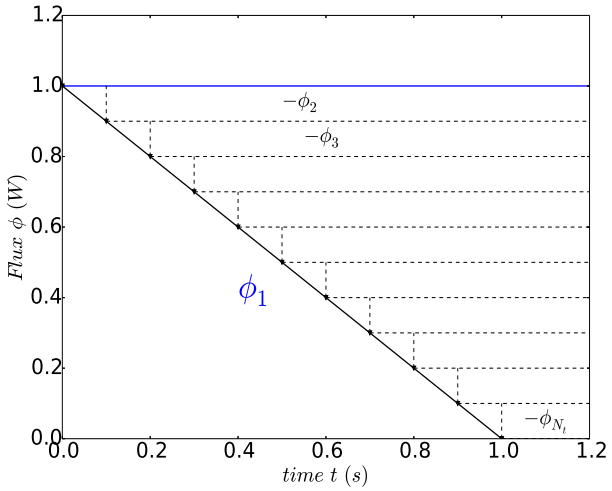

Figure 6.18: Time discretization of ϕ. In this example, ϕ decreases linearly with time. All the flux increments are constant within their time interval. For instance, ϕ_1 is applied from $t = 0$ and is constant within the studied time interval.

6.3.3 Expression of the gap of temperature: the thermal resistance and capacitance, and profiles of heat generation

In this work, we consider that heat is generated inside a thin interface layer which is comprised between the contact zones of both surfaces. Thus, heat can be distributed within this layer and there will be a temperature jump between the two solids. In the following, the gap of temperature $\theta_1 - \theta_2$ is expressed as a function of the heat distribution and the physical properties of the interface.
Let us consider the i^{th} contact point. At this point, there is a temperature jump and heat is generated within the thin layer according to a given mode of generation. In this work, we propose that this zone is modeled as a system of n thermal components (see Fig.6.19). Additionally, generation of heat is represented by a discrete set of heat sources ϕ^l distributed along the layer. The total heat generated at this contact point is thus given by

$$\phi_{ik} = \sum_{l=0}^{l=n} \phi_{ik}^l$$

For ϕ_1, we will make use of the decomposition introduced in section 6.3.1, i.e

$$\phi_1 = \psi + \lambda$$

Thus, we introduce the following space-time discretization of ψ and λ

$$\psi(x,y,t) = \sum_{i=1}^{N_{xy}} \sum_{k=1}^{N_t} \mathbf{1}_i(x,y)\, \mathbf{1}_k(t)\, \psi_{ik}$$

and

$$\lambda(x,y,t) = \sum_{i=1}^{N_{xy}} \sum_{k=1}^{N_t} \mathbf{1}_i(x,y)\, \mathbf{1}_k(t)\, \lambda_{ik}$$

In the i^{th} point and at the scale of the l^{th} component, there is a jump of temperature $\theta_{iN}^l - \theta_{iN}^{l-1}$ at time $t = t_N$. This jump of temperature can be modeled as a local thermal resistance (see Fig.6.19(a)) or a system combining a thermal resistance and a thermal capacitance (see Fig.6.19(b)).
For the first case, the jump of temperature of the l^{th} component reads

$$\theta_{iN}^l - \theta_{iN}^{l-1} = R^l \sum_{k=1}^{N-1} \varphi_{ik}^l$$

where φ_{ik}^l is the flux which goes through the component at time $t = t_k$ and R^l is the thermal resistance. For the second case, a thermal capacitance C^l is introduced and the temperature reads

$$\theta_{iN}^l - \theta_{iN}^{l-1} = \sum_{k=1}^{N-1} \left(1 - \exp\left(-\frac{t_N - t_k}{R^l C^l}\right)\right) R^l\, \varphi_{ik}^l$$

This exponential law is chosen based on a phenomenological description of thermal phenomena. Indeed, the capacitance represents the mass effect. As long as C^l increases, the time necessary to reach the steady state increases.
Considering the presence of heat sources, we have

$$\varphi_{ik}^{l-1} - \varphi_{ik}^l = \phi_{ik}^{l-1}$$

From these equations, we found that the gap of temperature in the i^{th} point at $t = t_N$ reads

$$(\theta_2 - \theta_1)_{iN} = \sum_{k=1}^{N-1} \sum_{m=1}^{n} \left(1 - \exp\left(-\frac{t_N - t_k}{R^m C^m}\right)\right) R^m(\psi_{ik} + \lambda_{ik}) - \sum_{k=1}^{N-1} \sum_{m=0}^{n-1} \sum_{l=0}^{m} \left(1 - \exp\left(-\frac{t_N - t_k}{R^{m+1} C^{m+1}}\right)\right) R^{m+1} \phi_{ik}^l$$

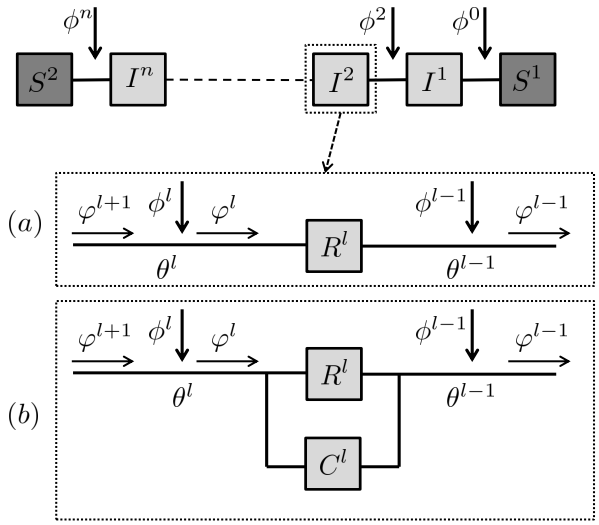

Figure 6.19: Schema of the interface

6.3.4 Solving of thermal contact problem

The contact problem can now be solved by replacing the different functions by their discrete expressions. Considering the j^{th} point and the time step t_{N+1} where $0 \leq N < N_t$, the equation (6.11) reads

$$\begin{aligned}
&\sum_{i=1}^{N_{xy}}\sum_{k=1}^{N}\psi_{ik}\left(T_1+T_2\right)\left(x_j-x_i,y_j-y_i,t_{N+1}-t_k\right)+\sum_{k=1}^{N}\sum_{m=1}^{n}\left(1-\exp\left(-\frac{t_{N+1}-t_k}{R^mC^m}\right)\right)R^m\psi_{jk}\\
&=\sum_{i=1}^{N_{xy}}\sum_{k=1}^{N}\sum_{l=0}^{l=n}\phi_{ik}^{l}T_2\left(x_j-x_i,y_j-y_i,t_{N+1}-t_k\right)+\sum_{k=1}^{N}\sum_{m=0}^{n-1}\sum_{l=0}^{m}\left(1-\exp\left(-\frac{t_{N+1}-t_k}{R^{m+1}C^{m+1}}\right)\right)R^{m+1}\phi_{jk}^{l}\\
&-\sum_{i=1}^{N_{xy}}\sum_{k=1}^{N}\lambda_{ik}\left(T_1+T_2\right)\left(x_j-x_i,y_j-y_i,t_{N+1}-t_k\right)-\sum_{k=1}^{N}\sum_{m=1}^{n}\left(1-\exp\left(-\frac{t_{N+1}-t_k}{R^mC^m}\right)\right)R^m\lambda_{jk}
\end{aligned}$$

Since $\psi=0$ for $t<t_N$, we have

$$\begin{aligned}
&\sum_{i=1}^{N_{xy}}\psi_{iN}\left(T_1+T_2\right)\left(x_j-x_i,y_j-y_i,t_{N+1}-t_N\right)+\sum_{m=1}^{n}\left(1-\exp\left(-\frac{t_{N+1}-t_N}{R^mC^m}\right)\right)R^m\psi_{jN}\\
&=\sum_{i=1}^{N_{xy}}\sum_{k=1}^{N}\sum_{l=0}^{l=n}\phi_{ik}^{l}T_2\left(x_j-x_i,y_j-y_i,t_{N+1}-t_k\right)+\sum_{k=1}^{N}\sum_{m=0}^{n-1}\sum_{l=0}^{m}\left(1-\exp\left(-\frac{t_{N+1}-t_k}{R^{m+1}C^{m+1}}\right)\right)R^{m+1}\phi_{jk}^{l}\\
&-\sum_{i=1}^{N_{xy}}\sum_{k=1}^{N}\lambda_{ik}\left(T_1+T_2\right)\left(x_j-x_i,y_j-y_i,t_{N+1}-t_k\right)-\sum_{k=1}^{N}\sum_{m=1}^{n}\left(1-\exp\left(-\frac{t_{N+1}-t_k}{R^mC^m}\right)\right)R^m\lambda_{jk}
\end{aligned}\tag{6.14}$$

By reporting this equation in each contacting point, the following matrix equation is obtained

$$\mathbf{A}^N\boldsymbol{\Psi}^N=\boldsymbol{\Phi}^N-\boldsymbol{\Lambda}^N\tag{6.15}$$

where

$$A_{ij}^N = (T_1 + T_2)\,(x_j - x_i, y_j - y_i, t_{N+1} - t_N) + \sum_{m=1}^{n} \left(1 - \exp\left(-\frac{t_{N+1} - t_N}{R^m C^m}\right)\right) R^m \delta_{ij} \tag{6.16}$$

and

$$\Phi_j^N = \sum_{i=1}^{N_{xy}} \sum_{k=1}^{N} \sum_{l=0}^{l=n} \phi_{ik}^l T_2\,(x_j - x_i, y_j - y_i, t_{N+1} - t_k) + \sum_{k=1}^{N} \sum_{m=0}^{n-1} \sum_{l=0}^{m} \left(1 - \exp\left(-\frac{t_{N+1} - t_k}{R^{m+1} C^{m+1}}\right)\right) R^{m+1} \phi_{jk}^l \tag{6.17}$$

and

$$\Lambda_j^N = \sum_{i=1}^{N_{xy}} \sum_{k=1}^{N} \lambda_{ik}\,(T_1 + T_2)\,(x_j - x_i, y_j - y_i, t_{N+1} - t_k) + \sum_{k=1}^{N} \sum_{m=1}^{n} \left(1 - \exp\left(-\frac{t_{N+1} - t_k}{R^m C^m}\right)\right) R^m \lambda_{jk} \tag{6.18}$$

and δ_{ij} is the Kronecker symbol.

6.3.5 Solving scheme

In order to solve this equation, the matrix equation problem is transformed into a minimization problem by defining the objective function f

$$f\left(\boldsymbol{\Psi}^N\right) = \frac{1}{2}\,{}^t\left(\mathbf{A}^N\boldsymbol{\Psi}^N - \boldsymbol{\Phi}^N + \boldsymbol{\Lambda}^N\right).\left(\mathbf{A}^N\boldsymbol{\Psi}^N - \boldsymbol{\Phi}^N + \boldsymbol{\Lambda}^N\right) \tag{6.19}$$

This form has been chosen rather than

$$\frac{1}{2}\,{}^t\boldsymbol{\Psi}^N\mathbf{A}^N\boldsymbol{\Psi}^N - {}^t\boldsymbol{\Psi}^N\left(\boldsymbol{\Phi}^N - \boldsymbol{\Lambda}^N\right)$$

because the matrix $\mathbf{A}^N$ is not symmetric. This asymmetry is due to the velocity.
The gradient of f reads

$$\boldsymbol{\nabla} f = {}^t\mathbf{A}^N\left(\mathbf{A}^N\boldsymbol{\Psi}^N - \boldsymbol{\Phi}^N + \boldsymbol{\Lambda}^N\right) \tag{6.20}$$

Besides, the real contact area has to be considered to solve the thermal contact problem. For this aim, the contact mechanics problem is first solved using optimization techniques (the reader may refer to [Waddad *et al.*(2016)] for more details). Then, the contact area and the contact pressure field can both be defined. From the contact pressure p_n, the frictional heat can be computed by

$$\phi = \mu p_n V$$

where μ is the friction coefficient and V is the linear velocity.
From the contact area, an additional equation is obtained, which is of the type

$$\mathbf{P}\boldsymbol{\Psi}^N = \mathbf{0} \tag{6.21}$$

The matrix $\mathbf{P}$ defines the contact constraints prescribed by the real contact area geometry. The shape of $\mathbf{P}$ is (N_{xy}, Nr), with N_r the number of surface squares which are in contact. In this matrix, 1 corresponds to a non-contacting point while 0 is for those in contact.
Besides, it is of interest to note that the matrix $\mathbf{A}^N$ is time-independent because the time step $t_{N+1} - t_N$ remains the same for N ranging from 1 to N_t. Thus, this matrix is computed at the beginning of the

simulation.
Furthermore, the minimization technique has been chosen to avoid the computational cost of direct inversion of the matrix system in Eq.(6.15) which could become tremendous if a fine mesh is used. Thus a Newton algorithm is used to optimize the function f, which is a gradient based method, considering the constraints (6.21). Moreover, the computation of f and its gradient requires the construction of the matrix $\mathbf{A}^N$ and a matrix product. These two operations require a considerable memory storage and could increase considerably the computational time.
In order to increase the efficiency of the model, the matrix product is replaced by a discrete convolution and the Fast Fourier transform (FFT). For more details, the reader may refer to this work [Gallego *et al.*(2010)]. However, considering the velocity effect, the convolution technique is just an approximation of the matrix product. Indeed, the coefficients of $\mathbf{A}^N$ depends on the distance separating the contact point to the center of rotation. Nevertheless, in this work, the convolution has been used because the dimensions of the contact area are meaningless when compared to the radius of rotation R_c (i.e $R_c \gg L_x$ and $R_c \gg L_y$). This restrictive approximation has been used only to make benefits from the many advantages of the discrete convolution.
Therefore, using the FFT and the discrete convolution, the function f reads

$$f\left(\boldsymbol{\Psi}^N\right) = \frac{1}{2}\,t\left(\mathcal{F}^{-1}\left(\mathcal{F}\left(\mathbf{A}^N\right).\mathcal{F}\left(\boldsymbol{\Psi}^N\right)\right) - \boldsymbol{\Phi}^N + \boldsymbol{\Lambda}^N\right).\left(\mathcal{F}^{-1}\left(\mathcal{F}\left(\mathbf{A}^N\right).\mathcal{F}\left(\boldsymbol{\Psi}^N\right)\right) - \boldsymbol{\Phi}^N + \boldsymbol{\Lambda}^N\right) \quad (6.22)$$

where $\mathcal{F}$ is the FFT operator and $\mathcal{F}^{-1}$ is the inverse of the FFT.
As summary of this paragraph, we present the main steps of the thermal contact algorithm solving :

1. Definition of the studied geometry, surface roughness and physical properties;
2. Space-time discretization;
3. Computation of contact area A_r and pressure p_n using a contact mechanics model;
4. Computation of heat space-time distribution ϕ;
5. Solving of the thermal contact problem :
   - Computation of the matrix $\mathbf{A}^N$ from Eq.(6.16)
   - for $N = 1...t_{N_t}$:
     (a) $\boldsymbol{\Phi}^N$ and $\boldsymbol{\Lambda}^N$ are respectively computed from Eq.(6.17) and Eq.(6.18);
     (b) $\boldsymbol{\Psi}^N$ is found by minimizing the objective function f (see Eq.(6.19) or Eq.(6.22));
     (c) ϕ_1 and ϕ_2 are computed at $t = t_N$;
     (d) Computation of Φ_1 and Φ_2 and deduction of p_1 and p_2;
   - Computation of surface temperature T_1 and T_2;

6.3.6 The special case of a perfect contact : equal surface temperatures in contact zones

In this case, the gap of temperature vanishes in all the contact points and the different matrices involved in the contact problem read

$$A_{ij}^N = (T_1 + T_2)\,(x_j - x_i, y_j - y_i, t_{N+1} - t_N)$$

$$\Phi_j^N = \sum_{i=1}^{N_{xy}} \sum_{k=1}^{N} \sum_{l=0}^{l=n} \phi_{ik}^l T_2 \left(x_j - x_i, y_j - y_i, t_{N+1} - t_k\right)$$

$$\Lambda_j^N = \sum_{i=1}^{N_{xy}} \sum_{k=1}^{N} \lambda_{ik} \left(T_1 + T_2\right) \left(x_j - x_i, y_j - y_i, t_{N+1} - t_k\right)$$

The next section is dedicated to the results of the thermal contact problem. Several case studies are analyzed. The effect of velocity, contact area, roughness and the gap of temperature induced by contact local imperfections and the heat generation profile, are all studied in the following section.

6.4 Results and case studies

6.4.1 Model presentation

We consider a solid cube S_2 in contact with a rotating solid S_1 (see Fig.6.20). The dimensions of the contact zone and its localization with respect to the center of rotation are presented in Tab.6.2. The disk surface is flat while the static solid surface is rough, and its dimensions are $1mm \times 1mm$. Roughness is obtained from numerical surface generation techniques [Persson *et al.*(2002)] which are fractal based. Indeed, a self-affine surface is generated using a power-law spectral density. The surface sample considered in this study is illustrated in Fig.6.21. The fractal dimension is 0.59, the cutoff wave vectors are 2 and 10 and the surface is Gaussian with a root mean square equal to $6.49\mu m$.
The surface is discretized into 150×150 square elements. Hence, the unit square dimensions are $6.66 \times 6.66\mu m^2$. This size is sufficient for the considered scale of roughness. Indeed, a comparison has been done using this size and a coarser one ($10 \times 10\mu m^2$) and the results were practically identical. Thus, the present work concerns only the results obtained with the refined size (i.e $6.66 \times 6.66\mu m^2$). Furthermore, the material properties of both solids are presented in Tab.6.2 and the coefficient of friction is $\mu = 0.4$.
In this simulation, the solid S_2 is moved in the normal direction against the rotating solid S_2 with a motion δ. Thermo-mechanical deformations are not considered in this study. Using, the contact mechanics model, The contact area and the contact stress distribution have been computed. In Fig.6.22, the distribution of contact pressure is presented. The contact is localized on a few small contact zones. The fraction of the real contact area is 1.48%. The displacement that has been prescribed is $\delta = 10\mu m$. The displacement field in the surface of S_2 is shown in Fig.6.23.
In the following, several case studies are presented to study heat partition and surface temperature evolution.

$y_c\ (mm)$	$x_c\ (mm)$	$L_x\ (mm)$	$L_y\ (mm)$	μ
70.7	70.7	1	1	0.4

Table 6.2: Position of S_2 and the dimensions of the contact zone

	$\chi\ (m^2/s)$	$\kappa\,(W.m^{-1}.K^{-1})$	$E\ (GPa)$	ν
Solid S_1	10^{-5}	50	220	0.33
Solid S_2	35.10^{-7}	5	4	0.15

Table 6.3: The contacting solids thermal and mechanical properties

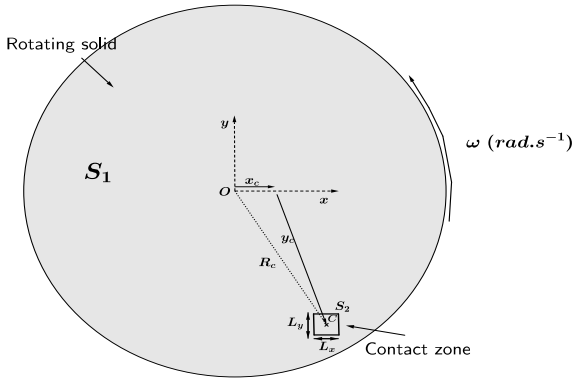

Figure 6.20: Schema of the interface

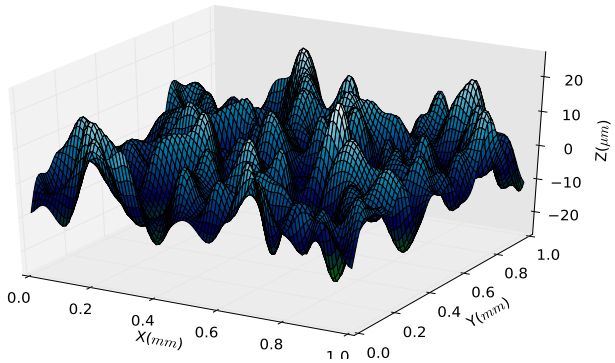

Figure 6.21: Profile of the studied fractal surface. The root mean square is $6.49\mu m$. The fractal dimension is 0.59 and the cutoff wave vectors are 2 and 10

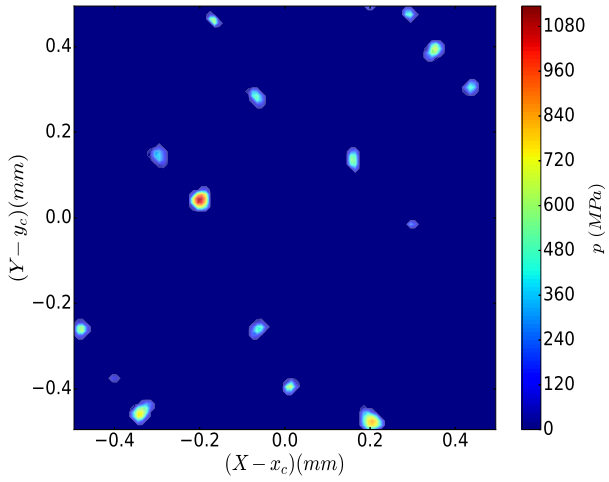

Figure 6.22: Contact pressure distribution for $\delta = 10\mu m$

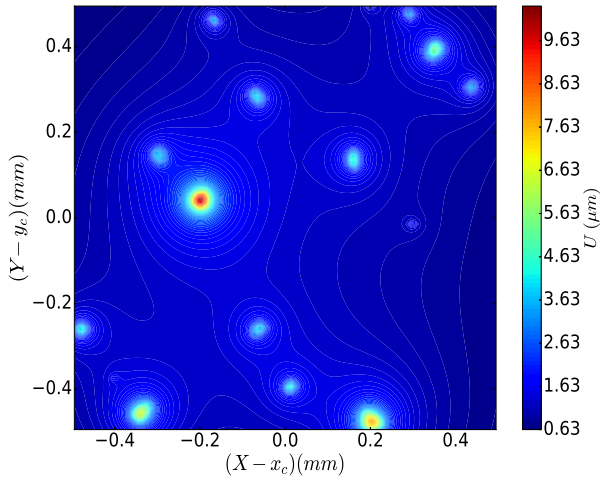

Figure 6.23: Normal displacement field for $\delta = 10\mu m$

6.4.2 Parametric study : case of a perfect contact

In this section, several case studies are presented with the purpose of analyzing the influence of velocity, load and roughness on heat distribution in the interface. For these case studies, perfect contact conditions are considered. Indeed, the continuity of temperature field is assumed within all contact points. The presence of an interface layer will be considered latter. In the different studies, the analysis concerns the evolution of the maximal temperature T_{max} with time t and the contact area fraction (%). Also, the parts of heat that go within each of the contacting solids are studied.

6.4.2.1 Influence of the velocity

In this case study, the velocity of S_1 is varied from 1 to 100 $rad.s^{-1}$. Thus, the amount of heat produced is constant within time. The studied interval of time is $[0, 4.5\,ms]$. For a fraction of contact area equal to 1.48%, the evolution of the coefficients of heat partition p_1 and p_2 with time is presented in Fig.6.24. As we can see, for the different velocities, almost 95% of heat goes to S_1. The part of heat p_1 increases with velocity. The evolution of the coefficients p_1 and p_2 is time dependent for $t \leq 2ms$. For $t \geq 2ms$, heat partition is almost steady. In the same figure, the slope of the evolution of both heat partition coefficients is shown. These curves confirm the observations made before.

	Case 1	Case 2	Case 3	Case 4
ω $(rad.s^{-1})$	1	10	50	100

Table 6.4: Angular velocity for the 3 studied cases

In order to evaluate the influence of the contact area on heat partition, we analyzed the thermal contact for different amounts of contact area. The amount of heat released for the different configurations is presented in Fig.6.25. The total heat depends on the contact pressure which increases with the contact area. Hence, the heat released increases with contact area.
In Fig.6.26 are shown the evolution of p_1 and p_2 with the contact area for the different velocities. These coefficients have been calculated for a time step for which the heat distribution is steady. As we can see from this figure, heat distribution is slightly affected by contact area. This slight variation of heat partition can be due to weak thermal diffusion for the case of very small contact areas. Thus, heat partition is mostly affected by velocity and the thermal properties of the contacting solids rather than the contact area.
With regard to surface temperature, Fig.6.27 presents the evolution of the steady maximal temperature T_{max} with the contact area. It is clear that both of contact area fraction and velocity affect this quantity. Indeed, increasing the contact area leads to increasing the pressure level. The increase of velocity and/or pressure results in a rise of the amount of heat released, and subsequently, the temperature level.
The distribution of surface temperature for both solids is shown in Figs.6.28-6.29. The velocity considered here is $100rad.s^{-1}$. The maximal temperature that is reached is $451°C$. One can remark the distortion of the temperature field on the mobile side of the interface. The direction of the hot zones is parallel to the velocity vector.
In this case study, it is shown that, for a fixed velocity within time, a steady state is reached within a time less than $1ms$ and that heat partition is strongly affected by velocity and thermal properties. Besides, velocity and contact area affect more the maximal reached temperature.

6.4.2.2 Influence of the velocity profile

In the previous case study, the velocity has been fixed, thus the amount of heat was constant within time. In this case study, we consider that solid S_1 was rotating at $t = 0$ with $\omega_0 = 10$ $rad.s^{-1}$. As contact is created at $t = 0$, the velocity decreases linearly according to Eq.(6.6) until it reaches a new velocity ω_1 at $t = t_0$. In this case study, t_0 is fixed at $100ms$ while ω_1 is varied from 5 to 0 $rad.s^{-1}$ (see Tab.6.5). For $\omega_1 = 0rad.s^{-1}$, the deceleration is $-10m.s^{-2}$. The studied interval of time is $[0, 200\,ms]$.
For this case study, we consider a fraction of contact area equal to 1.48%. In Fig.6.30 is shown the amount of heat Φ released within the time for the three considered cases. For $t \leq 100ms$, heat is decreasing linearly with velocity until t reaches $100ms$. From $100ms$, heat is constant.

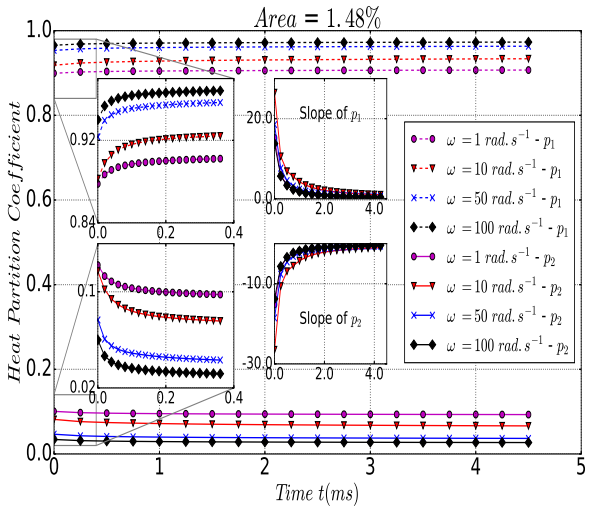

Figure 6.24: Time evolution of heat distribution for a given contact area

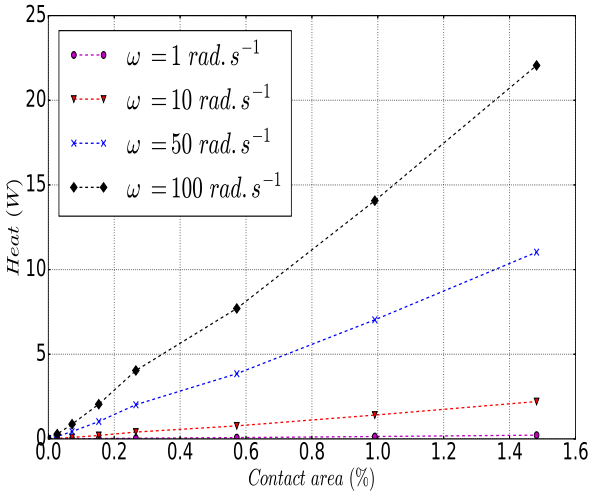

Figure 6.25: Total heat evolution with velocity and contact area. The total heat increases as the pressure increases with contact area

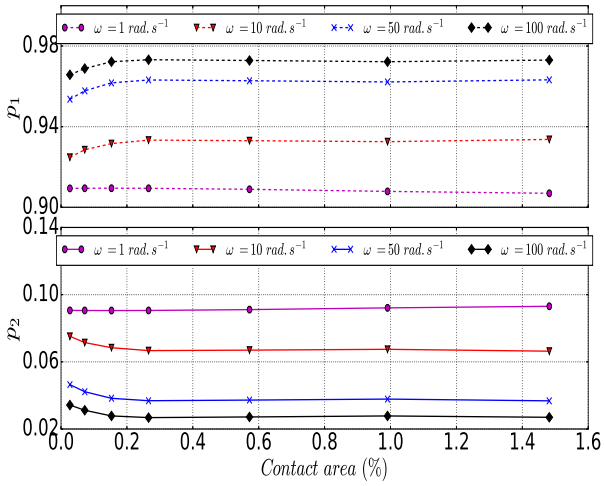

Figure 6.26: Evolution of the stationary heat distribution with contact area

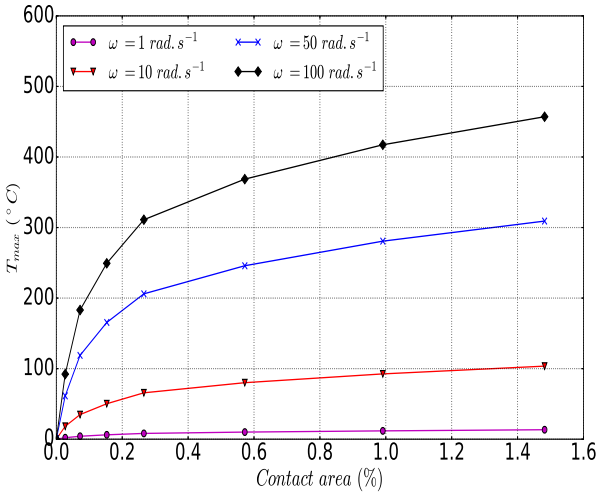

Figure 6.27: Evolution of the maximal steady temperature with contact area

In Fig.6.31, the time evolution of Φ_1 and Φ_2 is presented. It is clear that these quantities decrease with the decrease of Φ. For $\omega_1 = 0$, at $t = 100ms$, one can see that the sign of Φ_1 has changed. This means that heat is flowing from S_1 to S_2. This is essentially due to the absence of a heat source outside the two solids, so the solid S_1 gives heat to S_2 to maintain the thermal equilibrium. A similar observation can also be made for $\omega_1 = 1$. Here, the source of heat is insufficient and the maintain of the equilibrium is ensured by the heat flowing from the mobile side to the static one.
In Fig.6.32 are shown the coefficients of heat partition. For $\omega_1 = 5\ rad.s^{-1}$, the evolution of these coefficients is not affected. For the other cases, this evolution is considerable. As we can see, the decrease

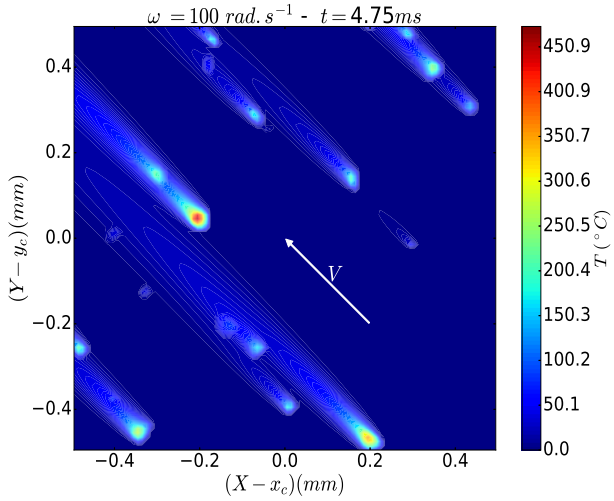

Figure 6.28: Surface temperature of solid S_1 (Mobile side)

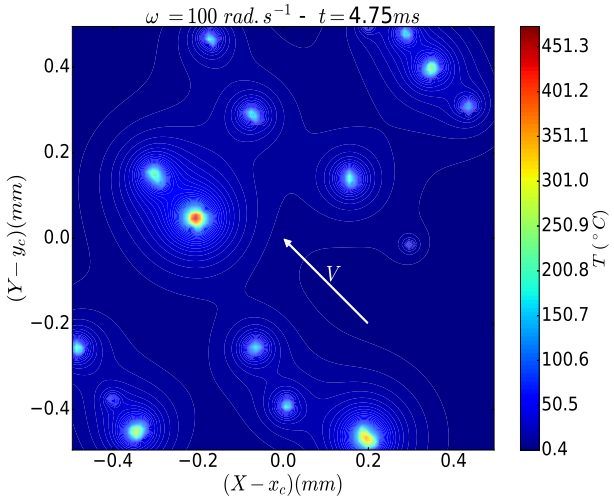

Figure 6.29: Surface temperature of solid S_2 (Static side)

of the velocity is followed by a decrease of p_1 and an increase of p_2. However, from the moment when the release of heat is constant, heat partition evolution retrieves progressively its initial evolution. This was predictable as the generation of heat becomes stable.
The maximal temperature evolution within time is presented in Fig.6.33. As the heat released within time decreases, the temperature decreases. For the case where the velocity vanishes at $t_0 = 100ms$, the temperature elevation almost vanishes in just $100ms$. For the other cases, a steady temperature is reached within $100ms$. This temperature is the same as the one reached if the final velocity has been considered from $t = 0$.
The temperature field at $t = 108ms$ is presented in Fig.6.34 (resp. Fig.6.35) for the surface of the mobile solid (resp. the static solid). The considered final velocity here is $\omega_1 = 0$. As we can see, the shape of the temperature distribution, at the scale of an asperity, is distorted in the mobile side of the contact. Indeed, the decrease of velocity leads to a reverse of the direction of heat flowing throw the mobile solid in several zones. These zones correspond to the side of asperities that get into contact first, which here corresponds to the left side of asperities. Therefore, this reverse heat leads to a local diminution of temperature in these zones.
From this case study, the effect of the velocity profile has been highlighted. It is shown that heat partition is transient when velocity evolves in time. When velocity attempts a steady state, the heat partition becomes steady.

	Case 1	Case 2	Case 3
$\omega_0\ (rad.s^{-1})$	10	10	10
$\omega_1\ (rad.s^{-1})$	5	1	0
$t_0\ (ms)$	100	100	100

Table 6.5: Parameters of the velocity profile (Eq.(6.6)) for the 3 studied cases

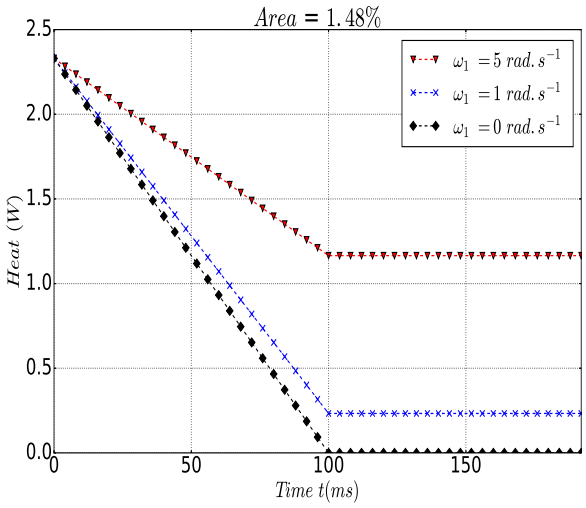

Figure 6.30: Time evolution of the released heat. From $t = 100ms$, the amount of heat is constant

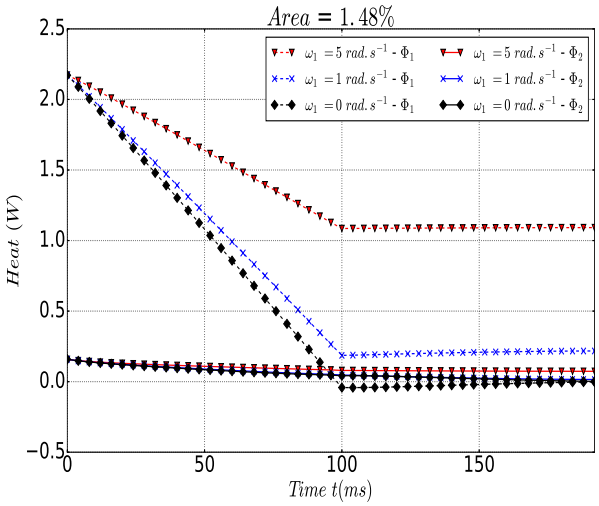

Figure 6.31: Time evolution of heat distribution

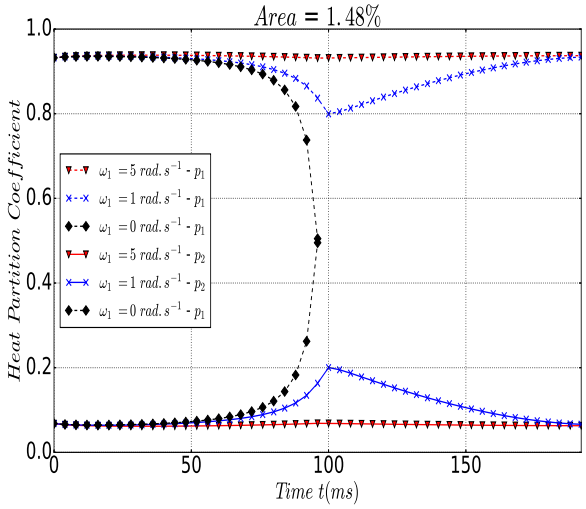

Figure 6.32: Time evolution of heat partition coefficients

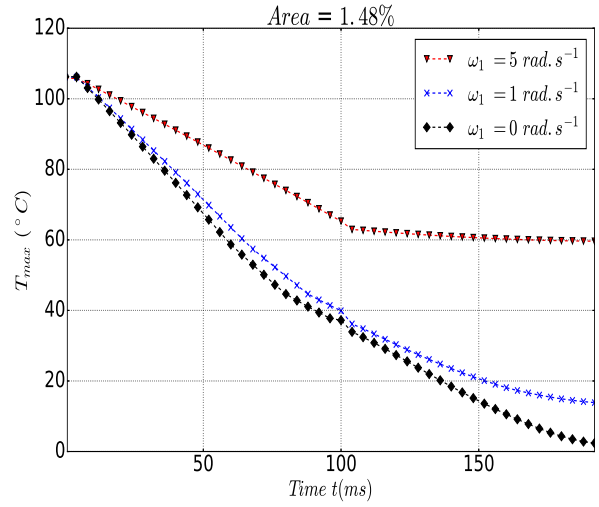

Figure 6.33: Time evolution of the maximal temperature

6.4.2.3 Influence of the ratio between conductivities

In the above case studies, the ratio between the two solid conductivities ($k = \kappa_2/\kappa_1$) was fixed at 0.1. By making some algebraical operations, it is easy to show, for the case of a perfect contact, that heat partition depends on this ratio with respect to the velocity. Of course, the temperature level is inversely proportional to the solid conductivity with respect to the heat applied. Therefore, in this paragraph, our interest is focused only on the influence of this ratio on heat partition.
The ratio k is varied from 0.1 to 2 and velocity is fixed within time. In Fig.6.36 (resp. Fig.6.37) is shown the evolution of heat coefficient p_1 with contact area, for a large time, and for an angular velocity

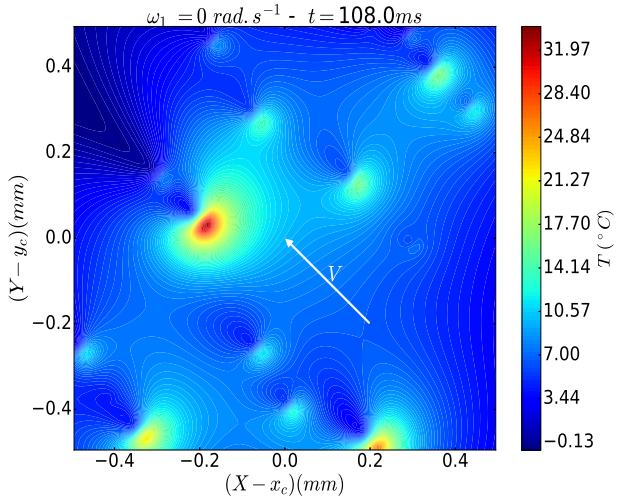

Figure 6.34: Temperature distribution on the mobile side

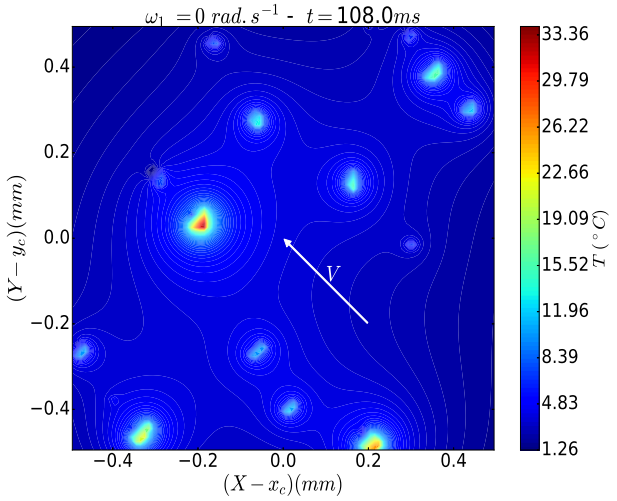

Figure 6.35: Temperature distribution on the static side

$\omega = 10\ rad.s^{-1}$ (resp. $100\ rad.s^{-1}$). From these figures, one can see that the ratio k affects strongly heat distribution. Indeed, p_1 decreases if k increases and this for the whole range of the considered contact areas. This is because if k increases, the second solid will need more heat to respect the thermal equilibrium between the two solids.
Moreover, it appears that p_1 is affected by the contact area. This dependency, as can be seen from the two figures, is amplified by increasing k with respect to velocity. Thus the influence of the contact area on the thermal equilibrium between the two solids depends on the ratio between their conductivities.

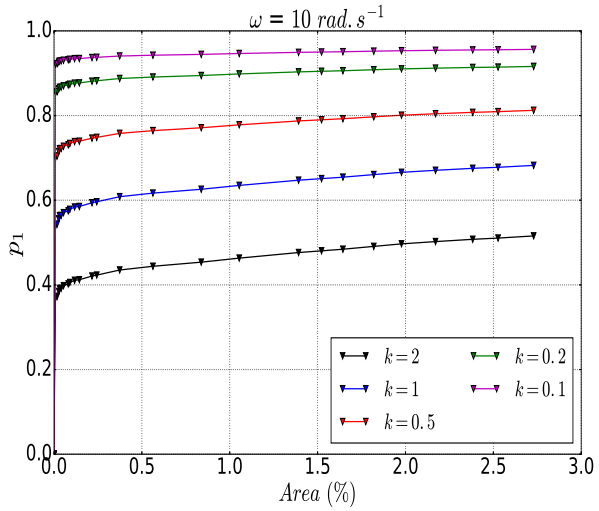

Figure 6.36: Evolution of the heat partition coefficient p_1 with contact area for different values of k and $\omega = 10\ rad.s^{-1}$

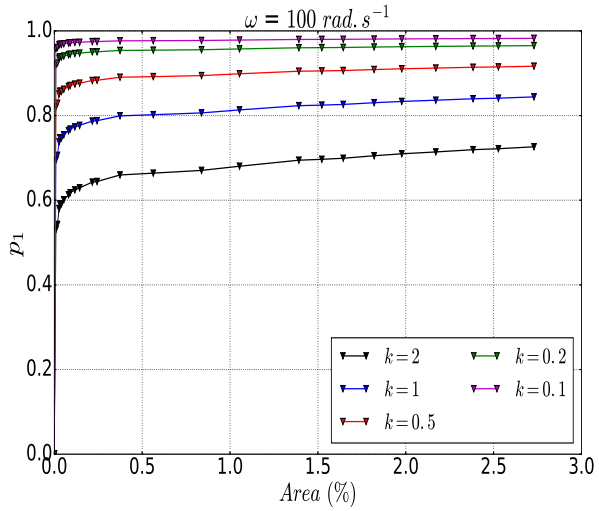

Figure 6.37: Evolution of the heat partition coefficient p_1 with contact area for different values of k and $\omega = 100\ rad.s^{-1}$

6.4.2.4 Influence of roughness

In the present paragraph, the effect of roughness is studied. For this aim, 10 different random samples have been generated numerically with different geometrical parameters. These samples are characterized by their root mean squares (RMS). Comparing to the previous sample, the same cutoff wave vectors have been conserved while the amplitude and the fractal dimension have been slightly changed. This means that the scale is the same for all the studied samples while the root mean square varies. In this study, the velocity is fixed within time.
First, the contact area evolution with the contact pressure is presented in Fig.6.38 for the different samples. From this figure, the discrepancy between the mechanical response of the different surfaces is clear. With regard to heat distribution, the evolution of heat partition coefficients is shown in Fig.6.39. It is clear from this figure that the different studied surfaces give approximately the same thermal response. The maximum difference does not exceed 1% which is meaningless with respect to heat coefficients.
However, the very low impact of roughness on heat distribution is not observed for the local maximal temperatures. The evolution with the contact area of this quantity is shown in Fig.6.40 for all the studied surfaces. One can see the difference in maximal temperature levels for the different surfaces. Indeed, the maximal temperature is directly linked to the maximum local pressure reached within the contact area with respect to velocity.
In Fig.6.41, the maximal temperature evolution with the root mean square is shown for a mean pressure equal to 3 MPa. As we can see, the maximal temperature tends to increase with the RMS. Indeed, RMS is high for surfaces having small asperities (small radius of curvature). Thus, for these small asperities, a high pressure is reached and so on for the local temperature.
Up to now, the perfect contact conditions have been considered and a surface heat generation has been considered. In what follows, we consider a temperature jump at the interface and many volume profiles of heat generation are examined.

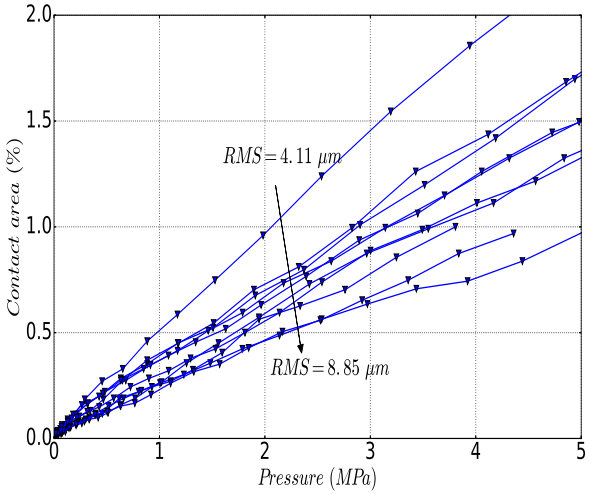

Figure 6.38: Load evolution with contact area for the studied samples

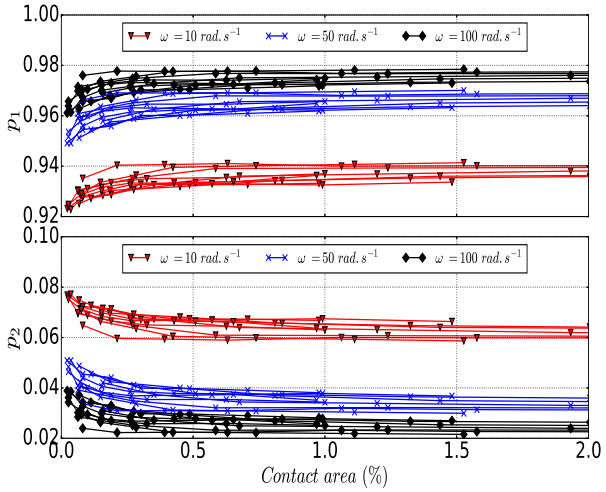

Figure 6.39: Steady heat distribution evolution with contact area

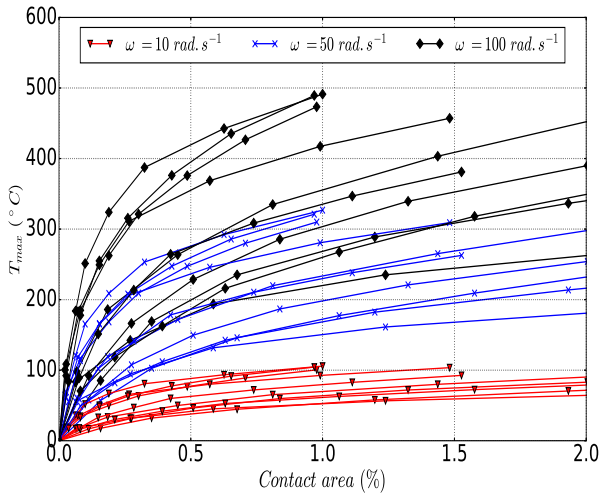

Figure 6.40: Maximal temperature evolution with contact area

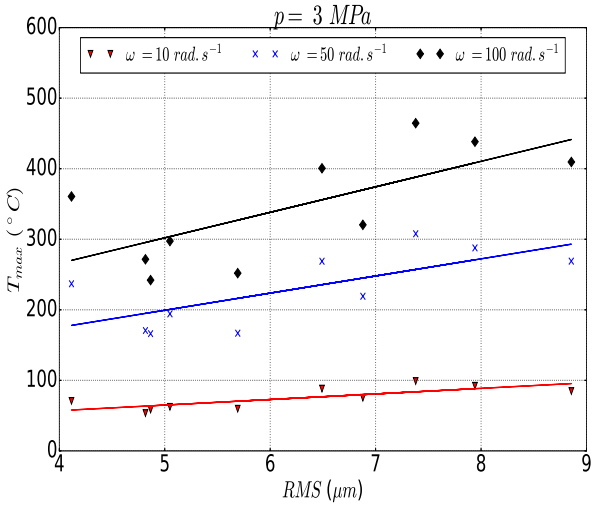

Figure 6.41: Influence of the RMS on the maximal temperature for $p = 3MPa$

6.4.3 Influence of the gap of temperature

In this section, the gap between the temperature of the two surfaces is considered. Several profiles of heat generation are investigated. Also, the effects of the local thermal resistance and capacitance are highlighted. To simplify the study, these parameters are fixed within the interface.

6.4.3.1 Influence of the heat generation profile

The exact location of the produced heat is not known for certain, many profiles of heat generation can be imagined. Therefore, we propose in this study 3 examples of heat distribution within a contact point (see Fig.6.42). A surface heat distribution in a plane between the two contacting points can be studied (see Fig.6.42(a)). A volume heat distribution is also possible within the interface layer. This heat can be distributed uniformly (see Fig.6.42(b)) or in a linear way (see Fig.6.42 (c)). In the linear case, the maximum of heat would be near to the sliding solid. For the three considered profiles, a study has been performed on the same sample studied in the first case study with a velocity of 100 $rad.s^{-1}$. The contact area is fixed at 1.48 %. For the interface, 10 components are considered. For each one of them, the capacitance C is 10^4 and the resistance R is 10^{-8}.
In Fig.6.43, the heat partition coefficients evolution with time is shown. As we can see, these coefficients are slightly affected by the profile of heat generation. However, it is clear that the volume heat generation leads to a decrease in the amount of heat that goes into the sliding solid. With regard to the maximal temperature (see Fig.6.44), the maximal temperature is reached in the static solid and especially for the case where heat is distributed uniformly within the interface. This is quite predictable, since in this case an important part of heat is created near to the static solid. Comparing to the other cases, the largest part of heat is generated near to the sliding solid, thus a considerable part goes to the sliding solid.

6.4.3.2 Influence of the thermal resistance

In this case study, we consider a volume uniformly distributed profile of heat and the capacitance is fixed at 10^4 for the 10 components of the interface. The thermal resistance has been varied and its impact on

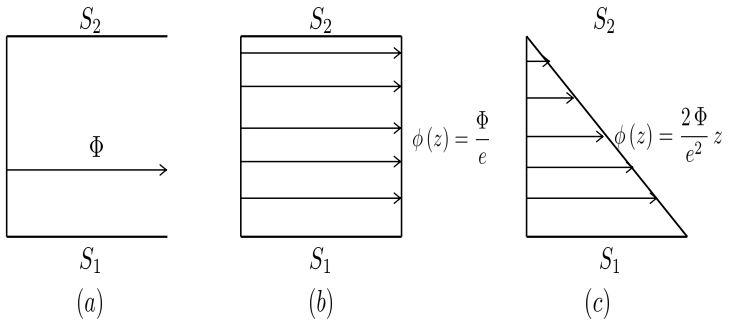

Figure 6.42: Heat generation profiles: (a) a plane heat distribution (b) a uniform distribution of heat and (c) a linear distribution of heat

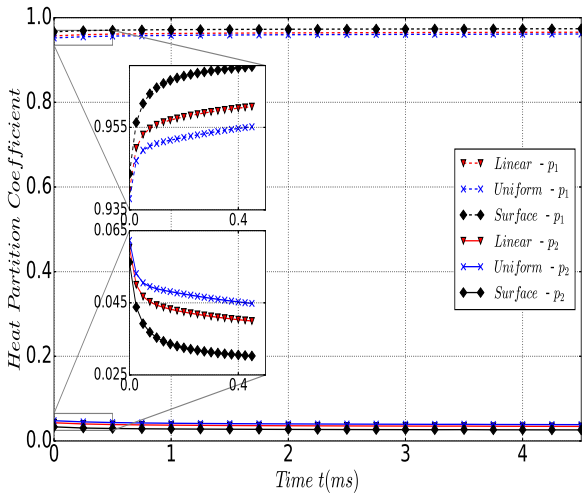

Figure 6.43: Time evolution of heat partition coefficients for the 3 studied profiles

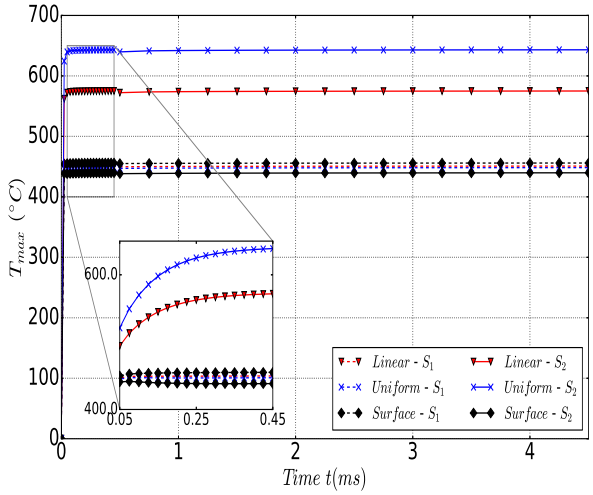

Figure 6.44: Influence of the profile of heat generation on the maximal reached temperature in both sides

the heat partition (resp. the maximal temperature) is highlighted in Fig.6.45 (resp. Fig.6.46). As we can see, the augmentation of the thermal resistance leads to a slight decrease of p_1. Subsequently, the gap between the maximal temperature of the two surfaces expands as the resistance increases. Additionally, the temperature evolution with time becomes low as long as the resistance decreases.

6.4.3.3 Influence of the thermal capacitance

In this case, the resistance is fixed at 10^{-8} and the capacitance is varied. Also, heat is uniformly distributed within the interface volume. As we can see from Fig.6.47, the capacitance affects heat partition only for $t \leq 0.5\,ms$. After this time, heat partition reaches a steady state. With regard to the maximal temperature evolution with time, shown in Fig.6.48, the effect of the capacitance is remarkable. Increasing this quantity, increases the time necessary to reach the steady temperature. The gap of temperature reached at the

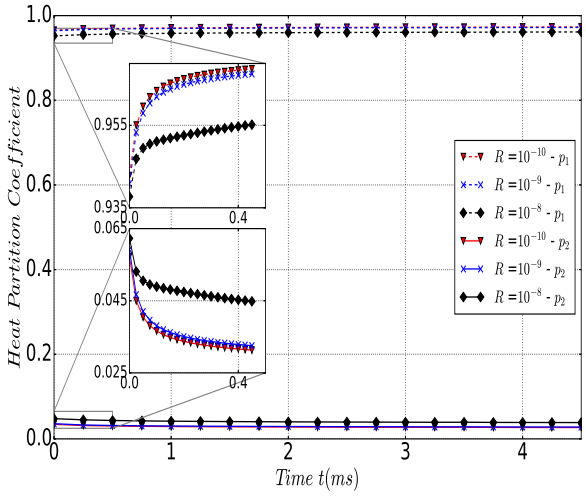

Figure 6.45: Influence of the thermal resistance on the time evolution of heat partition coefficients

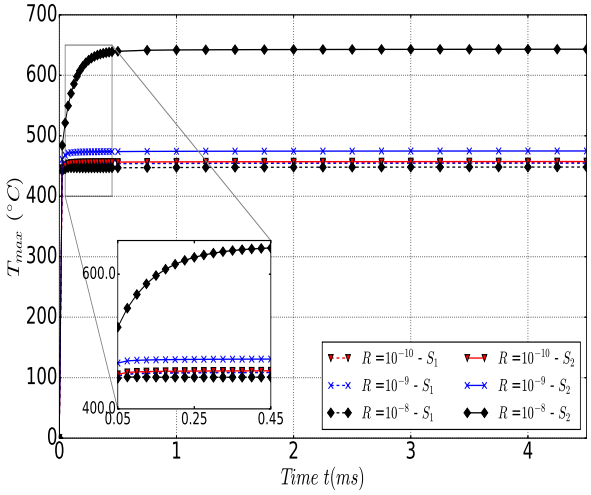

Figure 6.46: Influence of the thermal resistance on the maximal temperature in both sides

end is the same for all the studied cases. This is normal, as the gap is fully controlled by the thermal resistance.

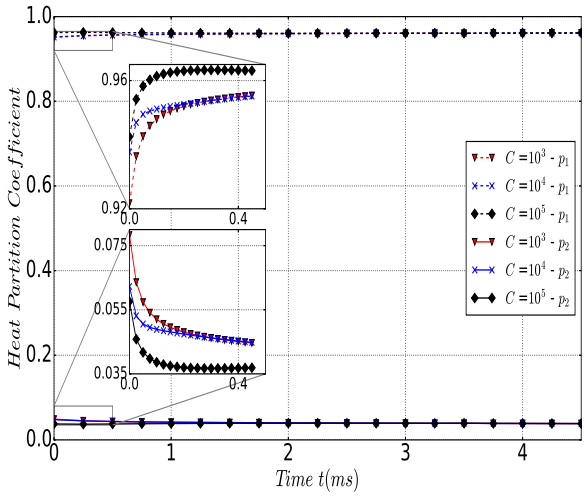

Figure 6.47: Influence of the thermal capacitance on the time evolution of heat partition coefficients

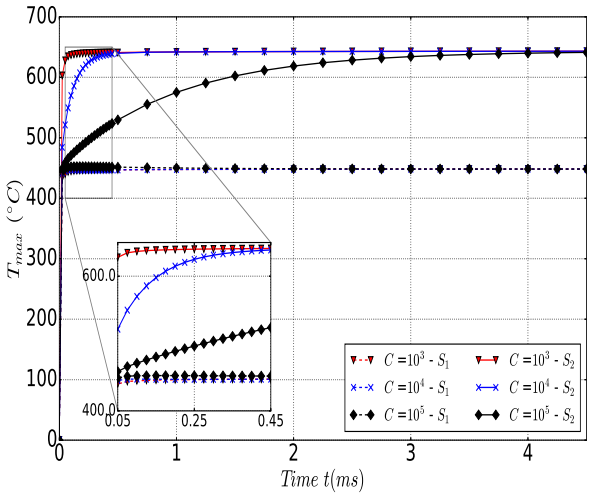

Figure 6.48: Influence of the thermal capacitance on the maximal temperature in both sides

From these studies, the effect of the properties of the interface and the heat generation profiles have been examined. As we can see, the interface influences slightly the heat partition, but the gap between the maximal temperature reached in the two solids is clearly affected. However, one must keep in mind that the ratio between the two solids conductivities is fixed here at 0.1. And as it has been presented in the previous section, this ratio can affect drastically the thermal balance. Thus, one could expect a major

impact of the interface parameters on heat partition if this ratio changes.
Furthermore, by these case studies, the objective was clearly to test the sensitivity of the thermal contact problem to the assumptions considered in the interface. Besides, the interface parameters have been introduced to get more realistic results based on a more realistic contact conditions. However, the choice of these parameters presents a difficulty that has to be overwhelmed in future works by using more sophisticated numerical tools that go beyond the considered scale in this study and a refined description of the physical phenomena occurring at these scales. In the next section, heat conduction induced by the presence of remote prescribed temperatures is studied.

6.5 The steady heat conduction in a sliding contact : consideration of non-zero infinity temperatures

In this section, we consider the stationary heat conduction in a sliding contact. Indeed, in the previous section, the studied system was isolated. Thus, the temperature rise takes its origin only from the heat produced at the interface. However, in real systems, this can not be true. Heat can flow from remote sources and/or temperature may not vanish far from the interface. This can influence the process of heat partition.
In this work, as the solids are assumed to be semi-infinite regions, it is assumed that the temperatures at infinity are non-zero and that the velocity is constant. These temperatures induce a large-scale constricted heat that flows into the two solids through the interface. Of course, this assumes that these temperature are enough remote to be affected by the interface. Therefore, in addition to the heat source present at the interface, there is a heat flowing throw the interface which is produced by the temperatures at the infinity.
In order to solve this problem, we can dissociate the two thermal problems. First, the heat generation problem can be solved using the same approach described in the above section but with a little adjustment to consider only the steady state. Second, the conduction problem is solved by matching the surface temperature at each point and reversing the heat flow direction using the idea proposed by Barber[Barber(1970)].
Combining the two solutions and considering that there is no gap of temperature between the two surfaces, we obtain

$$(F_1^s + F_2^s)(\phi_1) = F_2^s(\phi) + \theta_2^0 - \theta_1^0 \tag{6.23}$$

where F_1^s (resp. F_2^s) is respectively the steady version of F_1 (resp. F_2) and θ_1^0 (resp. θ_2^0) is the temperature at the infinity of solid S_1 (resp. S_2).
The surface temperatures of S_1 (resp. S_2) reads

$$\theta_1 = F_1^s(\phi_1) + \theta_1^0 \ \left(\text{resp. } \theta_2 = F_2^s(\phi_2) + \theta_2^0\right) \tag{6.24}$$

Eventually, the presence of a thin interface layer can also be considered but it is not the object of this section. The contact problem is solved using the same technique of optimization. The different variables are spatially discretized and the discrete convolution is used instead of the matrix product. The objective function is given by

$$f\left(\boldsymbol{\Phi_1}^N\right) = \frac{1}{2}\,{}^t\left(\mathbf{F}\boldsymbol{\Phi_1} - \boldsymbol{\Theta}\right).\left(\mathbf{F}\boldsymbol{\Phi_1} - \boldsymbol{\Theta}\right) \tag{6.25}$$

where

$$F_{ij} = (T_1 + T_2)(x_j - x_i, y_j - y_i, \infty)$$

$$\Theta_j = \sum_{i=1}^{N_{xy}} \phi_i T_2 \left(x_j - x_i, y_j - y_i, \infty\right) + \theta_2^0 - \theta_1^0$$

Unlike the transient problem treated in the last section, the thermal equilibrium equation is only spatial. Hence, no temporal scheme is needed to solve this problem. The minimization of the objective function is performed with quadratic programming as it has been presented in section 6.3.5. In the following, some results are presented and the effect of heat flowing from non-zero infinity temperatures is highlighted.

6.5.1 Results

We consider the same model studied in section 6.4. In order to highlight the effect of non vanishing temperatures at infinity, different values of them are considered in this study. In Tab.6.6 are summarized the values of these boundary temperatures. Two constant velocities are considered : 10 and 100 $rad.s^{-1}$. In Figs.6.49-6.50, are shown the evolution of the coefficient of heat partition p_1 with the contact area, for the two studied velocities. From these figures, we can see that p_1 increases as long as θ_1^0 is great than θ_2^0 (cases $C1$-$C4$), and the reverse is also true (cases $C5$-$C8$). Indeed, if $\theta_1^0 > \theta_2^0$, heat will flows from S_1 to S_2, and if we consider the heat source at the interface, the part of heat that goes to S_1 will be less than the one corresponding to zero temperature at infinity, and thus p_1 will decrease. If $\theta_1^0 < \theta_2^0$, an additional part of heat will go to S_1, and thus p_1 will increase.
Furthermore, we can see that increasing the contact area decreases the effect of infinity temperatures. This is essentially due to the fact that increasing contact area, leads to an increasing in the heat generated at the interface. Subsequently, the distribution of heat becomes less dependent on infinity temperatures. Moreover, the influence of these temperatures depends on the velocity. Indeed, the heat supplied at the interface for 100 $rad.s^{-1}$ is greater than the one flowing from solid boundaries. Thus, the effect of infinity temperatures is marginal in this case. But for 10 $rad.s^{-1}$, the amount of heat generated is less than the one induced by infinity temperatures.
Therefore, heat distribution is affected by the thermal balance between heat generated at the interface and heat flowing from solid boundaries. Consequently, the surface temperature is modified. Figs.6.51-6.52 present the evolution of the maximal temperature with the contact area, for the same case studies. As we can see, if $\theta_1^0 > \theta_2^0$ the maximal temperature is increasing with θ_1^0, but if $\theta_1^0 < \theta_2^0$, the maximal temperature is almost not affected except if the contact area is relatively very small. The impact of conduction depends not only on infinity temperatures but also the ratio between the two solid conductivities. Indeed, the relatively high conductivity of S_1 ($\kappa_1 = 10\ \kappa_2$) makes the gradient of temperature in S_1 lower than the one in S_2. Thus, the offset of temperature, that is observed in these figures, exists only if S_1 is hotter than S_2 (i.e $\theta_1^0 > \theta_2^0$). Moreover, if the velocity is weak or the contact area is very small, the mechanism which is predominant is the conduction between solid boundaries and the surface temperature level is prescribed by infinity temperatures. For instance, this is the case for case $C8$ and $\omega = 10\ rad.s^{-1}$ and a contact area less than 0.6%.

Cases	C1	C2	C3	C4	C5	C6	C7	C8
θ_1^0 ($^\circ C$)	1	10	50	100	0	0	0	0
θ_2^0 ($^\circ C$)	0	0	0	0	1	10	50	100

Table 6.6: The temperatures at the infinity for the different case studies

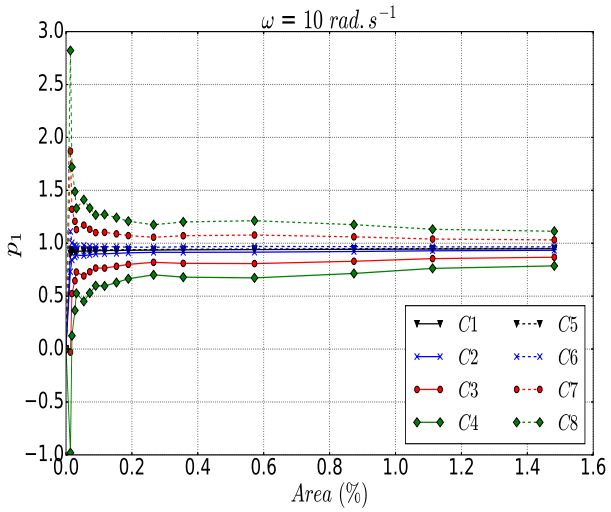

Figure 6.49: Evolution of heat coefficient partition p_1 with contact area for $\omega = 10\ rad.s^{-1}$

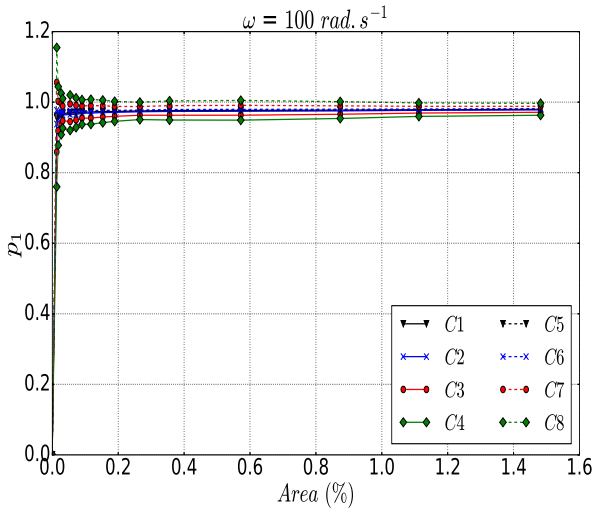

Figure 6.50: Evolution of heat coefficient partition p_1 with contact area for $\omega = 100\ rad.s^{-1}$

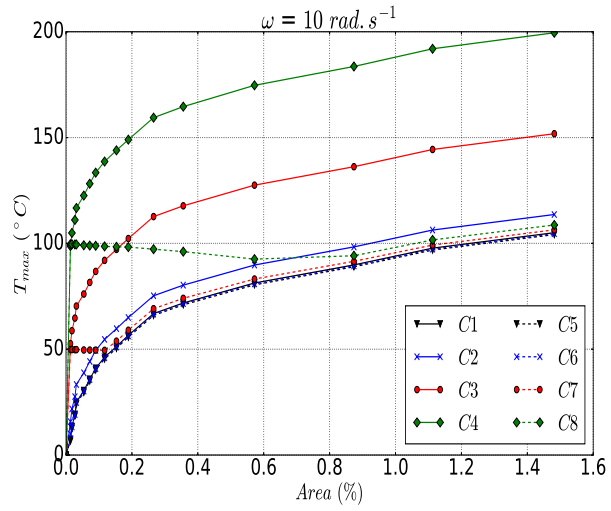

Figure 6.51: Impact of remote temperatures on the maximal temperature with contact area for $\omega = 10\ rad.s^{-1}$

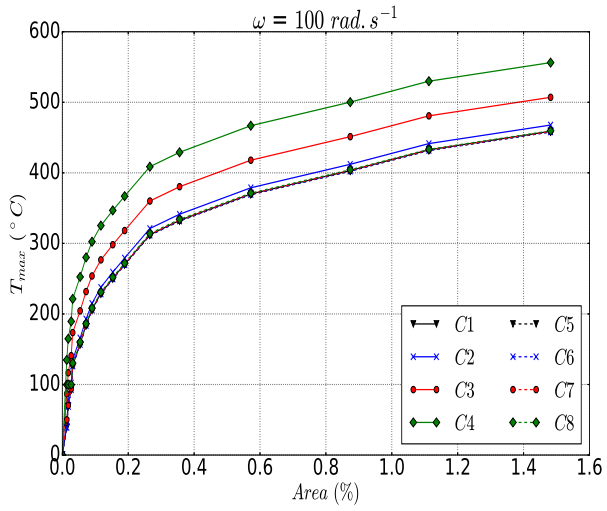

Figure 6.52: Impact of remote temperatures on the maximal temperature with contact area for $\omega = 100\ rad.s^{-1}$

Conclusions

In this work, heat partition and surface temperature in sliding contact problems have been studied using a numerical model based on heat source theory. In this model, surface roughness and velocity are both considered. Also, heat is produced within the contact surface or a thin layer introduced between the two contacting solids. The problem is discretized and is transformed into a linear system that is solved with optimization techniques. FFT technique is used to reduce the computational time. Moreover, the effect of remote prescribed temperatures has been also introduced in the steady state problem.

Through a parametric study, outcomes such as the evolution of the maximal temperature and the coefficients of heat partition, have been presented and show plausible behaviors.
From the obtained results, it has been shown that heat partition essentially depends on solids velocities and the ratio between their conductivities. With regard to the contact area, it has been shown that its effect is mainly controlled by this ratio. Also, several surface samples have been studied and the effect of roughness, quantified by the standard deviation, has been presented. As is shown, roughness affects slightly heat distribution, but influences the maximal reached temperature. Moreover, the consequences of a time-dependent velocity have been highlighted. Both heat partition and the maximal temperature are highly affected by the transient decrease of velocity.
Furthermore, the effect that can engender a volume heat production and/or the presence of wear debris have been considered by introducing a thin small layer at the interface. This interface has been modeled by a set of thermal components composed from a thermal resistance and a capacitance. Heat is generated within this components. A case study has been realized to highlight the effect of the profile of heat generation and the presence of the layer. Different profiles of heat generation have been tested and it appears that they influence only the jump of temperature at the interface. Also, results show that the jump between the two surfaces temperature is mainly controlled by the thermal resistance. Also, the mass effect that slows the temperature rise is also induced by the capacitance. However, from a physical point of view, more tools are needed to identify properly the properties of the interface layer and the profile of heat generation.
Otherwise, these results have been obtained for an isolated case where the only source of heat is the interface. As it is not the case for real systems, in the last part of this work, remote prescribed temperatures have been considered. Results show that a temperature difference between solid remote boundaries causes a heat flowing through the interface which affect considerably heat partition and the temperature field.
Finally, many improvements can be done to the present model, in particular thermo-mechanical coupling between the shear process and frictional heat generation. Also, in this work, it is supposed that all the frictional energy is converted to heat, which is not 100 % true. Indeed, only a major part transforms to heat and its amount may depend on several mechanisms that have to be identified properly.

Acknowledgments

The present research work has been supported by the International Campus on Safety and Intermodality in Transportation, the Hauts-de-France Region, the European Union, the Regional Delegation for Research and Technology, the Ministry of Higher Education and Research, the French National Research Agency (ANR COMATCO), and the National Center for Scientific Research. The authors gratefully acknowledge these institutions for their support.

Bibliography

[Archard(1959)] Archard, J. F. *The temperature of rubbing surfaces.* Wear, 1959, 2(6), 438-455.

[Barber(1970)] Barber, J. R. *The conduction of heat from sliding solids. International Journal of Heat and Mass Transfer.* International Journal of Heat and Mass Transfer, 1970, 13(5), 857-869

[Blok(1937)] Blok, H. *Theoretical Study of Temperature Rise at Surfaces of Actual Contact under Oiliness Conditions.* Proc. Inst, of Mechanical Engineers General Discussion of Lubrication, 1937, 2, 222-235.

[Blok(1963)] Blok, H. *The flash temperature concept.* Wear, 1963, 6(6), 483-494.

[Bos and Moes(1995)] Bos, J., & Moes, H. *Frictional heating of tribological contacts.* Journal of tribology, 1995, 117(1), 171-177.

[Bush *et al.*(1975)] Bush, A., Gibson, R. & Thomas, T. *The elastic contact of a rough surface.* Wear, Elsevier, 1975, 35, 87-111

[Carslaw and Jaeger(1959)] Carslaw, H. S., & Jaeger, J. C. *Conduction of heat in solids.* Oxford: Clarendon Press, 1959

[Chao and Trigger(1956)] Chao, B. T., & Trigger, K. J. C. *Temperature distribution at tool-chip and tool-work interface in metal cutting.* ASME, 1956.

[Ciavarella *et al.*(2006)] Ciavarella, M., Delfine, V. & Demelio, G. *A re-vitalized Greenwood and Williamson model of elastic contact between fractal surfaces.* Journal of the Mechanics and Physics of Solids, Elsevier, 2006, 54, 2569-2591

[Coulibaly *et al.*(2014)] Coulibaly, M., Chassaing, G., & Philippon, S. *Thermomechanical coupling of rough contact asperities sliding at very high velocity.* Tribology International, 2014, 77, 86-96.

[Denape and Laraqi(2000)] Denape, J., & Laraqi, N. *Aspect thermique du frottement: mise en évidence expérimentale et éléments de modélisation.* Mécanique & industries, 2000, 1(6), 563-579.

[Furey(1964)] Furey, M. J. *Surface temperatures in sliding contact.* ASLE TRANSACTIONS, 1964, 7(2), 133-146.

[Gallego *et al.*(2010)] Gallego, L. and Nelias, D. and Deyber, S. *A fast and efficient contact algorithm for fretting problems applied to fretting modes I, II and III.* Wear, 2010, 268, 208–222.

[Gecim and Winer(1985)] Gecim, B., & Winer, W. O. *Transient temperatures in the vicinity of an asperity contact.* Journal of tribology, 1985, 107(3), 333-341.

[Greenwood and Williamson(1966)] Greenwood, J. & Williamson, J. *Contact of nominally flat surfaces.* Proceedings of the Royal Society of London. Series A. Mathematical and Physical Sciences, The Royal Society, 1966, 295, 300-319

[Hou and Komanduri(2000)] Hou, Z. B., & Komanduri, R. *General solutions for stationary/moving plane heat source problems in manufacturing and tribology.* International Journal of Heat and Mass Transfer, 2000, 43(10), 1679-1698.

[Johnson(1987)] Johnson, K. L. *Contact mechanics.* Cambridge university press, 1987

[Kennedy(1984)] Kennedy, F. E., *Thermal and thermomechanical effects in dry sliding.* Wear, 1984, 100(1), 453-476.

[Komanduri and Hou(2001)] Komanduri, R., & Hou, Z. B. *Analysis of heat partition and temperature distribution in sliding systems.* Wear, 2001, 251(1), 925-938.

[Landman *et al.*(1993)] Landman, U., Luedtke, W.D., & Ringer, E.M. *Molecular dynamics simulations of adhesive contact formation and friction, in Fundamentals of Friction: Macroscopic and Microscopic Processes, Singer, I.L. and Pollock, H.M. (Eds.), Kluwer Academic Publishers, Dordrecht, 463.*. Kluwer Academic Publishers, 1993, Dordrecht, 463.

[Laraqi(1996)] Laraqi, N. *Phénomène de constriction thermique dans les contacts glissants.* International journal of heat and mass transfer, 1996, 39(17), 3717-3724.

[Laraqi *et al.*(2009)] Laraqi, N., Alilat, N., de Maria, J. G., & Baïri, A. *Temperature and division of heat in a pin-on-disc frictional device—exact analytical solution.* Wear, 2009, 266(7), 765-770.

[Persson *et al.*(2002)] Persson, B., Bucher, F. & Chiaia, B. *Elastic contact between randomly rough surfaces: comparison of theory with numerical results.* Physical Review-Series B-, American Physical Society, 2002, 65, 184106

[Sadowski *et al.*(2010)] Sadowski, P., & Stupkiewicz, S. *A model of thermal contact conductance at high real contact area fractions.* Wear , 2010, 268(1), 77-85.

[Salti and Laraqi(1999)] Salti, B., & Laraqi, N. *3-D numerical modeling of heat transfer between two sliding bodies: temperature and thermal contact resistance.* International Journal of Heat and Mass Transfer, 1999, 42(13), 2363-2374.

[Tian and Kennedy(1994)] Tian, X., & Kennedy, F. E., *Maximum and average flash temperatures in sliding contacts.* Journal of Tribology, 1994, 116(1), 167-174.

[Vick(2001)] Vick, B., & Furey, M. J. *A basic theoretical study of the temperature rise in sliding contact with multiple contacts.* Tribology International, 2001, 34(12), 823-829.

[Waddad *et al.*(2016)] Waddad, Y. , Magnier, V. , Dufrénoy, P. & De Saxcé, G. *A multiscale method for frictionless contact mechanics of rough surfaces.* Tribol. int., 2016, 96, 109-121.

[Willner(2008)] Willner, K. *Fully coupled frictional contact using elastic halfspace theory.* Journal of Tribology, American Society of Mechanical Engineers, 2008, 031405, 1–8.

[Zeng *et al.*(1997)] Zeng, Z., Brown, J. M. B., & Vardy, A. E. *On moving heat sources.* Heat and mass transfer, 1997, 33(1-2), 41-49.

Transition

Contact mechanics and wear issues have been studied in Part 1 of this thesis. The two first chapters of Part 2 deal with the thermal contact problem. This chapter aims to integrate these features into a large scale numerical model of a sliding contact system, with the objective of studying their effects on the system behavior.
Hence, in this chapter, we present a multi-scale strategy which embeds a macro-scale Finite Element model with surface parameters obtained from micro-contact calculations. These parameters evolve constantly as wear continues modifying the surface geometry. The different steps of the methodology are highlighted in this chapter and the micro-contact models are briefly presented, as they were already presented in the previous chapters.
As an application, a thermo-mechanical analysis of a pin-on-disc system is conducted. The results show the influence of interface phenomena on contact data such as temperature and pressure.

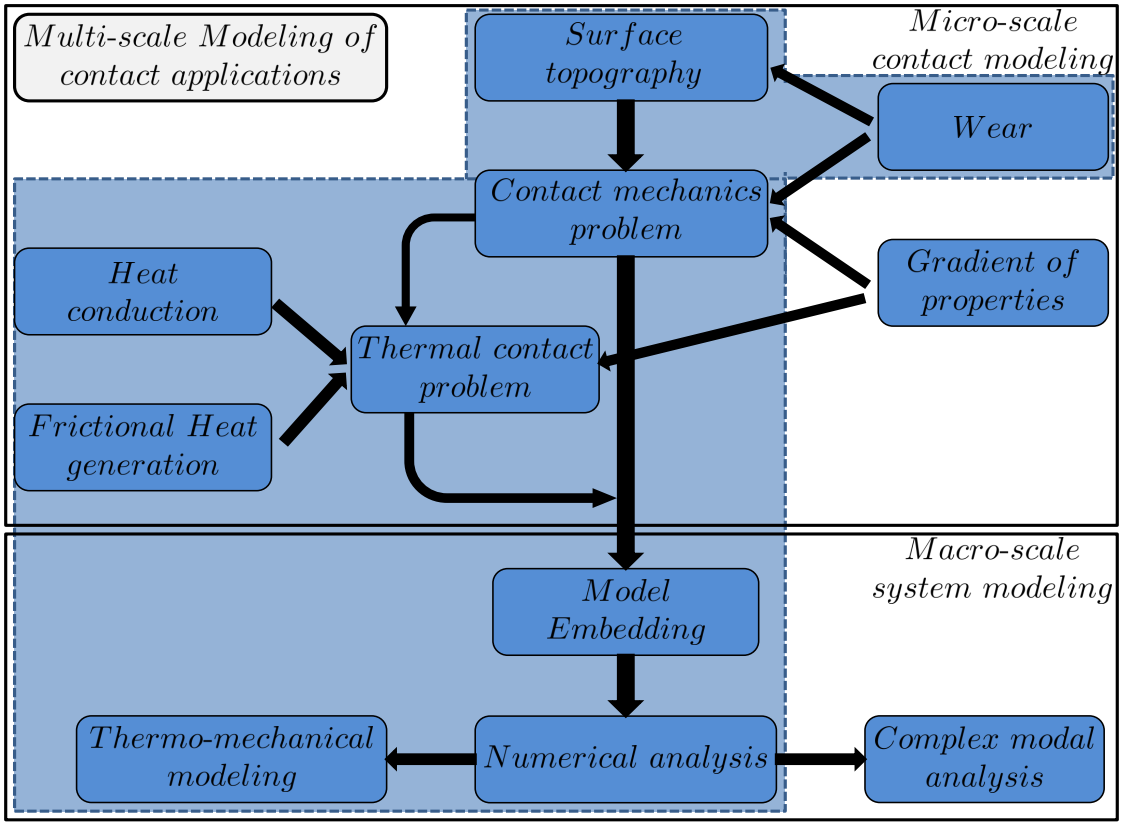

This figure presents the complete plan of this thesis. The placing of this chapter is highlighted by a blue box in the background.

Chapter 7

Multi-scale thermo-mechanical modeling of a pin-on-disc system

Contents

Multi-scale thermo-mechanical modeling of a pin-on-disc system

Y. Waddad, V. Magnier, P. Dufrénoy, G. De Saxcé

Université de Lille Nord de France, F-59000 Lille, France
Lille1-LML, F-59655 Villeneuve d'Ascq, France
CNRS, FRE 8107, F-59655 Villeneuve d'Ascq, France

Abstract

This work presents a multi-scale strategy for thermo-mechanical simulation of sliding systems taking into account contact phenomena occurring at much lower scales than the system's one. At macro-scale, a finite element model is considered to model the system interactions considering a thermo-elastic behavior. At micro-scale, based on our previous works, the thermal and mechanical contact problems are solved considering surface roughness and wear. For this aim, the surface is discretized into a grid of square elements and the discrete convolution technique is used with the FFT to accelerate the solving scheme. Concerning wear, Archard's law is used with a wear rate coefficient depending on temperature. From these models, contact parameters such as stiffness and heat partition coefficient are integrated into the macro-scale model, and this for each surface element. Moreover, the solving scheme is transient allowing to update the surface topography under wear effect.
As an example, this multi-scale strategy is used to study the thermo-mechanical behavior of a pin-on-disc system. With this model, the influence of the interface behavior and wear on the system response, are clearly shown. Conversely this strategy gives results locally, close to the physical mechanisms involved in the contact. A comparison is performed with a classical model considering perfect contact conditions.

keywords : Contact analysis, Surface Roughness, Multi-scale Approaches, Finite Element Modeling, Wear, Thermo-mechanical Analysis, FFT technique

7.1 Introduction

In frictional systems, as brakes, the contact interface behavior has a key role on performances. Indeed, the contact interface is the location where kinetic energy is transformed into frictional heat energy. As a consequence, high temperatures, resulting from frictional heat, are reached within these zones. This heating induces wear and local damages that could affect and change the tribological behavior of the contact interface [Archard(1959)]. Furthermore, wear is also responsible of a continuous modification of the contact interface by redistributing the contact area during loading. This evolution modifies the contact conditions and subsequently the interaction between the system components. Thereby, in a braking system, the contact surface and local temperatures vary according to the combination of heating and dilation but also wear which is itself influenced by temperature.
In this regard, the aim of the present work is to present an efficient numerical strategy of thermo-mechanical system simulation which considers the contact interface evolution, in order to highlight the impact of the contact interface on the thermo-mechanical behavior of the process and conversely.
From a numerical point of view, the main challenge is to propose a framework which considers both the macro-scale interactions between the system components, and on the other side, the interface phenomena occurring at a lower scale than the system's one (i.e meso and micro-scale). Usually only the macro-scale is considered while the other one is neglected. For example, in [Newcomb(1960), Day and Newcomb(1988),

Kao *et al.*(2000), Dufrénoy and Weichert(2003)], thermo-mechanical modeling have been performed by considering a flat contact with a perfect interface. Contact modeling at this stage is limited to flat surfaces because the explicit meshing of contact roughness in this kind of models is computationally expensive. Thus, the strategy that we propose in this work allows to consider contact phenomena in large-scale modeling. Furthermore, in these strategies, the heat released at the interface is distributed between the contacting solids using a heat coefficient calculated from the thermal effusivity. However, this approach does not consider the velocity and the real contact area effect on heat partition.

As regards the problem of micro-scale contact mechanics simulation between rough surfaces, most of the contact models use the concept of surface asperities introduced in the classical work of[Greenwood and Williamson(1966)]. Many improvements of this model have been proposed, for instance by including interactions of asperities[Ciavarella *et al.*(2006), Waddad *et al.*(2016)]. Other multi-scale approaches have been developed with spectral density [Persson *et al.*(2005)]. Numerical methods have been also used to solve the rough contact problem, using optimization techniques, either with the finite element method[Pei(2005)] or the discretized half space theory[Willner(2008)]. The latter presents the advantage of a reduced CPU time especially if the Fast Fourier Transform (FFT) is used to accelerate the solving scheme[Gallego *et al.*(2010)]. The concept of this method has been extended to model the rough contact of multi-layered solids [Waddad *et al.*(2017^b)].

Furthermore, the thermal contact of rough surfaces has been the subject of many works. For the static contact, the theoretical framework was firstly proposed in the pioneering works [Cooper *et al.*(1969), Mikic(1974)]. For sliding contacts, most of the works are based on the method of heat sources which was developed in the works of [Blok(1937), Carslaw and Jaeger(1959)]. Based on this technique, we proposed a numerical approach that takes into account both heat conduction and heat generation [Waddad *et al.*(2017^d)]. This model uses the FFT technique and optimization schemes.

The surface temperature is crucial for micro-contact analysis as it can be used to estimate the wear volume. Indeed, the high temperatures reached within the contact surface lead to wear. As regards wear modeling, a large variety of wear models has been proposed in [Meng(1995)] based on several theoretical and experimental works that exist in the literature. From these models, the amount of worn volume can be expressed as a function of contact load, sliding distance and a wear rate that depends on material properties and wear mode. However, the difficulty in wear modeling is that there is no universal model that can be applied to all situations[Williams(1999)]. Indeed, most of the existing models are empirical. Nevertheless, it appears that most of the wear mechanisms (e.g. abrasive and adhesive modes) can be described with Archard's law [Archard(1953), Kato(2002)]. In this case, wear volume is proportional to the normal load and the sliding distance. Yet, wear rate depends on the type of wear and has to be identified with appropriate experiments. For instance, wear rate corresponding to adhesive wear of metals has been quantified by [Archard(1953)], depending on the operating conditions and material properties.

In this work, we propose a multi-scale numerical strategy which considers both macro and micro-scale features. As an application, a thermo-mechanical analysis of a pin-on-disc system is performed. At macro-scale a finite element model is developed for the system. As mentioned before, the explicit meshing of contact roughness in this kind of models is computationally expensive, so the studied contact surface remains flat. Then, the system's model is embedded, with the contact surface behavior, using an approach developed in [Waddad *et al.*(2016)]. This multi-scale homogenization technique is done zone by zone, so that each zone has its local contact properties. The implementation of this technique allows to get a macroscopic contact localizations depending only on the size and the geometry of each homogenized zone. The strategy incorporates three mains steps. First, the micro-contact modeling is performed with the mechanical, thermal and wear modeling strategies that we have developed in the previous works (see [Waddad *et al.*(2016), Waddad *et al.*(2017^a), Waddad *et al.*(2017^b), Waddad *et al.*(2017^c), Waddad *et al.*(2017^d)]). From micro-scale modeling, the computed parameters are integrated into the macro-scale

model [Waddad *et al.*(2016)]. Then, a transient thermo-mechanical analysis is performed. At the end of this step, a second micro-scale analysis is conducted to analyze the surface evolution. After this step, the time is updated and a new analysis is performed taking into account the new surface topography and the initial temperature field for this time step. The different steps of the strategy are presented in the first section. Then, the micro-contact modeling features are briefly described. The results obtained, with this strategy, on a pin-on-disc system, are presented in the last section. Besides, a comparison with a numerical model considering a perfect contact is performed with the aim to highlight the interface role on the system behavior.

7.2 Presentation of the multi-scale modeling strategy

7.2.1 Global strategy

The aim of this work strategy is to integrate the contact interface behavior in a macroscopic numerical model without representing the real interface topography (see Fig.7.1). This choice is motivated by the fact that there is a large gap between the system's scale and the roughness one where the micro contact interface phenomena are taking place. For this reason, the contact interface is flat in the macro-scale model but embedded with many parameters that traduce the real surface behavior.
In this work, our focus is on the thermo-mechanical modeling of frictional sliding systems. Comparing to the classical approaches, the architecture of our work incorporates additional steps which take into account the micro-contact behavior and the interaction between the contact interface and the global system behavior.
The architecture of this work is presented in Fig.7.2. Starting from a numerical large scale model and initial time t, the studied surface is identified and its initial topography is defined either from real surface measurements or numerical tools of surface generation (for e.g. fractal techniques). During a time step Δt and using the real surface topography, a micro contact analysis is done to define interface parameters that are integrated into a large scale thermo-mechanical analysis where the interface is flat(embedding strategy). This analysis is transient and covers the interval time Δt. Subsequently, a post process of the macro-scale stresses and temperatures issued from this calculation are integrated into a micro-scale post analysis. The objective of this step is to evaluate the impact of the macro-scale behavior on the contact interface, by considering wear process for instance. At the end of this step (i.e at $t + \Delta t$), the time of simulation is updated and a new micro-contact analysis is performed to evaluate the new interface parameters, and so forth until the time simulation ends.
As we can see, this strategy is made from multiple loops made from sequential steps where there is a continuous exchange between the macro-scale analysis and the micro-scale modeling. Note that the contact surface is divided into many zones, where each zone has its proper geometry and roughness. Thus, the micro-contact analysis is performed for each zone separately. Nevertheless, the interactions between these zones are considered in a macroscopic way. Indeed, the contact pressure (resp. the heat) applied in the other zones causes a displacement (a temperature elevation) in the considered surface element. This is what we call "macro-scale" interactions that are induced by the macro-scale contact system. In the micro-contact analysis, these features are considered as boundary conditions and are assumed not to be affected by the micro-contact analysis.
In order to give more details on the proposed strategy, Figs.7.3, 7.5 and 7.4 highlight each of the main steps of the model. In Fig.7.3, the micro-contact analysis is presented. In this step, the contact mechanics problem is solved and both the contact stiffness and the local contact pressure are identified using roughness parameters and material properties. Using the contact pressure and sliding parameters, the frictional heating problem is solved and heat partition coefficients and surface temperature are expressed

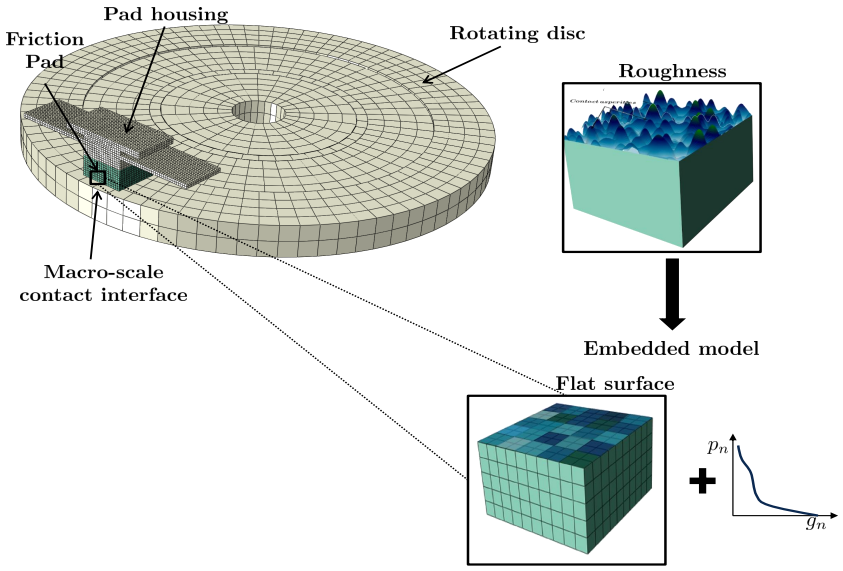

Figure 7.1: Schematic of a sliding contact application with the multiscale strategy. The real contact area is affected by roughness and its evolution with sliding. At the macro-scale, the surface is flat but embedded by the interface behavior considering roughness.

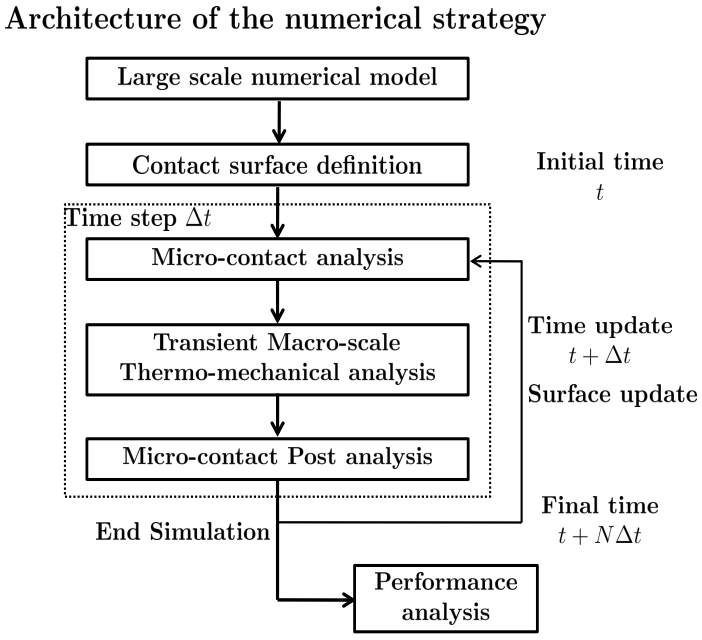

Figure 7.2: Architecture of the numerical strategy of contact modeling

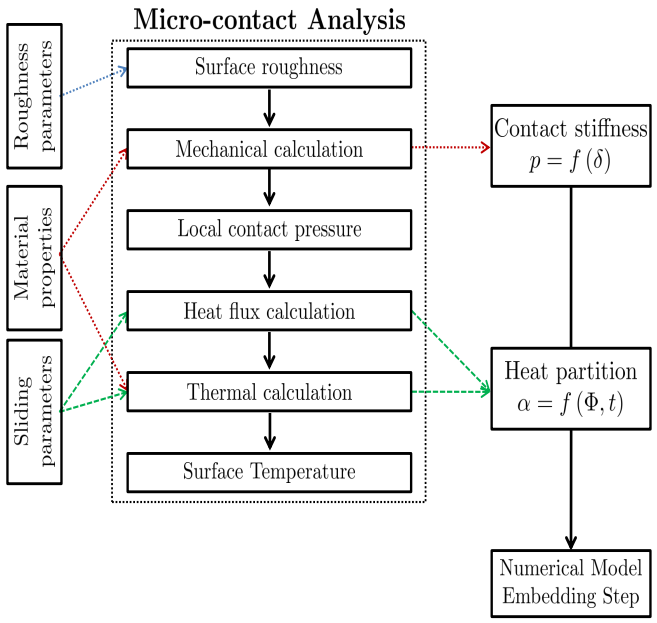

Figure 7.3: Steps of the micro-contact analysis which defines contact parameters

as a function of the contact pressure. At the end of this step, for each zone of the studied surface, the large scale numerical model is embedded with the computed interface parameters.
Fig.7.4 presents the large scale numerical analysis steps. It consists of a sequentially decoupled thermo-mechanical analysis. In this model, the static contact problem under sliding conditions is first solved. Then, the thermal transient problem is solved by converting the total power of contact shear stresses into heat. Heat is partitioned according to heat coefficient partition computed with the micro-contact model. Subsequently, the contact problem is solved by considering thermal expansion due to the rise of temperature. This operation is performed for a time step δt. At the end, the time is updated and the two operations are repeated sequentially until the total time increment Δt is reached. Furthermore, it is important to note that the two solids are mechanically connected by contact stiffness but their thermal degrees of freedom are totally disconnected. Indeed, heat is distributed directly using the heat partition coefficients that are issued from micro-contact calculations. Thus, the thermal conductance parameter is not used as it will go for the cooling stage which is not analyzed in this work.
From this macro-scale simulation, the post-process is done to obtain the distribution of contact pressure and the temperature. These data will serve to perform a micro-contact post analysis as presented in Fig.7.5. Indeed, for each contact zone, using the macro-scale pressure, the local pressure is obtained from the contact mechanics model. Using the thermal model, the micro-scale local surface temperature is obtained taking into account the macro-scale temperatures. The latter are uniform within the studied zone. With both these calculations, the micro contact data are computed based on macro-scale interactions.
Then, the surface topography is modified by considering the wear process. Indeed, wear is modeled with Archard's law using a wear rate coefficient depending on the surface temperature. Besides, wear analysis is conducted within the whole time step (from t to $t + \Delta t$) to consider a progressive evolution of the surface during this step time.
Once the surface of each contact zone is updated, the time is incremented and a new simulation is performed with the new surface topography. Note that the temperature obtained with the macro-scale simulation is integrated into both the subsequent macro-scale and micro-scale simulation as an initial temperature field.
Otherwise, it is important to note that several simplified assumptions have been considered : the friction coefficient is fixed, only one surface is worn, the thermal expansions are not considered at micro-scale and the micro-contact mechanics model does not consider the effect of friction on the contact distribution. Nevertheless, the two last points are considered at the macro-scale simulation level. In the following, a brief review of the micro-contact models is presented.

7.2.2 Micro-contact modeling

In order to solve the micro-contact problem for each zone of the contact surface, the surface of the considered zone is discretized into a grid made from $N_{xy} = N_x \times N_y$ small squares having the same size (see Fig.7.6). The studied interval of time $[0, t]$ is also discretized into N_t equal small intervals. The surface height, the stresses and the heat flux in each single square are assumed to be uniformly distributed on it. The material of the solid can be either homogeneous or heterogeneous by considering a multi-layered solid.
Several approaches can be used to solve the contact problem. In this work, we use the approach developed in [Waddad *et al.*(2017^d)]. This model is based on the discrete convolution and the FFT technique. Indeed, the pressure is a discrete convolution of the surface displacements. The problem is solved by minimizing a functional depending on the contact pressure and taking into account contact constraints.
By reporting the same concept to treat the thermal contact problem, both the thermal conduction and heat generation problems have been analyzed in [Waddad *et al.*(2017^b), Waddad *et al.*(2017^c)]. In the

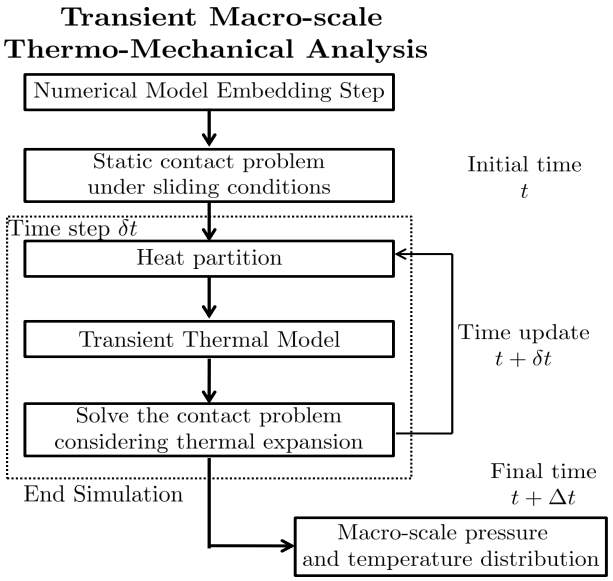

Figure 7.4: Steps of the macro-scale thermo-mechanical analysis

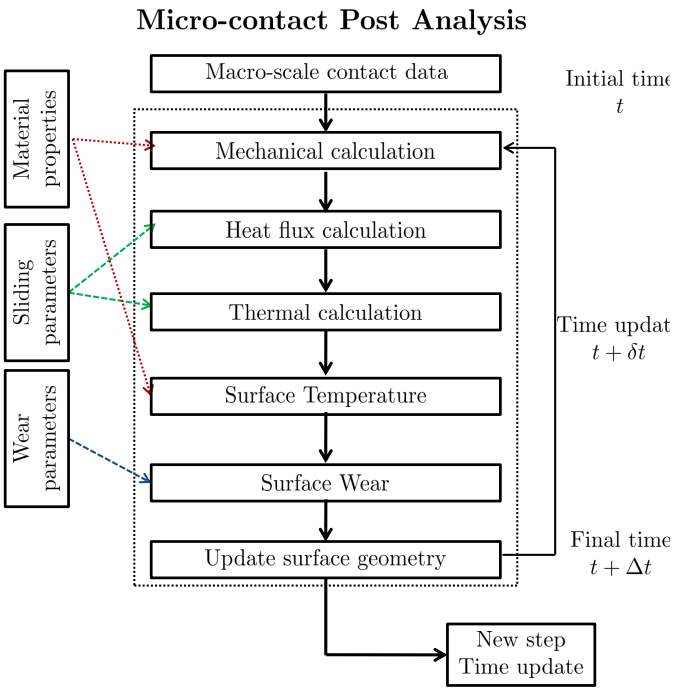

Figure 7.5: Steps of the micro-contact post analysis which updates the surface geometry

heat generation problem, the released energy is computed from the work of the frictional forces. Friction forces are computed from normal forces via a fixed friction coefficient. Here, we assume that friction does not modify the contact area and that the contact is entirely sliding. The interface is considered as a source of heat which is distributed over the superior face of each body. Moreover, the solving scheme is performed by matching the temperatures at the interface. Thus, within the real contact area, the temperature of the disc is equal to the temperature of the other solid. Additionally, remote temperatures are also considered as boundary conditions. By introducing an external heat, these temperatures could affect the heat distribution[Waddad *et al.*(2017[c])].

As regards wear modeling, this process is modeled with Archard's law using a wear rate coefficient. The volume of wear is obtained by summing the volumetric wear of each individual micro-contact [Waddad *et al.*(2017[d])]. Moreover, this coefficient depends on the local temperature of each micro-contact point. Indeed, wear increases with the temperature elevation caused by the frictional sliding. Otherwise, the volume of wear is assumed to leave the contact entirely. Therefore, no debris circulation and compaction are considered.

As is mentioned before, the micro-contact calculations are performed by considering the effect of the pressure and heat in the other surface elements in a homogenized way as boundary conditions. Note that this feature has not been considered in the previous works.

In the next section, we present a thermo-mechanical simulation considering the interface behavior and its evolution. The sliding contact application is a pin-on-disc system.

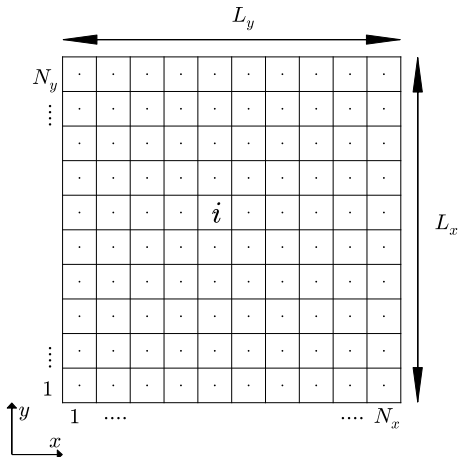

Figure 7.6: Schematic of the grid used for each surface element. The surface dimensions are $L_x \times L_y$ and contain $N_x \times N_y$ square elements

7.3 Description of the numerical model

7.3.1 Numerical model of a pin-on disc system

A 3D finite element model is proposed for a pin-on disc system which has been developed from a bench test designed in our laboratory [Duboc(2013)]. The model is made of several components. Essentially, there is a pin-housing, a disc and a friction pin maintained by a thin plate (see Fig.7.1 and 7.7). At the remote extremities of the thin plate a normal load $F = 200\,N$ is applied which permits to enforce contact between the pin and the disc.
Additionally, lateral displacements are blocked in the plate extremities and the disc is rotating with a constant velocity $\omega = 200\,rpm$. The outer radius of the disc is $107.5mm$ and the inner one is $12.5mm$. This corresponds to a dissipated power $P = 3.75kW$ which is constant in time. Contact is maintained for a period $t = 30s$, thus the total dissipated energy is $0.1\,MJ$.
The pin-housing, the thin plate and the disc are made of steel while the pin is made of a sintered material used for braking applications. Material properties are reported in Tab.7.2. The whole model is composed of 22100 hexahedron elements and 29800 nodes. For the pin, the mesh element size is fixed to $1 \times 1\ mm^2$. As regards thermal boundary conditions, the initial temperature is $T_0 = 20°C$. Moreover, the convection is not considered, as its influence is limited during the heating sequence. Thus, thermal diffusion simulation is conducted under adiabatic conditions. Note that all the parameters are reported in Tab.7.1.
As the model contains several components, the connection between a component and an other has to be defined appropriately. Thus, tie elements are introduced between the pin and the thin plate, and between the pin-housing and the plate, to ensure the perfect continuity between them. The contact between the disc and the pin, of which the dimensions are $20 \times 20mm^2$, is the main issue of this work. In order to highlight the effect of this interface, two kinds of models are proposed :

- In the first one, the contact is assumed to be perfect and the penalty method is chosen for this purpose. The contact is frictional and the friction coefficient is fixed to 0.4. Thus, the interface behavior is not considered in this model. Here, the classical thermo-mechanical modeling approach is adopted and no attention will be accorded to the interface effect (see Fig.7.4). Moreover, heat is distributed between the contacting solids using a constant and uniform heat partition coefficient

and wear is not considered.

- In the second kind, the interface behavior is considered. In this case, the interface is assumed to be rough. To simplify the study, only the roughness of the friction pin is considered and the disc surface is flat. Basing on the multi-scale strategy presented in the first section (see Figs.7.1-7.2), the interface behavior is integrated into the model. Moreover, a frictional behavior is also considered with the same friction coefficient used for the first model. For micro-scale calculations, each surface element is discretized into 50×50 elements. Thus, the size of each square element is $20 \times 20\,\mu m^2$.

Furthermore, the surface roughness of the pin has been generated numerically using fractal techniques[Persson *et al.*(2005)]. The root mean square (RMS) is $10.35\,\mu m$. The cutoff wave vectors are 1 and 50 and the fractal dimension is 0.6. The surface used in this study is shown in Fig.7.8.
As regards wear, the wear rate coefficient evolves depending on temperature. The evolution of this parameter is shown in Fig.7.9. The estimation of this parameter has been obtained from the experiments realized by [Mann(2017)] on the material used for the pin. Indeed, the weight loss of a sample has been measured during braking tests at different temperatures. From the loss of material, the wear rate has been deduced. As we can see from this figure, wear increases with temperature especially above $200°C$.

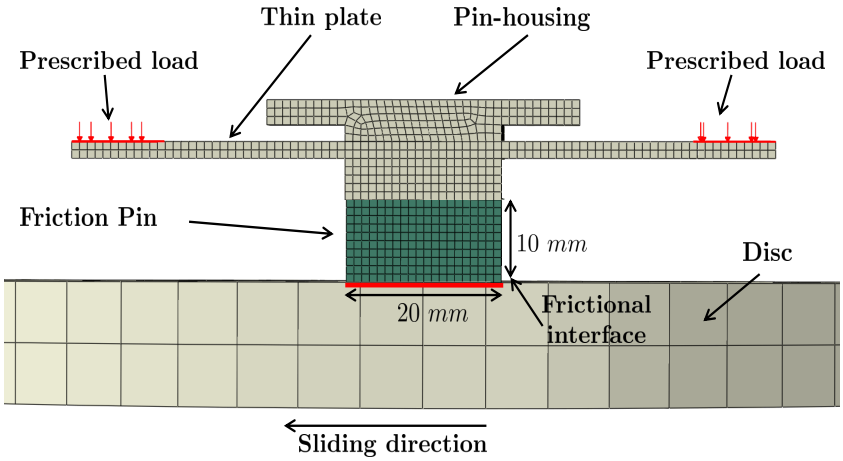

Figure 7.7: Schematic of the pin-on-disc model. The dimensions of the contact interface are $20 \times 20\,mm^2$

R_{min} (mm)	R_{max} (mm)	$\omega(rpm)$	T_0 $(°C)$	μ	$F(N)$	N_x	N_y	N_t	N	$t(s)$
80	100	200	20	0.4	200	50	50	10	50	30

Table 7.1: Parameters of the study

7.3.2 Results

For the two considered models (perfect contact and embedded contact), simulation results are presented in this section. For both cases, the contact pressure is shown for $t = 0.6s$ and $t = 30s$ in Fig.7.10. With

	$\chi\ (m^2/s)$	$\kappa\,(Wm^{-1}K^{-1})$	$E\ (GPa)$	ν	$\alpha\,(K^{-1})$
Friction Pad	$8.3.10^{-6}$	35	5	0.3	5.10^{-6}
Other components	10^{-5}	50	220	0.3	10^{-5}

Table 7.2: The contacting solids thermal and mechanical properties

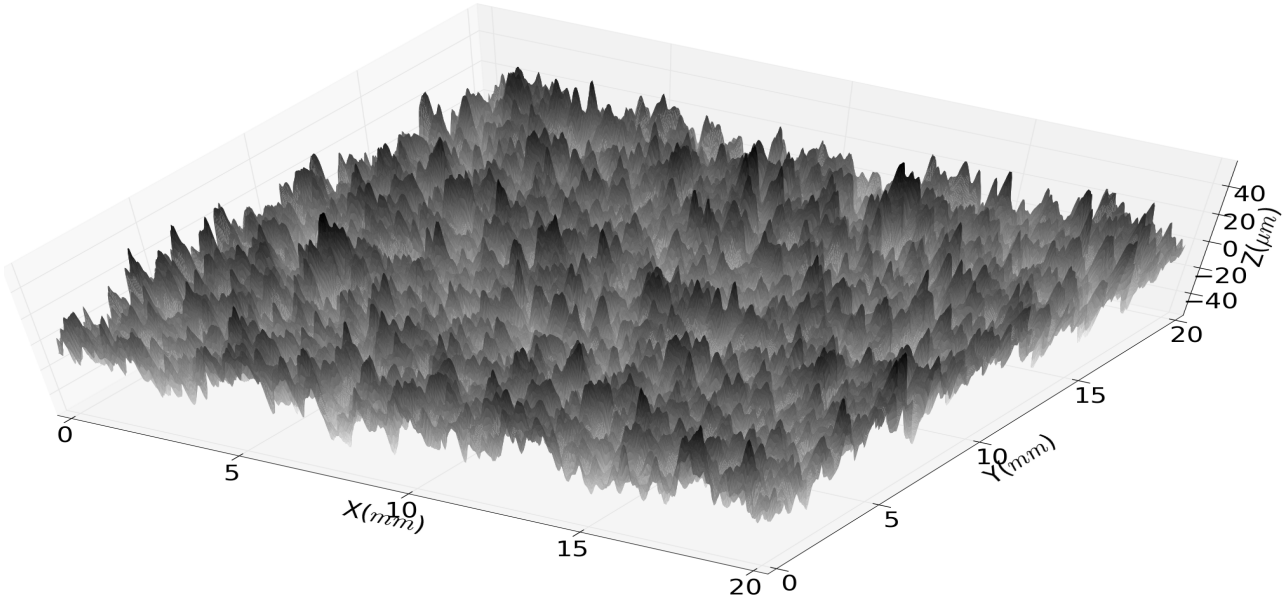

Figure 7.8: Schematic of the rough surface considered in this study. The surface height is comprised between -45 and 45 μm and the root mean square is $13\mu m$

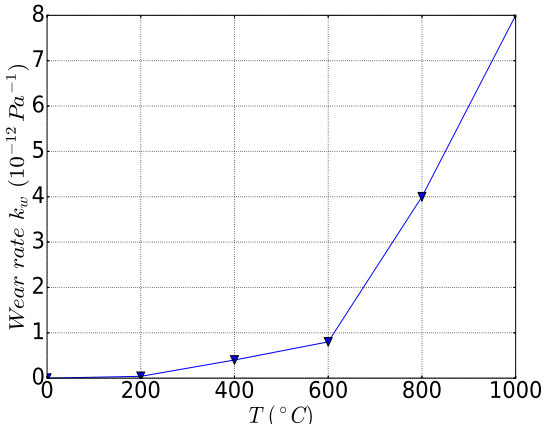

Figure 7.9: Evolution of the wear rate coefficient with the temperature level

regard to the case of perfect contact, the obtained distribution of pressure is classical, corresponding to the case of a static frictional contact, for which the maximal pressure is reached at the inner side of the

leading edge of the surface. The introduction of the interface behavior modifies the pressure distribution. As we can see, the contact pressure is concentrated within few zones which represent the macroscopic contact area. Furthermore, the consideration of wear reduces the maximum pressure and the contact load is better distributed with wear. Indeed, in the embedded model, the maximal pressure decreases with time from 6 MPa to 2.73 MPa after 30 s of contact, while in the perfect contact model, the pressure is quasi-steady since wear is not considered.

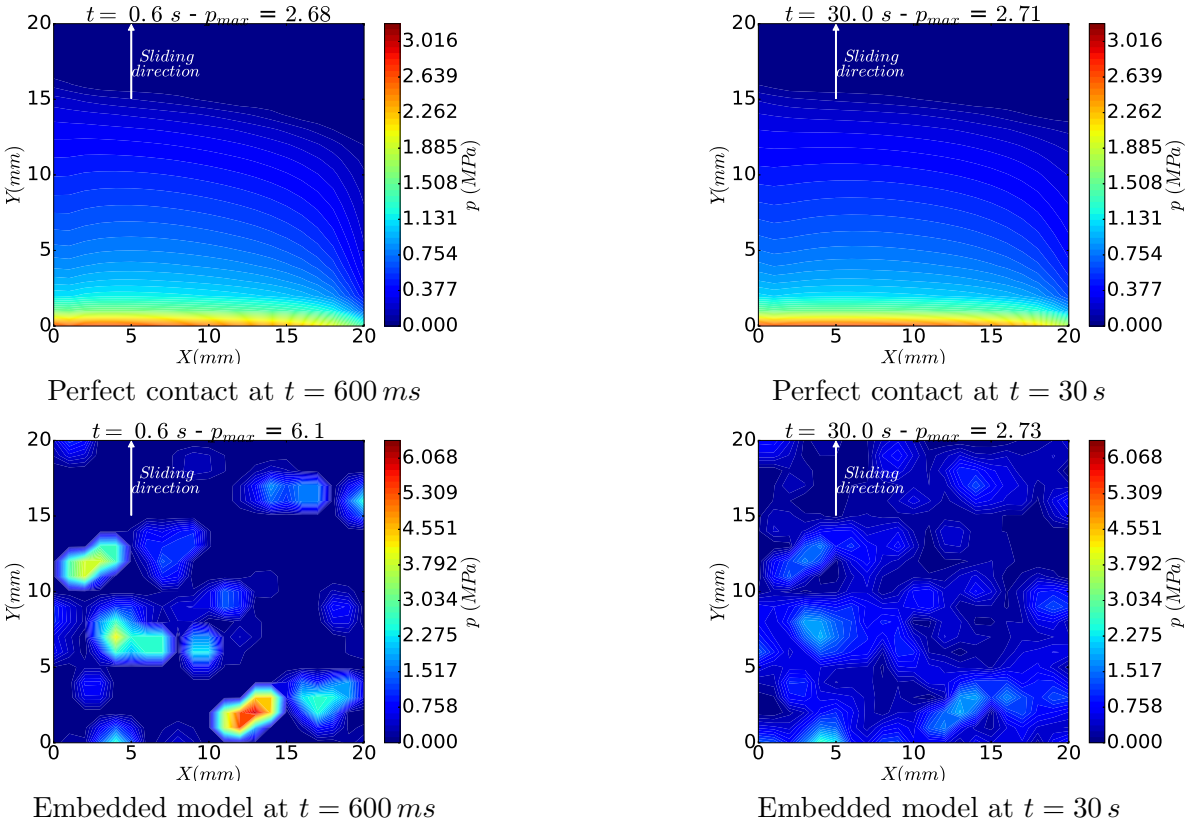

Figure 7.10: Evolution of the contact pressure in the frictional pin for the perfect contact case and the rough contact case

In Fig.7.11 are shown the corresponding surface temperatures for the two simulations. The high temperatures are reached in the zones where the contact pressure is locally high. For both simulations, considering the pressure distribution, the heated zones do not cover all the contact area. With thermal diffusion, the temperature increases with time in the zones where the pressure is weak. At ($t = 30\,s$), the maximal temperature is $50°C$ for the embedded model whereas for the perfect contact case its value is $64°C$. Initially ($t = 0.6\,s$), as we can see, the maximal temperature was reached in the embedded model rather than the perfect contact model. This evolution can be explained by the fact that in the embedded model, the pressure was high initially. With wear, the decrease of pressure in the initially loaded zones and the increase of pressure in the new contact zones, both have led to a reduced elevation of the maximal temperature comparing to the perfect contact model, where the pressure, subsequently the released heat, are both stabilized.

The temperature level depends mainly on the heat partition coefficients. As regards this parameter, the percentage of heat going to the friction pin depends on the radial position of the surface element and pressure. The maximal, minimal and mean coefficients evolution with time, for each surface element, are

shown in Fig.7.12. These coefficients correspond to the case of the embedded model and are obtained from micro-contact calculations. As can be seen from this figure, this percentage is quasi steady ranges from 10 to 21 % while the mean coefficient is 14%. On the other side, for the perfect contact model, the heat partition coefficient has been fixed to 14% corresponding thus to the mean coefficient of heat partition obtained from micro-contact calculations. The reason of this choice is to avoid a considerable gap of temperatures between the two models. However, if we had chosen a less coefficient as the one calculated from the thermal effusivity, this coefficient would be fixed to 4% which in turn would have led to lower levels of temperature. In this case, the maximal temperature in the perfect contact model would be $31°C$ instead of $64°C$. The difference between the two methods is due to the fact that micro-contact calculations are performed by matching the temperature at the interface considering the velocity and the real contact area. In contrast, the coefficient computed with effusivity does not consider these aspects.

Other interesting informations are the micro maximal pressure and temperatures. These variables are

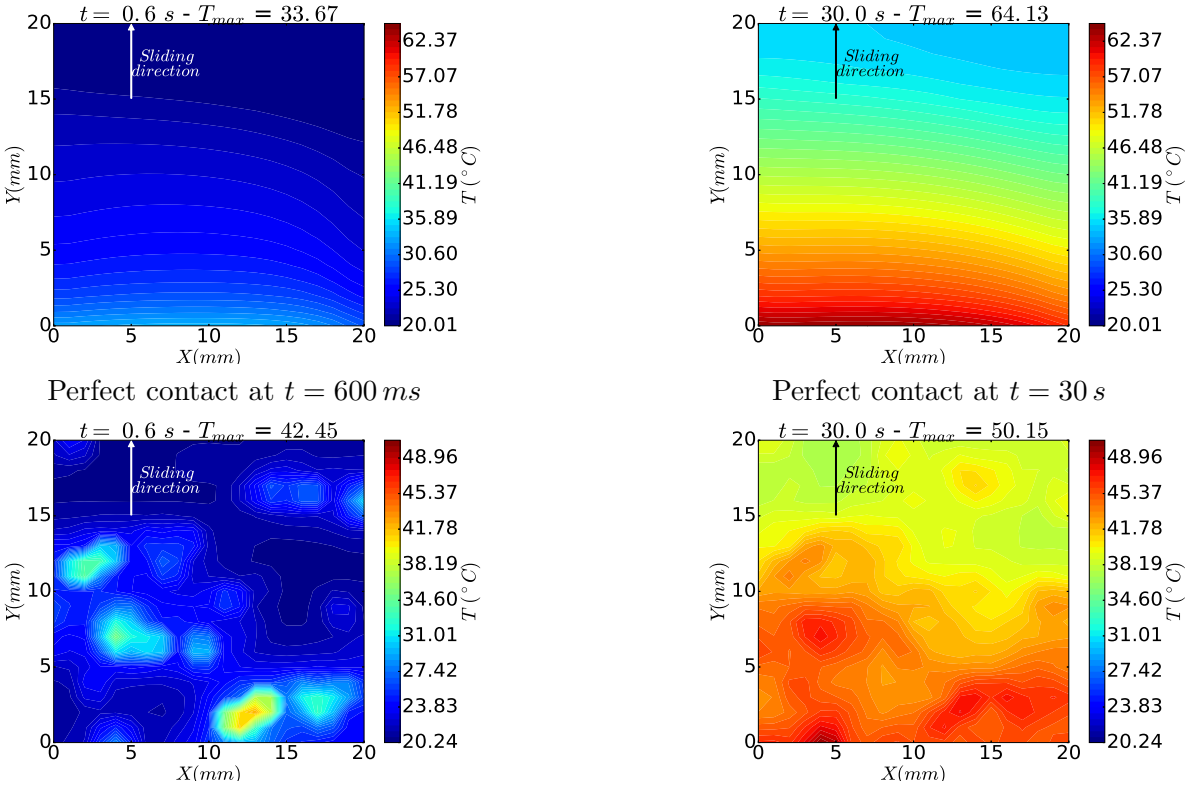

Figure 7.11: Evolution of the surface temperature in the frictional pin for the perfect contact case and the rough contact case

obtained from micro calculations and concern only the embedded model. Fig.7.14 (resp. Fig.7.15) shows the evolution of the maximal pressure (resp. the maximal temperature) with time. In the same graphs, the evolution of the corresponding macroscopic values is also shown.

On one side, as we can see from these curves, the micro-contact variables decrease with time until they reach a stabilized evolution, while the macroscopic ones vary slightly. The sharp decrease of the micro data is essentially due to wear. Indeed, wear leads to the creation of flat zones in place of the initial asperities, leading thus to well distributed mechanical and thermal loads. Also, one can remark that the maximal micro temperature approximates the macro scale one, as time continues forward. On the other

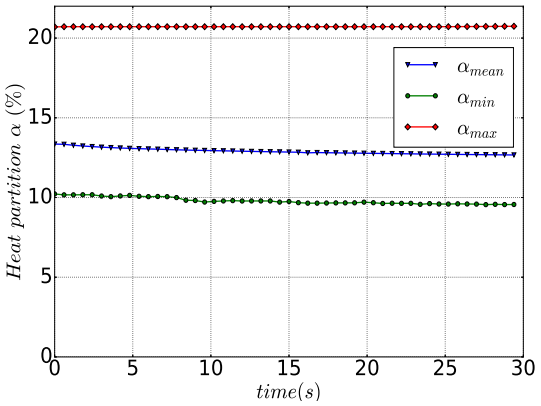

Figure 7.12: Evolution of the heat partition coefficient with time for the embedded model

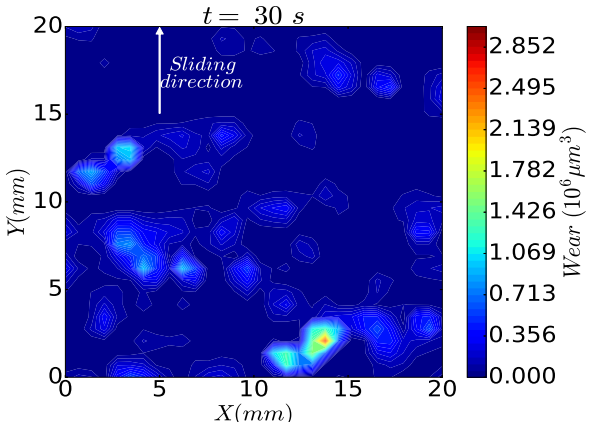

Figure 7.13: Macro-scale wear map in the embedded model

side, the slight increase of the macro-scale temperature is due to the diffusion process and the decrease of pressure.
The micro-contact analysis is prominent since it gives an information about the evolution of local data which are a source of local damage and melting. Thus, the FEM model plays a key role in defining the macro-scale interactions between the different contact zones, while the micro-contact analysis gives a refined response at the scale of surface asperities.

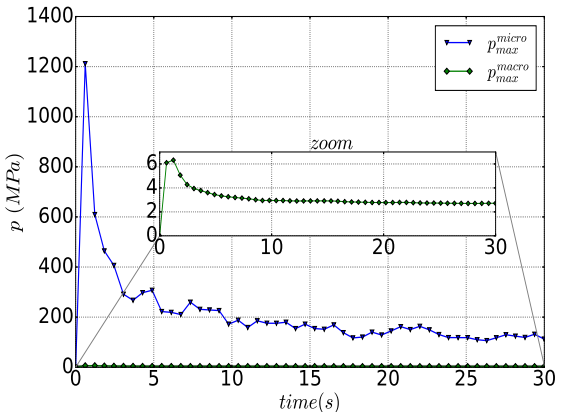

Figure 7.14: Evolution of the maximal pressure at both scales for the embedded model

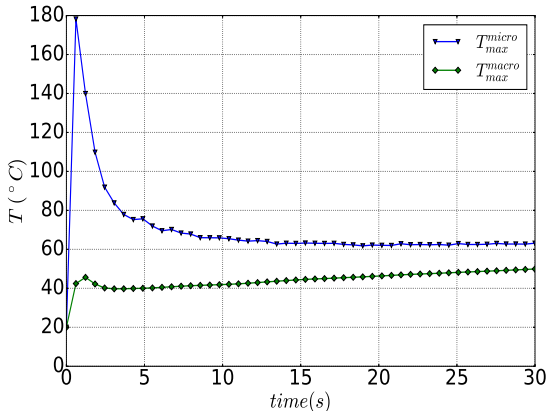

Figure 7.15: Evolution of the maximal temperature at both scales for the embedded model. The micro-scale temperature is the same for the disc and the pin.

Furthermore, Fig.7.16 presents the evolution of wear volume during contact and Fig.7.17 the corresponding maximal wear depth. From the two figures, one can see that wear is maximal in the beginning, then the slope of its evolution decreases with time. The maximal wear depth at $30\,s$ is $28\,\mu m$ and the total wear volume is $38.10^6 \mu m^3$. The decrease of these quantities follows the decrease of both pressure and temperature. Thus, wear becomes steady with time within this interval of time. Moreover, Fig.7.13 shows a macro-scale wear map of the contact surface at the end of simulation. The distribution of wear volume

corresponds to contact zones where the pressure and temperature are high.
Otherwise, one could expect a different evolution if, for instance, the studied interval time or the rotating speed or the load were greater than the ones considered in this study. Indeed, as shown in the different figures, and especially the ones that show the distribution of pressure and temperature fields, the variation of these fields is a bit soft and there is no sharp changes in the macro distribution of the contact. Hence, it will be interesting to go beyond the loading parameters chosen for this simulation. In addition, the surface roughness RMS evolution is shown in Fig.7.18. From this graph, one can see that the initial RMS has been reduced by almost $0.2\,\mu m$ which is too low comparing to the roughness amplitude of the surface. Hence, the rough surface has been subjected to mild wear during $30\,s$ of contact.
Furthermore, for the embedded model, the surface temperature of the disc is shown in Fig.7.19. Comparing to the pin surface, the rise of temperature is very low. Nevertheless, it is important to note that micro-contact calculations predict the same surface temperature for the disc and the pin, which is not the case at macro-scale calculations. Also, the shape of temperature field looks like hot bands or rings. Note that this gradient of temperature is similar to the one obtained with the perfect contact model. Also, one can see that there is many large thermal localizations which are mainly due to the disc size mesh, which is larger than the one considered for the friction pin.
Finally, concerning the computational time, this simulation has been performed within almost 6 days. At each time increment, the micro-contact calculations are parallelized and last almost $60\,min$ while the macro-scale analysis lasts about $2\,h$. For information, these calculations have been performed with a machine containing 5 multi-core processors, where each processor contains 16 cores.
The consideration of the micro-contact phenomena have increased the computational time by almost 30% of the necessary time for a classical macro-scale calculation. As the simulation was focused specially on the pin surface, the disc data analysis needs a more refined mesh to capture precisely the thermal gradient on its surface, which in turn will considerably increase the computational time.

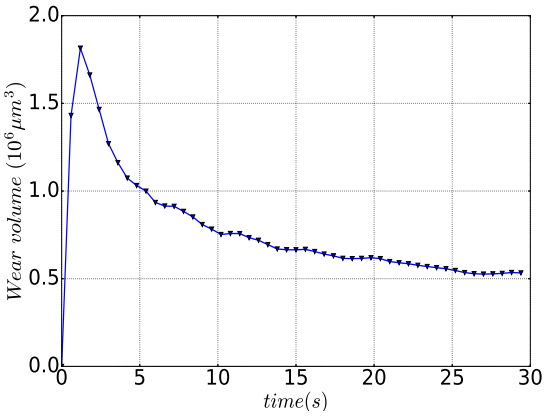

Figure 7.16: Wear volume evolution through the simulation of the embedded model. The total cumulated wear volume at $30s$ of braking is $38.10^6 \mu m^3$

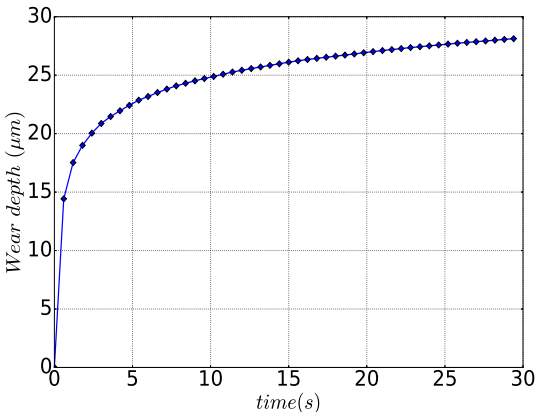

Figure 7.17: Evolution of the maximal wear depth in the embedded model. The maximal cumulated wear depth is $28\,\mu m$

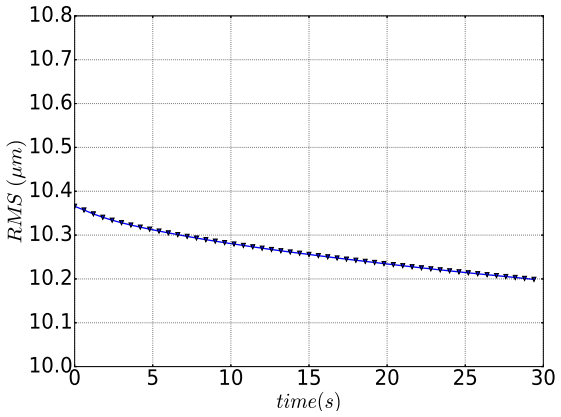

Figure 7.18: Decrease of the surface roughness root mean square with the wear process.

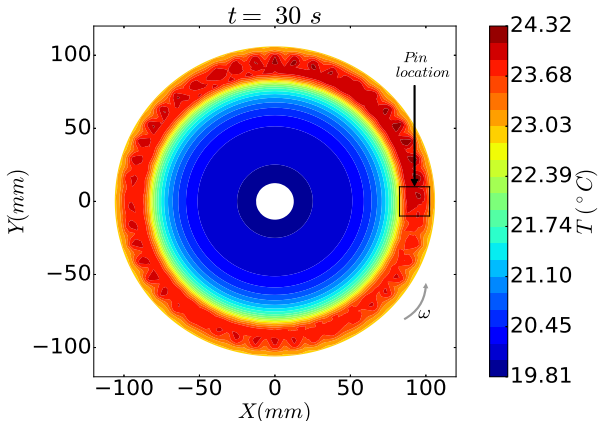

Figure 7.19: Surface temperature of the disc in the embedded model

7.4 Conclusions

A multi-scale thermo-mechanical strategy has been presented in this work to model complex systems including frictional contact. This strategy considers both the system's scale and the local contact interface behavior and evolution. The interface modeling is devoted to thermal, mechanical and wear issues.
At the macro-scale, a classical FEM approach considering a flat contact between the mating solids, thermal expansion and boundary conditions, is adopted. In order to integrate the micro-contact features, the studied interface is embedded with several parameters issued from micro-contact calculations like heat partition coefficients and contact stiffness and conductance.
Micro-contact modeling has been extended from previous works. Some aspects and assumptions of the models that we have used in this study have been briefly presented. Basically, these models consist of discretizing the surface and using the discrete convolution with the FFT technique. The thermal and mechanical problems are both solved with constrained optimization algorithms. As regards wear modeling, the classical Archard's model was used with a wear rate coefficient depending on temperature. As an example of the strategy, we have presented a pin-on-disc system that is used to characterize materials for braking application. A sliding contact sequence has been studied considering the interface evolution. The obtained results show a smooth and slight variation of macro-contact data. By contrast, the micro-contact analysis shows a considerable decrease of micro-contact data (local pressure and temperature) with time due to wear, which is stabilized within few seconds. Moreover, the consideration of micro-contact analysis gives additional informations on thermal and stress localizations, wear volume spatial distribution and time evolution.
The multi-scale strategy proposed in this work exhibits the strong interactions presents between the interface scale and the system's one during time. It constitutes an efficient basis toward more realistic modeling approaches of contact applications. Indeed, several improvements can be done, in particular by considering micro-scale thermal expansions that could modify the contact area. Moreover, wear modeling can be improved by considering an appropriate wear model/wear rate for the studied contact system. Furthermore, the wear volume is assumed to leave entirely the contact zone, while it is well known that a considerable part of wear particles integrate what is commonly known as the tribologic circuit. Finally, the evolution of material properties has not been considered in this work. For instance, it will be interesting to investigate, in future works, the case where a gradient of properties already exist using a micro-contact

model adequate to this situation as the one we have developed in the previous works.

Bibliography

[Archard(1953)] Archard, J. F. *Contact and rubbing of flat surfaces*. Journal of Applied Physics, 1953, 24(8), 981-988.

[Archard(1959)] Archard, J. F. *The temperature of rubbing surfaces*. Wear, 1959, 2(6), 438-455.

[Blok(1937)] Blok, H. *Theoretical Study of Temperature Rise at Surfaces of Actual Contact under Oiliness Conditions*. Proc. Inst, of Mechanical Engineers General Discussion of Lubrication, 1937, 2, 222-235.

[Carslaw and Jaeger(1959)] Carslaw, H. S., & Jaeger, J. C.*Conduction of heat in solids*. Oxford: Clarendon Press, 1959

[Ciavarella *et al.*(2006)] Ciavarella, M., Delfine, V. & Demelio, G. *A re-vitalized Greenwood and Williamson model of elastic contact between fractal surfaces*. Journal of the Mechanics and Physics of Solids, Elsevier, 2006, 54, 2569-2591

[Cooper *et al.*(1969)] Cooper, M. G., Mikic, B. B., & Yovanovich, M. M. *Thermal contact conductance*. International Journal of heat and mass transfer, 1969, 12(3), 279-300.

[Day and Newcomb(1988)] Day, A..J & Newcomb, T.P. *The dissipation of frictional energy from interface of an annular disc brake*. Proc. Inst. Mech. Eng. Part F: J Rail Rapid Transit, 1988, 202, 91-99.

[Duboc(2013)] Duboc, M., *Etude multi-échelle du crissement : dispositif expérimental et éléments de compréhension*. Université de Lille , 2013

[Dufrénoy and Weichert(2003)] Dufrénoy, P., & Weichert, D. *A thermomechanical model for the analysis of disc brake fracture mechanisms*. Journal of Thermal Stresses, 2003, 26(8), 815-828.

[Dufrénoy *et al.*(2016)] Dufrénoy, P., Magnier, V., Waddad, Y., Brunel, J. F., & De Saxcé, G. *A Multiscale Model of a Disc Brake Including Material and Surface Heterogeneities*. SAE Int. J. of Passenger Cars-Mechanical Systems, 2016, 9, 1136-1143.

[Gallego *et al.*(2010)] Gallego, L., Nelias, D. & Deyber, S. *A fast and efficient contact algorithm for fretting problems applied to fretting modes I, II and III*. Wear, 2010, 268, 208–222.

[Greenwood and Williamson(1966)] Greenwood, J. & Williamson, J. *Contact of nominally flat surfaces*. Proceedings of the Royal Society of London. Series A. Mathematical and Physical Sciences, The Royal Society, 1966, 295, 300-319

[Hetzler and Willner(2012)] Hetzler, H. & Willner, K. *On the influence of contact tribology on brake squeal*. Wear, 2012, 46, 237-246

[Johnson(1987)] Johnson, K. L. *Contact mechanics*. Cambridge university press, 1987

[Kao *et al.*(2000)] Kao, T., Richmond, J.W., Douarre, A. *Brake disc hot spotting and thermal judder: an experimental and finite element study.* Int. J. Vehicle Des., 2000, 23, 276-296.

[Kato(2000)] Kato, K. *Wear in relation to friction—a review.* Wear, 2000, 241(2), 151-157.

[Kato(2002)] Kato, K. *Classification of wear mechanisms/models.* Proceedings of the Institution of Mechanical Engineers, Part J: Journal of Engineering Tribology, 2002, 216(6), 349-355.

[Masen(2005)] Masen, M. A., De Rooij, M. B., & Schipper, D. J. *Micro-contact based modelling of abrasive wear.* Wear, 2005, 258(1), 339-348.

[Meng(1995)] Meng, H. C., & Ludema, K. C. *Wear models and predictive equations: their form and content.* Wear, 1995, 181, 443-457.

[Mikic(1974)] Mikić, B. B. *Thermal contact conductance, theoretical considerations.* International Journal of heat and mass transfer, 1974, 17(2), 205-214.

[Newcomb(1960)] Newcomb, T.P. *Temperatures reached in disc brakes.* J. Mech. Eng. Sci., 1960, 2(3), 167–177.

[Pei(2005)] Pei, L., Hyun, S., Molinari, J. F. & Robbins, M. O.*Finite element modeling of elasto-plastic contact between rough surfaces.* Journal of the Mechanics and Physics of Solids, 2005, 53, 2385-2409

[Persson *et al.*(2005)] Persson, B., Albohr, O., Tartaglino, U., Volokitin, A. & Tosatti, E. *On the nature of surface roughness with application to contact mechanics, sealing, rubber friction and adhesion.* Journal of Physics: Condensed Matter, IOP Publishing, 2005, 17, R1-R62

[Mann(2017)] Mann, R., *Experiments and thermomechanical modelling of braking application and friction material characterization with loading history effect.* Université de Lille , 2017

[Waddad *et al.*(2016)] Waddad, Y. , Magnier, V. , Dufrénoy, P. & De Saxcé, G. *A multiscale method for frictionless contact mechanics of rough surfaces.* Tribol. Int., 2016, 96, 109-121.

[Waddad *et al.*(2017^a)] Waddad, Y. , Magnier, V. , Dufrénoy, P. & De Saxcé, G. *A new contact model for multi-layered solids with rough surfaces.* In preparation.

[Waddad *et al.*(2017^b)] Waddad, Y. , Magnier, V. , Dufrénoy, P. & De Saxcé, G. *Heat conduction in multi-layered solids with rough surfaces.* In preparation.

[Waddad *et al.*(2017^c)] Waddad, Y. , Magnier, V. , Dufrénoy, P. & De Saxcé, G. *Heat partition and surface temperature in sliding contact problems.* In preparation.

[Waddad *et al.*(2017^d)] Waddad, Y. , Magnier, V. , Dufrénoy, P. & De Saxcé, G. *Numerical analysis of wear in a rough contact for multi-layered solids.* In preparation.

[Willner(2008)] Willner, K. *Fully coupled frictional contact using elastic halfspace theory.* Journal of Tribology, American Society of Mechanical Engineers, 2008, 031405, 1–8.

[Williams(1999)] Williams, J. A. *Wear modelling: analytical, computational and mapping: a continuum mechanics approach.* Wear, 225, 1-17.

Conclusions and prospects

The development of efficient, reliable and durable friction brake systems remains one of the most essential challenges in the urban transportation industry. In these applications, the contact interface separating the static part and the moving part is central to the system functioning, as it represents the place where the mechanical energy is dissipated.
Clearly, friction transforms energy into heat, leading thus to increasing temperature which can be harmful to the disc and the friction material (wear, damage, cracks, etc.). Also, a small part of energy can be converted into acoustic energy contributing to noise pollution (e.g. squeal). Thus, the knowledge of the phenomena governing in the contact interface is crucial to improve braking systems with respect to the different requirements to which they are subjected.
As regards the contact interface, when two solids are mating with each other, the real contact area is much smaller than the apparent one. The knowledge of this area is important as it influences the different exchanges between them (e.g. bearing load and heat transfer). In fact, solid bodies have rough surfaces, leading thus to the creation of separated contact spots where the asperities of the mating surfaces are in contact. Hence, these exchanges are mainly performed through these spots. Furthermore, the real contact area evolves constantly considering contact phenomena (e.g. thermal and mechanical loadings and wear). In particular, material removal due to wear, modifies the surface topography and consequently affects the contact interactions. Conversely the system modifies the loading conditions and consequently the contact surface area. This interaction between scales plays a key role in the system behavior and should be considered in its development.
To address contact issues, manufacturers had implemented solutions which are based on the use of feedback based tests. However this kind of methods is very costly and inefficient in front of the new technical and environmental requirements. Furthermore, experiments can not measure contact surface data (e.g. temperature, pressure, contact area, etc). Therefore, theoretical modeling and numerical simulations can help to fill this gap, benefiting thus from the recent advances in the computing industry.
Thus, the objective of the present work is to propose a numerical strategy consisting in modeling macro-scale contact applications like braking systems with realistic assumptions made at the contact interface considering micro-contact phenomena, unlike the classical approaches which assume surface flatness and perfect contact conditions. This challenge has been overcome by building a methodology which associates a large scale Finite Element model of the system and several refined micro-contact models considering only the interface and covering the thermal, mechanical and wear features.
To address the problematic of the thesis, we analyzed in the first part the contact mechanics issue, while in the second one, we studied the thermo-mechanical contact behavior. In the two parts, we presented the key elements of micro-contact modeling and analyzed their predictions. Then, contact applications have been studied with the aim of investigating the role of the interface in their behavior.

In the first chapter of the thesis, we developed a contact model that considers surface asperities as elliptic paraboloids which interact with each other. The analysis is performed by minimizing an objective function based on contact kinematic constraints. The obtained results point out the role of interactions in defining contact stiffness. Moreover, the predictions of the micro-contact model are consistent with the classical contact theories. Thereafter, this model has been used to embed a numerical large scale model using a non-linear stiffness of the penalty method. This strategy has been verified with finely meshed Finite Element resolutions. Also the computational time was considerably reduced from several hours to a few minutes.
In the second chapter, the micro-contact model has been extended to study the case of solids with a normal gradient of elastic properties. This model considers the material as a multi-layered system and uses the concept of the transfer matrices. Then, the one asperity problem has been solved with Abel transform. The obtained solution has been used to develop a contact model for rough surfaces. Here again, the results have been compared to Finite Element calculations. Besides, the effect of the elastic properties of solid layers on stiffness and contact area has been shown.
Since the contact is sliding in braking systems, the effect of wear has been introduced by assuming a fully sliding state. Also, it has been assumed that friction forces do not modify the contact area. Thus, we adopted the Coulomb's law of friction to calculate the frictional work responsible for wear. Furthermore, wear has been modeled with Archard's law considering a wear rate coefficient. Here, the total volume of wear is obtained by summing all the volumetric volumes at contact points. Furthermore, to solve this problem, we considered that the surface is discretized into many square elements instead of asperities. This choice has been made to take advantage of the linearity of this solution and to avoid the complexity of analytic terms in asperity based solutions. Moreover, the FFT technique has been used to accelerate the resolution scheme.
With this model, two parametric studies have been carried out with the aim of showing the effect of wear step and the influence of solid layers on wear. In particular, results show that a compliant surface layer decreases the local pressure, stiffness and the amount of wear, and increases the contact area.
The last chapter of the first part has been devoted to study the influence of the contact interface on the dynamic behavior of a complete brake system. The objective of this work was to identify the effect of surface roughness on modal coupling that could lead to instabilities in the presence of friction. For this, a Finite Element Analysis of a complete brake has been conducted using the embedding strategy presented in the first chapter. This analysis consisted in a quasi-static stress analysis followed by a complex eigenvalue analysis to identify the system frequencies and modes. These calculations have been performed on several samples. From the results, the link between the interface behavior and the modal coupling was clearly shown. Indeed, braking system instabilities are strongly affected by the interface behavior. The modification of contact parameters may conduct some unstable modes to become stable and some eigenvectors to lock-in. Moreover, it has been observed that the variability of the dynamic behavior is more relevant especially at high frequencies for which the friction pad behavior is more influent.

After analyzing the mechanical aspects of the contact problem in the first part, we addressed the thermal features in the second part, with the objective of studying the thermo-mechanical behavior of sliding contact systems.
In the fifth chapter, heat conduction through a rough interface has been analyzed considering a static contact, a steady state and a normal gradient of thermal and mechanical properties. This problem has been solved using Fourier transform and the transfer matrix technique to consider the gradient of properties. The obtained results have been compared to FEM calculations and a good agreement has been found between the two methods. A parametric study has been carried out and the studied cases demonstrate the great impact of roughness, solid-layers and local thermal resistance on the thermal conductance.

Thereafter, the frictional transient heat generation has been considered in the penultimate chapter. This problem has been solved with the heat source method and the FFT. From this model, heat partition coefficients and surface temperature have been computed for several case studies considering roughness, velocity profile, contact interface conditions, heat profile, etc. The results show that heat partition essentially depends on solids velocities and the ratio between the contacting solids conductivities. Also the contact area seems to slightly affect this parameter but affects mainly the surface temperature. Furthermore, it has been shown that the thermal phenomena are very fast. Indeed, the maximal temperature is reached within few milliseconds if the rate of heat is steady within time.
Moreover, heat conduction in sliding contact problems, has been analyzed under stationary assumptions considering a gap of bulk temperature between the two bodies in contact. Results show that a temperature difference between solids causes a heat flowing through the interface which affects considerably the partition of heat and the temperature field. For low velocities, this additional heat has a major impact on surface temperature. If the speed or the contact area are high, the frictional heat increases which reduces considerably the impact of heat conduction on the distribution of heat.
Finally in the last chapter, a multi-scale analysis of a pin-on-disc system is presented, considering all the studied micro-contact features in this thesis. At the macro-scale, a classical FEM approach considering a flat contact between the mating solids has been adopted. Then the interface has been embedded with contact parameters obtained with micro-contact calculations like heat partition coefficients, contact stiffness and conductance. The role of the micro-contact behavior in modifying the contact pressure and the temperature fields is clearly shown. Moreover, the micro-scale calculations give information on local contact surface data, considering the macro-scale interactions, which is hardly feasible from an experimental point view.

From the results of this thesis, we clearly highlight the role of the micro-contact features in the definition of the macro-scale system behavior. Nevertheless, to improve this research work, there are considerable key points that have to be addressed in future works. First, to get more reliable results, it is necessary to perform more parametric studies by varying several parameters such as roughness, material properties, loading and velocity. In particular, with regards to surface roughness, all the calculations have been performed on some numerical samples generated with a given spectrum density. It would be interesting to realize more parametric studies on real measured surfaces and to extend the study to cover a broad range of wave vectors.
Second, regarding the multi-scale modeling strategy, some of the main points that could be enhanced are reported in the following :

- The computational time could be more optimized. This could be done by modeling only the steady thermal micro-contact problem. Indeed, the micro-contact phenomena are very fast comparing to the macro-scale ones. Thus, the consideration of the steady problem should not influence significantly the obtained solution. Conversely, this will reduce considerably the computational time necessary for micro-contact calculations.

- The macro-scale thermal boundary conditions consider that the external faces are free from any prescribed heat conditions. This aspect was not considered in the thermal micro-contact problem as the medium at this scale is considered as a half space. Therefore, to improve this point, the solution considering bulk temperatures effect could be used for this issue. These temperatures are induced by heat accumulation which could differ between the two bodies.

- The friction material is heterogeneous and has a complex behavior that has not been addressed in this study as we focused on the surface effect and only the normal gradient of properties was

studied. In fact, friction materials contain several components with different sizes and behaviors. With loading effects, the friction material properties evolve considerably (damage and visco-elasto-plastic behavior). Thus, it will be worthy to address these features as they could modify the contact properties.

- With the high localized temperatures reached within the micro-scale contact interface, the thermal expansion could be considered as it could affect the contact area and the distribution of contact stresses.

Other features that could be also considered, at mid-term, concern wear and the third body modeling. These points are listed below :

- Wear modeling could be improved with a convenient law considering material properties and the predominant wear mechanisms (abrasion, adhesion,etc.). This can be performed by analyzing these mechanisms at more refined scales using for instance particle based methods. The chosen scale depends on the material properties and the predominant mechanism of wear. Besides, this could result in an additional embedding which considers these low scales.

- Wear volume is assumed to leave entirely the contact interface while a part of it integrates the tribological circuit. The circulation of wear debris, the creation of the third body by their compaction and its damage modifies the contact dynamic and temperature. Modeling of the third body is strongly linked to wear modeling, as wear mechanisms define the process of material removal. Therefore, it is interesting to propose a strategy to model these issues.

Finally, experimental tests must be conducted to measure the different physical parameters used in this work, and then, the multi-scale strategy can be verified by comparing simulation results with experimental measurements conducted in dyno tests for instance.